

From Structural Complexity to Structure-Property Relationships in Intermetallics:
Development of Density Functional Theory-Chemical Pressure Analysis

By

Joshua Engelkemier

A dissertation submitted in partial fulfillment of the requirements for the degree of

Doctor of Philosophy

(Chemistry)

at the

UNIVERSITY OF WISCONSIN-MADISON

2016

Date of final oral examination: 27 May 2016

This dissertation is approved by the following members of the Final Oral Committee:

Daniel C. Fredrickson, Associate Professor, Chemistry

J. R. Schmidt, Associate Professor, Chemistry

Kyoung-Shin Choi, Professor, Chemistry

Clark R. Landis, Professor, Chemistry

Dane Morgan, Professor, Materials Science and Engineering

© 2016 Joshua Michael Engelkemier

ALL RIGHTS RESERVED

Abstract

The unparalleled structural diversity of intermetallic compounds provides nearly unlimited potential for the discovery and optimization of materials with useful properties, such as thermoelectricity, superconductivity, magnetism, hydrogen storage, superelasticity, and catalysis. This same diversity, however, creates challenges for understanding and controlling the unpredictable structure of intermetallic phases. Moreover, the fundamental design principles that have proven so powerful in molecular chemistry do not have simple analogues for metallic, solid state materials.

One of these basic principles is the concept of atomic size effects. Especially in densely packed crystal structures where the need to fill space is in competition with the atoms' preferences for ideal interatomic distances, substitution of one element in a compound for another with similar chemical properties yet different atomic size can have dramatic effects on the ordering of the atoms (which in turn affects the electronic structure, vibrational properties, and materials properties). But because the forces that hold metallic phases together are less easily understood from a local perspective than covalent or ionic interactions in other kinds of materials, it is usually unclear whether the atoms are organized to optimize stabilizing, bonding interactions or rather forced to be close together despite repulsive, steric interactions.

This dissertation details the development of a theoretical method, called Density Functional Theory-Chemical Pressure (DFT-CP) analysis, to address this issue. It works by converting the distribution of total energy density from a DFT calculation into a map of chemical pressure through a numerical approximation of the first derivative of energy with respect to voxel volume. The CP distribution is then carefully divided into contact volumes between neighboring atoms, from which it is possible to determine whether atoms are too close together (positive CP) or too far away from each other (negative CP).

This technique is used in combination with the concept of structural plasticity (Berns, 2014) to demonstrate how complex intermetallic phases can be understood as a response of simpler structure types to the destabilizing buildup of CP. From this point of view, interfaces created in complex structures relieve the CP manifest in the more basic, parent structures. This is shown specifically for $\text{Ca}_{36}\text{Sn}_{23}$ relative to a hypothetical W_5Si_3 -type Ca_5Sn_3 phase, LnMn_xGa_3 ($\text{Ln} = \text{Ho-Tm}, x < 0.15$) compared to unstuffed AuCu_3 -type LnGa_3 structures, and structural derivatives of CaCu_5 - and HoCoGa_5 -type compounds.

As a direct result of the technical developments necessitated by these analyses on structural complexity in intermetallics, a further connection is made in this thesis between the calculated CP schemes and the frequencies of vibrational modes in MgCu_2 -type CaPd_2 , the Cr_3Si -type superconductor Nb_3Ge , and CaCu_5 -type CaPd_5 . Local chemical interactions revealed by DFT-CP analysis are used to identify structure-property relationships for the pseudogap in the phonon density of states (DOS) of CaPd_2 , the higher critical temperature of Nb_3Ge vs. Nb_3Sn , and the wide diversity of structures based on the CaCu_5 type.

To my friends and family, for the inspiration to keep moving forward.

Acknowledgements

Graduate school has been an intense period of growth – intellectually, professionally, and even emotionally – but it’s the people I’ve encountered along the way that have made it worthwhile.

I was fortunate to join the Fredrickson group at the start of my graduate career, although I had no inclination toward solid state chemistry at the time. Danny, I appreciate your continuous enthusiasm for science, your understanding in hard times, and your passion for quality in your students as well as your research program.

Without the faithful crew of the Chemical Pressure rowboat, I couldn’t have possibly made it safely to harbor. Veronica, you’ve been a mentor, a friend, and an inspiration. You taught me so much more than chemistry. Yiming, you’ve graciously helped me countless times, and I’m grateful to have gone through this experience with you. Brandon, I can only hope that I was half as supportive to as you’ve been to me.

Much acknowledgement is in order to my fellow theorists, Tim, Vince, Katie, and Dan, for the many insightful conversations about science, life, and everything in-between. To the rest of the group: Rie, Amelia, Anastasiya, Gordon, Leland, Hillary, Nick, Arthur, and Alex, each of you has left an indelible mark on my life. Thank you for the good times.

I’m indebted to Paul McGuire for addressing my computational questions and problems with infinite patience. I’d also like to recognize Arrietta Clauss, Kristi Heming, and April Sonnentag for helping out in a million little ways that made graduate school more bearable.

I'm thankful that my peers gave me the opportunity to serve on the Graduate Student-Faculty Liaison Committee. Ryan, Vanessa, Alyssa, Emily, and Val, we journeyed a long, hard road together, but I couldn't have asked for better company.

I'm deeply grateful for Theresa Windus at Iowa State University, without whose guidance I wouldn't have aspired to apply to graduate school, and for Bain Alexander, without whom I wouldn't have known I could achieve so much.

Lastly, I'd like to thank my family and the friends who've been like family to me, for reminding me that there's a great big world out there to enjoy.

Table of Contents

Abstract	i
Acknowledgments	iv
Table of Contents	vi
List of Figures	xii
List of Tables	xvii
1. Introduction	1
1.1 The nature of atomic size	1
1.2 Connecting reality to theory	4
1.3 Chemical Pressure	7
1.4 Outline of thesis	9
1.5 References	13

2. First-Principles Elucidation of Atomic Size Effects Using DFT-Chemical Pressure Analysis: Origins of $\text{Ca}_{36}\text{Sn}_{23}$'s long-period superstructure	15
2.1 Abstract	15
2.2 Introduction	16
2.3 Our model system	18
2.4 Computational procedures	22
2.5 Creating chemical pressure maps	23
2.6 Isotropic core component averaging	28
2.7 Integration and projections of the CP distribution around atoms	31
2.8 The contact volume integration scheme	34
2.9 Chemical pressure analysis of $\text{Ca}_{36}\text{Sn}_{23}$	39
2.10 Conclusions	43
2.11 References	45
3. Filling in the Holes: Structural and Magnetic Properties of the Chemical Pressure Stabilized LnMn_xGa_3 ($\text{Ln} = \text{Ho-Tm}$; $x < 0.15$)	50
3.1 Abstract	50
3.2 Introduction	51
3.3 Experiment section	53

3.4	Results and discussion	56
3.5	Conclusions	72
3.6	Tables	73
3.7	References	78
4.	Progress in Visualizing Atomic Size Effects with DFT-Chemical Pressure Analysis: From Isolated Atoms to Trends in AB₅ Intermetallics	81
4.1	Abstract	81
4.2	Introduction	83
4.3	Computational procedures	86
4.4	Grid unwarping near atomic centers	88
4.5	Grid unwarping between atoms	93
4.6	Hirshfeld-inspired contact volumes	97
4.7	Stability trends in AB ₅ intermetallics	106
4.8	Conclusions	114
4.9	References	116

5. Chemical Pressure Schemes for the Prediction of Soft Phonon Modes: A Chemist's Guide to the Vibrations of Solid State Materials	121
5.1 Abstract	121
5.2 Introduction	123
5.3 The CaPd ₂ model system	126
5.4 Connecting chemical pressure to vibrational properties	130
5.5 Calibration of the CP integration scheme	132
5.6 Chemical Pressure in the interpretation of phonon frequencies	139
5.7 Application to the superconductor Nb ₃ Ge	145
5.8 Phonons in the CaCu ₅ type: a precursor to structural complexity	148
5.9 Conclusions	152
5.10 Technical procedures	154
5.11 References	157
6. Electronic and Chemical Pressure Effects on the Stability Range of Intermetallic Intergrowths: Pushing the Limits of the HoCoGa₅ type with ScTGa₅ phases	162
6.1 Abstract	162
6.2 Introduction	163
6.3 Experimental	165

6.4	Results and discussion	170
6.5	Conclusions	186
6.6	References	187

Appendices

A.	Supplemental Information for Chapter 2	191
A.1	Treatment of the $P_{\text{remainder}}$ components	191
A.2	ABINIT input file for the calculation of nonlocal energies atom by atom	196
A.3	Optimized structures, total energies, and breakdowns of total pressures by energy terms	200
A.4	References	204
B.	Supplemental Information for Chapter 4	205
B.1	Detailed technical procedures	205
B.2	Structural parameters	207
B.3	Discussion of the prevalence of highly positive CP features in the atomic core regions that are oriented between internuclear vectors, rather than along them	210
B.4	Voxel volume calculation in distorted grid	215
B.5	References	218

C. Supplemental Information for Chapter 5	219
C.1 Technical details	219
C.2 Optimized structural parameters	220
D. Supplemental Information for Chapter 6	223
D.1 Additional computational details	223
D.2 Optimized structural parameters	224
D.3 Chemical Pressure calibration to phonon modes and density of states	226
E. Source code for the DFT-Chemical Pressure package	229
E.1 Annotated C code	229

List of Figures

Chapter 1.

- | | | |
|-----|--|---|
| 1.1 | Unit cell of the complex intermetallic compound NaCd_2 | 3 |
| 1.2 | Schematic representation of the connection between interatomic distance, energy, and chemical pressure in a two-dimensional system | 5 |

Chapter 2.

- | | | |
|-----|--|----|
| 2.0 | Intense chemical pressure between the calcium atoms in Ca_5Sn_3 identified in 2-D maps and projections onto spherical harmonics | 16 |
| 2.1 | The crystal structure of $\text{Ca}_{36}\text{Sn}_{23}$, whose stability has been attributed to the Ca-Ca repulsion that would occur in its W_5Si_3 -type parent structure | 19 |
| 2.2 | A family of long-period superstructures of the W_5Si_3 type with regularly spaced planar interfaces perpendicular to the c axis | 20 |
| 2.3 | The model of Corbett et al. for the instability of W_5Si_3 -type structures in phases with large electropositive atoms in the W -type positions, illustrated with Ca_5Sn_3 | 21 |
| 2.4 | Non-ideal interatomic distances and local chemical pressures resulting from electronic packing frustration | 24 |
| 2.5 | Cross-sections of the chemical pressure map of a hypothetical W_5Si_3 -type Ca_5Sn_3 phase, taken through the $x=0$ plane | 27 |
| 2.6 | The dependence of chemical pressure schemes of atoms in the hypothetical Ca_5Sn_3 structure on the method of dividing voxels among the atoms | 36 |
| 2.7 | Comparison of the DFT-chemical pressure distributions in a hypothetical W_5Si_3 -type Ca_5Sn_3 phase, and the observed superstructure variant $\text{Ca}_{36}\text{Sn}_{23}$ | 40 |

2.8	Chemical pressure release in the chains of Ca-centered tetrahedra on going from the hypothetical W_5Si_3 -type Ca_5Sn_3 to the observed structure of $Ca_{36}Sn_{23}$	42
-----	---	----

Chapter 3.

3.0	Crystal structure of LnM_xGa_3 ($x < 0.15$) compounds shown with the chemical pressure schemes for its constituent structural units	51
3.1	Experimental M-Ga distances and isosurfaces of the Fourier electron density	57
3.2	Crystal structures of $TmGa_3$ (AuCu ₃ type) and Ho_4FeGa_{12} (Y_4PdGa_{12} type)	59
3.3	Temperature-dependent magnetic susceptibility for LnM_xGa_3	60
3.4	Field-depended magnetization for LnM_xGa_3	61
3.5	DFT-chemical pressure analysis for three AuCu ₃ -type phases	66
3.6	Driving forces for guest atom incorporation revealed through DFT-CP analysis	70

Chapter 4.

4.0	Schematic illustration of chemical pressure in an AB_5 compound of the AuBe ₅ structure type	83
4.1	Examples of structural types whose stability ranges are empirically connected to atomic size	87
4.2	DFT-chemical pressure maps for individual atoms isolated in large unit cells	92
4.3	Cross sections for the DFT-CP maps of a variety of intermetallic phases	95

4.4	Comparison of integrated DFT-CP schemes and contact volumes for CaPd_2	101
4.5	Comparison of DFT-CP anisotropy schemes calculated for CaAu_5	107
4.6	Effect of the use of Hirshfeld-inspired contact volumes on the integrated DFT-CP results for CaAu_5 (AuBe_5 type)	110
4.7	DFT-CP analysis of the AB_5 structure types CaCu_5 and AuBe_5	112

Chapter 5.

5.0	Low-frequency phonons in the band structures of Cr_3Si -type superconductors connected to chemical pressure quadrupoles	123
5.1	Crystal structure and earlier chemical pressure scheme for Laves phase CaPd_2	125
5.2	Comparison of integrated DFT-CP schemes and contact volumes for CaPd_2	127
5.3	The chemical pressure concept interpreted in terms of the essentially universal energy curve for interatomic interactions	131
5.4	LDA-DFT phonon band structure and density of states for CaPd_2	133
5.5	Effect of charge on the electron density profiles of Ca and Pd used in the Hirshfeld-inspired CP integration method	135
5.6	Role of ionic charge in the CP scheme of CaPd_2	136
5.7	CP scheme of CaPd_2 obtained using an ionicity calibrated to the phonon DOS	138
5.8	Movement of the atoms in CaPd_2 for each of the optical modes at Γ , overlaid onto the CP scheme	140
5.9	Major features of the phonon DOS of CaPd_2 interpreted in terms of the CP scheme and phonon modes	144

5.10	Connection between vibrational properties and structure revealed for the Cr ₃ Si-type superconductor Nb ₃ Ge using CP analysis	146
5.11	Structure-property relationships derived from CP analysis for CaPd ₅	149

Chapter 6.

6.1	Photograph of a flux-grown crystal of ScCoGa ₅	170
6.2	Crystal structures of ScTGa ₅ (T = Fe, Co, Ni) as an intergrowth of AuCu ₃ -type and fluorite-type slabs	171
6.3	Electrical resistivity measurements as a function of temperature	173
6.4	Calculated density of states for ScTGa ₅ (T = Fe, Co, Ni)	174
6.5	The reversed approximation Molecular Orbitals for ScNiGa ₅	176
6.6	Localized isolobal bonding orbitals for ScNiGa ₅	179
6.7	Elements that occur in HoCoGa ₅ -type gallides and indides	180
6.8	Chemical Pressure scheme for ScNiGa ₅	182
6.9	Structural derivatives of the HoCoGa ₅ type for gallium compounds	183
6.10	Stability map for Ln-T-Ga structures as a function of Ln size and electron count	185

Appendix A.

A.1	Comparison of resulting CP schemes for different treatments of components of the remainder term	196
-----	---	-----

Appendix B.

B.1	Positive chemical pressure shown for a series of solid state structures	212
B.2	The difference between the local potential surfaces of Si from the expanded unit cell volume to the contracted unit cell volume, corrected for distortion	213
B.3	The DFT-CP schemes calculated for elemental Si	214

Appendix D.

D.1	Chemical Pressure scheme for ScNiGa ₅ using ionic electron density profiles	226
D.2	LDA-DFT phonon band structures and density of states for ScTGa ₅	226
D.3	Lower-frequency phonon modes plotted with CP for ScNiGa ₅ at the Γ point	227
D.4	Higher-frequency phonon modes plotted with CP for ScNiGa ₅ at the Γ point	228

List of Tables

Chapter 3.

3.1	Crystallographic parameters for LnGa_3	73
3.2	Atomic positions for LnGa_3	74
3.3	Selected interatomic distances of LnGa_3	74
3.4	Crystallographic parameters for LnMn_xGa_3 ($x \approx 0.05$)	75
3.5	Atomic positions for LnMn_xGa_3 ($x \approx 0.05$)	75
3.6	Selected interatomic distances for LnMn_xGa_3 ($x \approx 0.05$)	76
3.7	Crystallographic parameters for LnMn_xGa_3 ($x \approx 0.10-0.15$)	76
3.8	Atomic positions for LnMn_xGa_3 ($x \approx 0.10-0.15$)	77
3.9	Selected interatomic distances for LnMn_xGa_3 ($x \approx 0.10-0.15$)	77
3.10	Magnetic parameters for single crystalline LnMn_xGa_3 ($\text{Ln} = \text{Ho}, \text{Er}, \text{Tm}$)	77

Chapter 6.

6.1	Crystallographic parameters for ScTGa_5 ($\text{T} = \text{Fe}, \text{Co}, \text{Ni}$)	167
6.2	Atomic positions and lattice parameters	168
6.3	Selected interatomic distances	168

Appendix A.

A.1	Unit cell parameters for the VASP optimized structures of Ca_5Sn_3 and $\text{Ca}_{36}\text{Sn}_{23}$	200
A.2	Reduced coordinates for atoms in the VASP optimized structure of Ca_5Sn_3	200
A.3	Reduced coordinates for atoms in the VASP optimized structure of $\text{Ca}_{36}\text{Sn}_{23}$	201
A.4	Data on the total energies and pressure components of structures considered	204

Appendix B.

B.1	Computational parameters and total energies	206
B.2	Unit cell parameters for DFT-optimized structures	207
B.3	Atomic coordinates for all single-atom calculations	207
B.4	Atomic coordinates for the ABINIT-optimized SrAg_5 structure	207
B.5	Atomic coordinates for the ABINIT-optimized La_5Sn_3 structure	207
B.6	Atomic coordinates for the ABINIT-optimized NbGa_3 structure	208
B.7	Atomic coordinates for the VASP-optimized Ni_3C structure	208
B.8	Atomic coordinates for the ABINIT-optimized CaCu_5 structure	209
B.9	Atomic coordinates for the ABINIT-optimized CaCu_5 structure (AuBe_5 -type)	209
B.10	Atomic coordinates for the ABINIT-optimized CaAu_5 structure (CaCu_5 -type)	210
B.11	Atomic coordinates for the ABINIT-optimized CaAu_5 structure (AuBe_5 -type)	210

Appendix C.

C.1	Computational parameters and total energies for CP calculations with ABINIT	219
C.2	Computational parameters for response function calculations with ABINIT	219
C.3	Computational parameters and total energies for Bader calculations with VASP	220
C.4	Unit cell parameters for DFT-optimized structures	220
C.5	Fractional atomic coordinates for the ABINIT-optimized CaPd ₂ structure	220
C.6	Fractional atomic coordinates for the VASP-optimized CaPd ₂ structure	221
C.7	Fractional atomic coordinates for the ABINIT-optimized Nb ₃ Ge structure	221
C.8	Fractional atomic coordinates for the VASP-optimized Nb ₃ Ge structure	221
C.9	Fractional atomic coordinates for the ABINIT-optimized CaPd ₅ structure	222
C.10	Fractional atomic coordinates for the VASP-optimized CaPd ₅ structure	222

Appendix D.

D.1	Computational parameters and total energies of CP calculations with ABINIT	222
D.2	Computational parameters of phonon calculations with ABINIT	222
D.3	Computational parameters and total energies of raMO and Bader calculations with VASP	223
D.4	Unit cell parameters for DFT-optimized structures	223
D.5	Fractional atomic coordinates for the ABINIT-optimized ScFeGa ₅ structure	223

D.6	Fractional atomic coordinates for the VASP-optimized ScFeGa ₅ structure	223
D.7	Fractional atomic coordinates for the ABINIT-optimized ScCoGa ₅ structure	224
D.8	Fractional atomic coordinates for the VASP-optimized ScCoGa ₅ structure	224
D.9	Fractional atomic coordinates for the ABINIT-optimized ScNiGa ₅ structure	224
D.10	Fractional atomic coordinates for the VASP-optimized ScNiGa ₅ structure	224

Chapter 1.

Introduction

1.1. The nature of atomic size

The reassuring notion that matter has a certain size and shape breaks down when we examine chemical compounds at the atomic level, where the bizarre laws of quantum mechanics govern reality; they tell us that electrons cannot be pinned down to a definite location, making the volume (perhaps better described as spatial influence) of atoms fundamentally ambiguous. Moreover, the outermost valence electrons are not attributable to any one atomic nucleus. Instead, they are shared among atoms in a real material, either locally in covalent bonds – as exemplified by the sp^3 -hybridized carbon network in diamond – or in delocalized interactions – such as described by the nearly free electron model of metals.

For decades chemists have nonetheless invoked the idea of atomic size to rationalize empirical trends in physical phenomena as diverse as non-ideality in gases,¹ steric effects in organic reactions,² the Hume-Rothery rules of solid solutions in alloys,³ structural distortions in perovskites,^{4,5} and phonon-scattering by guest atoms in thermoelectric materials.^{6,7} The practical utility of this concept has led to the tabulation of covalent, metallic, and ionic radii for most of the elements, oftentimes based on average interatomic distances. However, these radii are highly dependent on the chosen reference materials, because distances can vary widely from one substance to another. This is especially true in the solid state where the various

chemical preferences of the elements must be balanced against the essential need to fill space – without atoms getting too close to each other either.

Despite this caveat, the idea of atomic size continues to be propagated, even in introductory chemistry curriculums, and indeed, the simplicity of the concept is its greatest asset. The crystal structure of most pure metals, like iron or gadolinium, can be readily understood by a close-packing of hard spheres of a single metallic radius. Likewise, diamond can be described as an assembly of tetrahedrally-coordinated balls of carbon atoms. Atomic radii work well to explain the structure in these two cases because all the atoms are working toward the same goal: pure metals are as dense as possible to optimize the long-range Ewald energy, and diamond has its characteristic structure to optimize strong covalent bonds. When atoms are in competition to optimize different types of chemical interactions within the same structure, however, empirical radii become far less useful.

Such is the case for complex intermetallic phases, materials composed of two or more metals. Take, for example, the compound formed if elemental gadolinium, iron, and carbon are combined together in a particular ratio, $\text{Gd}_{13}\text{Fe}_{10}\text{C}_{13}$. Even though it is composed of almost $\frac{2}{3}$ metallic elements, it has one of the smallest known distances between iron atoms, suggestive of covalent Fe-Fe multiple bonds.⁸ Perhaps even more surprising is the crystal structure of NaCd_2 . Rather than forming an alloy with sodium and cadmium atoms randomly occupying the same sites in a close-packed lattice, the actual unit cell contains nearly 1200 atoms and has a volume of about $28,500 \text{ \AA}^3$ (Figure 1.1).⁹⁻¹¹ A compound as complicated as this one cannot be understood by a simple packing of spheres.¹²

Inasmuch as the ability to determine what holds complex intermetallics together in such elaborate, long-range order is interesting for its own sake, it is also necessary; without basic theoretical models, there

is little hope of relating chemical composition to crystal structure, and without the ability to control structure, the pursuit of materials with enhanced and tunable properties is severely hindered (properties such as thermoelectricity,¹³ superconductivity,¹⁴ and catalysis¹⁵). It would be like trying to synthesize an organic molecule absent of any knowledge of Lewis structures or valence bond theory.

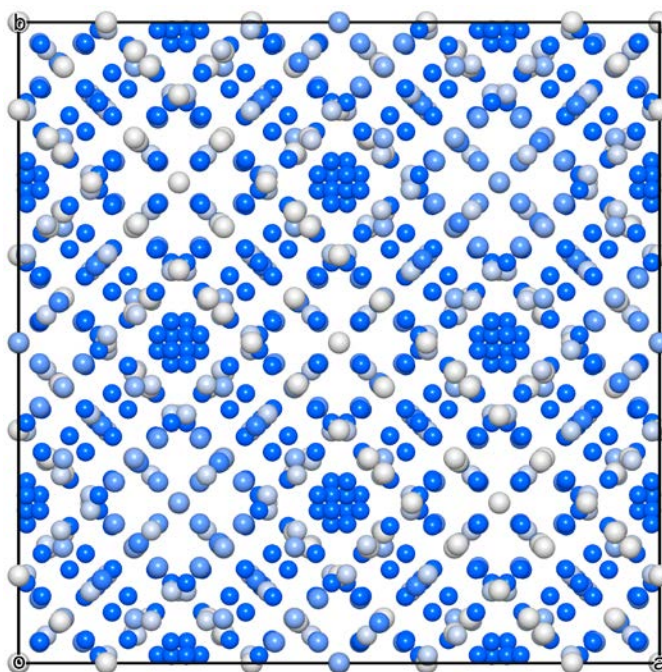


Figure 1.1. The giant, complex crystal structure of the intermetallic compound NaCd_2 , which has nearly 1200 atoms in its unit cell. Na atoms are shown in gray, Cd atoms in blue, and atoms at mixed sites in a weighted combination of gray and blue. Simple models of metallic atoms packing together to fill space efficiently fail to provide insight into such an intricate structure.

Because of this lack of simple bonding theory for intermetallics, quantum mechanical calculations would seem like the natural alternative: they do not require any prior assumptions about the chemical nature of a compound (e.g. if the atoms are held together by covalent, metallic, or ionic interactions) but

neither do they produce data that can be easily interpreted with intuitive chemical principles. As mentioned at the start of this Chapter, the tenants of quantum mechanics preclude a natural definition of atomic size. Even though all the necessary physical information should, in principle, be contained within the results of such a calculation, that information needs to be converted into something akin to the practical, empirical concept of atomic size in order to interpret the results with chemical intuition.

1.2. Connecting reality to theory

In order to make progress toward this end, take a step back for a minute, and consider the essentially universal energy vs. distance curve shown in Figure 1.2a for the potential between two atoms. As the atoms approach each other from a long way apart (right to left on the abscissa), potential energy gradually decreases to a minimum at some ideal length, but at even shorter distances, the energy starts to exponentially increase as the core electrons on the two atoms overlap. This straightforward relationship between energy and interatomic distance for two isolated atoms makes the ideal distance easy to determine: whatever bond length is calculated to have the lowest total energy (using the term bond loosely). However, the situation becomes more ambiguous when there are many atoms interacting simultaneously.

For simplicity's sake, then, consider a uniform, two-dimensional layer of closest-packed atoms, as depicted in Figure 1.2b. Each atom is in an identical environment to every other one, meaning that it is possible for all interatomic distances to be optimized at the same time. In contrast, one of the gray atoms has been replaced by a smaller black one in Figure 1.2c. The six gray atoms around it have shifted closer to compensate for the change, but this movement also forces the gray atoms to be nearer to each other, shorter than their ideal in 1.2b. Since every interaction can no longer be optimized, internal stress occurs

in the structure: the black atom is too small for its coordination environment, but the six grey atoms are too large to get any closer.

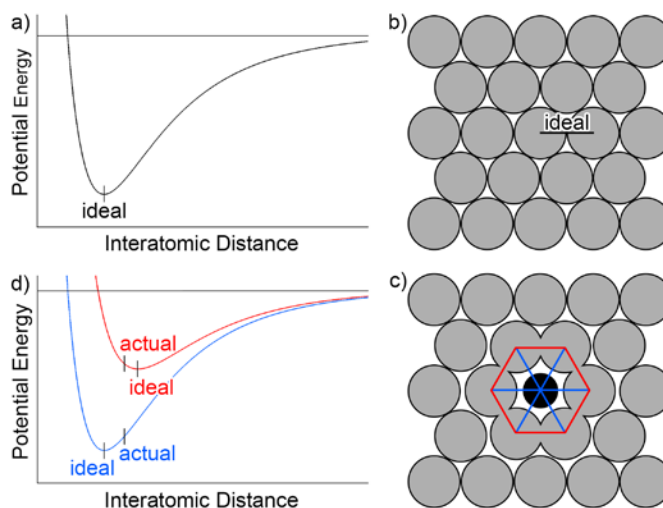


Figure 1.2. An illustration of the connection between interatomic distance, energy, and chemical pressure. (a) The essentially universal potential for the interaction between two atoms. At some ideal distance, energy is minimized. (b) A two-dimensional layer of closest-packed atoms. All neighboring atomic contacts are equidistant to each other at the ideal length. (c) The same layer of atoms with one gray atom replaced by a smaller black one. Its six neighbors have shifted closer to compensate (blue lines), but in the process they have also become closer to each other (red lines). (d) The situation in (c) is represented by two potential energy curves with different ideal interatomic distances: longer for the gray contacts (red curve) and shorter for the interaction between the black atom and a gray atom (blue curve). A compromise is reached at an intermediate distance, resulting in positive chemical pressure between gray atoms (negative slope on the red line) and negative chemical pressure all around the black atom (positive slope on the blue line).

The potential energy curves plotted in Figure 1.2d illustrate the situation in 1.1c. The red curve represents the energy between gray atoms, and the blue curve represents the interaction between the black

atom and its gray neighbors. Even though the two potentials suggest very different ideal distances, the actual interatomic distances in Figure 1.2c are equal (red and blue line segments), and thus, a forced compromise exists between the smaller black atom's desire for contraction of the structure and the larger gray atoms' desire for expansion to alleviate homoatomic repulsion.

Up to this point, the black atom has been presupposed to be too small for its environment *a priori*, and then the effect that that would have on the local bond energy between neighboring atoms has been discussed. The opposite approach, though, is more pragmatic: calculate the energy among nearby atomic contacts to determine whether they are too close or too far from each other, and thus, whether they are too large or too small for their local coordination environments.

However, while it may be standard to calculate the overall, total energy of a crystalline compound with current computational methods, there are two major issues in trying to determine the energy of specific atomic contacts. (1) Most components of the total energy cannot be neatly separated into contributions from individual atoms, and (2) the ideal energy between two atoms in any given chemical system is not known beforehand, so the bond energy alone – even if it could be extracted from the total energy – would not indicate whether interatomic distances are too long or too short.

1.3. Chemical Pressure

A solution to the second problem is suggested by the potential energy curve itself (Figure 1.2a). In order to determine whether a bond length is too long or too short for a pair of isolated atoms, the only necessary information is whether the interatomic distance falls to the left or to the right of the minimum energy, i.e. whether the slope of the potential at a given point on the curve is negative or positive, respectively. An analytical solution for the slope would be quite difficult to ascertain in practice, but a numerical approximation of the first derivative requires only one additional energy calculation, by taking the difference in energy divided by the difference in distance. For a three-dimensional structure – where changing one interatomic distance affects many others – the analogous procedure is to take the difference in energies divided by the difference in unit cell volumes, one of which has been isotropically expanded or contracted to vary all interatomic distances simultaneously:

$$p_{physical} = - \left(\frac{\partial U_{total}}{\partial V_{cell}} \right)_S \approx - \frac{U_2 - U_1}{V_2 - V_1} \quad (1.1)$$

As Equation 1.1 shows, the change in total energy with respect to change in total volume corresponds to the macroscopic property of physical pressure (at fixed entropy),¹⁶ which typically sums to zero. For the purpose of approximating the first derivative of specific atomic contacts, however, the analogous localized quantity is deemed *chemical pressure* (CP):

$$p_{physical} = \sum p_{chemical} = \sum_{atoms} - \left(\frac{\partial U_{local}}{\partial V_{contact}} \right)_S \approx \sum_{atoms\ i \neq j} - \frac{U_2^{ij} - U_1^{ij}}{V_2^{ij} - V_1^{ij}} \quad (1.2)$$

Whereas physical pressure is the result of an externally applied force on a material, chemical pressure arises from the internal stress inherent to a crystal lattice. Positive CP indicates a steric repulsion between nearby atoms that favors expansion of the structure (such as between gray atoms in Figure 1.2c), and negative CP indicates an under-optimized bonding interaction that favors contraction of the structure (such as between the black and gray atoms).

Now that a skeleton framework of how to convert total energy into information about interatomic distances has been discussed, the other major issue in Section 1.2 needs to be addressed: most components of the total energy are not functions of individual atoms. Indeed, the definition of chemical pressure given in Equation 1.2 includes a currently undefined sum over the atoms and their pairwise interactions, but a partial solution can be found in a particular formulation of quantum mechanics called Density Functional Theory (DFT).¹⁷⁻¹⁸

DFT makes it possible to calculate most of the components of the energy on a grid of points in space as a function of the continuous electron density distribution instead of discrete atoms. This implies that Equation 1.2 can be rewritten in terms of three-dimensional grid points (volume elements called voxels) to create a map of the chemical pressure across the unit cell:

$$p_{physical} = \sum_{x,y,z} p_{chemical}^{voxel} \approx \sum_{x,y,z} -\frac{U_2^{voxel} - U_1^{voxel}}{V_2^{voxel} - V_1^{voxel}} \quad (1.3)$$

Equation 1.3 brings the CP method much closer to its original goal, but now the definition has lost the concept of atoms.

As such, one final step is needed to recover the perspective of atomic interactions: allocation of the nearly continuous CP map among the atomic centers – bringing this discussion full circle. Everything up to this point was motivated by the fact that quantum mechanics does not have a natural way to specify the volume of an atom, and yet atomic boundaries must be chosen before the atoms' more rigorous spatial influence can be determined with DFT-Chemical Pressure (DFT-CP) analysis. Therefore, much of the work described in the following chapters is focused on developing solutions to this crucial paradox.

The efforts start with the demonstration of a space-partitioning scheme that largely negates the need to define atomic boundaries at all, instead defining contact volumes between pairs of neighboring atoms. This contact volume scheme undergoes increasingly more sophisticated refinements in later chapters, culminating with a way to externally validate the resulting CP schemes with the phonon density of states. However, during this process of refining the contact volumes, insight into the softness or hardness of the phonon modes was gained almost on accident; the necessity of technical improvements to DFT-Chemical Pressure analysis led to a practical tool for identifying vibrational structure-property relationships in complex intermetallic compounds.

1.4. Outline of thesis

As already mentioned, a critical improvement to the DFT-CP methodology is introduced in the next chapter, in which the chemical pressure map is integrated over regions of space between atomic contacts

rather than around individual atoms. The utility of this switch to contact volumes – away from Voronoi cells and Bader basins – is demonstrated with $\text{Ca}_{36}\text{Sn}_{23}$, a structural derivative of the common W_5Si_3 type. The $\text{Ca}_{36}\text{Sn}_{23}$ structure is characterized by the insertion of a “defect” plane into the unit cell of the more basic structure that serves to relieve strong positive CP between Ca atoms. Additionally, isotropic core averaging is introduced as a way to reduce the amount of artificial CP around atomic centers in the map.

In Chapter 3, DFT-CP is used to understand the chemical stability afforded by transition metal stuffing atoms into an otherwise AuCu_3 -type lattice for several magnetic gallides, LnMn_xGa_3 ($\text{Ln} = \text{Ho-Tm}$, $x < 0.15$). The ability to “dope” transition metals into this set of compounds is rationalized by the need for shorter Ga-Ga interatomic distances, as evidenced by the prevalence of negative CP between them. The effect of the structural changes on the magnetic properties is also discussed, and some counterintuitive attributes are explained about strong negative CP, relative to the strong positive CP in Chapter 2.

Major advancements to the DFT-CP methodology are described in detail in Chapter 4: most importantly, core unwarping and Hirshfeld-inspired integration. Core unwarping replaced the isotropic core averaging procedure from Chapter 2 by explicitly correcting most of the artificial CP around atomic core regions through an interpolation of grid points to their original positions in the non-expanded/contracted unit cell. Likewise, Hirshfeld-inspired integration is an improved version of the contact volume scheme from Chapter 2 that uses atomic electron density profiles for determining the size and shape of the contact volumes, instead of a purely distance-based criterion. The dramatic effect of these changes on the CP

schemes of certain types of structures is demonstrated with several common AB_2 and AB_5 intermetallic phases.

Another significant refinement of the Hirshfeld-inspired integration scheme is detailed in Chapter 5: phonon-calibrated ionic profiles. Whereas Hirshfeld-inspired integration in Chapter 4 accounted for the natural difference in the spatial extent of atoms for different elements, the use of ionic profiles – instead of neutral-atom electron density profiles – allows for differentiation between atoms of the same element that are in distinct chemical environments. The charges of the ionic profiles for a Laves phase, $CaPd_2$, are calibrated to its phonon density of states, providing external validation of the resulting CP scheme. In turn, the CP scheme is used to interpret the full set of phonon modes at the Γ point in terms of local atomic interactions. Specific CP features, especially CP quadrupoles, are connected to soft and hard atomic motions. This knowledge is then applied to explain the trend in critical temperatures for the superconductor Nb_3Ge and related materials, and to understand the wide diversity of structural derivatives that exist based on the $CaCu_5$ structure type.

Finally in Chapter 6, DFT-CP is once again applied to some transition metal gallides, $ScTGa_5$ ($T = Fe, Co, Ni$), in demonstration of how the CP approach can be combined with reversed approximation Molecular Orbital (raMO) theory to probe the stability range of a particular structure type in terms of both atomic size and electron count simultaneously. The two analyses are used together to draw connections with more complex gallium compounds, rationalizing an entire series of structures that does not exist for the analogous indium superconductors.

The appendices provide Supporting Information for the chapters, including DFT-optimized geometries of structures, computational parameters, and various technical considerations not included in the main chapters. Also included is the current source code for the CP analysis program. Recent developments have made it possible to use DFT calculations as input for the CP program that are spin-polarized or use Generalized Gradient Approximation (GGA) exchange-correlation functionals, although none of the CP schemes in this text required those functionalities.

It remains to be seen what insights DFT-Chemical Pressure analysis could bring to other kinds of solid-state materials. In principle, the CP methodology should be applicable to any system where a DFT calculation gives reliable results, because despite the technical complexities, it simply converts the existing energy data into chemical pressures between the atoms. By extracting local atomic interactions from the total energy, it restores the chemically intuitive concept of atomic size – revealing whether atomic contacts are too close or too far apart from each other – from unintuitive quantum mechanical calculations. Chemical Pressure analysis, while still young and untested in certain ways, has nonetheless provided a way forward toward understanding the origins of structural complexity in intermetallics, and moreover, toward identifying the complex connections between crystal structure and materials properties.

1.5. References

- (1) van der Waals, J. D. Nobel Lectures, Physics 1901-1921; Elsevier Publishing Company: New York, 1967, pp 254-265.
- (2) Smith, M.; March, J. March's advanced organic chemistry: reactions, mechanisms, and structure; 6th ed.; Wiley-Interscience: Hoboken, NJ, 2007, pp 397-401.
- (3) Hume-Rothery, W.; Powell, H. M. *Z. Kristallogr.* **1935**, *91*, 23.
- (4) Goldschmidt, V. M. *Mat.-Nat.* **1926**, *K1*, 8.
- (5) Glazer, A. *Acta Crystallogr. B* **1972**, *28*, 3384.
- (6) Nolas, G. S.; Cohn, J. L.; Slack, G. A.; Schujman, S. B. *Appl. Phys. Lett.* **1998**, *73*, 178.
- (7) Nolas, G. S.; Cohn, J. L.; Slack, G. A. *Phys. Rev. B* **1998**, *58*, 164.
- (8) Hadler, A. B.; Fredrickson, D. C. *J. Am. Chem. Soc.* **2012**, *134*, 10361.
- (9) Bergman, G.; Waugh, J. L. T.; Pauling, L. *Acta Crystallogr.* **1957**, *10*, 254.
- (10) Samson, S. *Nature.* **1962**, *195*, 259.
- (11) Yang, Q.-B.; Andersson, S.; Stenberg, L. *Acta Crystallogr. B.* **1987**, *43*, 14.
- (12) Fredrickson, D. C.; Lee, S.; Hoffmann, R. *Angew. Chem. Int. Ed.* **2007**, *46*, 1958.
- (13) Sootsman, J. R.; Chung, D. Y.; Kanatzidis, M. G. *Angew. Chem. Int. Ed.* **2009**, *48*, 8616.
- (14) Klimczuk, T.; Wang, C. H.; Gofryk, K.; Ronning, F.; Winterlik, J.; Fecher, G. H.; Griveau, J.-C.; Colineau, E.; Felser, C.; Thompson, J. D.; Safarik, D. J.; Cava, R. J. *Phys. Rev. B* **2012**, *85*, 174505.
- (15) Armbrüster, M.; Kovnir, K.; Behrens, M.; Teschner, D.; Grin, Y.; Schlögl, R. *J. Am. Chem. Soc.* **2010**, *132*, 14745.

(16) McQuarrie, D. A.; Simon, J. D. *Physical chemistry: a molecular approach*; University Science Books: Sausalito, CA, 1997, pp 896-899.

(17) Hohenberg, P.; Kohn, W. *Phys. Rev.* **1964**, *136*, B864.

(18) Kohn, W.; Sham, L. J. *Phys. Rev.* **1965**, *140*, A1133.

Chapter 2.

First-Principles Elucidation of Atomic Size Effects Using DFT-Chemical Pressure Analysis: Origins of $\text{Ca}_{36}\text{Sn}_{23}$'s Long-Period Superstructure

This chapter has been published: Engelkemier, J.; Berns, V. M.; Fredrickson, D. C. *J. Chem. Theory Comput.* **2013**, *9*, 3170-3180. The specific analyses detailed in this chapter were the work of Engelkemier, but contributions to the general theoretical developments described below and to the preparation of the manuscript were made by both Berns and Engelkemier.

2.1. Abstract

The space requirements of atoms are empirically known to play key roles in determining structure and reactivity across compounds ranging from simple molecules to extended solid state phases. Despite the importance of this concept, the effects of atomic size on stability remain difficult to extract from quantum mechanical calculations. Recently, we outlined a quantitative yet visual and intuitive approach to the theoretical analysis of atomic size in periodic structures: the DFT-Chemical Pressure (DFT-CP) analysis. In this Chapter, we describe the methodological details of this DFT-CP procedure, with a particular emphasis on refinements of the method to make it useful for a wider variety of systems. A central improvement is a new integration scheme with broader applicability than our earlier Voronoi cell method: contact volume space-partitioning. In this approach, we make explicit our assumption that the pressure at each voxel

is most strongly influenced by its two closest atoms. The unit cell is divided into regions corresponding to individual interatomic contacts, with each region containing all points that share the same two closest atoms. The voxel pressures within each contact region are then averaged, resulting in effective interatomic pressures. The method is illustrated through the verification of the role of Ca-Ca repulsion (deduced earlier from empirical considerations by Corbett and coworkers) in the long-period superstructure of the W_5Si_3 -type exhibited by $Ca_{36}Sn_{23}$.

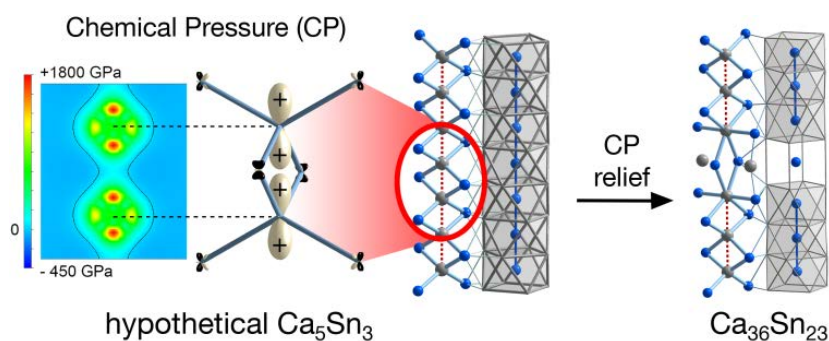


Figure 2.0. Intense chemical pressure between the calcium atoms in Ca_5Sn_3 can be identified in 2-D maps (left) and projections onto spherical harmonics. This pressure is relieved on altering the structure to increase the distance between calcium atoms, forming $Ca_{36}Sn_{23}$.

2.2. Introduction

The concept of atomic size is frequently evoked in the rationalization of experimentally observed chemical phenomena. Examples across the broad spectrum of chemistry include the non-ideality of gases,¹ steric repulsion between alkyl groups influencing the outcomes of organic reactions,² the radius ratio rules

for rationalizing the crystal structures of ionic salts,^{3,4} and the vibrational freedom of rattling atoms in clathrate- or skutterudite-based thermoelectric materials.^{5,6} Despite its rich history, the space requirement of atoms remains essentially an empirical notion, largely based on observed interatomic distances and the compilation of these observations in tables of atomic radii. While methods exist for partitioning space between atoms, as offered by Bader's Quantum Theory of Atoms in Molecules,^{7,8} theoretical approaches are needed for determining how a structure's stability is affected by the encroachment of one atom upon another atom's domain. Such methods would be valuable for verifying the role of atomic sizes indicated by empirical observations, and elucidating the specific ways in which these sizes wield their influence.

For solid state inorganic compounds this need is pressing, particularly for intermetallic phases. Since the pioneering work of Hume-Rothery, atomic size has been recognized as a key factor in the structural preferences of intermetallics.⁹⁻¹² More recently, there has been an emerging theme of size effects interacting with electronic factors to determine the observed structural chemistry.¹³⁻¹⁷ Investigating such interactions is quite challenging, however, as the absence of bonding schemes tying composition to geometry makes it difficult to distinguish close contacts supported by substantial bonding from those that are in fact repulsive but forced together by the constraints of atomic packing.

We recently outlined an approach for revealing local interatomic pressures that arise in such circumstances: the DFT-Chemical Pressure (CP) analysis,¹⁸ which offers theoretical insights into size effects and how they emerge from an electronic context. The DFT-CP analysis can be viewed as a chemical application of the concept of stress density,¹⁹⁻²⁴ in which the total pressure of a system is spatially resolved into a pressure map. Our approach differs from previous work in this area in two respects. First, rather than deriving analytical relationships between the ground state wavefunctions and the stress density, we focus on

developing a practical interface with electronic structure programs, particularly the freely-available, open source ABINIT package.^{25,26} This is achieved by taking the simpler method of numerically differentiating energy density grids obtained from a calculation's output. The second difference is in our emphasis on the interpretation of the pressure maps. In moving away from considerations of the formalism of stress densities toward visualization of the conflicts underlying them, vivid schemes for the stability of intermetallic structures arise that are capable of inspiring new experimental endeavors.

In this Chapter, we build on our earlier outline of the DFT-CP analysis. In the process of describing the methodological details of this approach, we will present improvements that develop the DFT-CP analysis into a generally usable tool for the analysis of bonding optimization in solid state materials. These improvements include a more meaningful treatment of the pressures observed in the regions of the ion cores, and a more reliable method for dividing space between the atoms during the integration of the pressure maps. In addition, we will demonstrate the application of this improved analysis to an intermetallic system with interesting structural chemistry: that of the superstructure variants of the W_5Si_3 structure type in the Ca-Sn system.

2.3. Our model system

As we develop the DFT-CP method in this Chapter, we will use the complex crystal structure of $Ca_{36}Sn_{23}$ (Figure 2.1) as a model system.^{27,28} This compound belongs to a family of intermetallics adopting long-period superstructures of the common W_5Si_3 structure type (Figure 2.1a).²⁷⁻³⁴ The W_5Si_3 parent structure is easily visualized as a checkerboard arrangement of columns of Si-centered W square antiprisms

and columns of W-centered Si tetrahedra. These two column types extend along the c -axis, with the square antiprisms and tetrahedra of each column linked through shared faces and edges, respectively.

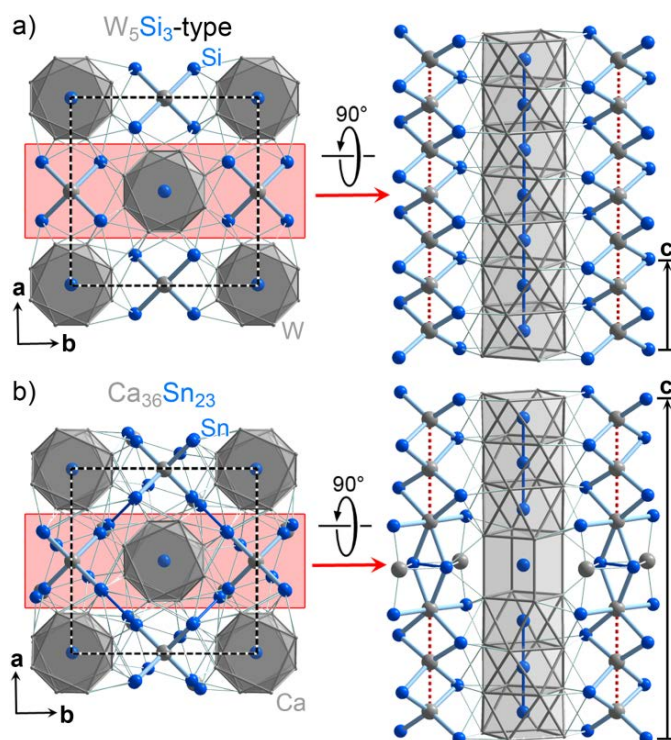


Figure 2.1. The crystal structure of $Ca_{36}Sn_{23}$, whose stability has been attributed to the Ca-Ca repulsion that would occur in its W_5Si_3 -type parent structure. (a) The structure of W_5Si_3 . (b) The $Ca_{36}Sn_{23}$ structure, which is generated through the introduction of planar defects into the W_5Si_3 -type at regular intervals perpendicular to c .

In $Ca_{36}Sn_{23}$ and a number of other phases, defect variants of the W_5Si_3 type are adopted in which planar interfaces are inserted perpendicular to c (as shown on the right side of Figure 2.1b). At each of these interfaces, the progression along the columns of square antiprisms is interrupted by the incorporation of a cube. The columns of tetrahedra are similarly interrupted, with coordination of the interfacial Ca atoms

changing from tetrahedral to octahedral. In $\text{Ca}_{36}\text{Sn}_{23}$, these interfaces occur at regular intervals of six square-antiprisms along c , corresponding to three unit cells of the W_5Si_3 basic structure. For other members of this family, other interface distributions are observed (Figure 2.2). In the structures of $\text{Ca}_{31}\text{Sn}_{20}$ and $\text{Pu}_{31}\text{Pt}_{20}$, the interface layers are separated from each other by slabs of the W_5Si_3 type five square antiprisms thick. For Y_3Rh_2 and $\text{Ca}_{16}\text{Sb}_{11}$, the slab thickness decreases to respectively three and two square antiprisms.

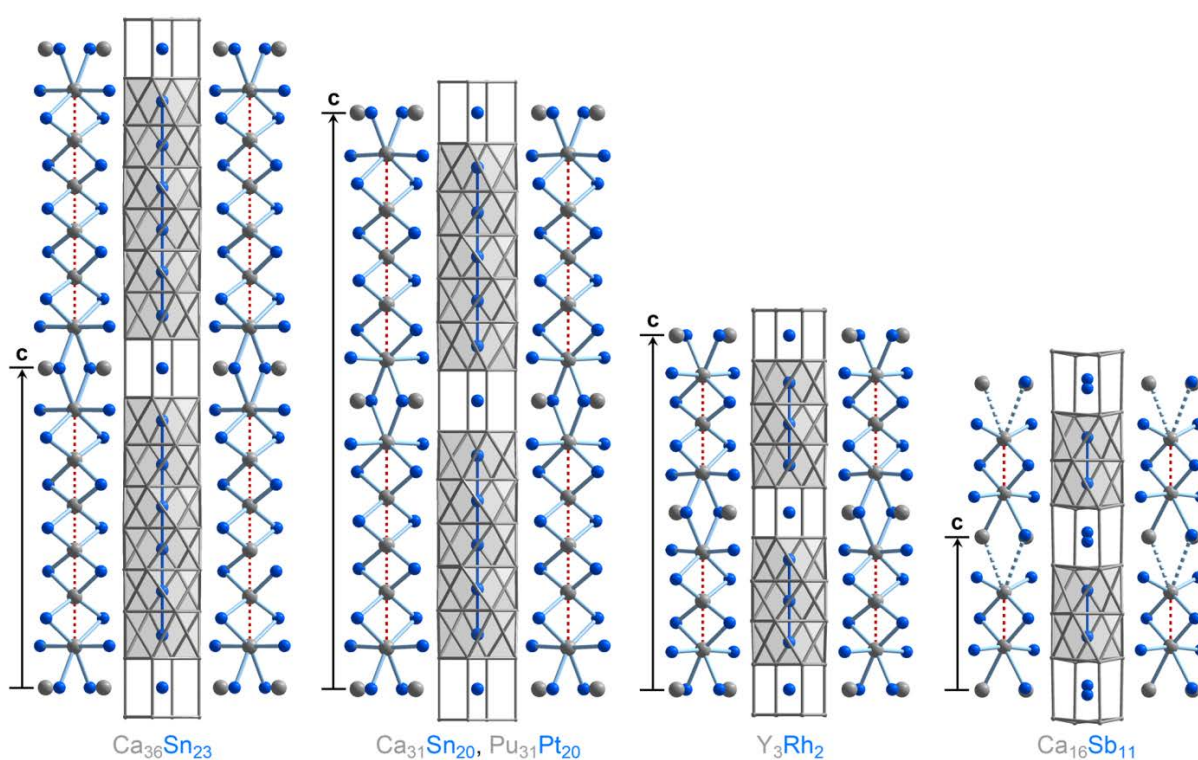


Figure 2.2. A family of long-period superstructures of the W_5Si_3 type with regularly spaced planar interfaces perpendicular to the c axis.

The gradual shrinking of the W_5Si_3 -type domains across this series is an impressive illustration of the structural flexibility obtained in intermetallic phases, and raises the question of what driving forces motivate such progressions. For this particular series, Corbett and coworkers have provided a plausible explanation for the instability of the simple W_5Si_3 type in, for instance, the Ca-Sn system: in a hypothetical Ca_5Sn_3 phase, the neighboring Ca atoms in the tetrahedral chains would be expected to have unusually short distances to each other (3.3 Å, by our estimation; see Figure 2.3), suggesting that the Ca atoms may be too large for their coordination environment.³⁴ The interfaces in the observed superstructures in this series could serve to alleviate interatomic repulsion at such contacts.

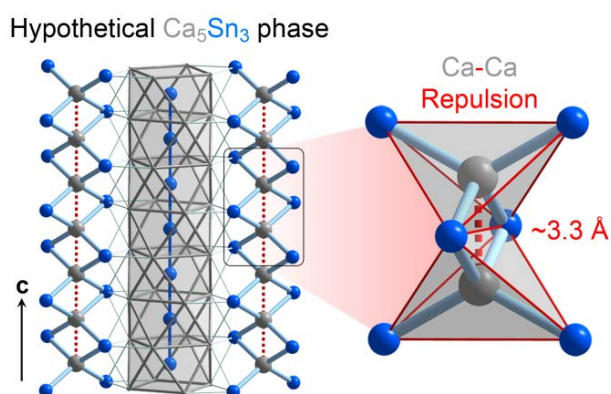


Figure 2.3. The model of Corbett et al. for the instability of the W_5Si_3 -type structures in phases with large electropositive atoms at the W-type positions, illustrated with Ca_5Sn_3 . The placement of Ca in the edge-sharing tetrahedral chains running along c leads to uncomfortably close Ca-Ca contacts. The superstructures of the W_5Si_3 type observed in these systems are hypothesized to relieve interatomic repulsion at these contacts.

Atomic size thus appears to be playing a part in the structural series of Figure 2.2. How might electronic structure calculations be used to support and inform this view? Over the course of this paper, we will see that the DFT-Chemical Pressure analysis provides a first-principles approach to this problem, which reveals in graphical and intuitive terms not only the Ca-Ca repulsion in a hypothetical W_5Si_3 -type basic structure, but also its release upon moving to the observed $Ca_{36}Sn_{23}$ structure. A first step will be introducing some improvements to the original DFT-CP scheme described earlier, which makes the method more amenable to systems with atoms of very different sizes and valence electron counts.

2.4. Computational procedures

For all calculations on $Ca_{36}Sn_{23}$ and a hypothetical W_5Si_3 -type Ca_5Sn_3 phase, two planewave-based DFT codes were used because of their complementary strengths. The Vienna Ab initio Simulation Package (VASP)^{35,36} was used for the geometrical optimization of the two structures due to the highly efficient potentials provided with the package, requiring relatively low energy cut-offs. The geometrical optimizations were performed in two steps: first the ion positions were optimized within a unit cell of fixed dimensions, then all structural parameters were optimized simultaneously. All calculations used the local-density approximation (LDA), and were carried out in the high precision mode, corresponding to an energy cutoff of 106.4 eV. The calculations employed $4 \times 4 \times 8$ and $4 \times 4 \times 2$ Monkhorst-Pack k-point meshes³⁷ for Ca_5Sn_3 and $Ca_{36}Sn_{23}$, respectively, and the ultrasoft pseudopotentials provided with the package.³⁸

The ABINIT package^{25,26} was used for generating the necessary data for the DFT-CP analysis of the VASP-optimized structures, because of the exquisite degree of detail and transparency in its output. For

each structure, the raw data for the CP analysis was obtained through three single-point calculations spanning a volume range of 0.6%. The calculations employed the LDA exchange-correlation functional of Goedecker, Teter, and Hutter,³⁹ and the Hartwigsen-Goedecker-Hutter (HGH) pseudopotentials provided with the package.⁴⁰ The energy cutoff was set to 816 eV for the calculations on $\text{Ca}_{36}\text{Sn}_{23}$ and Ca_5Sn_3 when the valence-only Ca HGH potential was used. For Ca_5Sn_3 , calculations were also carried out using the semicore Ca HGH potential; here the energy cutoff was set to 1088 eV. These values were found to converge the energy of formation of the hypothetical Ca_5Sn_3 phase to less than 0.5 meV/atom. Monkhorst-Pack k-point meshes³⁷ distributing $4\times 4\times 2$ and $4\times 4\times 8$ points through the Brillouin zone were used for the $\text{Ca}_{36}\text{Sn}_{23}$ -type and W_5Si_3 -type phases, respectively. The spacing of the voxels (determined by the fast Fourier transform grids) was set to $108\times 108\times 192$ and $108\times 108\times 72$ grids for $\text{Ca}_{36}\text{Sn}_{23}$ and Ca_5Sn_3 , respectively.

2.5. Creating chemical pressure maps

To set-up the discussion of our improvements to the DFT-Chemical Pressure (CP) scheme and its application to $\text{Ca}_{36}\text{Sn}_{23}$, let's briefly review the method. The basis of the DFT-CP analysis is the electronic-packing frustration model (Figure 2.4) for the interaction of electronic interactions and atomic size in condensed matter systems.^{41,42} Dense atomic packing constraints can lead to correlations between interatomic distances within a structure. Such correlations make it difficult to independently optimize the interactions between different pairs of atoms. The size of atoms becomes manifest when the formation of a chemical bond at one contact requires shortening at other contacts for which there is not sufficient electronic support. Such tension would be expected to result in non-optimal interatomic distances (Figure 2.4b) and

local pressures acting between the affected atoms, which might be referred to with the term *chemical pressure* (CP) to distinguish them from physical pressures exerted on the system externally.

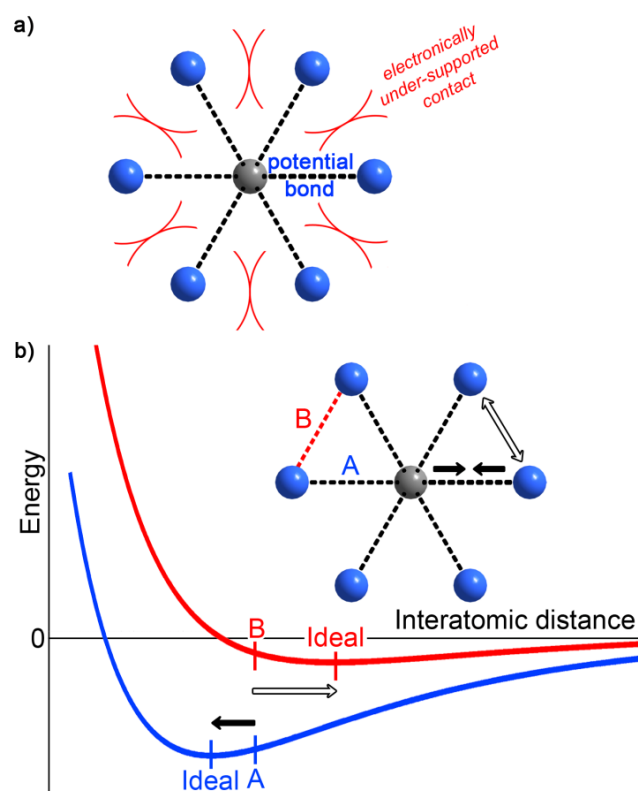


Figure 2.4. Non-ideal interatomic distances and local chemical pressures resulting from electronic packing frustration (EPF).

(a) A schematic illustration of the electronic packing frustration model. Reproduced from Ref. 39 with the permission of the American Chemical Society. (b) The compromise between the need for contraction along some contacts (A) and expansion along others (B) leads to non-optimal distances. The slope of the energy vs. distance curves at the observed distance is related to a local pressure acting at that contact.

The formalism of the quantum mechanical stress density¹⁹⁻²³ offers one approach for determining how such pressures are distributed in a crystal structure. In the DFT-CP analysis, a simpler avenue is taken, in

which the structure is divided into a grid of voxels (small finite volume elements) and the pressure experienced by each voxel is calculated as follows.

We begin with the expression for the total energy for a system calculated with Kohn-Sham DFT:⁴³

$$E_{total} = \iiint_{\substack{\text{unit} \\ \text{cell}}} \left(\sum_n c_n \psi_n^* \nabla^2 \psi_n + \left(V_{local} + \frac{1}{2} V_{Hartree} + \epsilon_{XC}(\rho) \right) \rho(\vec{r}) \right) dV + E_{Ewald} + E_{nonlocal} + E_{\alpha} \quad (2.1)$$

In this expression, the terms under the integral represent the kinetic energy of the system and the local contributions to the potential energy, measured relative to the reference state of an exchange-correlation-free homogeneous electron gas interacting with the ion cores. Outside the integral, the $E_{Ewald} + E_{\alpha}$ terms together give the energy of that reference state, and $E_{nonlocal}$ provides the potential energy resulting from any nonlocal components of the atomic pseudopotentials (an additional term $E_{kT-Entropy}$ can be added to correct the total energy from any smearing of the band occupancies about the Fermi energy).

The next step in the determination of the DFT-CP distribution is to recognize that the E_{total} expression has the form of the integral over an energy density plus a remainder:

$$E_{total} = \iiint_{\substack{\text{unit} \\ \text{cell}}} \rho_{energy}(\vec{r}) dV + E_{remainder} \quad (2.2)$$

which can be represented more conveniently for numerical work as a sum over an grid of voxel energies plus a remainder:

$$\begin{aligned} E_{total} &\approx \sum_n^{N_{\text{voxels}}} \rho_{energy}(\vec{r}) V_{\text{voxel}} + E_{remainder} \\ &\approx \sum_n^{N_{\text{voxels}}} E_{\text{voxel},n} + E_{remainder} \end{aligned} \quad (2.3)$$

where N_{voxels} is the number of voxels into which the unit cell volume (V_{cell}) is divided, and V_{voxel} is the volume of each voxel, i.e. $V_{\text{voxel}} = V_{\text{cell}}/N_{\text{voxels}}$.

Once the total energy is mapped spatially in this way, a similar spatial distribution of the pressure is obtained by taking the negative derivative of E_{total} with respect to V_{cell} :

$$\begin{aligned}
 P &= -\frac{\partial E_{\text{total}}}{\partial V_{\text{cell}}} = -\frac{\partial}{\partial V_{\text{cell}}} \left(\sum_n^{N_{\text{voxels}}} E_{\text{voxel},n} + E_{\text{remainder}} \right) \\
 &= -\frac{\partial}{\partial V_{\text{cell}}} \left(\sum_n^{N_{\text{voxels}}} E_{\text{voxel},n} \right) + P_{\text{remainder}} \\
 &= -\frac{1}{N_{\text{voxels}}} \left(\sum_n^{N_{\text{voxels}}} \frac{\partial E_{\text{voxel},n}}{\partial V_{\text{voxel}}} \right) + P_{\text{remainder}} \\
 &= \frac{1}{N_{\text{voxels}}} \sum_n^{N_{\text{voxels}}} P_{\text{voxel},n} + P_{\text{remainder}} \tag{2.4}
 \end{aligned}$$

so that the total pressure experienced by the structure, P , becomes resolved into an average over the voxel pressures ($P_{\text{voxel},n}$) plus a remainder pressure arising from the components of the total energy.⁴⁴ In practice, this differentiation is performed numerically by constructing energy grids from the output of ABINIT calculations^{25,26} on a structure at two slightly different volumes, taking the difference, and dividing by the difference in voxel volumes.

What then is the $P_{\text{remainder}}$ term? In Section A.1 of the Supporting Information, we describe how in principle the pressure contributions from E_{Ewald} , E_a , and E_{nonlocal} can be apportioned among the atoms or interatomic regions of the structure. However, in each case, one encounters an unacceptable degree of ambiguity

in applying the procedure which leads to unreliable results. Through work with several intermetallic systems, we have concluded that the best treatment of $P_{\text{remainder}}$ is also the simplest: we consider it as corresponding to a homogeneous background pressure, which can then be added to each of the voxel pressures.

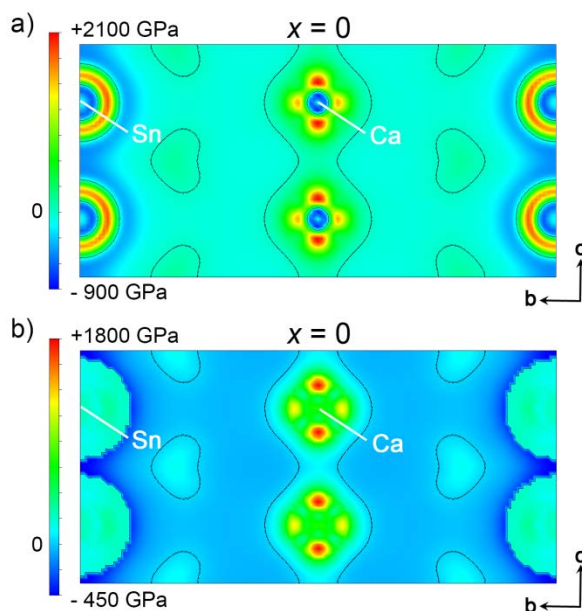


Figure 2.5. Cross-sections of the chemical pressure (CP) map of a hypothetical W_5Si_3 -type Ca_5Sn_3 , taken through the $x=0$ plane. The cross-sections are shown (a) before and (b) after flattening of the spherically symmetric oscillations emanating from the ion cores. Black contours corresponding to $CP=0$ are overlaid on the map. See text for details.

For metallic phases lacking localized bonds, the pressure grids resulting from this procedure tend to have high-magnitude features near the nuclear positions, occurring in the midst of relatively flat negative background pressure. This is illustrated for a hypothetical W_5Si_3 -type phase Ca_5Sn_3 (the parent structure of the more complex $Ca_{36}Sn_{23}$ structure we discussed above) in Figure 2.5a. Here, cross-sections of the CP

map are taken perpendicular to the a -axis and centered on the unusually close Ca-Ca contacts. The pressures in the map are indicated using colors ranging from dark blue (-900 GPa) to red (+2100 GPa). The most vivid variations in color occur near the nuclear positions, where negative pressures at the atom centers give way to intense positive pressures slightly further out, arranged in a ring for the Sn and in a cross for the Ca. As the distance from the nuclei increases, the voxel pressures gradually converge on a relatively flat background pressure.

2.6. Isotropic core component averaging

The presence of strong CP oscillations emanating from the ion cores poses a number of problems for the interpretation of the CP maps. First, the magnitudes of the pressures encountered during these undulations dwarf those appearing in the interatomic regions of the map. This makes more subtle features of the map difficult to detect. A second undesirable aspect of these oscillations is that they tend to mask any directional dependence of the pressures in the core region, as might emerge from an interatomic interaction. Finally, as the core region contains both large positive and negative pressures, it is difficult to gauge the net pressure near the nucleus. As we are using pseudopotentials, the question of how seriously to take these oscillations is important. They occur largely in the pseudopotential core regions, where the correspondence is weakest between the true wavefunctions of the system and the pseudo-wavefunctions of the calculation. In other words, their specific forms are artificial products of the atomic pseudopotentials.

The form of the pseudopotential near the core is typically chosen to be mathematically convenient while still reproducing key atomic properties. Likewise, we can substitute the oscillatory CP features with

a simpler CP distribution that captures the same net pressure and directional dependence upon integration over the core region. In order to accomplish this, we have developed an *isotropic core component averaging* procedure for use in the generation of DFT-CP maps.

We begin by choosing a radius for the core region of an atom, typically about 1.0 Å. The voxels within this distance of the nuclear position will be subject to this procedure while all others will be left unchanged. Next, the pressure for any voxel in the core region, say the n th voxel in the grid, is written in terms of its deviation from the average P for that voxel's distance from the nucleus, $r_{n-ion} = |\vec{r}_{voxel,n} - \bar{R}_{ion}|$:

$$\begin{aligned} P_{voxel,n} &= \left[P_{voxel,n} - \overline{P_{voxel}(r_{n-ion})} \right] + \overline{P_{voxel}(r_{n-ion})} \\ &= \Delta P_{voxel,n} + \overline{P_{voxel}(r_{n-ion})} \end{aligned} \quad (2.5)$$

In other words, the core voxel pressures are written as the sum of an anisotropic function, representing the directional dependence of the core pressures, and a spherically symmetric function.

The oscillations around the core occur predominantly in the latter function, the isotropic core component. These can be removed by simply replacing the values of this function with its average within the core region:

$$P_{isotropic\ core} = \frac{\int_0^{r_{core}} \overline{P_{voxel}(r_{n-ion})} \cdot 4\pi(\vec{r}_{n-ion})^2 dr_{n-ion}}{\frac{4}{3}\pi r_{core}^3} \quad (2.6)$$

In this way, the modified voxel pressures are calculated as

$$P_{voxel,n} = \Delta P_{voxel,n} + P_{isotropic\ core} \quad (2.7)$$

Under this transformation, both the anisotropic component and the average of the isotropic function are left unchanged. As such, the net pressure within the core region and the directional dependence are preserved.

In Figure 2.5b, we replot the DFT-CP cross-section of the hypothetical Ca_5Sn_3 structure through the $x=0$ layer, this time with the isotropic core component averaging applied with core radii of 0.8 Å for Ca and 1.3 Å for Sn. For both atom types, there is significant reduction in the variation of pressures in the core region. In the case of Sn, the ripples of color are now replaced with a virtually uniform cyan, corresponding to a slightly positive pressure, distributed over large circles with pixilated edges. This pixilation marks the discontinuous change in the CP distribution upon leaving the averaged core region. This offers a much more straightforward view of the Sn's core pressures than the untreated CP map of Figure 2.5a: the Sn cores have net positive pressures which are essentially isotropic.

The Ca cores in this plot become similarly smoother. Upon averaging over the spherically symmetric components, the blue cores at the atom centers disappear, yielding a distribution that is uniformly positive. A highly anisotropic character to the Ca core also becomes more apparent. Red spots appear just above and below the Ca nuclear pressures, indicating colossal positive pressures of 1800 GPa. These positive CP features lie along the unusually short Ca-Ca contacts of the structure (2.96 Å in our LDA-DFT optimized geometry), to which Corbett and coworkers attributed the nonexistence of this compound. This is the first of several indications we will see in the DFT-CP analysis of this system of the truly repulsive nature of the interactions at these contacts.

Another difference between the CP maps of Figures 2.5a and 2.5b is notable. Upon removing the oscillatory character of the core pressures, the pressure range seen in the structure shrinks from 3000 GPa

down to 2250 GPa. This 750 GPa reduction in the pressure range captured by the color map allows for a greater contrast between features in the space outside of the cores, although in this case the repulsive character of the Ca-Ca contacts remains the most striking aspect of the map.

2.7. Integration and projections of the CP distribution around atoms

The results of the isotropic core component averaging described in the last section reinforce the view of the CP distribution as consisting of core regions with net positive pressure immersed in a background of negative pressure. Interpreting the overall pressure exerted by the interatomic contacts on each atom then requires an integration of the pressure map and its directionality around the atom's position.

The angular dependence of the pressure distribution surrounding an atom plays a central role here. Because of this, we will now describe in detail our procedure for determining the pressures experienced by the atoms along different directions. This process begins with a projection of the CP distribution onto spherical harmonics as follows:

$$a_{lm} = \frac{1}{N_{\text{voxels,atom}}} \sum_n w_{n,\text{atom}} P_{\text{voxel},n} Y_{l,m}(\theta_n, \phi_n) \quad (2.8)$$

where $w_{n,\text{atom}}$ is the fraction of voxel n 's pressure that is attributed to the atom in question, $N_{\text{voxels,atom}} = \sum_n w_{n,\text{atom}}$ is the number of voxels belonging to the atom, and (θ_n, ϕ_n) are the angular components of the spherical polar coordinates of voxel n with the origin being the atom's nucleus. The projections a_{lm} can be used to reconstruct this angular distribution—or the chemical pressure anisotropy, $CP_{\text{aniso}}(\theta, \phi)$, of the atom—where all pressure contributions are now mapped onto the unit sphere:

$$CP_{aniso}(\theta, \phi) = \sum_{l \leq l_{max}} \left(\sum_{-l \leq m \leq l} a_{lm} Y_{l,m}(\theta, \phi) \right) \quad (2.9)$$

with l_{max} being the l index of the highest order spherical harmonics to be included in the projection.

The interpretation of this function is made clear by taking a closer look at the a_{00} coefficient. As $Y_{0,0} = 1/(4\pi)^{1/2}$, a_{00} is simply calculated as

$$a_{00} = \frac{1}{N_{voxels,atom}} \sum_n w_{n,atom} P_{voxel,n} \sqrt{\frac{1}{4\pi}} = P_{atom} \sqrt{\frac{1}{4\pi}} \quad (2.10)$$

where P_{atom} is the nominal average pressure experienced by the atom. The summation of terms giving rise to the $CP_{aniso}(\theta, \phi)$ function then begins as

$$CP_{aniso}(\theta, \phi) = P_{atom} \sqrt{\frac{1}{4\pi}} \cdot \sqrt{\frac{1}{4\pi}} + \dots = \frac{P_{atom}}{4\pi} + \dots \quad (2.11)$$

In this way, the higher order terms describe how the CP anisotropy function differs from a sphere whose radius is proportional to the average pressure of the atom.

The role of the $1/4\pi$ factor in Equation 2.11 can be understood by taking the integral of the function over the unit sphere. In this case all of the higher-order terms integrate to zero, and we are left with

$$\begin{aligned} \int_{\phi=0}^{\phi=2\pi} \int_{\theta=0}^{\theta=2\pi} \sin(\theta) CP_{aniso}(\theta, \phi) d\theta d\phi &= \int_{\phi=0}^{\phi=2\pi} \int_{\theta=0}^{\theta=2\pi} \sin(\theta) \frac{P_{atom}}{4\pi} d\theta d\phi \\ &= \frac{P_{atom}}{4\pi} \int_{\phi=0}^{\phi=2\pi} \int_{\theta=0}^{\theta=2\pi} \sin(\theta) d\theta d\phi = P_{atom} \quad (2.12) \end{aligned}$$

The integral thus recovers the average pressure for the atom. The factor $\sin(\theta)d\theta d\phi/4\pi$ can then be thought of as a weight in averaging over the sphere.

We now arrive at a straightforward means of interpreting the numerical values of the $CP_{aniso}(\theta, \phi)$ function: Multiplying the function by 4π yields the net pressure experienced along each direction, $P_{atom}(\theta, \phi)$, i.e.

$$P_{atom}(\theta, \phi) = 4\pi \cdot CP_{aniso}(\theta, \phi) \quad (2.13)$$

$$P_{atom} = \overline{P_{atom}(\theta, \phi)} = \int_{\phi=0}^{\phi=2\pi} \int_{\theta=0}^{\theta=2\pi} P_{atom}(\theta, \phi) \frac{\sin(\theta)d\theta d\phi}{4\pi} \quad (2.14)$$

Once the $P_{atom}(\theta, \phi)$ function is calculated, it can be easily represented graphically using radial plots, as in Figure 2.6. In these images, a CP surface is plotted on each atom, with the distance of the atom to a point on the surface with coordinates (θ, ϕ) being proportional to the magnitude of the CP experienced along that direction. The signs of the pressures are given by the color of the surface. Black features in the plots correspond to directions along which contraction is favorable (evoking the image of a black hole pulling inwards on its surroundings). Lobes in white indicate directions for which expansion is desired (by analogy with the bright radiance of white hot stars).

There are two parameters involved in the creation of such plots: the l_{max} value and the form of the weighting scheme leading to the $w_{n,atom}$ values. l_{max} simply determines to what detail the angular distributions of the CP map is captured. From our experience, setting l_{max} beyond 4 or 5 substantially increases the processing time without leading to any significant changes in the qualitative pressure schemes. For this reason, we use 4 here for the upper limit. The selection of the scheme for distributing the voxel pressures among the atoms is a more involved issue, and is the focus of the next section.

2.8. The contact volume integration scheme

In the projections of the CP map described above, a key parameter is the way in which the structure is divided among the atoms. For the Sr-Ag and Ca-Ag structures we examined earlier,¹⁸ we tested several schemes for this, including the use of fixed spheres around the atomic positions, the division of space into Voronoi cells⁴⁵ ($w_{n,atom}=1$ if voxel n is within the Voronoi cell of the atom), and the atomic domains revealed through the use of Bader's Quantum Theory of Atoms in Molecules.^{7,8} For these cases, the Voronoi cell approach provided results that were easiest to interpret, in that the CP surfaces on pairs of atoms agreed most closely in their signs and magnitudes along the vector separating them. Unresolved is whether the Voronoi scheme works in all cases, and if not, what would provide a more robust partitioning of space.

In Figure 2.6a, we explore this question by showing CP anisotropy surfaces calculated for a W_5Si_3 -type Ca_5Sn_3 phase, the hypothetical parent to the complex $Ca_{36}Sn_{23}$ structure, integrated with the Voronoi scheme. The results are shown using two Hartwigsen-Goedecker-Hutter pseudopotentials for Ca available with the ABINIT package, to explore how stable the CP picture is to changes in the modeling of the core regions of the atom. The calculation leading to the image in the left panel employed the semicore Ca potential, in which the usual Ca $4s^2$ set of valence electrons is expanded to include lower energy $3p^6$ and $3s^2$ electrons, for a total of 10 valence electrons/Ca atom. The right panel shows the result using the valence-only potential, in which just the Ca $4s^2$ electrons are considered explicitly.

Similarities and differences between the two plots occur. In both cases, the surfaces on the tetrahedrally-coordinated Ca atoms exhibit white lobes pointing across the shared tetrahedral atoms toward their Ca neighbors. This indicates that positive, repulsive pressures occur at these contacts, as is consistent with the unusually short Ca-Ca distances here (2.94 Å in our LDA-DFT optimized structures). However, the

shapes of these calcium CP surfaces differ dramatically. For the Ca semicore calculation, triangular positive pressure lobes, resembling the bodies of squid, point toward the neighboring Ca atoms. In the valence-only Ca result, long, nearly cylindrically symmetric lobes appear in these places instead. Additional positive pressure features occur around the equator of the CP anisotropy surfaces.

The remaining features in the plot are more difficult to interpret. The Sn atoms appear with black bulbous surfaces, but whose relative sizes and shapes vary between the two plots. For the two results a similar story emerges of Ca-Ca repulsion against a backdrop of the other interactions, but the inconsistencies indicate that the Voronoi approach is rather sensitive to the details of the treatment of the core region.

A more basic drawback of using the Voronoi approach in this system can be seen by beginning with points on the black Sn surfaces in either image and following some of these directions toward the neighboring Ca atoms. In many cases the black Sn surfaces point to white features on Ca surfaces. Along the Ca-Sn contacts, then, we see desires for contraction on the Sn and for expansion on the Ca. Missing here is an immediate answer to the issue of whether these Ca-Sn contact distances are too long or too short.

Unlike the Ca-Ag and Sr-Ag structures we examined earlier, it appears that drawing boundaries between atomic cells at the mid-points between contacts is too crude of an assumption for this system. One could imagine moving the boundaries back and forth to make the atomic cells better reflect the relative sizes of the atoms. Such a procedure is included in our latest version of the *CPintegrate* program, using the additively-weighted Voronoi method.⁴⁵ We have found, however, that this approach is of limited use, particularly when examining combinations of atoms with very different numbers of core-like electrons in their valence sets.

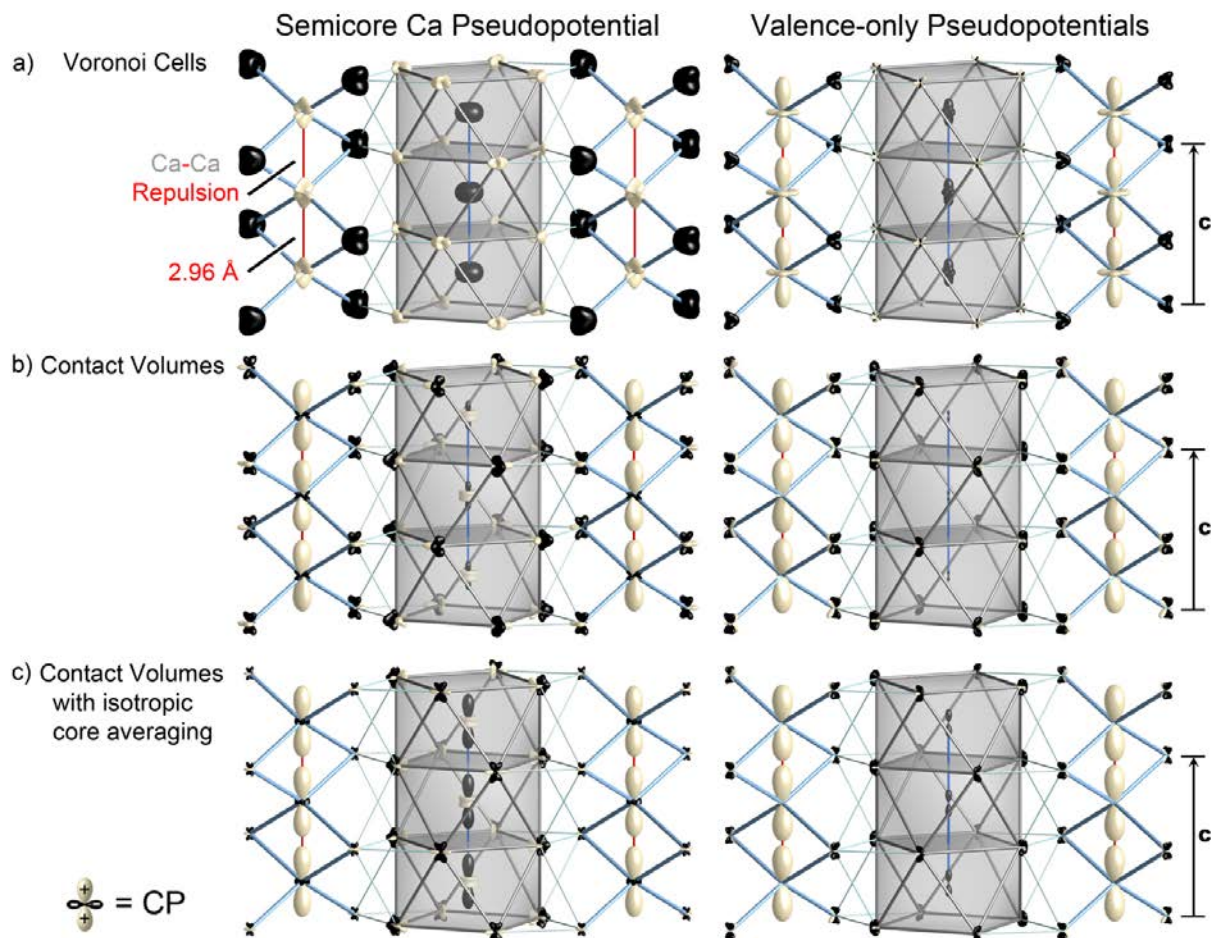


Figure 2.6. The dependence of the chemical pressure (CP) anisotropies of atoms in the hypothetical Ca_5Sn_3 structure on the method of dividing voxels among the atoms, employing Ca pseudopotentials treating semicore electrons explicitly (left column) and as part of the pseudopotential core (right column). The CP distribution around each atom is shown as a radial plot, with the distance between the atom's nucleus and a point on the surface being proportional to the pressure magnitude along that direction. The color of the surface indicates the sign of the pressure: black for negative, white for positive. The plots are shown for results obtained when (a) dividing space into the Voronoi cells of the atoms, (b) dividing space into contact volumes, within which the distributions are averaged before carrying out the projections, and (c) applying the contact volume scheme to a CP map that has undergone isotropic core component averaging. The final method yields the greatest agreement between the two calculations using different models for the Ca core. The scales of the CP surfaces in the various panels are chosen for maximum clarity rather than consistency.

A first step toward a more generally useful integration scheme is to clearly express our assumptions about how the CP map should be interpreted. While the pressure calculated for each voxel in the unit cell is a function of the full electronic structure of the compound, we expect that the atoms closer to a voxel will play larger roles in determining its pressure. For the purposes of interpreting the CP map in terms of pair-wise interatomic interactions, *we will assume that a voxel's pressure is an expression of the interaction between its two closest atoms.* The involvement of other atoms in that voxel's pressure will appear as modulations to the degree of optimization of that specific interatomic interaction.

Once this assumption is articulated, a straightforward approach emerges to obtaining CP anisotropy surfaces that are reflective of the net interactions between an atom and its neighbors. We begin by dividing the unit cell into regions of space whose voxels are associated with the same interatomic contact, regions which we will refer to as *contact volumes*. We then average the pressures of the voxels within each contact volume to obtain average interatomic pressures.⁴⁶ Next, in order to evenly distribute the pressures between the atoms at each contact, the individual voxel pressures are replaced with the average pressures for their contact volumes. Finally, the voxels are assigned with a weight of one half to both atoms of their contacts, and the projections described in the last section are carried out.

The CP anisotropy surfaces resulting from the application of this contact volume integration scheme are presented in Figure 2.6b, where the agreement between the semicore Ca and valence-only Ca results is substantially improved. In particular, the shapes of the positive pressure lobes along the short Ca-Ca contacts are now quite similar. Also, the placement of these black and white lobes now appears to be coordinated between the atoms. In going through the structure contact by contact, one finds that in each case the CP anisotropy surfaces on both sides of interatomic vectors are the same color. In particular, the majority

of the contacts between atoms of different layers along the c -direction appear with black CP lobes. These contacts are overly long and call for the contraction of the structure's c -axis. Such contraction is prevented, of course, by the strained Ca-Ca contacts within the tetrahedral chains.

The largest difference between the semicore and valence-only results is perhaps in the CP surfaces on the Sn atoms with square-antiprismatic coordination. For the semicore calculation, functions resembling d_{z^2} orbitals appear on these Sn atoms, with black lobes pointing up and down toward the Sn atoms in neighboring antiprisms, and a white torus of positive pressure directed at the surrounding Ca atoms. On moving to the valence-only result, these Sn CP anisotropy surfaces virtually vanish. In looking closely at the image, a tiny black dumbbell is barely visible at each of these sites.

This difference can be partially bridged with the application of the isotropic core component averaging procedure discussed earlier. This is shown in Figure 2.6c using the core radii of 0.8 and 1.3 Å for Ca and Sn, respectively. The vertical lobes of d_{z^2} -like surfaces for the Sn atoms in the semicore calculation have grown at the expense of the torus, leading to a surface more closely approximating a black dumbbell. Meanwhile, the black dumbbell of the valence-only calculation has grown closer to the sizes of the black lobes on the semicore result.

At this point, one could imagine making refinements on the contact volume scheme to further improve the agreement between the two choices of pseudopotentials. Indeed, the assumption that each voxel is influenced by its two closest atoms is crude in several ways. It neglects the differing sizes of atoms of different elements, and has the potential to coarsely cut off the influence of other neighboring atoms that might be only slightly further out. In the newest version of our *CPintegrate* program, we have included

preliminary code for a scheme in which Hirshfeld weights⁴⁷ are used in determining the relative importance of the contacts that a voxel could participate in. For Ca_5Sn_3 , this yields pictures similar to those of Figure 2.6c, but the option is still under development.

Even with its simplistic assumptions, the contact volume scheme offers a much clearer picture of the competing interactions within Ca_5Sn_3 than the Voronoi scheme. In the application of the DFT-CP method to a number of intermetallic phases, we have seen that these results are representative: in each case the contact volume integration scheme provides a chemically-meaningful interpretation of the CP map.

2.9. Chemical pressure analysis of $\text{Ca}_{36}\text{Sn}_{23}$

In the above sections, we worked through the technical details of the DFT-CP analysis and refinements to the method to improve its generality. Having built this foundation, we will now demonstrate the use of this approach in the theoretical investigation of the experimentally-deduced role of size-effects in solid state structures. As a model system we will use the superstructure series based on the insertion of planar interfaces into the W_5Si_3 type (Figures 2.1 and 2.2). The driving force for such superstructure ordering was hypothesized by Corbett et al. to be the presence of overly short contacts between the larger, more electropositive atoms in the centers of the edge-sharing tetrahedra in the basic structure (Figure 2.3).

As a first step in exploring this idea, let's look again at the CP distribution in a hypothetical W_5Si_3 -type Ca_5Sn_3 phase, as would arise from removing the interfaces from the $\text{Ca}_{36}\text{Sn}_{23}$ or $\text{Ca}_{31}\text{Sn}_{20}$ structures. In Figure 2.7a, we show the LDA-DFT optimized structure of this phase (using the valence-only Ca pseudo-potential), overlaid with its atomic CP anisotropy surfaces.

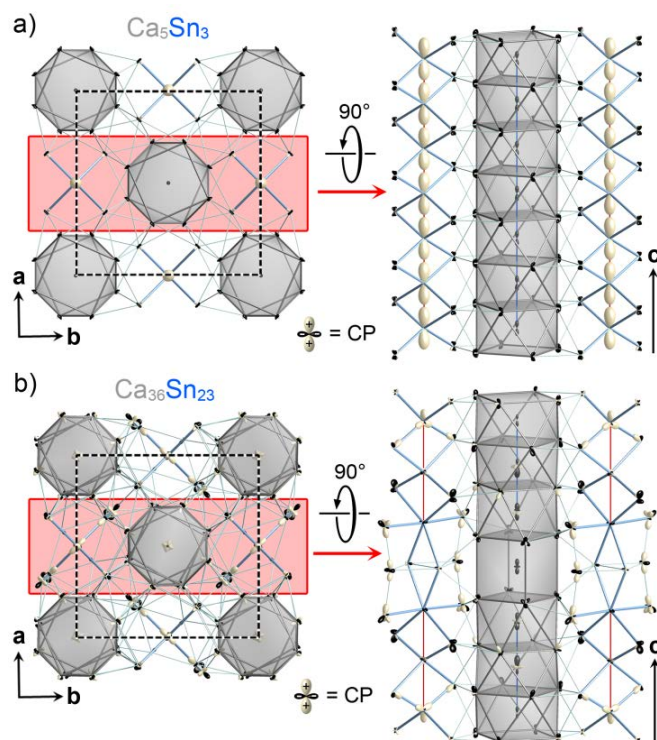


Figure 2.7. Comparison of the DFT-chemical pressure (CP) distributions in (a) a hypothetical W_5Si_3 -type Ca_5Sn_3 phase, and (b) the observed superstructure variant $Ca_{36}Sn_{23}$. See the caption of Figure 2.6 for plotting conventions. The CP surfaces of panels a and b are plotted at the same scale, allowing direct comparison of their features.

For the most part, the features of the plot appear very small. The exception occurs in the chains of edge-sharing tetrahedra: for the Ca atoms at the tetrahedral centers, large white lobes are pointing up and down toward the Ca atoms in the neighboring tetrahedra (right panel). These are the largest lobes in the structure, corresponding to a positive pressure of 176 GPa. As these lobes occur along the Ca-Ca contacts in the tetrahedron chains, this suggests that the Ca-Ca distances within these chains are overly short.

Expansion of the structure to alleviate these positive pressures would then be desirable. However, such a response is prevented by the remainder of the structure, which appears decorated by small, black negative

pressure features. These results confirm the model of Corbett and coworkers of the W_5Si_3 structure type being destabilized by the presence of large electropositive atoms in the tetrahedron centers.

How might the insertion of interfaces relieve these positive pressures experienced by the tetrahedrally-coordinated Ca atoms? Symmetry plays a role in the CP situation of these atoms. The contacts above and below each Ca are equivalent by the mirror planes of the W_5Si_3 type's space group, $I4/mcm$. Moving upwards away from the Ca atom below would increase the positive pressures along the contact above, and vice versa. The insertion of a defect plane either above or below a Ca atom would break this stalemate by providing open space for the atom to move into.

In Figure 2.7b, we test this expectation by plotting the CP anisotropy surfaces for the $Ca_{36}Sn_{23}$ structure, in which interfaces cut the Ca_5Sn_3 structure into 3-unit-cell-thick slabs. The right panel of Figure 2.7b focuses on the region near one of the interfaces. Red bars are used to connect the Ca atoms corresponding to tetrahedrally-coordinated Ca atoms in the hypothetical Ca_5Sn_3 phase. Along these red bars, the vertical white lobes corresponding to Ca-Ca repulsion have essentially vanished, with the exception of those furthest from the interface at the top and bottom of the panel.

As is shown in Figure 2.8, a comparison of the Ca coordination environment in the tetrahedral chain in the hypothetical Ca_5Sn_3 phase with those in $Ca_{36}Sn_{23}$ allows for this chemical pressure release to be framed in familiar chemical terms. In Ca_5Sn_3 , these atoms lie at the centers of edge-sharing tetrahedra of Sn. As is well-known from Pauling's rules,⁴⁸ the shared edges between tetrahedra force the tetrahedral centers into close proximity. The tetrahedral coordination environments of large atoms are thus expected to avoid fusing at edges. It would appear that $Ca@Sn_4$ tetrahedra lie in this category.

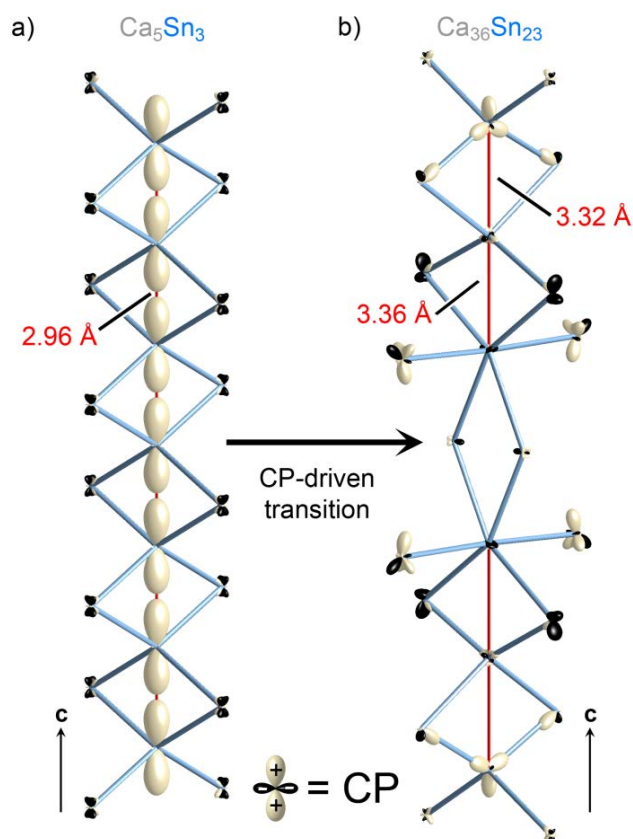


Figure 2.8. Chemical pressure release in the chains of Ca-centered tetrahedra on going from (a) the hypothetical W_5Si_3 -type Ca_5Sn_3 to (b) the observed structure of $\text{Ca}_{36}\text{Sn}_{23}$. Note that on going from (a) to (b) larger Ca-Ca distances are achieved by replacing edge-sharing tetrahedra with edge-sharing octahedra. As in Figure 2.7, the same scale is used for all CP surfaces. For plotting conventions, see the caption to Figure 2.6.

In the corresponding regions of $\text{Ca}_{36}\text{Sn}_{23}$, a simple solution to the issue of Ca-Ca repulsion is found. Each interface bisects a Ca-Ca pair in the tetrahedral chain and places four additional Sn atoms between them. Through the incorporation of these Sn atoms, the edge-sharing tetrahedral arrangement is converted to a pair of edge-sharing *octahedra*. This configuration is expected to be much less sterically demanding: the ideal Sn-Ca-Sn angles in these polyhedra decrease from 109.5° in the tetrahedra to 90° in the octahedra. As a result, the polyhedral edges occur further out from the centering Ca atoms, and the Ca-Ca

distances between neighboring polyhedra are substantially increased. This provides relief to the repulsive CPs between the Ca atoms at the interface (between which no positive CP lobe is apparent in Figure 2.8b), but also to the Ca atoms deeper in the W_5Si_3 -type slabs which are free to relax toward the space provided by the octahedral Ca atoms.

In the Ca-Sn system, the appearance of planar interfaces in the W_5Si_3 type, as in $Ca_{36}Sn_{23}$ and $Ca_{30}Sn_{21}$, can thus be seen as driven by chemical pressure. The picture which emerges from this analysis confirms the insightful model of Corbett et al. for this family of superstructure phases, and illustrates how DFT-CP analysis allows for the theoretical investigation and confirmation of hypotheses based on atomic size effects.

2.10. Conclusions

In this paper, we develop the idea behind DFT-chemical pressure (CP) analysis into a general tool for analyzing the role atomic size has in shaping the structures of solid state materials. We described several improvements over our earlier outline of the method, including (1) the use of isotropic core component averaging to make the essential CP features in the ion core regions more apparent in the CP maps, and (2) the creation of the contact volume integration scheme, in which interatomic interactions appear as mutually attractive or repulsive from the points of view of the participating atoms. The revised DFT-CP approach was then applied toward revealing the origin of the $Ca_{36}Sn_{23}$ structure, a superstructure variant of the W_5Si_3 type.

Our analysis of $\text{Ca}_{36}\text{Sn}_{23}$ confirmed the empirically-derived model of Corbett et al. for this family of structures: a hypothetical W_5Si_3 -type Ca_5Sn_3 phase would have chains of edge-sharing Ca-centered Sn tetrahedra, i.e. $(\text{CaSn}_{4/2})_\infty$, which would enforce unreasonably short Ca-Ca distances. Large positive CPs occur along these Ca-Ca contacts, indicating that the distances are indeed overly short. An advantage of the DFT-CP approach is that further details can be seen in how these distances are constrained by the remainder of the structure. For $\text{Ca}_{36}\text{Sn}_{23}$, the predominant features apart from the short Ca-Ca contacts are small black lobes pointing along a variety of interactions. Such details provide clarity and precision to the useful concept of “matrix effects.”⁴⁹⁻⁵¹

The DFT-CP analysis joins a number of other theoretical tools for extracting chemical insight from electronic structure results on solid state structures. Methods in common use include the crystal orbital overlap and Hamiltonian population analyses (COOP and COHP);⁵²⁻⁵⁴ the electron localization function (ELF) and its successor, the electron localization indicator (ELI);⁵⁵⁻⁵⁹ and the analysis of electron density features using the quantum theory of atoms and molecules (QTAIM).^{7,8} How does the DFT-CP analysis relate to these analytical tools?

A common feature of each of the other tools listed above is that they explore the presence or strength of bonding interactions in a system with a given geometry. For example, the COHP analysis for a contact quantifies the strength of that interatomic interaction, and whether this interaction would be strengthened or weakened by a change in the electron count of the compound. Similarly an ELI analysis reveals at what points in the structure electron pairs tend to be localized, which can then be correlated with the presence of bonds or lone-pairs.

The DFT-CP analysis provides complementary information: by determining the pressures at work at each interatomic contact, it reveals to what extent the bonding strength is optimized with respect to interatomic distances. Examining the geometrical arrangements made by these pressures throughout a structure can point to where frustration arises in the optimization of these interactions, and where structural transformations may be necessary. These insights may contribute to materials design principles, growing out of a tighter integration of the roles of electronics and atomic sizes in our understanding of solid state compounds.

Acknowledgements

We thank Brandon Kilduff for engaging discussions on the application of DFT-CP analysis to intermetallic phases, and Yiming Guo for suggesting improvements to the code of our DFT-CP programs. We also gratefully acknowledge the financial support of the National Science Foundation (NSF) through grant DMR-1207409. This research involved calculations using computer resources supported by NSF grant CHE-0840494.

2.11. References

- (1) van der Waals, J. D. *Nobel Lectures, Physics 1901-1921*; Elsevier Publishing Company: New York, 1967, pp 254-265.
- (2) Smith, M.; March, J. *March's advanced organic chemistry: reactions, mechanisms, and structure*; 6th ed.; Wiley-Interscience: Hoboken, NJ, 2007, pp 397-401.
- (3) Goldschmidt, V. M. *Trans. Faraday Soc.* **1929**, 25, 253.
- (4) Pauling, L. J. *Am. Chem. Soc.* **1927**, 49, 765.

- (5) Nolas, G. S.; Cohn, J. L.; Slack, G. A.; Schujman, S. B. *Appl. Phys. Lett.* **1998**, 73, 178.
- (6) Nolas, G. S.; Cohn, J. L.; Slack, G. A. *Phys. Rev. B* **1998**, 58, 164.
- (7) Bader, R. F. W. *Atoms in molecules: a quantum theory*; Oxford University Press: Oxford, England, 1994, pp 133-137.
- (8) Baranov, A.; Kohout, M.; Wagner, F. R.; Grin, Y.; Kniep, R.; Bronger, W. Z. *Anorg. Allg. Chem.* **2008**, 634, 2747.
- (9) Hume-Rothery, W.; Raynor, G. V. *The structure of metals and alloys*; 4th ed.; Institute of Metals: London, 1962, pp 217-245.
- (10) Laves, F. in *Theory of alloy phases; a seminar on theory of alloy phases held during the Thirty-seventh National Metal Congress and Exposition, Philadelphia, October 15 to 21, 1955*; American Society of Metals: Cleveland, 1956, pp 124-198.
- (11) Pearson, W. B. *The crystal chemistry and physics of metals and alloys*; Wiley-Interscience: New York, 1972, pp 73-79.
- (12) Simon, A. *Angew. Chem. Int. Ed. Engl.* **1983**, 22, 95.
- (13) Amerioun, S.; Häussermann, U. *Inorg. Chem.* **2003**, 42, 7782.
- (14) Mozharivskiy, Y.; Tsokol, A. O.; Miller, G. J. Z. *Kristallogr. Cryst. Mater.* **2006**, 221, 493.
- (15) Li, B.; Corbett, J. D. *Inorg. Chem.* **2007**, 46, 8812.
- (16) Xia, S.-q.; Bobev, S. J. *Am. Chem. Soc.* **2007**, 129, 10011.
- (17) Fredrickson, D. C.; Lidin, S.; Venturini, G.; Malaman, B.; Christensen, J. J. *Am. Chem. Soc.* **2008**, 130, 8195.
- (18) Fredrickson, D. C. *J. Am. Chem. Soc.* **2012**, 134, 5991.
- (19) Nielsen, O. H.; Martin, R. M. *Phys. Rev. B* **1985**, 32, 3780.
- (20) Godfrey, M. J. *Phys. Rev. B* **1988**, 37, 10176.
- (21) Ziesche, P.; Gräfenstein, J.; Nielsen, O. H. *Phys. Rev. B* **1988**, 37, 8167.
- (22) Filippetti, A.; Fiorentini, V. *Phys. Rev. B* **2000**, 61, 8433.

- (23) Rogers, C. L.; Rappe, A. M. *Phys. Rev. B* **2002**, *65*, 224117/1.
- (24) Treglia, G. In *Stress and strain in epitaxy; theoretical concepts, measurements, and applications*; Elsevier Science B.V.: 2001, pp 119-150.
- (25) Gonze, X.; Rignanese, G.-M.; Verstraete, M.; Beuken, J.-M.; Pouillon, Y.; Caracas, R.; Jollet, F.; Torrent, M.; Zerah, G.; Mikami, M.; Ghosez, P.; Veithen, M.; Raty, J.-Y.; Olevano, V.; Bruneval, F.; Reining, L.; Godby, R.; Onida, G.; Hamann, D. R.; Allan, D. C. *Z. Kristallogr.* **2005**, *220*, 558.
- (26) Gonze, X.; Amadon, B.; Anglade, P. M.; Beuken, J. M.; Bottin, F.; Boulanger, P.; Bruneval, F.; Caliste, D.; Caracas, R.; Cote, M.; Deutsch, T.; Genovese, L.; Ghosez, P.; Giantomassi, M.; Goedecker, S.; Hamann, D. R.; Hermet, P.; Jollet, F.; Jomard, G.; Leroux, S.; Mancini, M.; Mazevet, S.; Oliveira, M. J. T.; Onida, G.; Pouillon, Y.; Rangel, T.; Rignanese, G. M.; Sangalli, D.; Shaltaf, R.; Torrent, M.; Verstraete, M. J.; Zerah, G.; Zwanziger, J. W. *Comput. Phys. Commun.* **2009**, *180*, 2582.
- (27) Leon-Escamilla, E. A.; Corbett, J. D. *Inorg. Chem.* **1999**, *38*, 738.
- (28) Palenzona, A.; Manfrinetti, P.; Fornasini, M. L. *J. Alloys Compd.* **2000**, *312*, 165.
- (29) Moreau, J. M.; Paccard, D.; Parthé, E. *Acta Crystallogr. B* **1976**, *32*, 1767.
- (30) Cromer, D. T.; Larson, A. C. *Acta Crystallogr. B* **1977**, *33*, 2620.
- (31) Fornasini, M. L.; Franceschi, E. *Acta Crystallogr. B* **1977**, *33*, 3476.
- (32) Ganguli, A. K.; Guloy, A. M.; Leon-Escamilla, E. A.; Corbett, J. D. *Inorg. Chem.* **1993**, *32*, 4349.
- (33) Leon-Escamilla, E. A.; Hurng, W.-M.; Peterson, E. S.; Corbett, J. D. *Inorg. Chem.* **1997**, *36*, 703.
- (34) Ganguli, A. K.; Gupta, S.; Zhao, J.-T.; Alejandro Leon-Escamilla, E.; Corbett, J. D. *J. Solid State Chem.* **2005**, *178*, 2959.
- (35) Kresse, G.; Furthmüller, J. *Phys. Rev. B* **1996**, *54*, 11169.
- (36) Kresse, G.; Furthmüller, J. *Comput. Mater. Sci.* **1996**, *6*, 15.
- (37) Monkhorst, H. J.; Pack, J. D. *Phys. Rev. B* **1976**, *13*, 5188.
- (38) Vanderbilt, D. *Phys. Rev. B* **1990**, *41*, 7892.
- (39) Goedecker, S.; Teter, M.; Hutter, J. *Phys. Rev. B* **1996**, *54*, 1703.

- (40) Hartwigsen, C.; Goedecker, S.; Hutter, J. *Phys. Rev. B* **1998**, 58, 3641.
- (41) Fredrickson, D. C. *J. Am. Chem. Soc.* **2011**, 133, 10070.
- (42) Harris, N. A.; Hadler, A. B.; Fredrickson, D. C. *Z. Anorg. Allg. Chem.* **2011**, 637, 1961.
- (43) Martin, R. M. *Electronic structure : basic theory and practical methods*; 1st pbk. ed.; Cambridge University Press: Cambridge, UK ; New York, 2008, pp 255-256.
- (44) An interesting alternative spatial resolution of the pressure was recently described in Ouahrani, T.; Menendez, J. M.; Marqués, M.; Contreras-García, J.; Baonza, V. G.; Recio, J. M. *Europhys. Lett.* **2012**, 98, 56002. Here, the focus is on the inverse of the total pressure: $1/P = -\partial V/\partial E$. The $-\partial V/\partial E$ expression is then split into a sum of volume differentials for individual atomic cells (as obtained from a QTAIM analysis) over a common ∂E denominator. Each atomic ∂V is then proportional to an inverse atomic pressure.
- (45) Okabe, A.; Boots, B.; Sugihara, K.; Chiu, S. N. *Spatial tessellations: concepts and applications of Voronoi diagrams*; 2nd ed.; Wiley: Chichester ; New York, 2000, pp 123-127.
- (46) A relatively small group of voxels in any given structure may lie in the centers of the interstitial spaces that gives them a number of nearest neighbors at the same distance. As the number of first nearest neighbors grows beyond two, the number of contact volumes that a voxel can participate in rapidly grows. For simplicity, we treat such voxels as shared equally between its neighbors, without associating them to particular contact volumes. They are thus not included in the averaging within the contact volumes.
- (47) Hirshfeld, F. L. *Theoret. Chim. Acta* **1977**, 44, 129.
- (48) Pauling, L. *J. Am. Chem. Soc.* **1929**, 51, 1010.
- (49) Guloy, A. M.; Corbett, J. D. *Inorg. Chem.* **1996**, 35, 2616.
- (50) Maggard, P. A.; Corbett, J. D. *Inorg. Chem.* **1998**, 37, 814.
- (51) Maggard, P. A.; Corbett, J. D. *Inorg. Chem.* **2001**, 40, 1352.
- (52) Hughbanks, T.; Hoffmann, R. *J. Am. Chem. Soc.* **1983**, 105, 1150.
- (53) Hughbanks, T.; Hoffmann, R. *J. Am. Chem. Soc.* **1983**, 105, 3528.
- (54) Dronskowski, R.; Bloechl, P. E. *J. Phys. Chem.* **1993**, 97, 8617.
- (55) Becke, A. D.; Edgecombe, K. E. *J. Chem. Phys.* **1990**, 92, 5397.

(56) Savin, A.; Becke, A. D.; Flad, J.; Nesper, R.; Preuss, H.; von Schnering, H. G. *Angew. Chem. Int. Ed. Engl.* **1991**, *30*, 409.

(57) Savin, A.; Nesper, R.; Wengert, S.; Fässler, T. F. *Angew. Chem. Int. Ed. Engl.* **1997**, *36*, 1808.

(58) Kohout, M.; Pernal, K.; Wagner, F. R.; Grin, Y. *Theor. Chem. Acc.* **2004**, *112*, 453.

(59) Wagner, F. R.; Bezugly, V.; Kohout, M.; Grin, Y. *Chem. Eur. J.* **2007**, *13*, 5724.

Chapter 3.

Filling in the Holes: Structural and Magnetic Properties of the Chemical Pressure Stabilized LnMn_xGa_3 ($\text{Ln} = \text{Ho-Tm}$; $x < 0.15$)

This chapter has been published: Fulfer, B. W.; McAlpin, J. D.; Engelkemier, J.; McCandless, G. T.; Prestigiacomo, J.; Stadler, S.; Fredrickson, D. C.; Chan, J. Y. *Chem. Mater.* **2014**, *26*, 1170-1179. The theoretical analysis in this chapter was the work of Engelkemier and Fredrickson. All of the experimental measurements and results were made by Chan and coworkers.

3.1. Abstract

Single crystals of LnMn_xGa_3 ($\text{Ln} = \text{Ho-Tm}$; $x < 0.15$) were grown from a Ga self-flux. These compounds crystallize in a variant of the AuCu_3 structure type where Mn partially occupies the Ga_6 octahedral holes. Introduction of the Mn guest atoms allows for modulation of the structures and magnetic properties of their hosts: While TmGa_3 orders antiferromagnetically at ~ 4.2 K, TmMn_xGa_3 ($x = 0.05, 0.10$) remains paramagnetic down to 1.8 K. Ho and Er analogs order antiferromagnetically, with effective moments and Néel temperatures, respectively, decreasing and increasing as a function of Mn concentration. DFT-chemical pressure analysis elucidates the trends in the stability of LnGa_3 AuCu_3 -type phases and their stuffed derivatives. Guest atom insertion supports expansion of the filled octahedra, allowing relief of negative chemical pressures in surrounding Ga-Ga contacts.

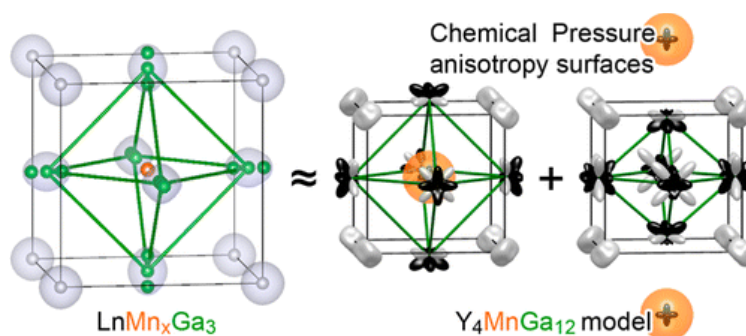


Figure 3.0. The crystal structure of newly synthesized LnMn_xGa_3 ($x < 0.15$) compounds can be understood as partially occupied $\text{Y}_4\text{MnGa}_{12}$ -type structures. Chemical Pressure (CP) analysis of the AuCu_3 -type Ga octahedra in the 4-1-12 phases reveal CP stabilization between Ga-Ga contacts in unstuffed octahedra due to the structural effect of stuffing Mn atoms in neighboring octahedra.

3.2. Introduction

A central problem in the field of materials chemistry is the ability to rationally tune the physical properties of a compound, so that it may be tailored to specific applications. For alloys and intermetallic phases, this process is complicated by the diverse ways in which phases may respond to chemical substitution, including phase segregation, structural progressions, and the formation of unexpected compounds. A potential model system for studying how the properties of intermetallics may be controlled is offered by the AuCu_3 structure type and its derivatives. Despite being one of the simplest inorganic crystal structures, the four atom unit cell of the AuCu_3 type underlies remarkable physical properties. This is illustrated by CeIn_3 which exhibits magnetically mediated superconductivity at the critical temperature (T_c) ~ 0.2 K at 27 kbar.^{1,2} Furthermore, the AuCu_3 -type is able to accommodate transition metal (M) atoms in its octahedral holes which could be used to tune properties of these compounds.³⁻⁸

Indeed, the presence and occupation pattern of the M guest atoms has been observed to have profound effects on the physical properties of these compounds. The simplest stuffing pattern is given by the Y_4PdGa_{12} -type Ln_4MGa_{12} phases (Ln = Lanthanide or similar electropositive element; M = transition metal), in which M occupies one quarter of the interstitial sites in the body centers of the $LnGa_3$ basic cells.³ Examples include Er_4PtGa_{12} and Ho_4PtGa_{12} whose magnetoresistance values reach the unusually high levels of 220 and 900 %, respectively.⁶ Meanwhile, Y_4FeGa_{12} is a weak itinerant ferromagnet with an ordering temperature of 36 K.⁷

Multiple reports indicate that other stuffing patterns can also arise, often with an effect on the magnetic properties of the material. Ln_4FeGa_{12} (Ln = Y, Tb-Er) adopt the ordered Y_4PdGa_{12} structure type except for the Er member, $Er_4Fe_{0.67}Ga_{12}$, which exhibits Ga site splitting and two Fe sites that are partially occupied.⁸ For $Y_4Mn_xGa_{12-y}Ge_y$ (x = 0.74-1.00, y = 0-4.0), Mn occupancy varies as a function of Ge concentration (y).⁹ At y = 4.0, the Mn site is near full occupancy (x = 0.95), and the phase is paramagnetic. However, at decreased Ge concentration (y = 1.0), the Mn occupancy decreases to x = 0.90, and the compound exhibits strong ferromagnetism with T_C = 223 K.⁹

Given the variety of structures arising on the Ln_4MGa_{12} compounds and the ways in which the M atoms affect the magnetic properties of their hosts, we were inspired to synthesize the Ln_4MnGa_{12} analogues of these compounds, and examine the driving forces leading to guest atom incorporation by these structures. In this Chapter, we describe a joint experimental and theoretical endeavor pursuing these aims. We present the crystal growth parameters, structural characterization, magnetic properties for high quality single crystals of $LnMn_xGa_3$ (Ln = Ho-Tm; x < 0.15), and electronic structure calculations using the DFT-chemical pressure analysis to explore the role Mn plays in stabilizing these compounds.

3.3. Experiment section

Synthesis. Single crystals of LnMn_xGa_3 ($\text{Ln} = \text{Ho-Tm}$) were grown from their constituent elements (> 99.9 % purity and used as received). Elements ($\text{Ln}:\text{Mn}:\text{Ga}$) were combined in three different reaction ratios – 1:0:15, 1:0.1:20, and 1:0.2:20 (combined weight of reactants was ~ 1 g) – to study the effect of varying Mn concentration. For each sample, the elements were placed in an alumina crucible, covered in quartz wool, and backfilled with $\sim 1/5$ atm of Ar in a fused silica tube prior to sealing the tube. All samples were heated to 1150 °C at a rate of 100 °C/h, held at 1150 °C for 5 h, slowly cooled to 550 °C at a rate of 5 °C/h, and finally cooled to 300 °C at a rate of 100 °C/h. When the temperature reached 300 °C, the samples were removed from the furnace, inverted with the crucible opening facing down, and centrifuged to remove excess Ga flux. Additional Ga adhering to the reaction products was removed by repeated sonication in hot water. The syntheses yielded high quality single crystals with cubic morphology, the largest of which were approximately 3 mm across a crystalline face.

Elemental Analysis. Elemental analysis of LnMn_xGa_3 ($\text{Ln} = \text{Ho-Tm}$; $x < 0.15$) single crystals was performed via energy-dispersive spectroscopy (EDS) using an EDAX detector fitted to a FEI Quanta 200 scanning electron microscope with an accelerating voltage of 15 kV. Single crystals were thoroughly polished prior to analysis in order to minimize the presence of possible surface impurities. At least 3 polished single crystals were taken per batch, each of which was analyzed at several points (≥ 7) for a period of no less than 30 s to ensure good crystal homogeneity. The atomic percentages were normalized to Ln. The results for compounds grown from reaction ratios of 1:0.2:20 ($\text{Ln}:\text{Mn}:\text{Ga}$) are $\text{Ho}_{1.00(2)}\text{Mn}_{0.12(1)}\text{Ga}_{2.80(5)}$, $\text{Er}_{1.00(6)}\text{Mn}_{0.09(3)}\text{Ga}_{2.67(10)}$, and $\text{Tm}_{1.00(8)}\text{Mn}_{0.10(3)}\text{Ga}_{2.70(16)}$, while normalized results for samples from the 1:0.1:20 ratio are $\text{Ho}_{1.00(7)}\text{Mn}_{0.071(18)}\text{Ga}_{2.75(12)}$, $\text{Er}_{1.00(6)}\text{Mn}_{0.087(17)}\text{Ga}_{2.69(13)}$, and $\text{Tm}_{1.00(5)}\text{Mn}_{0.087(17)}\text{Ga}_{2.70(10)}$.

While there is some deviation from the compositions determined from single crystal X-ray refinement, the data obtained confirm the incorporation of Mn into the AuCu₃-type frameworks. We also note that the compositions are consistently Ga poor relative to the expected Ln:Ga ratio of 1:3. As the crystals were obtained from Ga-rich fluxes, we attribute this to the semi-quantitative nature of the EDS measurements (estimated error bar = 10%), rather than to vacancies of the Ga sublattices.

Structure Determination. Single crystal samples were cut to appropriate sizes (exact dimensions given in Tables 3.1-3.9) and mounted on glass fibers with epoxy. The crystals were then screened by collecting X-ray diffraction data sets with an Enraf Nonius KappaCCD single crystal diffractometer equipped with Mo K α radiation ($\alpha = 0.71073 \text{ \AA}$) and graphite monochromator. This data was sufficient for the refinement of the structures of ErGa₃ and TmGa₃ (Tables 3.1-3.3). Due to the possibility of supercell formation in the Ln-M-Ga compounds,^{8,9} additional data with higher intensities were collected with a Bruker Kappa Apex II diffractometer equipped with a Mo K α ($\lambda = 0.71073$) source and a TRIUMPH monochromator. Collection of additional data, cell refinement, and data reduction were accomplished with the Bruker APEX2 software package. Crystallographic models for LnMn_{*x*}Ga₃ ($0 < x < 0.15$) were derived from data sets collected using the Bruker Kappa Apex II diffractometer (Tables 3.4 and 3.9).

Diffraction data from samples grown with the reaction ratio 1:0.2:20 of Ln:Mn:Ga were indexed to a $\sim 4 \text{ \AA}$ unit cell of the AuCu₃ structure type. Samples grown from all other reaction ratios (1:15 of Ln:Ga and 1:0.1:20 of Ln:Mn:Ga) were also indexed to primitive $\sim 4 \text{ \AA}$ cubic unit cells, indicative of the AuCu₃ structure type. Additional reflections suggesting supercell ordering were not evident. Systematic absences were also consistent with compounds crystallizing in the $Pm\bar{3}m$ space group, of the AuCu₃ structure type, rather than the $Im\bar{3}m$ space group of the Y₄PdGa₁₂ structure type. Preliminary crystallographic models

were obtained via direct methods with SIR97¹⁰ and were refined with SHELXL97,¹¹ or JANA2006.¹² Isosurfaces of the Fourier electronic densities were visualized with the program VESTA 3.¹³

Magnetic Property Measurements. Single crystals were selected from LnMn_xGa_3 ($\text{Ln} = \text{Ho-Tm}$; $x < 0.15$) samples, all of which exhibited a cubic habit. In preparation for magnetic properties measurements, the crystals were polished on all of their faces and oriented using a single crystal X-ray diffractometer. Magnetic properties data were then obtained using a Quantum Design Magnetic Property Measurement System (MPMS). Magnetization as a function of temperature was measured in zero field cooled conditions from 1.8 – 30 K in an applied field of 100 Oe and from 1.8 – 390 K in an applied field of 1000 Oe. Field-dependent magnetization measurements were conducted at 2 K from 0 – 7 T.

Electronic Structure Calculations. DFT-Chemical pressure analyses¹⁴⁻¹⁶ were performed for geometrically optimized AuCu_3 -type phases LnGa_3 ($\text{Ln} = \text{Sc, Y, La}$), and the $\text{Yb}_4\text{PdGa}_{12}$ -type phases $\text{Y}_4\text{MGa}_{12}$ ($\text{M} = \text{Fe, Mn}$), based on the output of LDA-DFT calculations made with the ABINIT^{17,18} program, as described previously. For the ABINIT calculations, the norm-conserving pseudopotentials of Hartwigsen, Goedecker, and Hutter (HGH) were employed,¹⁹ along with the LDA exchange correlation functional of Goedecker, Teter, and Hutter.²⁰ The calculations on AuCu_3 -type and $\text{Yb}_4\text{PdGa}_{12}$ -type phases used Γ -centered $9 \times 9 \times 9$ and $5 \times 5 \times 5$ k-point grids, respectively. The energy-cut offs were set to 55 Ha for LaGa_3 , YGa_3 , $\text{Y}_4\text{MnGa}_{12}$, and $\text{Y}_4\text{FeGa}_{12}$, and 70 Ha for ScGa_3 .

Chemical pressure maps were constructed from the ABINIT output using the program *CPcalc_abinit*. Isotropic core component averaging at this step was found to have little effect on the final overall results, and was not used. The integration was performed using the contact volume scheme¹⁴ with *CPintegrate*. Projections of pressures surrounding each atom were carried out on real spherical harmonics with $l \leq 5$.

The most important theoretical parameter affecting the CP results is the choice of pseudopotential models for the atoms. The HGH pseudopotential set offers “semicore” and “valence-only” options of Sc, Y, Mn, Fe, and Ga, while for La only a semicore potential is available. The valence-only option corresponds to the chemically intuitive treatment of the Sc 4s/3d, Y 5s/4d, Mn 3d, Fe 3d, and Ga 4s/4p electrons as part of the valence set, while the semicore potentials also include deeper subshells of the atoms. Our experimentation with these options shows that the highly localized 3d electrons considered in the Ga semicore pseudopotential give rise to such large energy densities that they dominate the CP map using the current method for their generation. Methods for a better treatment of such intense core pressures are under development, but for the results presented in this paper, semicore pseudopotentials were used for Sc, Y, and La, while valence-only potentials were used for Ga, as well as for Mn and Fe.

3.4. Results and discussion

The crystal structures of LnMn_xGa_3 ($\text{Ln} = \text{Ho, Er, Tm}$). Our syntheses in the Ln:Mn:Ga systems ($\text{Ln} = \text{Ho, Er, Tm}$) were motivated by the prospect of using guest atoms to modulate the physical properties of AuCu_3 -type LnGa_3 lattices. The products obtained from reaction ratios Ln:Mn:Ga of 1:0.1:20 and 1:0.2:20 show several indications that such Mn incorporation is occurring. Inclusion of Mn in the structure leads to larger unit cell parameters and thus, longer Ln-Ln and Ln-Ga ($\text{Ln} = \text{Ho-Tm}$) distances. Peaks in the Fourier difference map from the single crystal X-ray diffraction data are also apparent on the $1b$ site ($1/2, 1/2, 1/2$), the preferred position for M atom incorporation (Figure 3.1). Refinements of the Mn occupancies at this site converge to ~ 0.05 for samples grown with a ratio of 1:0.1:20 (Table 3.5) and to ~ 0.10 - 0.15 for samples grown with a ratio of 1:0.2:20 (Table 3.8). The Mn content thus varies with the Mn

loading of the sample, but the range is limited. Increasing the amount of Mn to 1:0.4:20 or 1:1:20 does not lead to an increased Mn concentration, and the upper bound for Mn content appears to be $x \sim 0.15$ for LnMn_xGa_3 .

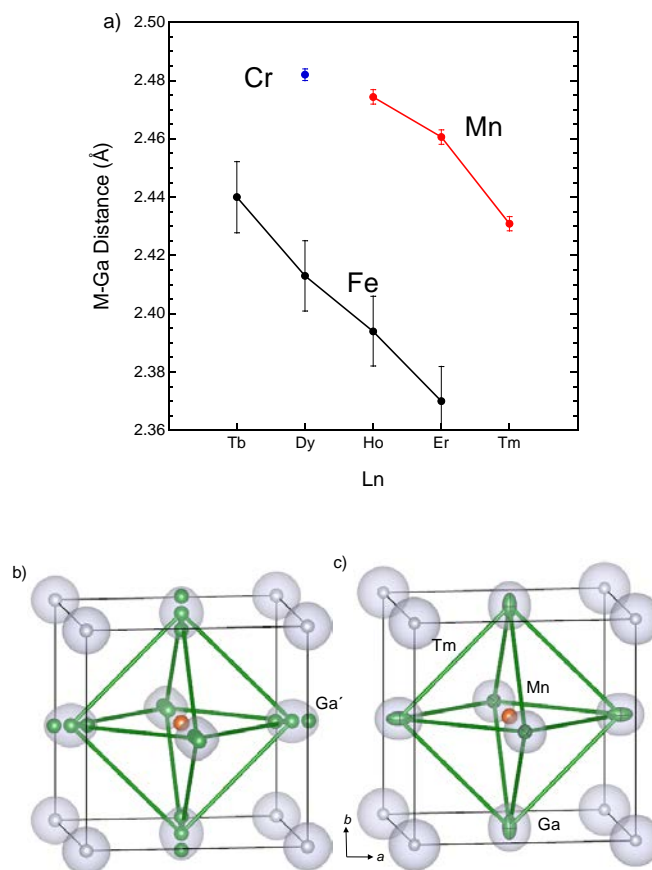


Figure 3.1. (a) M-Ga distances for Ln-M-Ga compounds. Cr and Fe distances were obtained from B. R. Slater *et al.*⁸ and B. L. Drake *et al.*,⁷ respectively. (b) $\text{TmMn}_{0.10}\text{Ga}_3$ unit cell, where Tm atoms are light gray spheres, Mn are orange spheres, Ga (3c) and Ga' (6f) are green spheres. (c) $\text{TmMn}_{0.05}\text{Ga}_3$ unit cell, where Tm atoms are light gray, Mn are orange, and Ga are green. In (b) and (c) isosurfaces of the Fourier electron density are drawn at the level of 25 electrons/Å³.

Examination of the Fourier electron density indicates that the positions of the Ga atoms are affected by the presence or absence of Mn. For large Mn contents ($x \sim 0.10-0.15$), this response is large enough that split position model for the Ga is warranted (see Figure 3.1 and Tables 3.7-3.9). The first Ga site $(0, 1/2, 1/2)$ is occupied when Mn is not present on either side of the Ga atom, while the second Ga site (Ga'), at $(\pm x, 1/2, 1/2)$, is occupied when Mn is present on one side, resulting in Mn-Ga' distances ~ 2.4 Å (Table 3.9). These Mn-Ga' distances are very similar to M-Ga distances reported for ordered Y_4PdGa_{12} -type Ln_4MGa_{12} ($Ln = Tb-Er$; $M = Cr, Fe$; see Figure 3.1a) compounds, which show ordered incorporation of M atoms in a $2 \times 2 \times 2$ supercell of the $AuCu_3$ type (see Figure 3.2).^{7,8} The model is thus consistent with the Mn atoms having coordination environments that are locally similar to those in the Y_4PdGa_{12} -type compounds. However, few indications of superstructuring were evident in the diffraction data, and the crystallographic model outlined above describes compounds as having random occupancy of the holes due to insufficient Mn incorporation.

For $LnMn_{0.05}Ga_3$, with its low Mn content, the range of Ga positions was small enough that a split position model was not needed. In fact, modeling two separate Ga sites led to higher R_1 values than using a single Ga site with elongated anisotropic atomic displacement parameters (ADPs). Of course, modeling a single Ga site with ADPs that are elongated in the direction of Mn has a similar physical meaning to using a split model; when Mn is present, Ga is forced away to a reasonable distance of approximately 2.4 Å, which is represented by the Ga' site in the split model or the far ends of the elongated ellipsoid defined by the anisotropic ADPs.

From this structural analysis, it is clear that stuffing the structure with Mn is accompanied by atomic displacements of the Ga. That these motions are not necessarily of an energetic detriment is illustrated by

the observation of the stuffed AuCu_3 -type phase HoMn_xGa_3 , when HoGa_3 itself does not adopt the AuCu_3 type. The availability of Mn in the $\text{Ho}:\text{Mn}:\text{Ga}$ reactions seems to stabilize the AuCu_3 -type framework of HoMn_xGa_3 over the hexagonal $\beta\text{-HoGa}_3$ ²¹ phase. Guest atom incorporation can thus affect the stability of AuCu_3 -type lattices. In the next section, we will see how guest atoms can also influence the magnetic properties of these phases.

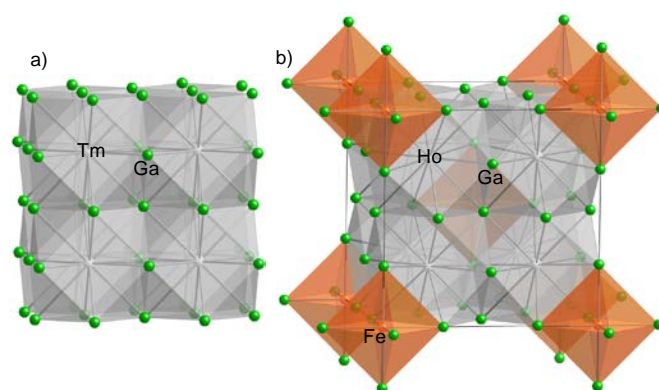


Figure 3.2. The crystal structure of (a) TmGa_3 (AuCu_3 type), and (b) $\text{Ho}_4\text{FeGa}_{12}$ ($\text{Y}_4\text{PdGa}_{12}$ type). Each crystal structure is depicted with cuboctahedra consisting of Ga atoms (green spheres) drawn around the Tm and Ho atoms (light gray spheres). The Fe atoms (orange spheres) occupy one fourth of the Ga_6 octahedral holes of the HoGa_3 basic structure.

Magnetic Properties. Temperature-dependent magnetic susceptibilities measured for single crystalline HoMn_xGa_3 , ErMn_xGa_3 , and TmMn_xGa_3 are shown in Figures 3.3a-c. For all three systems, the curves show a strong dependence on the Mn content, x , indicating that the presence of guest atoms has an influence on the magnetic properties. To quantify this effect, effective magnetic parameters were obtained for each compound by fitting its data above 50 K to a modified Curie-Weiss equations $\chi(T) = \chi_0 + C/(T - \theta)$,

where C is the Curie constant, θ is the Weiss temperature, and χ_0 is the temperature independent contribution to the susceptibility (Table 3.10). The effects of Mn addition were also probed with field-dependent magnetization data at 2 K (Figures 3.4a-c). In the following, we will discuss the resulting picture for how Mn modulates the properties of each LnMn_xGa_3 series individually, and then offer some possible explanations.

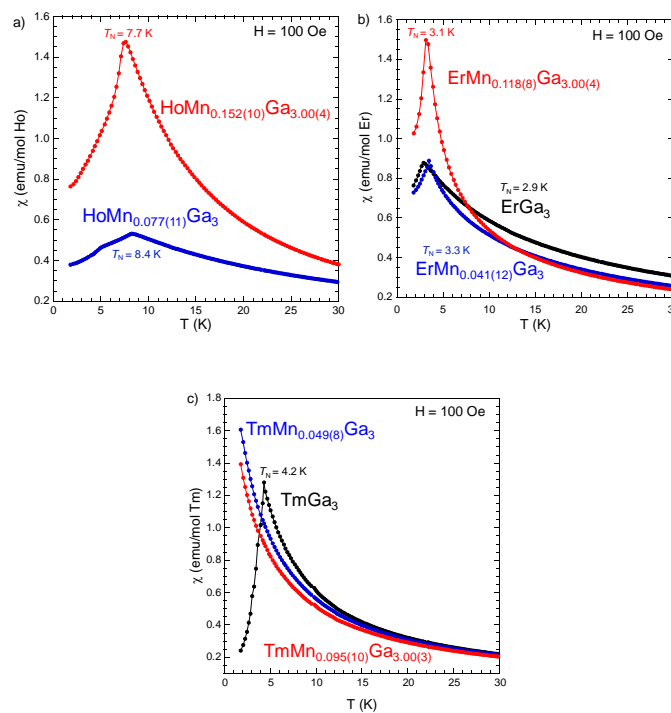


Figure 3.3. Temperature-dependent magnetic susceptibility for LnMn_xGa_3 ($\text{Ln} = \text{Ho}$ (a), Er (b), Tm (c)) at an applied field of 100 Oe.

HoMn_xGa_3 ($x < 0.15$). The effective magnetic moments of the HoMn_xGa_3 series are $\mu_{\text{eff}} = 10.616(4)$ μ_{B}/Ho for $x = 0.077(11)$ and $\mu_{\text{eff}} = 10.15(1)$ μ_{B}/Ho for $x = 0.164(6)$. The effective moment of the former is consistent with a free Ho^{3+} ion ($\mu_{\text{calc}} = 10.61$ μ_{B}), while the latter is approximately 0.5 μ_{B}/Ho less than

that of Ho^{3+} . The values of θ_W similarly decrease as Mn increases. Maxima are present in the susceptibilities at $T_N = 8.4$ K for $\text{HoMn}_{0.077(11)}\text{Ga}_3$ and $T_N = 7.7$ K for $\text{HoMn}_{0.152(10)}\text{Ga}_3$, indicating the onset of long range antiferromagnetic order. These ordering temperatures compare well with the antiferromagnetic ordering temperatures of $\text{Ho}_4\text{CrGa}_{12}$ ($T_N = 7.5$ K) and $\text{Ho}_4\text{FeGa}_{12}$ ($T_N = 9$ K). When comparing these HoMn_xGa_3 compounds with $\beta\text{-HoGa}_3$ ($T_N = 6.15$ K), it is apparent that the ordering temperature is higher for the Mn-containing phases.²² This could be a result of an increased concentration of conduction electrons that is provided by Mn, which would enhance the RKKY interactions and increase the ordering temperature.

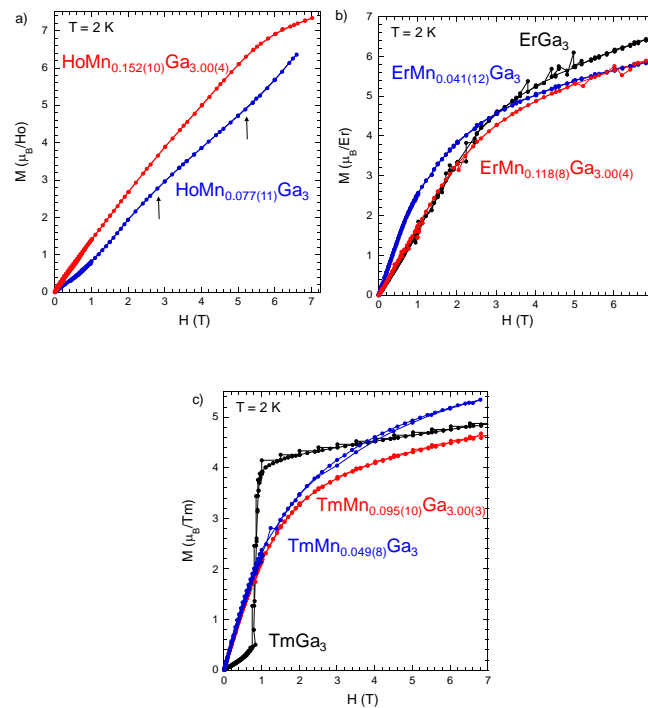


Figure 3.4. Field-dependent magnetization for LnMn_xGa_3 ($\text{Ln} = \text{Ho}$ (a), Er (b), Tm (c)) collected at 2 K. Nonlinear portions of the data are marked with black arrows in panel (a).

The magnetization of $\text{HoMn}_{0.077}\text{Ga}_3$ (Figure 3.4a) increases smoothly with applied field up to ~ 7 T and does not exhibit any saturation behavior. The magnetization of $\text{HoMn}_{0.164}\text{Ga}_3$ likewise increases with an applied field up to ~ 5.5 T, at which point the magnetization values begin to saturate. This behavior is similar to that seen in isothermal field-dependent magnetization data of $\text{Ho}_4\text{MGa}_{12}$ ($M = \text{Cr, Pd, Pt}$)^{6,8} analogues.

The addition of Mn also effects the multiple metamagnetic transitions exhibited by β - HoGa_3 at $T = 1.37$ K when a magnetic field is applied along the c -axis. As this metamagnetic behavior arises from interplanar and intraplanar Ho-Ho antiferromagnetic couplings in the hexagonal β - HoGa_3 structure,²² the stabilization of the cubic variant of HoGa_3 by Mn incorporation would be expected to have a disruptive effect. Indeed, the field-dependent magnetization for the HoMn_xGa_3 samples indicates a near breakdown of the metamagnetic properties of the original binary phase. Some artifacts of metamagnetism can be seen in the non-linearity of the data for $\text{HoMn}_{0.077}\text{Ga}_3$, but they are absent for $\text{HoMn}_{0.152}\text{Ga}_3$ whose magnetization displays linear field dependence to ~ 5.5 T.

ErMn_xGa_3 ($x < 0.15$). ErGa_3 , $\text{ErMn}_{0.041(12)}\text{Ga}_3$, and $\text{ErMn}_{0.118(8)}\text{Ga}_3$ order antiferromagnetically at 2.9 K, 3.3 K, and 3.1 K, respectively, while the effective magnetic moments are $\mu_{\text{eff}} = 10.095(4) \mu_{\text{B}}/\text{Er}$ for ErGa_3 , $\mu_{\text{eff}} = 9.522(4) \mu_{\text{B}}/\text{Er}$ for $\text{ErMn}_{0.041(12)}\text{Ga}_3$, and $\mu_{\text{eff}} = 9.494(7) \mu_{\text{B}}/\text{Er}$ for $\text{ErMn}_{0.118(8)}\text{Ga}_3$. Similar to the Ho analogues, the effective magnetic moments of ErMn_xGa_3 are close to those calculated for a free Ln^{3+} ion ($9.58 \mu_{\text{B}}$ for Er^{3+}), and decrease with increasing Mn concentration. Also mirroring the Ho analogues is the increase in the ordering temperatures for Mn-containing compounds over non-Mn-containing compounds, though the magnitudes of the increases are much less pronounced. As mentioned above, this increase in T_{N} could be due to the additional conduction electrons provided by Mn.

As in the Ho series, the ErMn_xGa_3 compounds show increasing magnetization values with increasing Mn content (Figure 3.4b). No hysteresis or saturation is observed up to an applied field of 7 T.

TmMn_xGa_3 ($x < 0.15$). The effective moments, $\mu_{\text{eff}} = 7.563(4) \mu_{\text{B}}/\text{Tm}$ for TmGa_3 , $\mu_{\text{eff}} = 7.464(1) \mu_{\text{B}}/\text{Tm}$ for $\text{TmMn}_{0.049(8)}\text{Ga}_3$, and $7.407(3) \mu_{\text{B}}/\text{Tm}$ for $\text{TmMn}_{0.095(10)}\text{Ga}_3$, decrease with increasing Mn concentration similar to those of the HoMn_xGa_3 and ErMn_xGa_3 compounds, with TmGa_3 having the closest effective moment to the calculated moment of the Tm^{3+} free ion ($7.56 \mu_{\text{B}}$). Also, TmGa_3 exhibits antiferromagnetic ordering at ~ 4.2 K, while $\text{TmMn}_{0.049(8)}\text{Ga}_3$ and $\text{TmMn}_{0.095(10)}\text{Ga}_3$ are paramagnetic down to 1.8 K, which indicates that the addition of Mn to TmGa_3 disrupts long range magnetic order. This behavior varies from that of the Ho and Er analogues previously discussed where the addition of Mn results in an increase of T_{N} .

Unlike the Ho and Er analogues, magnetization values for TmMn_xGa_3 (Figure 3.4c) decrease as the Mn concentration increases. The magnetization of TmGa_3 exhibits a large and sudden increase from a value of about $0.3 \mu_{\text{B}}/\text{Tm}$ to about $4 \mu_{\text{B}}/\text{Tm}$ at an applied field of ~ 0.8 T, followed by a smooth linear increase all the way through 7 T. This has been attributed, through specific heat and thermal transport measurements, to a structural transition driven by quadrupolar pair interactions.²³⁻²⁷ This feature is distinctly absent from the field-dependent magnetization curves of Mn-containing $\text{TmMn}_{0.049(8)}\text{Ga}_3$ and $\text{TmMn}_{0.095(10)}\text{Ga}_3$, which show no hysteresis or saturation up to an applied field of 7 T. This is consistent with Mn incorporation disrupting the local environments of the Tm atoms.

Interpretation of magnetic properties data. For all three LnMn_xGa_3 series of compounds, the effective magnetic moment was found to decrease as Mn is incorporated into the structure. One explanation for this could be that the addition of Mn decreases the interaction strength between Ln atoms by increasing

the Ln-Ln interatomic distance, as has been noted by Mar and coworkers for the insertion of Sn into LnSb₂ phases.^{28,29} Another cause could be crystal electric field (CEF) effects. Indeed, cubic LnGa₃ (Ln = Er, Tm) phases adopting the AuCu₃ structure type are known to exhibit unique magnetic properties resulting from CEF effects,^{25-27,30-32} and quadrupolar ordering.^{23-26,30-35} For TmGa₃, two first order transitions occur in a very narrow temperature range: a tetragonal distortion driven by quadrupolar ordering at T_Q = 4.29 K followed by an antiferromagnetic transition at T_N = 4.26 K. At temperatures below 4 K, CEF splitting of the Tm³⁺ states results in a nonmagnetic ground state. Certainly the presence of Mn in the body center of the unit cell in LnMn_xGa₃ compounds would affect the CEF of the lanthanide, though the specific consequences cannot be resolved without further experiments.

DFT-Chemical pressure analysis of guest atom incorporation. In the earlier sections of this paper, we have seen that several of the AuCu₃-type LnGa₃ phases can accommodate Mn guest atoms in their Ga₆ octahedra, and that the extent of this Mn incorporation modulates the magnetic properties of the host lattices. Understanding more about what makes this host-guest pairing favorable could provide insights into how similar structural modifications could be accomplished in other families of intermetallic compounds. Previously, Slater et al. have shown through COHP analysis on Y₄CrGa₁₂ that guest atom incorporation can lead to favorable Ga-guest bonding.⁸ Another clue to the forces at work here can be seen in the crystal structures of the LnMn_xGa₃ phases described above, and the previously reported Y₄PdGa₁₂-type superstructures: The inclusion of a stuffing atom involves substantial displacement of the surrounding Ga atoms (Figures 3.1b-c), reflecting the need for a local expansion of the structure to accommodate the atomic size of the guest atom.

A recently developed theoretical approach to investigating such size effects is the DFT-chemical pressure (CP) analysis,^{14,15} in which the results of DFT calculations are used to spatially resolve the total pressure a phase experiences into a pressure map over the structure. Integration of the pressure map within regions corresponding to interatomic contacts provides a representation of the local pressures experienced by the atoms along those contacts. An analysis of these local pressures can reveal cases of electronic packing frustration,³⁶ where contraction along contacts with negative pressures is prevented by steric hindrance at other contacts where the pressures are positive. The result is an array of *chemical pressures*, which can become severe enough to force superstructure formation.

Could chemical pressure effects be involved in the stuffing of the AuCu₃ type with transition metals? To answer this, we began by examining the AuCu₃-type LnGa₃ phases with Ln = Sc, Y, and La, such that the full range of atomic sizes of the lanthanides is spanned with non-magnetic metals. Also captured by this series is a trend in the stability of the AuCu₃ type: ScGa₃ crystallizes with this structure type,³⁷ and appears to refuse attempts to infuse it with guest atoms. YGa₃, on the other hand, does not exist independently,³⁸ but can be templated by transition metal atoms in the formation of Y₄PdGa₁₂-type compounds such as Y₄FeGa₁₂.⁷ Finally, a LaGa₃ AuCu₃-type architecture is so far unobserved with or without stuffing atoms.³⁹

The DFT-CP distributions obtained for this series help us explain these observations (Figures 3.5a-c). Following conventions established earlier, we represent the pressure distribution around each atom using a radial plot centered on that atom's nuclear position. The distance of a point on the surface from the nucleus is proportional to the pressure magnitude calculated for that direction. The sign of the pressure is given by the color of the surface. Black lobes represent directions along which contraction is favorable

(negative pressure), which are intended to evoke the image of a black holes acting within the structure.

White lobes indicate the opposite: positive pressures calling for the expansion of the lattice.

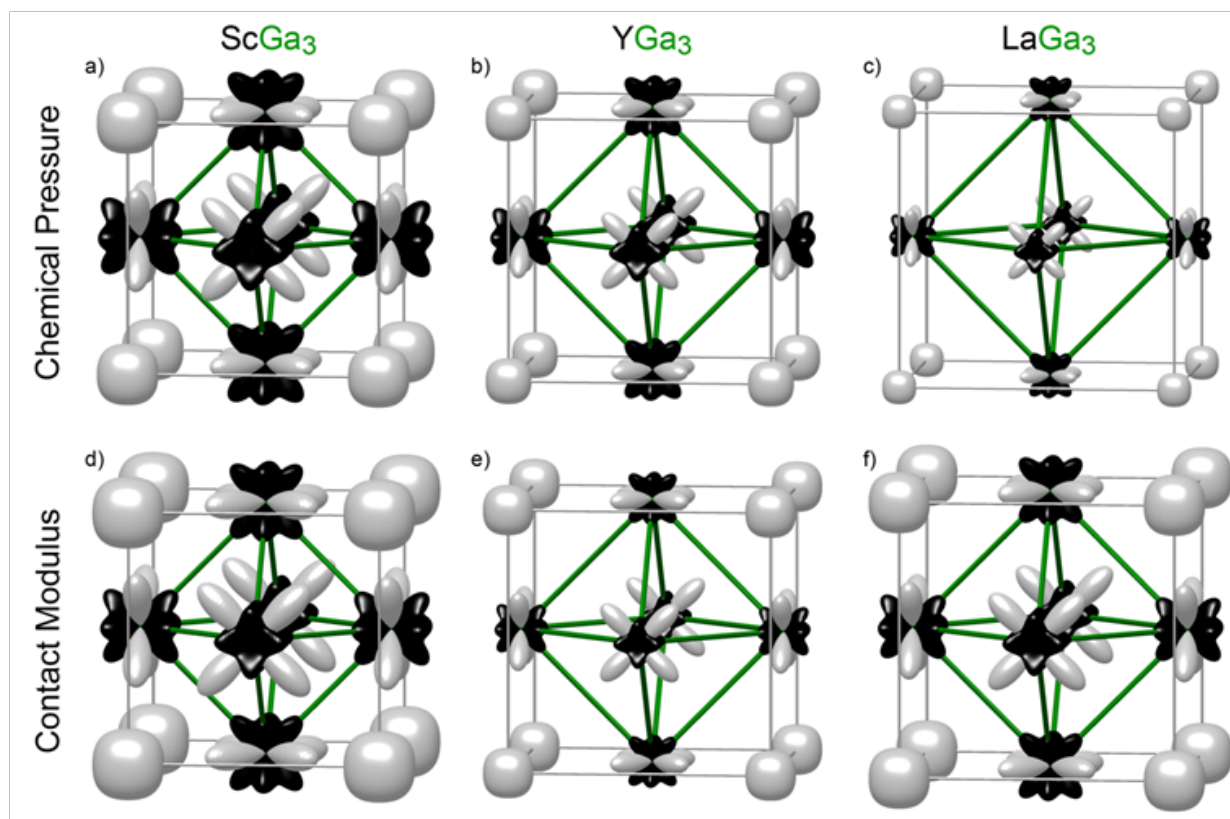


Figure 3.5. DFT-Chemical Pressure (CP) analysis for the AuCu_3 -type phases (a) ScGa_3 (experimentally observed), (b) YGa_3 (hypothetical) and (c) LaGa_3 (hypothetical). For (a)-(c), CP anisotropy surfaces are drawn for the three structures to scale. Black lobes on each atom correspond to directions of negative pressure (where contraction of the lattice would be favorable), while white lobes give directions along which the pressure is positive (where expansion would be favorable). (d)-(f) The contact moduli (see text) for the corresponding structures using the same conventions.

The three plots show similar arrangements of the lobes. The Ln atoms appear on the unit cell corners with white cuboidal surfaces. These atoms experience a nearly isotropic positive pressure, and are pushing

outwards on their surroundings. The Ga atoms at the unit cell face-centering positions bear complementary white lobes pointing toward the Ln neighbors, confirming the overly-short nature of the Ln-Ga contacts. The remainder of the Ga CP surfaces is black, indicating negative pressure, and points along Ga-Ga contacts.

These features tell of a tension between Ln-Ga and Ga-Ga interactions: the former is trying to expand the lattice while the latter is struggling to contract it. The equilibrium volume is reached when the two forces are balanced so that the net pressure is zero. While this tension is apparent in all three structures, the varying CP sizes across the series suggests variations in the conflict's severity, which may be connected to the observed structural chemistry. On moving from ScGa_3 to YGa_3 to LaGa_3 , the magnitudes of the features decrease. This trend indicates that the Ln atoms are being squeezed by the Ga sublattice with increasing strength on going from La to Y to Sc.

At first glance, this appears to be counterintuitive. Sc is the smallest of the Ln atoms here; why should it be subject to the greatest positive pressures? This discrepancy can be resolved by looking at the nature of the Ga-Ga interactions in more detail, particularly at the distance dependence of the Ga-Ga CPs. In the bottom row of Figure 3.5, we show radial plots for the negative derivative of the CP anisotropy surfaces with respect to relative volume changes to the structure ($-V d\text{CP}/dV$), which might be referred to as *contact moduli* (named by analogy to the macroscopic bulk modulus), using the same plotting conventions. The colors of the surface here now represent whether the pressure would be expected to increase or decrease upon changes in the unit cell volume. As will be described in detail in a future publication, white and black lobes in these surfaces correspond to two different bonding regimes for interatomic interactions.

For white surfaces, the pressure becomes less positive as the volume is increased. This mirrors the expectations of a harmonic potential: at very low volumes the pressure is large and positive, moves towards zero as the structure is expanded toward the equilibrium volume, and finally becomes negative as the equilibrium volume is exceeded. Such is the case in Figures 3.5d-f for the Ln-Ga interactions, and would be anticipated for any overly-short contacts.

Negative contact moduli, as are seen for the Ga-Ga interactions in Figures 3.5d-f, represent a very different situation: the pressure becomes more positive (or less negative) as the structure expands. While this seems contradictory, a familiar example can be found in the nearly universal shape of E vs. V curves for materials. Near the energy minimum, the curve is parabolic in shape corresponding to a positive contact modulus. As the volume is increased, however, the E vs. V curve begins to bend to shallower slopes, asymptotically approaching a horizontal line where the distances are so large that the interatomic interactions have become extinguished. Over this gradual decay, the pressure of the phase is actually becoming less negative as the structure expands. The contact moduli for interactions here are negative.

The negative contact moduli of the Ga-Ga sublattice then indicate that the forces acting along the Ga-Ga contacts are increasing as the distances decrease. Apparently, the Ga-Ga distances are so long relative to sum of the covalent radii that favorable interactions along these contacts are just beginning to be felt. In this case, larger negative chemical pressures between the Ga-Ga atoms in fact indicate more favorable interactions, at least until the E vs. V inflection point where the contact moduli cross from negative to positive.

From this point of view, the chemical pressure trends on going from La to Y to Sc can be readily interpreted. In LaGa_3 , the large size requirements of the La hold the Ga atoms apart to the extent that the Ga

atoms barely register the others' presence. Small negative CPs between the Ga atoms result. Switching the La atoms with the smaller Y allows for the Ga atoms to approach each other more closely. The Ga-Ga negative CP grows, and in the process, the Y is squeezed more tightly. This trend continues upon replacing Y with Sc, with greater bonding between the Ga atoms leading to more negative pressure within the Ga sublattice.

These results are consistent with the experimental data on the thermodynamic stability of AuCu₃-type phases in the La-, Y-, and Sc-Ga binary systems. Only ScGa₃ is observed to form, where the Ln atom size is the smallest. The non-existence of La- and Y-analogs hints at a breaking point where Ga-Ga interactions are so stretched that competing phases are preferred.

In the chemical pressure anisotropy surfaces of YGa₃ and LaGa₃, however, a method for stabilizing the AuCu₃-type can be perceived. The negative CP lobes on the Ga atoms all point along the edges of octahedra at the body-centering positions of the unit cell. This octahedral hole is then surrounded on all sides by negative CP features. Contraction of the octahedron would be one way to satisfy these negative CPs, but the octahedron is of course held open by the Ln-Ga interactions. Another way would be to simply fill the hole with something, much as the large void spaces of the CoSn structure type can accommodate guests to yield a variety of stuffed superstructures.^{40,41} From what we have seen above, it seems that late first-row transition metals can fill this role admirably. In fact, while YGa₃ is unobserved, its Fe-stuffed derivative Y₄FeGa₁₂ is observed to crystallize in the Y₄PdGa₁₂ structure type (Figure 3.2b).

The ways in which transition metal atom insertion can stabilize Ga-based AuCu₃-type lattices is illustrated in Figure 3.6, in which the CP anisotropies and contact moduli of YGa₃ are compared with those of Y₄FeGa₁₂ and a Y₄PdGa₁₂-type model of YMn_xGa₃. The M atom positions are indicated with large orange

spheres, made partially transparent to make the M CP features visible. Their insertion into the structure leaves many aspects of the CP scheme unchanged: the Ln-Ga contacts still bear positive CPs (and positive contact moduli), with the negative pressure being concentrated in the Ga sublattice, where the contact moduli are negative.

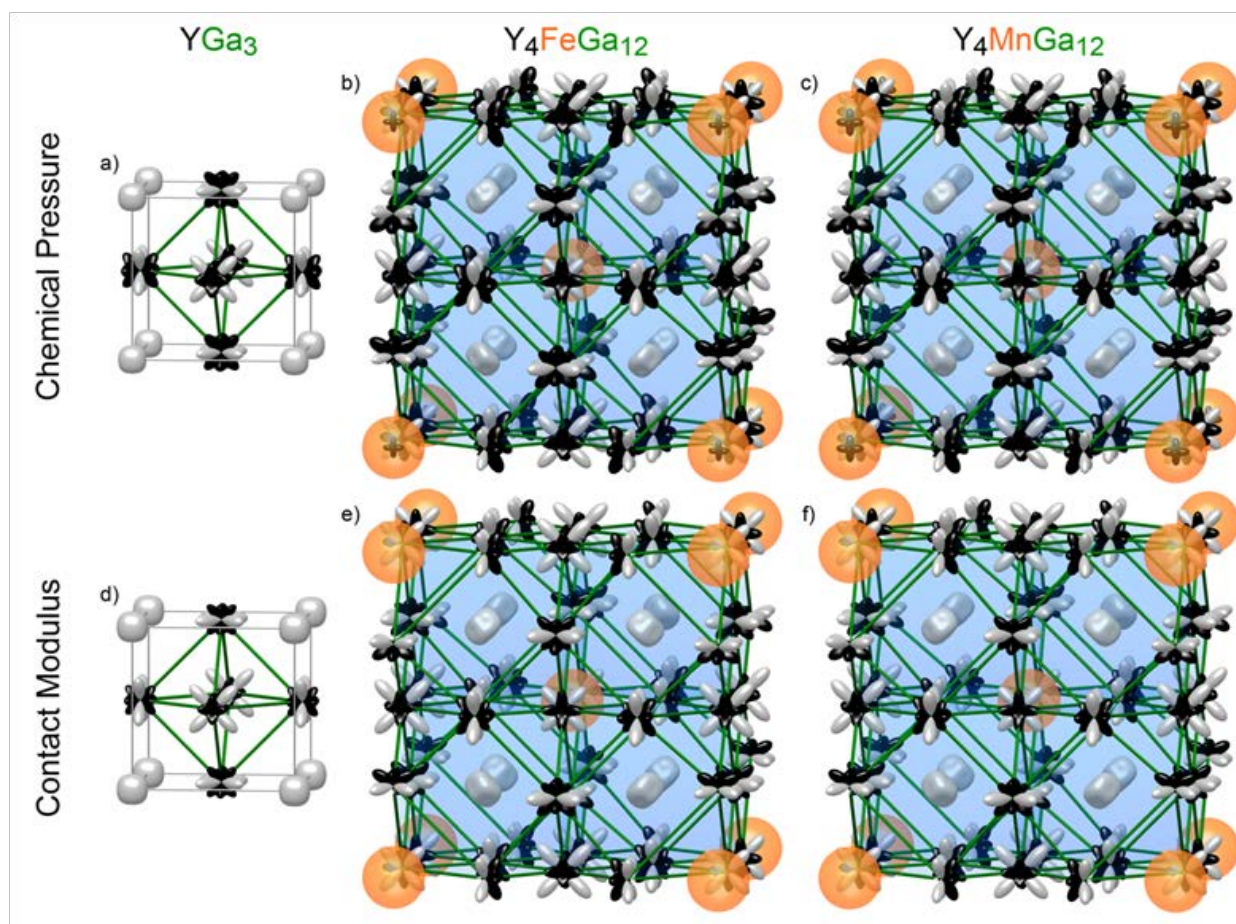


Figure 3.6. Driving forces for guest atom incorporation revealed through DFT-CP analysis. The top row shows CP anisotropy surfaces calculated for (a) AuCu₃-type YGa₃, (b) Y₄PdGa₁₂-type Y₄FeGa₁₂, and (c) Y₄PdGa₁₂-type Y₄MnGa₁₂. The bottom row, (d)-(f), presents the contact moduli for each structure. See the caption to Figure 3.5 for plotting conventions.

Substantial changes, however, are found in the ways the Ga negative pressures are distributed in the vicinity of the transition metal guest atoms. The transitional metal atoms themselves show very small CP lobes directed at their Ga neighbors and positive contact moduli, both indicators of nearly ideal distances. The surrounding Ga atoms show virtually no CP along the edges or toward the center of the octahedron. In effect, the over-extended Ga-Ga contacts of the unstuffed structure have been replaced with almost optimal transition metal-Ga interactions. The Mn@Ga_6 unit thus appears to be an advantageous motif in itself, but it also has beneficial effects on its surroundings. As we saw earlier in Figure 3.1, accommodating the Mn guest atoms requires the expansion of the Ga_6 host octahedra. This leads to the flattening of the neighboring, vacant octahedra, and the shortening of their edges. As these Ga-Ga contacts contract, larger negative pressures emerge as the distances move into the more attractive part of the Ga-Ga interaction potentials. Locally, the CP schemes in these compressed octahedra resemble the CP anisotropies of the Ga atoms in the experimentally observed ScGa_3 phase.

The M guest atoms thus play the role of structural supports when the Ln atoms are so large that the Ga-Ga contacts of a AuCu_3 -type phase become significantly stretched. They simultaneously replace overly long Ga-Ga contacts with essentially ideal M-Ga ones, and give the neighboring octahedra support for a tetragonal compression that shortens Ga-Ga contacts. In the $\text{Y}_4\text{PdGa}_{12}$ type, the placement of M atoms at the corners and body-centering positions of a $2 \times 2 \times 2$ supercell of the AuCu_3 structure type provides relief to all of the Ga atoms. Those Ga atoms that are not part of an octahedron hosting an M atom occur on octahedra that are compressed from opposite sides by a pair of M atoms. It is then easy to understand that if in YGa_3 the Y atoms are too large for a stable Ga sublattice, the placement of Fe atoms into the phase as in the experimentally observed $\text{Y}_4\text{PdGa}_{12}$ -type phase $\text{Y}_4\text{FeGa}_{12}$ could create a viable structure.

An open question is why the Mn series described in this paper should show a smaller extent of Mn incorporation than is seen in the Y_4PdGa_{12} -type phases. From the point of view of CP analysis, the consequences of Fe and Mn insertion seem to be very similar (Figure 3.6). Coming to a conclusive answer here may require studying CP distributions in larger supercells with fewer transition metals, and perhaps the inclusion of spin-polarization (not yet available in the existing DFT-CP code).

3.5. Conclusions

We have grown single crystals of $LnMn_xGa_3$ ($Ln = Ho-Tm$; $x < 0.15$). These compounds adopt a “stuffed” variant of the $AuCu_3$ structure type when Mn is present, where Mn fractionally occupies the body center position of the unit cell, displacing the surrounding Ga atoms toward the neighboring void spaces. Subtle changes are identified in the magnetic parameters of $LnMn_xGa_3$ ($Ln = Ho-Tm$; $x < 0.15$) as the concentration of Mn changes. A decrease in the effective magnetic moments of these compounds occurs with increasing Mn concentration. The decrease in effective magnetic moment is accompanied by an increase in magnetic susceptibility with increasing Mn concentration for Ho and Er analogues.

These trends are attributed either to increases in the Ln-Ln interatomic distances as a function of Mn incorporation or to changing the crystal electric field (CEF) of Ln by adding Mn, though additional experiments such as inelastic neutron scattering would be required to elucidate CEFs in these compounds. Mn-containing Ho and Er analogues order antiferromagnetically at slightly higher temperatures ($T_N > 7.7$ K and 3.1 K for $HoMn_xGa_3$ and $ErMn_xGa_3$, respectively) than do the non-Mn-containing analogues ($T_N = 6.2$ K and 2.9 K for β - $HoGa_3$ and $ErGa_3$, respectively). $TmGa_3$ exhibits antiferromagnetic order around 4.2 K due to CEF effects, whereas $TmMn_xGa_3$ compounds are paramagnetic down to 1.8 K. This is attributed

to a distortion of the Tm local environment upon the addition of Mn, which necessarily alters the CEF of Tm. Due to the range of Mn concentrations possible for LnMn_xGa_3 ($\text{Ln} = \text{Ho-Tm}$; $x < 0.15$), and the fact that CEF effects lead to interesting magnetic features in LnMn_xGa_3 , these compounds present a good opportunity to study how CEFs are affected by structural perturbations.

Using DFT-Chemical Pressure analysis, we have found that the source of this incorporation lies in the strained nature of the Ga sublattices of the LnGa_3 structures. The insertion of guest atoms allows expansion of the Ga sublattice around the guests, leading to compression of the neighboring Ga-Ga contacts. This picture may help identify void spaces accommodating to guest atoms in other structure types.

Acknowledgements

B.W.F., J.D.M., and J.Y.C. acknowledge financial support from NSF-DMR 1063735. J.P. and S.S. acknowledge support from NSF-DMR 0965009. The research at UW-Madison was supported by the NSF through grant DMR-1207409, and involved calculations using computer resources supported by the NSF grant CHE-0840494.

3.6. Tables

Table 3.1. Crystallographic parameters for LnGa_3

	ErGa_3	TmGa_3
crystal data		
space group	$Pm\bar{3}m$	$Pm\bar{3}m$
a (Å)	4.2149(10)	4.2027(10)
V (Å ³)	74.88(3)	74.23(3)
Z	1	1

crystal size (mm ³)	0.05 × 0.05 × 0.10	0.10 × 0.10 × 0.15
θ range (deg)	4.84-33.56	2.55-33.73
μ (mm ⁻¹)	54.087	56.176
data collection and refinement		
no. of collected reflections	1440	1155
no. of unique reflections	71	69
R_{int}	0.056	0.074
h	$-6 \leq h \leq 6$	$-6 \leq h \leq 6$
k	$-4 \leq k \leq 4$	$-4 \leq k \leq 4$
l	$-4 \leq l \leq 4$	$-3 \leq l \leq 4$
$\Delta\rho_{\text{max}}$ (e Å ⁻³)	0.798	1.375
$\Delta\rho_{\text{min}}$ (e Å ⁻³)	-0.796	-1.690
GoF	1.413	1.291
extinction coefficient	0.039(5)	0.035(11)
$R_1(F)$ for $F_o^2 > 2\sigma(F_o^2)$ ^a	0.0134	0.0266
$R_w(F_o^2)$ ^b	0.0360	0.0765

$$^a R_1 = \frac{\sum ||F_o| - |F_c||}{\sum |F_o|}$$

$$^b wR_2 = [\sum w(F_o^2 - F_c^2)^2 / \sum w(F_o^2)^2]^{1/2}; w = 1/[\sigma^2(F_o^2) + (0.0190 P)^2 + 0.1417 P] \text{ and } w = 1/[\sigma^2(F_o^2) + (0.0547 P)^2]; P = (F_o^2 + 2 F_c^2)/3 \text{ for ErGa}_3 \text{ and TmGa}_3, \text{ respectively.}$$

Table 3.2. Atomic positions for LnGa₃

atom	Wyckoff position	x	y	z	occupancy	U_{eq} (Å ²)
ErGa ₃						
Er	1a	0	0	0	1	0.0054(2)
Ga	3c	0	1/2	1/2	1	0.0097(3)
TmGa ₃						
Tm	1a	0	0	0	1	0.0058(5)
Ga	3c	0	1/2	1/2	1	0.0099(7)

Table 3.3. Selected interatomic distances (Å) of LnGa₃

interatomic distance	ErGa ₃	TmGa ₃
Ln–Ga (×12)	2.9804(2)	2.9718(5)
Ln–Ln (×6)	4.2149(10)	4.2027(10)

Table 3.4. Crystallographic parameters for LnMn_xGa_3 ($x \approx 0.05$, data collected with the Bruker Kappa APEXII diffractometer)

	$\text{HoMn}_{0.077}\text{Ga}_3$	$\text{ErMn}_{0.041}\text{Ga}_3$	$\text{TmMn}_{0.049}\text{Ga}_3$
crystal data			
space group	$Pm\bar{3}m$	$Pm\bar{3}m$	$Pm\bar{3}m$
a (Å)	4.2387(2)	4.2303(3)	4.2085(4)
V (Å ³)	76.155(6)	75.703(9)	75.539(12)
Z	1	1	1
crystal size (mm ³)	0.04 × 0.04 × 0.12	0.04 × 0.04 × 0.10	0.10 × 0.10 × 0.15
θ range (deg)	4.81-30.66	4.82-30.73	4.84-30.91
μ (mm ⁻¹)	55.571	53.618	56.147
data collection and refinement			
no. of collected reflections	986	1032	924
no. of unique reflections	42	42	42
R_{int}	0.0392	0.087	0.083
h	$-5 \leq h \leq 6$	$-6 \leq h \leq 6$	$-6 \leq h \leq 5$
k	$-6 \leq k \leq 6$	$-5 \leq k \leq 6$	$-5 \leq k \leq 6$
l	$-6 \leq l \leq 6$	$-4 \leq l \leq 4$	$0 \leq l \leq 6$
$\Delta\rho_{\text{max}}$ (e Å ⁻³)	0.956	1.244	0.579
$\Delta\rho_{\text{min}}$ (e Å ⁻³)	-0.584	-0.951	-0.596
GoF	1.384	1.186	1.140
extinction coefficient	0.181(12)	0.001(6)	0.046(4)
$R_1(F)$ for $F_o^2 > 2\sigma(F_o^2)$ ^a	0.0106	0.0202	0.0087
$R_w(F_o^2)$ ^b	0.0256	0.0484	0.0152

$$^a R_1 = \frac{\sum ||F_o| - |F_c||}{\sum |F_o|}$$

^b $wR_2 = [\sum w(F_o^2 - F_c^2)^2 / \sum w(F_o^2)^2]^{1/2}$; $w = 1/[\sigma^2(F_o^2) + (0.0154 P)^2 + 0.0367 P]$, $w = 1/[\sigma^2(F_o^2) + 0.6347 P]$, and $w = 1/[\sigma^2(F_o^2) + (0.0473 P)^2 + 0.0202 P]$; $P = (F_o^2 + 2 F_c^2)/3$ for $\text{HoMn}_{0.077(11)}\text{Ga}_3$, and $\text{ErMn}_{0.041(12)}\text{Ga}_3$, and $\text{TmMn}_{0.049(8)}\text{Ga}_3$, respectively.

Table 3.5. Atomic positions for LnMn_xGa_3 ($x \approx 0.05$)

atom	Wyckoff position	symmetry	x	y	z	occupancy	U_{eq} (Å ²)
$\text{HoMn}_{0.077(11)}\text{Ga}_3$							
Ho	1a	$m\bar{3}m$	0	0	0	1	0.0067(2)
Mn	1b	$m\bar{3}m$	1/2	1/2	1/2	0.077(11)	0.012(7)
Ga	3c	$4/m\bar{3}m$	0	1/2	1/2	1	0.0154(3)
Er	1a	$m\bar{3}m$	0	0	0	1	0.0076(5)
Mn	1b	$m\bar{3}m$	1/2	1/2	1/2	0.041(12)	0.0076(5)
Ga	3c	$4/m\bar{3}m$	0	1/2	1/2	1	0.0150(5)

TmMn _{0.049(8)} Ga ₃							
Tm	1a	<i>m3m</i>	0	0	0	1	0.00578(15)
Mn	1b	<i>m3m</i>	1/2	1/2	1/2	0.049(8)	0.010(8)
Ga	3c	4/ <i>mmm</i>	0	1/2	1/2	1	0.01276(19)

Table 3.6. Selected interatomic distances (Å) for LnMn_xGa₃ ($x \approx 0.05$)

interatomic distance	HoMn _{0.077} Ga ₃	ErMn _{0.041} Ga ₃	TmMn _{0.049} Ga ₃
Ln–Ga (×12)	2.9934(3)	2.9913(2)	2.9759(2)
Ln–Mn (×8)	3.6661(3)	3.6635(2)	3.6447(2)
Ln–Ln (×6)	4.2333(6)	4.2303(3)	4.2085(4)
Mn–Ga (×6)	2.1166(3)	2.1153(2)	2.1042(2)

Table 3.7. Crystallographic parameters for LnMn_xGa₃ ($x \approx 0.10$ -0.15)

	HoMn _{0.152(10)} Ga ₃	ErMn _{0.118(8)} Ga ₃	TmMn _{0.095(10)} Ga ₃
crystal data			
space group	<i>Pm3̄m</i>	<i>Pm3̄m</i>	<i>Pm3̄m</i>
<i>a</i> (Å)	4.2351(2)	4.2351(2)	4.2195(2)
<i>V</i> (Å ³)	75.961	75.961(6)	75.125(6)
<i>Z</i>	1	1	1
crystal size (mm ³)	0.01 × 0.06 × 0.06	0.01 × 0.05 × 0.06	0.01 × 0.06 × 0.08
θ Range (deg)	4.79-31.01	4.81-30.69	4.83-36.97
μ (mm ⁻¹)	55.067	53.786	55.89
data collection and refinement			
collected reflections	2870	1416	1512
unique reflections	44	42	61
<i>R</i> _{int}	0.055	0.0405	0.0434
<i>h</i>	-5 ≤ <i>h</i> ≤ 6	-5 ≤ <i>h</i> ≤ 6	-7 ≤ <i>h</i> ≤ 6
<i>k</i>	-6 ≤ <i>k</i> ≤ 5	-6 ≤ <i>k</i> ≤ 5	-6 ≤ <i>k</i> ≤ 6
<i>l</i>	-6 ≤ <i>l</i> ≤ 6	-6 ≤ <i>l</i> ≤ 6	-5 ≤ <i>l</i> ≤ 6
$\Delta\rho_{\max}$ (e Å ⁻³)	0.50	0.39	0.78
$\Delta\rho_{\min}$ (e Å ⁻³)	-0.52	-0.47	-0.56
GoF	1.28	1.23	1.15
extinction coefficient	0.322(15)	0.177(8)	0.065(7)
<i>R</i> ₁ (<i>F</i>) for $F_o^2 > 2\sigma(F_o^2)$ ^a	0.0114	0.0095	0.0133
<i>R</i> _w (F_o^2) ^b	0.0129	0.0095	0.0140

$$^a R_1 = \frac{\sum ||F_o| - |F_c||}{\sum |F_o|}$$

${}^b wR_2 = [\sum w(F_o^2 - F_c^2)^2 / \sum w(F_o^2)^2]^{1/2}$; $w = 1/[\sigma^2(F_o^2) + (0.0001 P)^2]$ for $\text{HoMn}_{0.152(10)}\text{Ga}_3$, $w = 1/[\sigma^2(F_o^2) + (0.000064 P)^2]$ for $\text{ErMn}_{0.118(8)}\text{Ga}_3$, and $w = 1/[\sigma^2(F_o^2) + (0.0001 P)^2]$ for $\text{TmMn}_{0.095(10)}\text{Ga}_3$; $P = (F_o^2 + 2 F_c^2)/3$.

Table 3.8. Atomic positions for LnMn_xGa_3 ($x \approx 0.10\text{-}0.15$)

atom	Wyckoff position	symmetry	x	y	z	occupancy	$U_{\text{eq}} (\text{\AA}^2)$
HoMn_{0.152(10)}Ga₃							
Ho	1a	<i>m3m</i>	0	0	0	1	0.00788(13)
Mn	1b	<i>m3m</i>	1/2	1/2	1/2	0.152(10)	0.0062(17)
Ga	3c	4/ <i>mmm</i>	0	1/2	1/2	0.634(10)	0.0090(3)
Ga'	6f	4 <i>mm</i>	0.0804(18)	1/2	1/2	0.183(5)	0.0090(3)
ErMn_{0.118(8)}Ga₃							
Er	1a	<i>m3m</i>	0	0	0	1	0.00811(10)
Mn	1b	<i>m3m</i>	1/2	1/2	1/2	0.118(8)	0.0069(19)
Ga	3c	4/ <i>mmm</i>	0	1/2	1/2	0.680(9)	0.0092(2)
Ga'	6f	4 <i>mm</i>	0.0786(18)	1/2	1/2	0.160(4)	0.0092(2)
TmMn_{0.095(10)}Ga₃							
Tm	1a	<i>m3m</i>	0	0	0	1	0.00752(9)
Mn	1b	<i>m3m</i>	1/2	1/2	1/2	0.120(4)	0.010(2)
Ga	3c	4/ <i>mmm</i>	0	1/2	1/2	0.743(8)	0.0088(2)
Ga'	6f	4 <i>mm</i>	0.0759(19)	1/2	1/2	0.143(4)	0.0088(2)

Table 3.9. Selected interatomic distances (\AA) for LnMn_xGa_3 ($x \approx 0.10\text{-}0.15$)

interatomic distance	HoMn _{0.152} Ga ₃	ErMn _{0.118} Ga ₃	TmMn _{0.095} Ga ₃
Ln–Ga ($\times 12$)	3.0063(2)	2.9947(2)	2.9836(2)
Ln–Ga' ($\times 12$)	3.0265(4)	3.0143(2)	3.0009(2)
Ln–Mn ($\times 8$)	3.6820(2)	3.6677(2)	3.6542(2)
Ln–Ln ($\times 6$)	4.2516(2)	4.2351(2)	4.2195(2)
Mn–Ga ($\times 6$)	2.1258(2)	2.1176(2)	2.1098(2)
Mn–Ga' ($\times 6$)	2.4744(4)	2.4606(2)	2.4309(2)

Table 3.10. Magnetic parameters for single crystalline LnMn_xGa_3 (Ln = Ho, Er, Tm)

compound	fit range (K)	$\chi_o (\times 10^{-4})^a$	θ_w (K) ^a	T_N (K)	$\mu_{\text{eff}} (\mu_B/\text{Ln})^{a,b}$
HoMn _{0.077(11)} Ga ₃	50-390	-8.1(4)	-17.26(5)	8.4	10.616(4)
HoMn _{0.152(10)} Ga ₃	50-390	19.9(9)	-7.56(12)	7.7	10.15(1)
ErGa ₃	50-390	0.3(4)	-10.95(5)	2.9	10.095(4)
ErMn _{0.041(12)} Ga ₃	50-390	-2.2(3)	-9.59(5)	3.3	9.522(4)
ErMn _{0.118(8)} Ga ₃	50-390	8.3(6)	-8.59(9)	3.1	9.494(7)
TmGa ₃	50-390	-3.30(9)	-2.70(2)	4.2	7.563(2)

TmMn _{0.049(8)} Ga ₃	50-390	-2.72(8)	-2.641(16)	-	7.464(1)
TmMn _{0.095(10)} Ga ₃	50-390	-3.0(2)	-2.67(4)	-	7.407(3)

^aUncertainties obtained from the fits to the modified Curie-Weiss law.

^bHo³⁺ $\mu_{\text{calcd}} = 10.61 \mu_{\text{B}}$, Er³⁺ $\mu_{\text{calcd}} = 9.58 \mu_{\text{B}}$, Tm³⁺ $\mu_{\text{calcd}} = 7.56 \mu_{\text{B}}$

3.7. References

- (1) Mathur, N. D.; Grosche, F. M.; Julian, S. R.; Walker, I. R.; Freye, D. M.; Haselwimmer, R. K. W.; Lonzarich, G. G. *Nature* **1998**, 394, 39.
- (2) Thompson, J. D.; Movshovich, R.; Fisk, Z.; Bouquet, F.; Curro, N. J.; Fisher, R. A.; Hammel, P. C.; Hegger, H.; Hundley, M. F.; Jaime, M.; Pagliuso, P. G.; Petrovic, C.; Phillips, N. E.; Sarrao, J. L. *J. Magn. Mater.* **2001**, 226-230, 5.
- (3) Vasilenko, L. O.; Noga, A. S.; Grin, Y. N.; Koterlin, M. D.; Yarmolyuk, Y. P. *Russ. Metall.* **1988**, 216.
- (4) Gumeniuk, R. V.; Stel'makhovych, B. M.; Kuz'ma, Y. B. *J. Alloys Comp.* **2003**, 352, 128.
- (5) Williams, W. M.; Moldovan, M.; Young, D. P.; Chan, J. Y. *J. Solid State Chem.* **2005**, 178, 52.
- (6) Cho, J. Y.; Moldovan, M.; Young, D. P.; Chan, J. Y. *J. Phys.: Condens. Matter* **2007**, 19, 266224.
- (7) Drake, B. L.; Grandjean, F.; Kangas, M. J.; Okudzeto, E. K.; Karki, A. B.; Sougrati, M. T.; Young, D. P.; Long, G. J.; Chan, J. Y. *Inorg. Chem.* **2010**, 49, 445.
- (8) Slater, B. R.; Bie, H.; Stoyko, S. S.; Bauer, E. D.; Thompson, J. D.; Mar, A. *J. Solid State Chem.* **2012**, 196, 409.
- (9) Francisco, M. C.; Malliakas, C. D.; Piccoli, P. M. B.; Gutmann, M. J.; Schultz, A. J.; Kanatzidis, M. G. *J. Am. Chem. Soc.* **2010**, 132, 8998.
- (10) Altomare, A.; Burla, M. C.; Camalli, M.; Cascarano, G. L.; Giacovazzo, C.; Guagliardi, A.; Moliterni, A. G. G.; Polidori, G.; Spagna, R. *J. Appl. Crystallogr.* **1999**, 32, 115.
- (11) Sheldrick, G. *Acta Cryst. A* **2008**, 64, 112.
- (12) Petříček, W.; Dušek, M.; Palatinus, L. (2006) Jana2006. The crystallographic computing system. Institute of Physics, Praha, Czech Republic.
- (13) Momma, K. I., F. *J. Appl. Cryst.* **2011**, 44, 1272.

- (14) Engelkemier, J.; Berns, V. M.; Fredrickson, D. C. *J. Chem. Theory Comput.* **2013**, *7*, 3170.
- (15) Fredrickson, D. C. *J. Am. Chem. Soc.* **2012**, *134*, 5991.
- (16) Fredrickson, D. C. *J. Am. Chem. Soc.* **2011**, *133*, 10070.
- (17) Gonze, X.; Amadon, B.; Anglade, P. M.; Beuken, J. M.; Bottin, F.; Boulanger, P.; Bruneval, F.; Caliste, D.; Caracas, R.; Côté, M.; Deutsch, T.; Genovese, L.; Ghosez, P.; Giantomassi, M.; Goedecker, S.; Hamann, D. R.; Hermet, P.; Jollet, F.; Jomard, G.; Leroux, S.; Mancini, M.; Mazevet, S.; Oliveira, M. J. T.; Onida, G.; Pouillon, Y.; Rangel, T.; Rignanese, G. M.; Sangalli, D.; Shaltaf, R.; Torrent, M.; Verstraete, M. J.; Zerah, G.; Zwanziger, J. W. *Comput. Phys. Commun.* **2009**, *180*, 2582.
- (18) Gonze, X.; Rignanese, G.-M.; Verstraete, M.; Beuken, J.-M.; Pouillon, Y.; Caracas, R.; Jollet, F.; Torrent, M.; Zerah, G.; Mikami, M.; Ghosez, P.; Veithen, M.; Raty, J.-Y.; Olevano, V.; Bruneval, F.; Reining, L.; Godby, R.; Onida, G.; Hamann, D. R.; Allan, D. C. *Z. Kristallogr.* **2005**, *220*, 558.
- (19) Hartwigsen, C.; Goedecker, S.; Hutter, J. *Phys. Rev. B* **1998**, *58*, 3641.
- (20) Goedecker, S.; Teter, M.; Hutter, J. *Phys. Rev. B* **1996**, *54*, 1703.
- (21) Cirafici, S.; Franceschi, E. *J. Less-Common Met.* **1981**, *77*, 269.
- (22) Czopnik, A. *Phys. Status Solidi A* **1995**, *147*, K35.
- (23) Deutz, A. F.; Brom, H. B.; Huiskamp, W. J.; De, J. L. J.; Buschow, K. H. J. *Physica B* **1989**, *160*, 83.
- (24) Gubbens, P. C. M.; Van, d. K. A. M.; Buschow, K. H. J. *Hyperfine Interact.* **1986**, *29*, 1343.
- (25) Morin, P.; Giraud, M.; Regnault, P. L.; Roudaut, E.; Czopnik, A. *J. Magn. Magn. Mater.* **1987**, *66*, 345.
- (26) Czopnik, A.; Iliw, N.; Stalinski, B.; Maedje, H.; Bazan, C.; Pott, R. *Physica B* **1985**, *130*, 262.
- (27) Banks, M. G.; Kremer, R. K.; Mannix, D.; Lapertot, G.; Murani, A. P. *Los Alamos Natl. Lab., Prepr. Arch., Condens. Matter* **2007**, *1*.
- (28) Mills, A. M.; Lam, R.; Ferguson, M. J.; Deakin, L.; Mar, A. *Coord. Chem. Rev.* **2002**, *233–234*, 207.
- (29) Deakin, L.; Ferguson, M. J.; Sprague, M. J.; Mar, A.; Sharma, R. D.; Jones, C. H. W. *J. Solid State Chem.* **2002**, *164*, 292.
- (30) Samsel-Czekala, M.; Kontrym-Sznajd, G.; Biasini, M. *Phys. Status Solidi C* **2006**, *3*, 179.

- (31) Biasini, M.; Kontrym-Sznajd, G.; Monge, M. A.; Gemmi, M.; Czopnik, A.; Jura, A. *Phys. Rev. Lett.* **2001**, *86*, 4616.
- (32) Murasik, A.; Czopnik, A.; Keller, L.; Fischer, P. *J. Magn. Magn. Mater.* **2000**, *213*, 101.
- (33) Chen, Y. Y.; Yao, Y. D.; Wang, C. R.; Lin, S. H.; Czopnik, A.; Ali, M. R.; Ho, J. C. *Phys. Rev. B* **2002**, *66*, 212404/1.
- (34) Pluzhnikov, V. B.; Czopnik, A.; Grechnev, G. E. *J. Phys. Condens. Mat.* **1999**, *11*, 4507.
- (35) Pluzhnikov, V. B.; Czopnik, A.; Eriksson, O.; Grechnev, G. E.; Fomenko, Y. V. *Low Temperature Physics* **1999**, *25*, 670.
- (36) Fredrickson, D. C. *J. Am. Chem. Soc.* **2011**, *133*, 10070.
- (37) Okamoto, H., Ga-Sc Phase Diagram, ASM Phase Diagram Center; P. Villars, editor-in-chief; H. Okamoto and K. Cenzual, section editors; <http://www1.asminternational.org/asmenterprise/apd>; ASM International, Materials Park, OH, 2006.
- (38) Okamoto, H., Ga-Y Phase Diagram, ASM Phase Diagram Center; P. Villars, editor-in-chief; H. Okamoto and K. Cenzual, section editors; <http://www1.asminternational.org/asmenterprise/apd>; ASM International, Materials Park, OH, 2006.
- (39) Palenzona, A.; Cirafici, S., Ga-La Phase Diagram, ASM Phase Diagram Center; P. Villars, editor-in-chief; H. Okamoto and K. Cenzual, section editors; <http://www1.asminternational.org/asmenterprise/apd>; ASM International, Materials Park, OH, 2006.
- (40) Venturini, G. Z. *Kristallogr.* **2006**, *221*, 511.
- (41) Fredrickson, D. C.; Lidin, S.; Venturini, G.; Malaman, B.; Christensen, J. J. *Am. Chem. Soc.* **2008**, *130*, 8195.

Chapter 4.

Progress in Visualizing Atomic Size Effects with DFT-Chemical Pressure

Analysis: From Isolated Atoms to Trends in AB₅ Intermetallics

This chapter has been published: Berns, V. M.; Engelkemier, J.; Guo, Y.; Kilduff, B. J.; Fredrickson, D. C. *J. Chem. Theory Comput.* **2014**, *10*, 3380-3392. The specific analyses detailed in this chapter were the work of Berns, but all authors made contributions to the general theoretical developments.

4.1. Abstract

The notion of atomic size poses an important challenge to chemical theory: empirical evidence has long established that atoms have spatial requirements, which are summarized in tables of covalent, ionic, metallic, and van der Waals radii. Considerations based on these radii play a central role in the design and interpretation of experiments, but few methods are available to directly support arguments based on atomic size using electronic structure methods. Recently, we described an approach to elucidating atomic size effects using theoretical calculations: the DFT-Chemical Pressure analysis, which visualizes the local pressures arising in crystal structures from the interactions of atomic size and electronic effects. Using this approach, a variety of structural phenomena in intermetallic phases have already been understood in terms that provide guidance to new synthetic experiments. However, the applicability of the DFT-CP method to the broad range of the structures encountered in the solid state is limited by two issues: (1) the difficulty

of interpreting the intense pressure features that appear in atomic core regions, and (2) the need to divide space among pairs of interacting atoms in a meaningful way. In this Chapter, we describe general solutions to these issues. In addressing the first issue, we explore the CP analysis of a test case in which no core pressures would be expected to arise: isolated atoms in large boxes. Our calculations reveal that intense core pressures do indeed arise in these virtually pressure-less model systems, and allow us to trace the issue to the shifts in the voxel positions relative to atomic centers upon expanding and contracting the unit cell. A compensatory grid unwarping procedure is introduced to remedy this artifact. The second issue revolves around the difficulty of interpreting the pressure map in terms of interatomic interactions in a way that respects the size differences of the atoms and avoids artificial geometrical constraints. In approaching this challenge, we have developed a scheme for allocating the grid pressures to contacts inspired by the Hirshfeld charge analysis. Here, each voxel is allocated to the contact between the two atoms whose free atom electron densities show the largest values at that position. In this way, the differing sizes of atoms are naturally included in the division of space without resorting to empirical radii. The use of the improved DFT-CP method is illustrated through analyses of the applicability of radius ratio arguments to Laves phase structures and the structural preferences of AB_5 intermetallics between the $CaCu_5$ and $AuBe_5$ structure types.

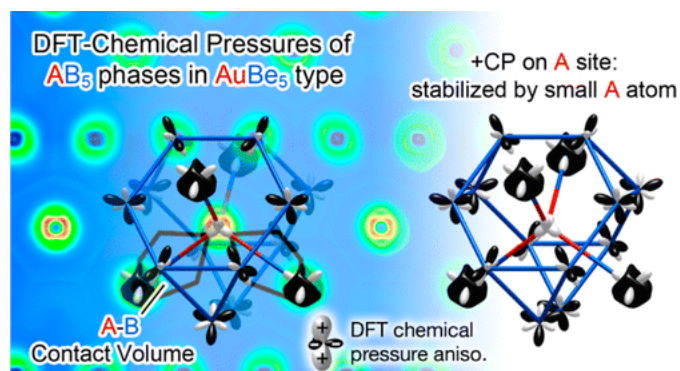


Figure 4.0. Schematic illustration of chemical pressure in an AB_5 compound of the $AuBe_5$ structure type. On the left, we see a 2-dimensional chemical pressure map, overlaid with key contact volumes. This new division of space enables analysis of the $AuBe_5$ structure type, which is shown to be stabilized by a small atom on the A site.

4.2. Introduction

While chemistry has long since stripped itself of the mysticism of the alchemists, its deep roots in experimental observation have led to a number of useful empirical concepts that have their own sort of poetry and allure, such as the chemical bond, electronegativity, and acidity. One goal of modern theoretical chemistry is the mapping of these notions to aspects of a compound's electronic structure, in ways that are both theoretically rigorous yet honor the richness of their historical uses and connotations. Atomic size is perhaps one of the most problematic of these empirical ideas. Experience with molecular and solid state structures suggests that atoms have measurable sizes,¹⁻³ yet the Schrödinger equation contains no terms involving atomic radii or explicit penalties for atoms encroaching upon each other. Indeed, the gradual and asymptotic decay of wavefunctions away from a system's nuclei is far from conducive to the construction of clear-cut boundaries defining the space occupied by individual atoms.⁴ Given the importance of atomic

size arguments throughout chemistry, theoretical tools which overcome these challenges could be extremely beneficial to deepening the roles theory can play in the design of experiments.

For inorganic solid state materials, the need for such theoretical methods for analyzing atomic size effects is particularly pressing, as can be seen in a quick survey of the recent literature. Atomic sizes or radius ratios are frequently invoked in discussions of the factors stabilizing particular crystal structures,⁵⁻¹⁶ and in the interpretation of physical properties in terms of the presence of rattling atoms or interstitial spaces for guest atoms.^{17,18} Furthermore, the empirical concept of chemical pressure, in which elemental substitutions create local stresses in a crystal structure, has been used as a framework for understanding relationships between composition and properties.¹⁹⁻²⁸

While energy terms corresponding to atomic size effects are difficult to extract from an electronic structure calculation, we have recently found that their impact on stability can be productively inferred from a quantum mechanical adaptation of the chemical pressure concept just mentioned.²⁹⁻³² The basis of this method is the recognition that the size requirements of atoms are most apparent when interatomic repulsion at one contact in a structure impedes bonding at other contacts. As the repulsion and bonding interactions cannot be optimized simultaneously, local stresses are expected to result which, unlike the atomic sizes themselves, can be evaluated naturally using quantum mechanics through such concepts as the stress density.³³⁻³⁸

The DFT-CP analysis offers a way to examine these local pressures using the results of standard electronic structure calculations. The method uses the density and potential grids determined in the course of a DFT calculation to create maps of the pressure within crystal structures, which reveal points of frustration within those structures. This approach has been particularly fruitful in the study of the structural

chemistry of intermetallic phases, where it has offered explanations for such phenomena as the creation of complex structures through the insertion of planar interfaces into simpler ones,^{30,32} the formation of local icosahedral order in quasicrystal approximants,^{39,40} and the ability of some AuCu₃-type lattices to accommodate guest atoms.⁴¹

Over the course of these and other applications, we have found that there are still several issues limiting the range of applicability of the DFT-CP analysis: (1) the proper treatment of the intense pressures that are calculated to occur near the core regions of an atom, and (2) the best scheme to interpret the pressure maps in terms of interatomic interactions.

In this Chapter, we will describe improved solutions to both of these challenges. Beginning with the CP calculations on individual atoms isolated in large unit cells, we will show that the introduction of an unwarping procedure to correct for the drift of the voxel positions relative to the nuclei upon expanding and contracting the unit cell can significantly reduce the severe pressures in the atomic core regions obtained in the original procedure. Including this step in the generation of CP-maps allows for more subtle CP features to come to the foreground, and eliminates the need for our earlier isotropic core averaging technique.

After describing this improved method for the construction of CP maps, we will then move to issues with their interpretation. As the CP distributions generally involve positive pressures near the core regions and negative pressures in the interstitial regions, evaluating the net pressure along a contact involves an averaging process over the voxels associated with that contact. The overall results are strongly tied to the scheme used in assigning these voxels to contacts. In our previous applications, we have found that assum-

ing that a voxel's pressure is determined by the contact between its two closest atoms often provided intuitive results. However, this purely geometrical construction does not always assign differing spheres of influence to atoms of vastly different sizes. In this Chapter, we present a more sophisticated approach inspired by the Hirshfeld method for calculating atomic charges,⁴² in which the electron density distributions of free atoms are used in determining which atoms will have the largest influence on a voxel's pressure.

In introducing these methodological improvements, we will make reference to structural trends in intermetallics that have been attributed to atomic size effects (Figure 4.1): the role of radius ratios in the Laves phases, and the transition from the CaCu_5 type to the AuBe_5 type for AB_5 intermetallics with increasingly small A atoms.⁴³ Through the use of the updated DFT-CP method, the latter structural trend will become simply explained as a CP-driven transition in line with the pressure-distance paradox.^{4,44} We anticipate that these results could provide a foundation for analyses of the origins of a series of complex intermetallic phases built from the intergrowth of the AuBe_5 and MgCu_2 types, at compositions near which a CaCu_5 -type phase might be expected, such as $\text{YbCu}_{4.5}$ with its giant 7,448-atom monoclinic unit cell.⁴⁵⁻⁴⁸

4.3. Computational procedures

Electronic structure calculations for the geometrical optimization of crystal structures and the output of electron densities, kinetic energy densities, and components of the Kohn-Sham potentials were carried out with the ABINIT program.^{49,50} All calculations employed the density functional theory (DFT) with the local density approximation (LDA) of Goedecker, Teter, and Hutter,⁵¹ and the HGH atomic pseudopotentials.⁵² Further details, including the energy cut-offs, number of k-points used in the calculations, and

the optimized atomic coordinates of the intermetallic structures discussed in this Chapter, are given in the Supporting Information.

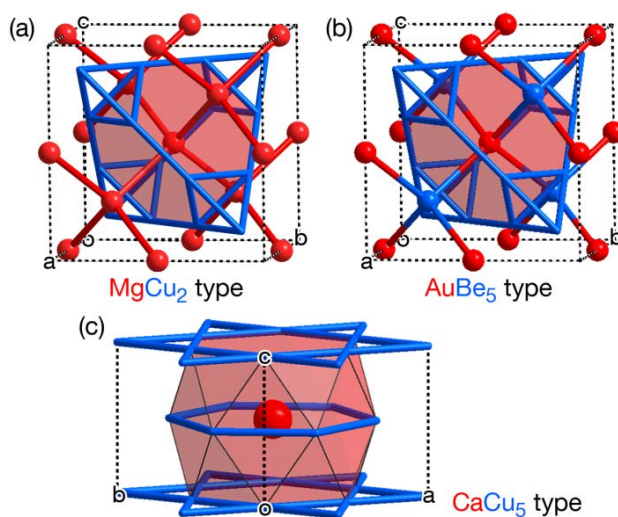


Figure 4.1. Structure types discussed in this Chapter whose stability ranges are empirically connected to atomic size: (a) The MgCu_2 (cubic Laves phase) type. (b) The AuBe_5 type. (c) The CaCu_5 type.

The output of the ABINIT calculations was used for the generation of CP maps through the scheme described below. The resulting CP maps were visualized with the program VESTA 3.⁵³ The projections of the CP maps onto spherical harmonics were plotted with Matlab. Software for the calculation and integration of CP maps using the method described in this paper is available at our research group website (<http://www.chem.wisc.edu/~danny>).

In the determination of Hirshfeld-inspired contact volumes, free atom electron densities were taken either from the ABINIT website, or calculated using the Atomic Pseudopotentials Engine (APE).⁵⁴

4.4. Grid unwarping near atomic centers

The basis of the DFT-CP method lies in the ability of the DFT total energy to be at least partially represented as an integral over a spatially resolved energy density:

$$E_{DFT} = \iiint_{\substack{\text{unit} \\ \text{cell}}} \rho_{energy}(\vec{r}) dV + E_{remainder} \quad (4.1)$$

where $E_{remainder}$ contains energetic contributions that are not easily traced to specific points in space, such as the Ewald energy and nonlocal components of the potential energy. Using the output of the ABINIT program, such an energy density function can be constructed in the form of discrete points on a grid, i.e.

$$E_{DFT} \approx \sum_n^{N_{voxels}} \rho_{energy}(\vec{r}_n) V_{voxel} + E_{remainder} = \sum_n^{N_{voxels}} E_n + E_{remainder} \quad (4.2)$$

where N_{voxels} and V_{voxel} are respectively the number of voxels in the structure's unit cell and the volume of each individual voxel.

When we recall that pressure and total energy are related as $P = -\partial E / \partial V$, a straightforward approach to constructing pressure maps emerges. We can simply generate energy grids for a structure at volumes that are slightly contracted and expanded relative to the geometry of interest, and use the resulting energy difference at each voxel as the basis for the calculation of voxel pressures:

$$P_n = -\partial E_n / \partial V \quad (4.3)$$

The representation of the total energy as a sum over an energy grid then gives way to the net pressure experienced by a phase being expressed as the average over a pressure grid:

$$\begin{aligned}
P &= -\frac{\partial E_{DFT}}{\partial V_{cell}} = -\sum_n^{N_{voxels}} \frac{\partial E_n}{N_{voxels} \partial V_{voxel}} - \frac{\partial E_{remainder}}{\partial V_{cell}} \\
&= \frac{1}{N_{voxels}} \sum_n^{N_{voxels}} P_n - P_{remainder}
\end{aligned} \tag{4.4}$$

In our applications of this procedure, we have found that a rather consistent result is obtained over a wide range of solid state compounds: the pressure maps are marked by intense pressures (of several TPa) near the core regions of the atoms, with much shallower features in the interstitial portions of the structure. The extreme magnitudes of these core pressures mean that success in the interpretation of the pressure map is strongly dependent on how the cores are divided among interatomic interactions.

A key question here is whether the strong pressures in the core regions represent the interactions between atoms, or are instead an artifact of the pseudopotential models for the atoms or the procedure for the generation of the pressure maps. A simple way to answer this question is to consider a case in which interatomic interactions should be absent: isolated atoms. In Figure 4.2a, we show cross-sections of CP maps calculated for individual atoms placed in large unit cells, for which the interatomic distances are sufficiently long (10 Å) that each atom should exhibit virtually no influence on its neighbors. Maps are shown for a variety of elements, but common features are present: the atomic position at the center of the map is clearly decorated with intense oscillating pressure features emanating from the atomic cores. Depending on the diffuseness of the valence electron wavefunctions, the scales of these features vary over a significant range: from 0.07 atomic units for the valence-only Ca pseudopotential, to 120 atomic units for the semi-core Ga pseudopotential. In all but the shallowest pseudopotentials, pressures of more than 1 atomic unit are attained. When we recall that 1 atomic unit of pressure is equal to 96,000 GPa, it is apparent that they

represent pressure responses that are incommensurately large relative to the minuteness of the perturbations on these systems induced by a small expansion or contraction of the unit cell.

Why should such strong pressures arise in the absence of interatomic interactions? An assumption of the above formulation of the DFT-CP approach is that upon changing a unit cell's volume, the features of the potentials and electron density expand or contract along with the voxel grid.³⁰ In this way, the pressure calculated for a specific voxel (P_n) is then related to the difference in energies calculated for that voxel in slightly expanded and contracted structures:

$$P_n^{DFT-CP} \approx - \frac{E_n^+ - E_n^-}{V_{voxel}^+ - V_{voxel}^-} \quad (4.5)$$

This may be expected to apply well to the regions in the interstitial spaces, where atoms are most responsive to changes in their surroundings. Near the atomic cores, however, where electrons cling tightly to the nuclei, such an assumption is harder to justify. In the cores, the depths of the atomic pseudopotentials are such that variations in the cell volume would represent only minor changes. The electron density would not be expected to migrate along with an expanded or contracted voxel grid.

It would seem that a more careful consideration is needed for the high electron densities of the core regions. The pressure response at these points in space might be better approximated by assuming that a volume element of fixed size and position relative to the associated atomic core should be sampled for the expanded and contracted structure.

This can be accomplished by supplementing the original DFT-CP methodology with an unwarping procedure. Consider energy density distributions calculated for the equilibrium geometry of a crystal structure, a slightly expanded structure, and a contracted structure, which we can represent respectively as

$\rho_{energy}^o(\vec{r})$, $\rho_{energy}^+(\vec{r})$, and $\rho_{energy}^-(\vec{r})$. If we then write the pressure of voxel n in terms of its relationship to its nearby atom j ($\vec{r}_n = \Delta\vec{r}_n^o + \vec{r}_{atom\ j}^o$), then the pressure at that point, assuming that the energy density does not dilate with the voxel grid, can be calculated as

$$P_n \approx - \frac{\{\rho_{energy}^+(\Delta\vec{r}_n^o + \vec{r}_{atom\ j}^+) - \rho_{energy}^-(\Delta\vec{r}_n^o + \vec{r}_{atom\ j}^-)\}V_{voxel}^o}{V_{voxel}^+ - V_{voxel}^-} \quad (4.6)$$

Calculating pressures in this way is complicated by the fact that the energy densities obtained over the course of a CP calculation are expressed in terms of the discrete points of a voxel grid. The vectors $\Delta\vec{r}_n^o + \vec{r}_{atom\ j}^+$ and $\Delta\vec{r}_n^o + \vec{r}_{atom\ j}^-$ then often will lie in between grid points, and the energy densities at those points cannot be determined exactly. Trilinear interpolation, however, can be used to obtain an estimate based on the values for the surrounding voxels. The magnitude of the errors is then related to the fineness of voxel grid spacing relative to the complexity of the electron density function.

This methodology is implemented in our current version of the program *CPmap*. The voxel energies for the expanded and contracted structure are first calculated according to Equation 4.2. The voxels are then associated with specific atomic cores, which can be done by specifying cutoff radii, using a Voronoi scheme,⁵⁵ a more complicated division of space as offered by Bader's QTAIM,⁵⁶ or, as we will describe in more detail below, a Hirshfeld-type weighting.⁴² The voxel centers in the expanded (\vec{r}_n^+) and contracted (\vec{r}_n^-) structures are then shifted to their corresponding positions relative to their atom's nuclear position as in the equilibrium volume structure ($\vec{r}_n = \Delta\vec{r}_n^o + \vec{r}_{atom\ j}^o$). Finally, the pressures at the voxel positions are calculated according to Equation 4.6.

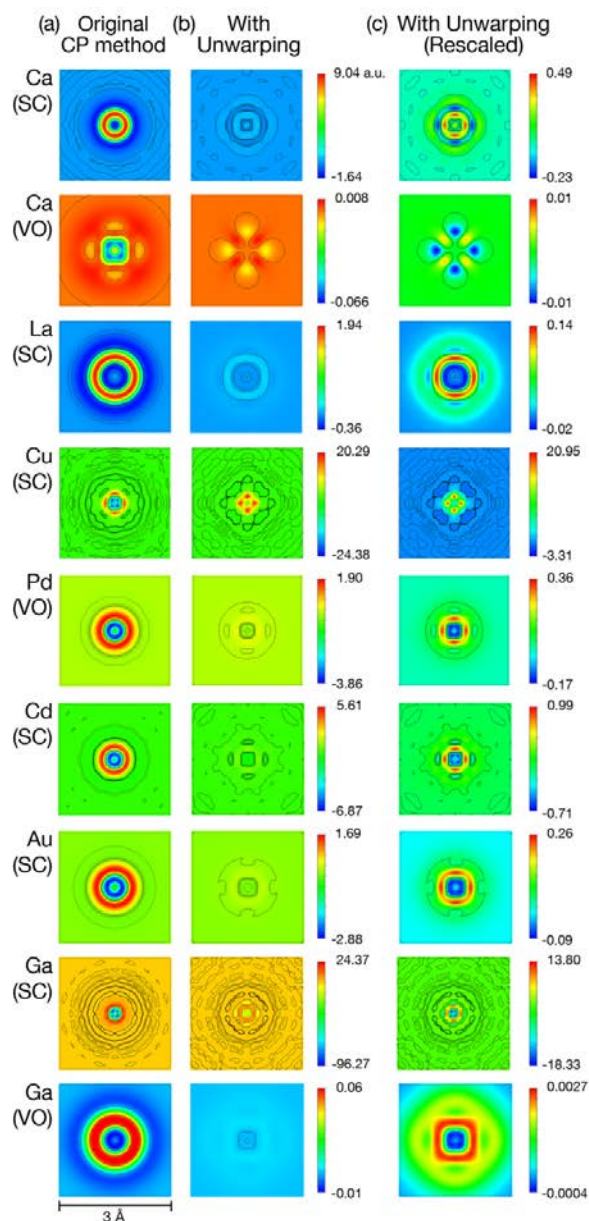


Figure 4.2. DFT-Chemical Pressure (CP) maps for individual atoms isolated in large unit cells (cell edges of 10 \AA). (a) Cross sections through the nuclear positions using the original DFT-CP scheme. (b) The corresponding CP maps calculated using the process for unwarping the energy grids near the atomic cores, plotted using the same color map as in (a). (c) The unwarping maps with the color map adjusted to a narrower range. Note that the unwarping procedure significantly reduces the strong core-like features around the atomic position (which should be essentially absent in these calculations on virtually isolated atoms). SC and VO refer to the semicore and valence-only versions of the atomic pseudopotentials, respectively, where applicable. Black contours trace isosurface levels at increments of 0.05 between -0.1 and 0.1 a.u.

As the shifts in the voxel positions represent a different sampling of the same energy density maps, this interpolation leads to only small changes to the total energy obtained by integrating over the voxel grid (ca. 0.05%). Any small residual pressure resulting from differences in the interpolation error for the expanded and contracted structures is added homogeneously to the pressure map.

In Figure 4.2b-c, we illustrate the effect of applying this fixed core correction procedure to atoms isolated in boxes. Figure 4.2b shows cross-sections of the pressure maps for the atoms drawn with the same color map as in Figure 4.2a. The correction leads to a substantial change in the pressure distribution. The original, strongly oscillating ripples of pressure are now replaced with flatter maps and less isotropic features. Figure 4.2c focuses on narrower pressure ranges to allow the more subtle features of these maps to be visible. Here, it can be seen that the variations are in many cases more associated with the corners and faces of the unit cell than with the distance to the atomic core.

4.5. Grid unwarping between atoms

Atoms in more realistic environments should also benefit from this type of core treatment. Figure 4.3a shows two-dimensional slices of CP maps calculated for a diverse array of intermetallic compounds. For most examples using the original method, the maps show the most intense pressures as nearly perfect circles around the atomic positions. These core regions are set against what appears to be a shallow, nearly homogeneous negative background pressure. As such features are reminiscent of our uncorrected treatment of the atoms-in-boxes of Figure 4.2a, it seems likely that implementing grid interpolations here should lead to more meaningful CP maps.

For voxels near the cores of any given atom, the path to applying the above procedure is clear: the voxels can be assigned to their nearby atom, and then treated according to Equation 4.6. The situation becomes less clear for voxels deeper in the interstitial spaces between the atomic cores, where the energy density features might be expected to migrate to various degrees with the voxel grid as the structure is expanded and contracted. How should the unwarping process be applied to these regions?

A voxel's position in the equilibrium grid can be represented in terms of its placement relative to any of the atoms in the structure:

$$\vec{r}_n = \Delta\vec{r}_{n,atom\ 1}^o + \vec{r}_{atom\ 1}^o = \Delta\vec{r}_{n,atom\ 2}^o + \vec{r}_{atom\ 2}^o = \dots \quad (4.7)$$

As we move to the expanded or contracted volumes, the various atoms will shift to different positions, so that the various equalities of Eq. 6.7 cannot be satisfied simultaneously if we keep the $\Delta\vec{r}_{n,atom\ j}^o$ vectors constant. Instead, we will need to decide to what degree each of the $\Delta\vec{r}_{n,atom\ j}^o$ terms will be weighted in the determination of the \vec{r}_n^+ and \vec{r}_n^- vectors.

One approach to determining these weights can be found in the Hirshfeld method for the extraction of atomic charges from electronic structure calculations.⁴² In the Hirshfeld approach, one begins with a hypothetical case in which the electron density of a compound is simply a superposition of free atom electron densities centered at the nuclear positions of a structure. The relative contributions from these free atom densities at a given point in space is then translated into relative weights for the apportioning of the true electron density between the atoms in the calculation of charges. The free atom electron densities thus serve as a measure of the distance dependence of each atom's influence.

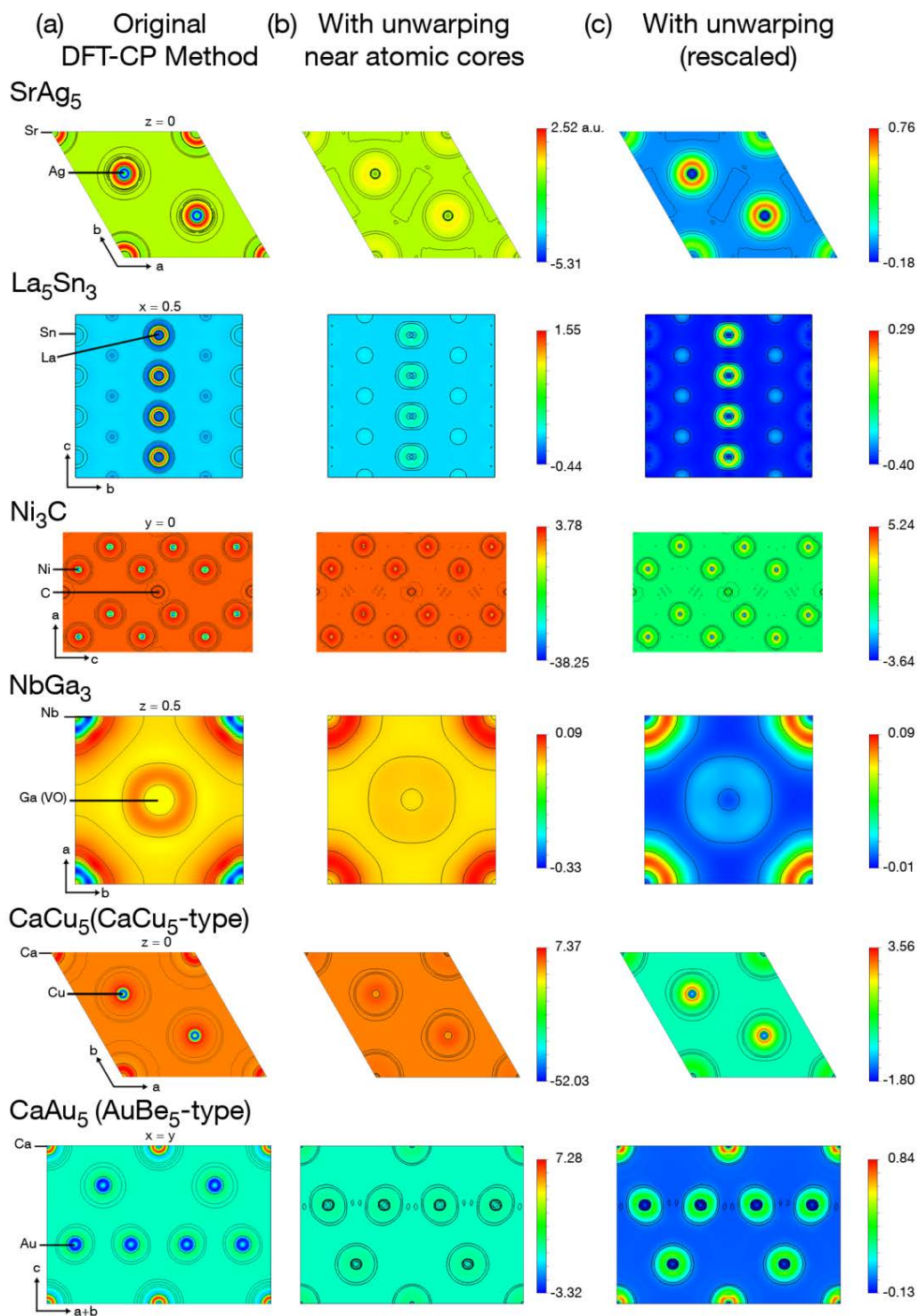


Figure 4.3. Cross sections for the DFT-CP maps of a variety of intermetallic phases calculated (a) before and (b) after the unwarping of the energy grids using the same color map, and (c) the unwarped maps plotted with more appropriately tailored color maps.

In a similar way, the Hirshfeld method for the atoms surrounding a voxel can be used in assigning weights to each of the equalities in Equation 4.7. We first define a Hirshfeld weight for the influence of atom j on the position of voxel n :

$$w_{j,n} = \frac{\rho_{atom\ j}^{FA}(\vec{r}_n^o)}{\sum_k^{all\ atoms} \rho_{atom\ k}^{FA}(\vec{r}_n^o)} \quad (4.8)$$

where $\rho_{atom\ k}^{FA}(\vec{r}_n^o)$ gives the electron density at the position of voxel n calculated for a free atom of the proper element centered at the nuclear coordinates of atom k .

Having defined these weightings, we can then use them in determining how much a voxel should maintain its position relative to each of the atomic centers as the cell is expanded and contracted for the calculation of CP maps:

$$\vec{r}_n^+ = \sum_j^{all\ atoms} w_{j,n} (\Delta\vec{r}_{n,j}^o + \vec{r}_{atom\ j}^+) \quad (4.9a)$$

$$\vec{r}_n^- = \sum_j^{all\ atoms} w_{j,n} (\Delta\vec{r}_{n,j}^o + \vec{r}_{atom\ j}^-) \quad (4.9b)$$

For voxels near an atomic core, the weight for that atom will dominate these averages, and the original atom-centered interpolation of the previous section is obtained.

In performing this distortion of the voxel grid around the atom centers, the grid points are no longer uniformly distributed, and the voxel volumes become varied throughout the structure. The calculation of the voxel pressures then becomes slightly modified from Equation 4.6:

$$P_n \approx - \frac{\rho_{energy}^+(\vec{r}_n^+) V_{voxel,n}^+ - \rho_{energy}^-(\vec{r}_n^-) V_{voxel,n}^-}{V_{voxel}^+ - V_{voxel}^-} \quad (4.10)$$

where the numerator involves the volumes of the specific voxel n in the expanded and contracted structures, and the denominator uses the average voxel volumes for the two structures. A discussion of the determination of the voxel volumes in the distorted grid is provided in the Supporting Information.

Turning on the unwarping procedure (Figure 4.3b-c) significantly reduces the magnitudes of the pressures of the core regions, allowing more subtle features in the interatomic regions to come more to the foreground. Also, in some cases, particularly La_5Sn_3 and CaAu_5 , the spherical character of the core regions has diminished, making the centers of the atoms appear more responsive to their surroundings. This is more consistent with the philosophy of pseudopotentials which aims to treat explicitly only those electrons that are perceptibly affected by interatomic interactions as part of the valence set.

4.6. Hirshfeld-inspired contact volumes

In the previous section, we saw how the features of a CP map could be substantially clarified by introducing a step in which corresponding grid points of the expanded and contracted unit cells are shifted to the same position in space relative to an atom assigned to it. By implementing this procedure, the severe isotropic pressures appearing around the atomic cores are reduced, allowing more subtle features to come to the foreground. Even with this improvement, however, the CP distributions still largely consist of positive regions around the atomic centers that are immersed in a shallower negative background pressure. In examining the overall pressures at particular interatomic contacts, we will then need to examine the net effect of these core-like and interstitial pressures through the integration of the pressure map within domains assigned to individual contacts.

In performing such an integration, the pressure between a pair of atoms will be given by

$$P_{jk}^{contact} = \sum_n^{N_{voxels}} w_{jk,n} P_n \quad (4.11)$$

where $w_{jk,n}$ is the fraction of the pressure at voxel n that is attributed to the interaction between atom j and atom k . The central challenge in carrying out the integrations in a meaningful way is then the determination of the proper weighting scheme, the set of $w_{jk,n}$'s. In our recent applications of the DFT-CP method, we derived our choice of weights from an assumption that a voxel's pressure is determined by the interaction of its two nearest atoms, i.e.

$$w_{jk,n} = \left. \begin{array}{l} 1, \text{ if atoms } j \text{ and } k \text{ are two closest to voxel } n \\ \frac{1}{m}, \text{ if } m \text{ contacts are tied in above criterion} \\ 0, \text{ if } j \text{ or } k \text{ are not two atoms closest to voxel } n \end{array} \right\} \quad (4.12)$$

This scheme is advantageous in its simplicity. However, as it is entirely based on geometrical constructions, it neglects the differing ranges of influence of different atom types, and should be considered as only a first step toward a more realistic division of space between contacts.

Over the course of our ongoing exploration of intermetallic phases using the DFT-CP method, we have found that for one large and important class of compounds, the Laves phases and their variants, refinements to the weighting scheme are particularly vital. In these AB_2 compounds (see Figure 4.1a for one example), the A positions (usually occupied by a relatively electropositive element) form a diamond network, a hexagonal diamond network, or an intergrowth of the two. The B atoms occupy the interstitial spaces of the A diamondoid framework, and form truncated tetrahedra (TT) around the A atoms. The resulting coordination environment around the A sites is known as a Friauf polyhedron, consisting of a TT of B atoms with A atoms sitting above the hexagonal faces of the TT.

The geometrical features of the Friauf polyhedron make it a challenging test case for the division of space among interatomic contacts. The A-A and A-B distances exhibit a ratio of 1.0445 (for the high symmetry MgCu_2 -type case), with the longer A-A lengths being consistent with the trend that the A sites are generally occupied by the larger atom type. However, using the distance-based criterion described above, the voxels inside the Friauf polyhedron will be assigned to the pairs of atoms to which they are closest. As the A-B interatomic distances are shorter than the A-A ones, these will tend to absorb more voxels, despite the A atoms being larger.

This dominance of the A-B contacts in the voxel assignments has interesting consequences for the integrated CP schemes. In Figure 4.4a, we show the results for the MgCu_2 -type phase CaPd_2 ,^{57,58} using the projection scheme described previously. Here, the distribution of voxel pressures around each atom is represented by radial surfaces around its nuclear position. The distance of a point on the surface from the nucleus is proportional to the sums of the voxel pressures along that direction, while the color of the surface gives the sign of the pressure. Lobes in black point along directions where the pressure is negative, i.e. contraction would be favorable, while portions of the surfaces in white correspond to positive pressures, where the structure would prefer to expand.

For the Friauf polyhedron of CaPd_2 using the original geometrical construction of contact volumes, the white and black features are divided largely by element type. The Ca atoms appear as black tetrapods, with large negative pressure lobes pointing along the Ca-Ca contacts (red). These forces calling for the contraction of the lattice are counteracted by white, positive pressure lobes along the Pd-Pd contacts (blue), with the Ca-Pd contacts appearing to be relatively satisfied. This result is encouraging in the sense

that the heteroatomic interactions, the usual driving force for the formation of a binary phase from its elements, are well-optimized.

However, inspection of the contact distances uncovers some counterintuitive aspects of this picture. Note that in the Ca-Ca/Pd-Ca distance ratio of 1.0445, the Ca-Ca contacts are only slightly longer than the Ca-Pd ones, despite the metallic radius of Ca being significantly larger than that of Pd (1.97 vs. 1.37 Å⁵⁹). As a consequence, the Ca-Ca distance is much shorter than the sum of the metallic radii (3.32⁵⁷ vs. 3.94 Å⁵⁹). This distance is still within the ranges observed for Ca-Ca interactions in the Inorganic Crystal Structure Database,^{60,61} but would hardly be the occasion for large negative pressures demanding even closer Ca-Ca contacts. If anything, a positive pressure pushing toward distances more in-line with twice the metallic radius would be expected.

A look at the volumes assigned to each contact in our integration provides an explanation for the appearance of these negative Ca-Ca pressures. In Figure 4.4b-c, we present a cross section of the DFT-CP map for CaPd₂ taken through one of the Ca-Ca contacts, with the boundaries between contact volumes drawn in black. The contact volume of the Ca-Ca interaction appears here as a diamond between the two atoms. A brief glance reveals why negative pressures are assigned to this contact: whereas positive pressure features occur around both the Ca atoms of the contact, only the tips of the narrow corners of the contact volume reach into these regions. Instead, the contact volume contains mainly the negative pressure interstitial space between the Ca atoms. The core regions themselves are dominated by Ca-Pd contact volumes.

In other words, the Ca-Pd distances are short enough relative to the Ca-Ca ones that the distance criterion grants them most of the Ca core voxels. As a result, only small positive pressure components are allocated to the Ca-Ca contacts, and negative pressures thus dominate despite the short Ca-Ca distances.

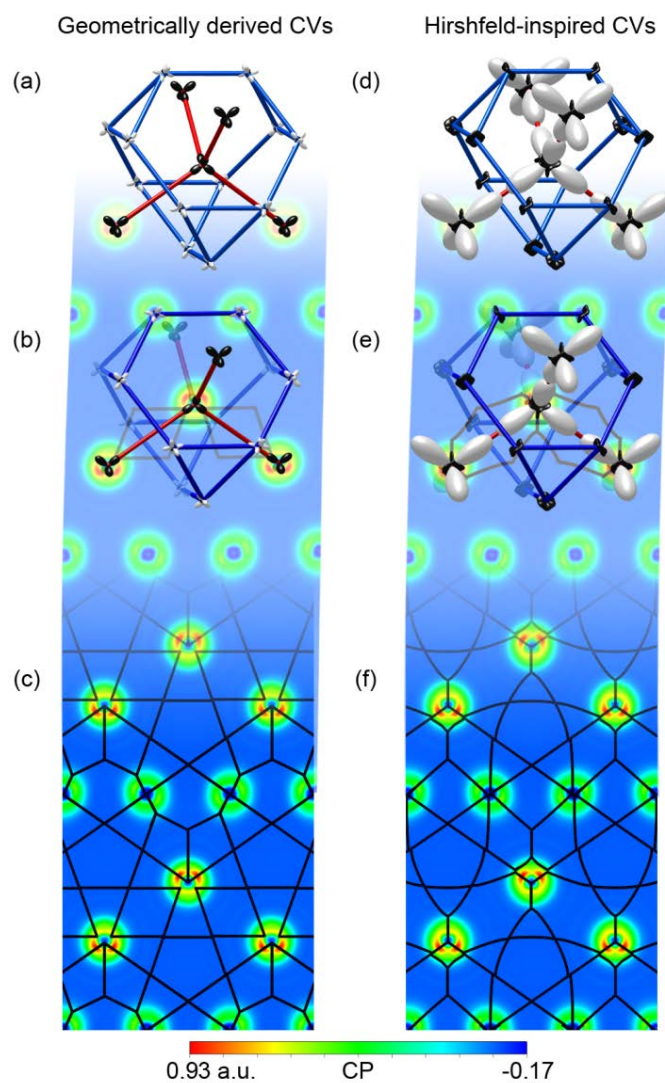


Figure 4.4. Comparison of integrated DFT-CP anisotropies and contact volumes for CaPd_2 . (a) The DFT-CP distribution calculated for CaPd_2 using the original contact volume (CV) scheme. (b) The DFT-CP distribution plotted together with a cross section of the original DFT-CP map. (c) The DFT-CP cross-section shown separately with the contact volume borders indicated. (d)-(e) The corresponding images generated using the Hirshfeld-inspired contact volume scheme (see text). In (a) and (d), the pressure distribution around each atom is represented by a radial plot, with the radial distance indicating the magnitude of the sum of voxel pressures along that direction. The sign of the pressure is indicated with color: black for negative (evoking the image of a black hole acting on the structure), white for positive.

Now that we see the origin of the Ca-Ca negative pressures, a way to correct the CP picture becomes apparent: the Ca-Ca contact volumes should be expanded into the Ca core regions to better reflect the larger size of the Ca atoms relative to Pd atoms. To do this, a change in the weighting scheme of Equation 4.12 is needed that takes into account the differing electronic structures of Ca and Pd atoms.

As for our grid-interpolation scheme above, the Hirshfeld approach can be adapted to this task, the essential change being that we are now assigning points in space to pairs of atoms rather than individual atoms. The influence of a contact on a point in space will depend on the sizes of the free atom electron densities for the two atoms at that point. A way of quantifying this is to consider the weights in Equation 4.11 as being proportional to the products of the free atom (FA) electron densities for the atoms of the contact:

$$w_{jk,n} \propto \rho_{atom\ j}^{FA}(\vec{r}_n) \cdot \rho_{atom\ k}^{FA}(\vec{r}_n) \quad (4.13)$$

In this way, every voxel would be shared among multiple contacts, with weights that are proportional to the overlaps between the FA electron densities for each contact.

In experimenting with such integration schemes, we have found that following through with this Hirshfeld-based approach in its entirety leads to some issues with interpretation: it is difficult to see which points in space are influencing which contacts. Instead, it is more practical to keep the division of space into discrete contact volumes as in Equation 4.12, but using the products of FA electron densities as a guide to their construction. The corresponding weighting is then:

$$w_{jk,n} = \left\{ \begin{array}{l} 1, \text{ if } \rho_{atom\ 1}^{FA}(\vec{r}_n)\rho_{atom\ 2}^{FA}(\vec{r}_n) \text{ is largest for } j, k \text{ pair} \\ \frac{1}{m}, \text{ if } m \text{ contacts are tied in above criterion} \\ 0, \text{ if } \rho_{atom\ 1}^{FA}(\vec{r}_n)\rho_{atom\ 2}^{FA}(\vec{r}_n) \text{ not largest for } j, k \text{ pair} \end{array} \right\} \quad (4.14)$$

The result of using this Hirshfeld-inspired scheme is shown in Figure 4.4d-e. The Ca-Ca contact volume (Figure 4.4e) now reaches much deeper into the Ca cores so that a corner lies on each Ca nuclear position. The angle at each of these corners has also expanded to encompass more of the core's volume. In fact, the core is now entirely divided between the four Ca-Ca contacts arranged in a tetrahedron around the central Ca atom.

At first glance, the new contact volume boundaries do not appear to align with the prominent features of the Ca core regions. In the cross-section of Figure 4.4f, each Ca atom exhibits a pair of red bulges corresponding to high positive pressures. Their directional character would lead us to think that they are associated with particular interatomic interactions. However they are almost perfectly bisected by the borders of the CVs, rather than being centered within a specific CV. A deeper investigation of these features resolves this apparent discrepancy. As is illustrated in the Supporting Information, we have found that the highest pressures within the core regions tend to accumulate in the spaces lying between important interatomic interactions, rather than along them. The source of this is a negative pressure contribution arising from the overlap of the local pseudopotentials along the interatomic vector. The core regions not aligned with these vectors then tend to be the spaces where the positive core pressures are most prominent.

The increased contribution from the Ca cores to the Ca-Ca contact volumes has a profound effect on the integrated CP distributions (Figure 4.4d). The Ca-Ca contacts now exhibit intense positive pressures that seem appropriate to the relatively short Ca-Ca distances. These positive pressures are balanced by the negative pressure lobes oriented along the Ca-Pd interactions. The Pd-Pd contacts, meanwhile, are largely devoid of CP features, indicating that the distances here are nearly optimal.

In comparing Figure 4.4a and 4.4d, it is somewhat surprising that they represent the same original CP map, and differ only in the integration scheme used. In what ways are they connected? To see their relationship to each other, it is helpful to note that the Ca-Ca contacts pass through hexagons of Pd atoms. The integrated pressures in this region of the structure will depend on the relative sizes and shapes of Ca-Ca, Ca-Pd, and Pd-Pd contact volumes. In the original scheme, the size of the Pd atoms is overestimated relative to the Ca ones, which leads to the Ca-Pd and Pd-Pd volumes dominating the positive cores of the Ca and Pd atoms. The result is positive pressures along the Pd-Pd interactions and only small negative pressures along the Ca-Pd ones.

In moving to the Hirshfeld-inspired scheme, the Ca-Ca volumes are increased at the expense of the Ca-Pd and Pd-Pd volumes. The contact volumes involving Ca then pick up more of the positive core pressures, leading to large positive pressures between the Ca atoms, the removal of positive pressures from the Pd-Pd interactions, and only smaller changes to the Ca-Pd interactions (which lose core contributions from the Ca but gain them from the Pd).

The better treatment of atomic sizes is not the only reason for which the revised CP scheme is attractive: it also corresponds closely with expectations based on the sphere-packing view of the Laves phases. Consider a MgCu_2 -type AB_2 structure constructed from hard spheres with radius r_A for the A atoms and r_B for the B atoms. The high symmetry of the structure means that the distances are entirely determined by the length of the cubic unit cell edge, and no other degrees of freedom exist for adjusting the structure to accommodate the values of r_A and r_B . If the B atoms are in contact with each other at an interatomic distance of $2 r_B$, then the surfaces of the A atoms touch each other when the r_A/r_B radius ratio is $(3/2)^{1/2} = 1.225$. However, the surfaces of the A atoms would not touch those of the B atoms until $r_A/r_B = (11/2)^{1/2}$.

$1 = 1.345$. As such, bringing the A and B spheres in contact would require allowing the A atoms to slightly interpenetrate each other.

We can now compare these radius ratios for that of the metallic radii for CaPd_2 , $r_{\text{Ca}}/r_{\text{Pd}} = 1.97 \text{ \AA}/1.37 \text{ \AA} = 1.44$. For this ratio, having sphere surfaces touch at the Pd-Pd or Ca-Pd contacts would require the Ca spheres to overlap. In this situation, positive pressures could be expected to arise between the Ca atoms as the structure strives to achieve closer contacts along the Pd-Pd and Ca-Pd interactions. This picture agrees well with the CP scheme of Figure 4.4d-f. We anticipate that the revised CP scheme obtainable for Laves phases will offer opportunities to examine the driving forces for the creation of complex structures through the fragmentation of these simpler structures,⁶²⁻⁷⁰ and will improve our ability to discern the reasons for the intergrowth of Ca-Cd and Cd-Cu interactions in the Bergman-type quasicrystal approximant $\text{Ca}_{10}\text{Cu}_2\text{Cd}_{27}$.

It is important to mention, however, that this result is dependent on the use of a semicore Ca pseudopotential in which not only the Ca 4s but also 3p and 3s electrons are considered as part of the valence set. Using a “valence-only” Ca pseudopotential with just the 4s electrons treated explicitly leads to a CP scheme similar to Figure 4.4a regardless of what map generation and integration procedures are applied. We believe that this can be attributed to the relatively high ionicity expected for the CaPd_2 phase. Indeed a Bader charge analysis using the *BADER* program⁷¹⁻⁷³ of our valence-only electron density for this phase gives a charge on the Ca atoms of +1.7, indicating that only 0.3 electrons lie near the Ca cores. With so few valence electrons present on Ca atoms, it is understandable that the explicit inclusion of semicore electrons would be necessary to model the atom’s responses to its surroundings. From this, we arrive at a recommendation that semicore potentials be used in cases where atoms are expected to be highly cationic.

Using the improved method including Hirshfeld-inspired contact volumes and interpolation within atomic cells, we have also been able to reproduce the conclusions of our earlier studies examining the stability of the complex Ca_2Ag_7 and $\text{Ca}_{36}\text{Sn}_{23}$ structures relative to simpler structural alternatives. In the remainder of this Chapter, we will describe a different application of the DFT-CP method: determining the role of atomic size in the relative stabilities of competing structure types. Our focus will be on the structural preferences of AB_5 structures for CaCu_5 - or AuBe_5 -type structures, for which atomic size has been considered a key factor.

4.7. Stability trends in AB_5 intermetallics

In the previous sections of this paper, we described improvements to the DFT-CP method, and showed how they offer a CP scheme for the Laves phase CaPd_2 that is in close accord with radius ratio considerations. Using the same implementation of the CP concept, it is also possible to explain the stability trends for another intermetallic structure type that is closely related to the Laves phases: the AuBe_5 type. This AB_5 structure type can be derived from the AB_2 MgCu_2 -type by replacing every other A atom in the structure with a B atom, i.e. $\text{A}_2\text{B}_4 \rightarrow \text{ABB}_4 = \text{AB}_5$ (Figure 4.1b). For AB_5 intermetallics with A being an alkaline earth or lanthanide and B being a late transition metal, the AuBe_5 type appears to be in competition with the more common CaCu_5 type. The factor determining the relative stabilities of these two structure types appears to be the relative sizes of A and B atoms,⁴³ an effect that should be amenable to CP analysis.

Let's begin by examining the DFT-CP distribution for a representative of the AuBe_5 type: CaAu_5 .⁷⁴ In Figure 4.5, we present CP anisotropy surfaces for this structure calculated with the range of procedures

discussed in the previous section. First, in Figure 4.5a, we show the result using the original methodology without interpolation within atomic cells and using a geometrical construction for the contact volumes. In Figure 4.5b-c, we turn on either the interpolation procedure or the Hirshfeld-inspired determination of contact volumes (CVs). Finally, in Figure 4.5d, we use the fully improved method, with both the interpolation and new contact volumes.

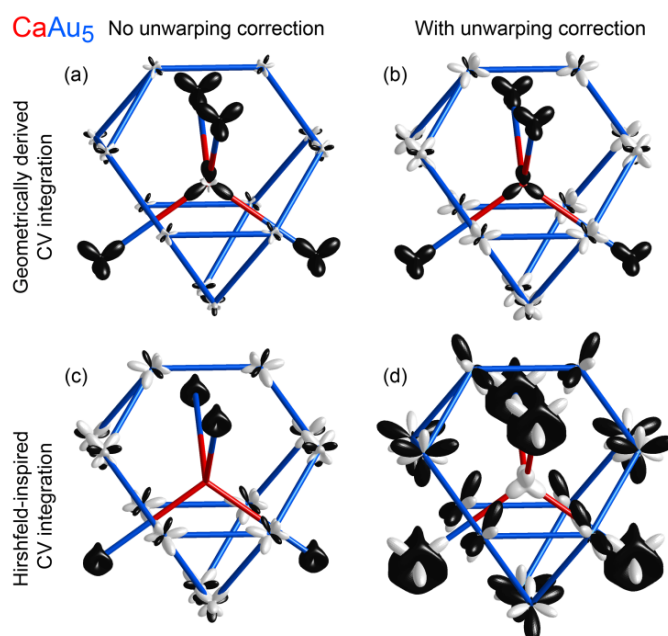


Figure 4.5. Comparison of DFT-CP anisotropy schemes calculated for CaAu_5 using (a) the original methodology, (b) the improved map generation (with the unwarping procedure applied) but original geometrically constructed contact volumes, (c) the original map generation but the Hirshfeld-inspired contact volume determination, and (d) the improved methods for the both the creation of maps and contact volumes. See the caption to Figure 4.4 for plotting contentions.

Using the original DFT-CP scheme, the integrated CP distribution closely resembles that obtained in this way for the Laves phase CaPd_2 (Figure 4.4a), despite having replaced four Ca-Ca contacts with Ca-

transition metal ones. Negative pressure lobes (black) point through the faces of the truncated tetrahedron just as in CaPd_2 , while the edges of the truncated tetrahedron itself are decorated with positive pressure lobes. The Ca atom, overall, has large negative pressure indicating that it would benefit from contraction of the lattice, which is prevented by positive pressures within the Au truncated tetrahedra. As such, this scheme predicts that the structure would be stabilized by replacing the Ca with a larger atom—which of course runs counter to the empirical trend of the AuBe_3 type being observed for small A atoms.

Turning on either the interpolation near atomic cores (Figure 4.5b) or the Hirshfeld-inspired CVs (Figure 4.5c), introduces qualitative changes to the CP distributions on the Ca@Au_4 tetrahedron, but leaves the positive pressures between the Au atoms of the truncated tetrahedron largely intact. The most dramatic change occurs upon turning on both features of the improved DFT-CP method simultaneously (Figure 4.5d). Here, positive CP lobes point along all of the Ca-Au contacts, while negative CP is reserved for the Au-Au interactions with the longest interatomic distances. Unlike that of the original DFT-CP scheme, the final integrated result is in close agreement with experimental trends: the positive pressures surrounding the Ca atoms indicate that the stability of this structure will be largely dependent on having a relatively small atom at this position.

In comparing Figure 4.5b and 4.5d, it is evident that the use of Hirshfeld-inspired CVs plays a significant role in obtaining positive pressures on the Ca sites. As for CaPd_2 , a comparison of the CVs generated with the original and Hirshfeld-inspired schemes is helpful in seeing how these differences arise (Figure 4.6). On moving from the MgCu_2 type to the AuBe_3 type, the relative interatomic distances are left unchanged. Because of this, the Ca-Ca geometrically derived CV in CaPd_2 (Figure 4.4b) is identical to the corresponding one in CaAu_5 (Figure 4.6b), although now it corresponds to a Ca-Au CV. In the slice

through the structure of Figure 4.6, this CV appears as a diamond-shaped polygon. Only the narrow corners of this polygon cross into the positive core regions of the Ca and Au atoms, leading to a net negative pressure for the contact.

As we switch to the Hirshfeld-inspired scheme, the larger size of the Ca atoms relative to Au will lead to the growth of the Ca-Au CVs at the expense of the Au-Au ones. Because the Ca is surrounded by Au atoms, in the shapes of the CVs near the Ca center are essentially unchanged. However, on the Au atoms, there is a marked expansion of the Ca-Au CVs into regions previously occupied by Au-Au ones (Figure 4.6c,f). The Au-Ca CVs then acquire more of the positive core pressures on the Au atoms, leading to the overall positive CPs between the Ca atom and its neighbors.

As we mentioned earlier, the positive pressures calculated for the Ca atom with the revised CP scheme (Figure 4.5d) suggest that the AuBe_5 type would be stabilized by the replacement of relatively small atoms on this site. Whether a AuBe_5 phase forms, however, is not just a factor of the favorability of that single phase, but will depend also on the free energy of the AuBe_5 -type compound relative to those with alternative structures (or multi-phase mixtures of compounds with an average A:B ratio of 1:5). For AB_5 intermetallics formed between an electropositive metal such as an alkaline earth or lanthanide (for the A sites) and a late transition metal (for the B sites), the AuBe_5 type has a fierce competitor: the CaCu_5 type (Figure 4.1c). What does the improved DFT-CP approach predict about the relative virtues of these two structure types?

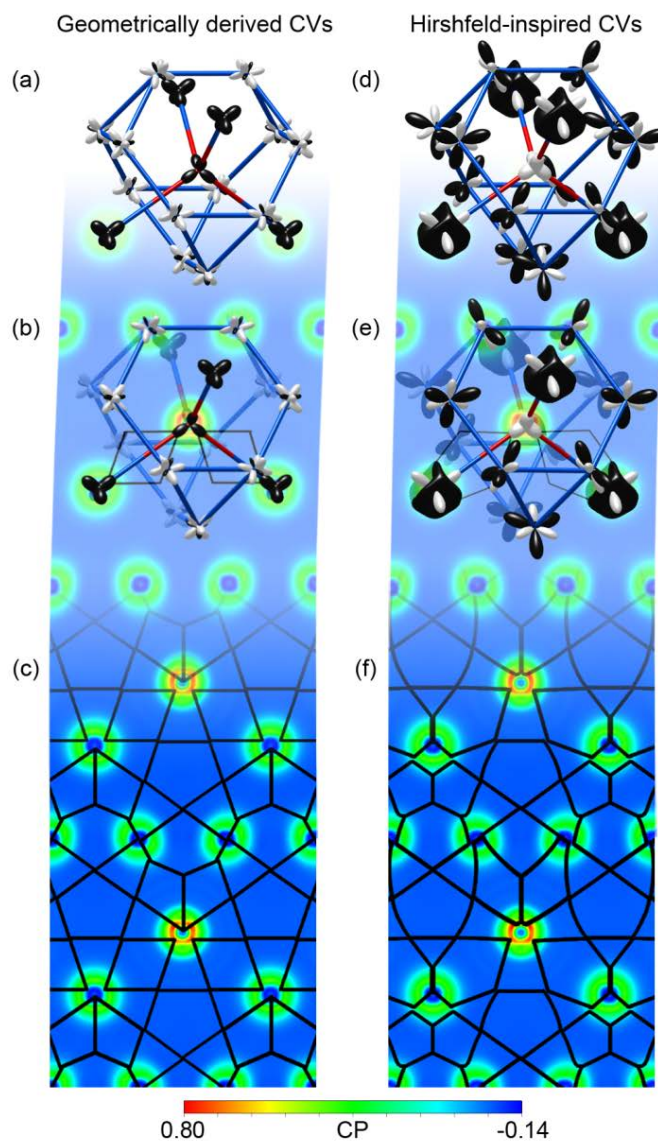


Figure 4.6. Effect of the use of Hirshfeld-inspired contact volumes (CVs) on the integrated DFT-CP results for CaAu_5 (AuBe_5 type). (a) Atomic DFT-CP anisotropy surfaces calculated for CaAu_5 using the original geometrical definition of CVs. (b) The DFT-CP anisotropy surfaces drawn in the context of a cross section of the DFT-CP map with two Ca-Au CVs in the original scheme indicated. (c) The same cross section of the CP map as in (b) with additional CV borders drawn. (d)-(f) The corresponding plots obtained using the Hirshfeld-inspired CV scheme. Note that the CV borders are determined only to the resolution of voxel grid used in the CP calculation. The smooth curves drawn should thus be considered as approximate. See the caption to Figure 4.4 for an explanation of plotting conventions for the DFT-CP anisotropies.

In Figure 4.7, we present a comparison of the CP schemes calculated for the CaCu_5 - and AuBe_5 -type structures for two different compounds: CaCu_5 and CaAu_5 , which are experimentally known to prefer the former and latter structure type, respectively (green boxes).^{74,75} The plots shown focus on the coordination environment of the Ca atoms (A site) as the relative size of the atom here has been perceived as a key factor in determining which structure type is adopted. In the CaCu_5 -type structures, this Ca environment consists of an 18-coordinate hexagonal polyhedron built from the layering of honeycomb and kagome sheets of Cu/Au atoms. For the AuBe_5 -type structures, the Ca coordination environment is the same Friauf polyhedron of Cu/Au atoms that we saw earlier in Figures 4.5 and 4.6.

A comparison of the results for CaCu_5 and CaAu_5 reveals that, while differences occur in the sizes of the various lobes, the qualitative features of the CP plots are very similar between the phases of the same structure types. For both CaCu_5 -type compounds, the Ca atom's CP surface has the shape of a d_{z^2} orbital, with negative lobes pointing up and down, and a torus of positive pressure running around the middle. This shape can be interpreted as the Ca atom desiring shorter contacts to the Cu/Au atoms in the layers above and below it, but longer contacts to those in the same plane. Overall, the pressures on the Ca sites are negative (-389 GPa on CaCu_5 and -21 in CaAu_5), indicating that the combined effect of the 12 overly long contacts to the Cu/Au atoms above and below, outweighs the 6 overly short contacts in the plane. The net negative CP for the Ca could be relieved by the placement of a larger atom on this site, leading to the prediction that the stability of the phase is enhanced for larger A atoms.

In both of the AuBe_5 -type phases, on the other hand, the Ca sites are subject to positive pressures, indicative of a desire for the expansion of the lattice. This driving force of enlarging the unit cell is resisted largely by the presence of negative pressure lobes between the Cu/Au atoms of the truncated tetrahedron

and the Cu/Au atoms on the diamondoid network, which like the Ca atoms lie in Friauf polyhedra. Due to the symmetry of the structure, the interatomic distances between the atoms in the Friauf polyhedra and their surroundings are the same, regardless of whether the position is occupied by a Ca atom or a Cu/Au one. As such, the structure would be best served by placing an atom on the Ca site with a size more similar to a Cu/Au atom, i.e. a smaller atom.

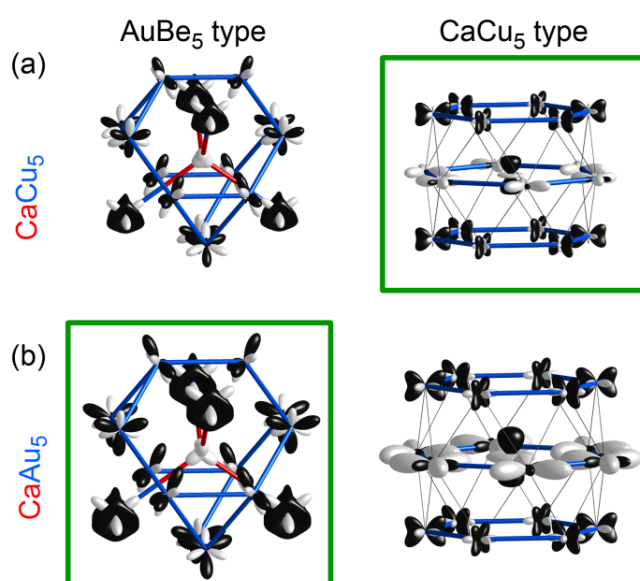


Figure 4.7. DFT-CP analysis of the AB₅ structure types CaCu₅ and AuBe₅. (a) CaCu₅ in the AuBe₅ and CaCu₅ types. (b) CaAu₅ in the same two structure types. Plotting conventions are given in the caption to Figure 4.4.

From these considerations, we can conclude that the CaCu₅ and AuBe₅ structure types are indeed tailored for a larger and smaller atom on the A atom positions, respectively. Let's now examine how the CP results for the experimentally observed phases compare with the hypothetical ones. As a first step, we need to calibrate ourselves in terms of the significance of the sizes of the CP features in Figure 4.7a. The CP

lobes for the two CaCu_5 phases in panel a are drawn to scale, as are the two CaAu_5 phases in panel b. Between the panels a and b, it is not practical to show the plots at the same scale: Cu with its highly localized 3d electrons generally shows inherently larger pressures numerically than Au, regardless of the structure. Instead panels a and b are scaled so that the relative features of the CaCu_5 - and AuBe_5 -type structures are maximally comparable.

A good place to begin is a comparison of the two AuBe_5 -type phases. As we noted earlier, the CP features are very similar between CaCu_5 and CaAu_5 in this structure type. However, a close examination of the Ca CP anisotropy surfaces for the two compounds reveals an important difference: in CaAu_5 the positive pressures around the Ca are largely focused along the diamondoid network. The contacts between the Ca and the truncated tetrahedron are more satisfied, and in fact represent the interactions in the structure that are most optimized. Upon replacing the Au atoms with smaller Cu ones to create a AuBe_5 -type CaCu_5 phase, we obtain a different situation. The smaller size of Cu translates into a larger relative size for the Ca, and now the positive pressures around the Ca are more uniformly distributed.

By contrast, the replacement for Au with the smaller Cu atoms to make the CaCu_5 -type CaCu_5 phase leads to a tighter coordination environment around the Ca. As a result, the size of the Ca CP features decreases in the CaCu_5 type during this substitution, relative to those of the AuBe_5 -type phase of the same composition.

These observations are in-line with the trend that moving from CaAu_5 to CaCu_5 increases the favorability of the CaCu_5 type relative to the AuBe_5 type. What is more difficult to determine is where the crossing point between the two structure types should occur. This difficulty, in fact, reflects one of the limitations of the use of the DFT-CP method in comparing very different crystal structures. Chemical pressures

represent derivatives of the total energy with respect to structural perturbations, and not the magnitudes of the total energy itself. For structures that are closely related, such as a superstructure and the basic structure that it is derived from, the CPs are charting similar energy vs. distance curves for interatomic interactions. As such, minimizing the CPs can be seen as a qualitative surrogate for the minimization of the total energy. For more distantly related structures, such as the CaCu_5 and AuBe_5 types, the energy vs. distance relationships may be expected to be quite different. We should then seek complementary methods, such as the crystal orbital Hamilton population,⁷⁶ to measure the magnitudes of the bond strengths to go along with the derivatives provided by the DFT-CP analysis.

4.8. Conclusions

The concept of chemical pressure offers a means to track the effects of atomic size on the electronic structure. In this Chapter, we have described advances in the generation of chemical pressure maps for solid state structures using the output of DFT calculations and the interpretation of these maps in terms of interatomic interactions. For the calculation of CP maps, we introduced a correction for the incompressibility of atomic cores in which voxel positions between structures of different sizes are interpolated to the same position relative to the atom with which they are associated. The result is the large reduction of the isotropic core pressures (by factors of up to 15) that have proven so challenging to analyze in previous applications of the DFT-CP approach.

We also introduced an improved scheme for assigning voxels to interatomic contacts for the integration of interatomic pressures: the use of Hirshfeld-inspired contact volumes. In this approach, the relative sizes of the free atom electron densities centered at the atomic positions within a crystal structure are used

to evaluate their relative degrees of influence on the pressure at a given voxel. The voxel is then assigned to the interaction between the pair of atoms whose influence is greatest on it. Through the use of the free atom electron density profiles, the differing size of the atoms becomes naturally incorporated into the construction of contact volumes, unlike our earlier geometrical procedure. This formalism is also easily generalized: the radial electron density of the free atom could easily be replaced in the input to the CP programs with other relevant profile functions, such as the local energy component of the atomic pseudopotentials.

The utility of the improved DFT-CP approach was illustrated using several structures whose stability ranges have been associated with atomic size effects: the MgCu_2 (cubic Laves phase), AuBe_5 , and CaCu_5 structure types. For the MgCu_2 -type CaPd_2 , the CP scheme obtained exhibited parallel features with the sphere-packing view of the Laves phases, and thus affirms the efforts of several researchers to apply and adapt radius ratio type analyses to this large family of compounds.^{2,77-79} In the case of competition between the AuBe_5 and CaCu_5 types for AB_5 structures, our analyses confirmed the role of atomic size in stabilizing one phase over the other. A moderately sized A atom is predicted to experience positive pressures in the AuBe_5 type, and negative pressures in the CaCu_5 type. Relatively large A atoms are then expected to prefer the CaCu_5 -type, while smaller A atoms would prefer the AuBe_5 type.

We have already found that these advances in the DFT-CP method have made its use much more straightforward for a wide variety of intermetallic systems, and are looking forward to exploring its capabilities through further applications. Motivated by the insights the method has provided regarding the factors influencing the stabilities of the Laves phases and the AB_5 structure types, we are particularly excited

to see what it might reveal concerning the complex intergrowth structures of the AuBe₃ and MgCu₂ structure types in lanthanide-copper systems, some with thousands of atoms per unit cell.⁴⁵⁻⁴⁸

Acknowledgement

We gratefully acknowledge the financial support of the National Science Foundation through grant DMR-1207409. This research involved calculations using computer resources supported by National Science Foundation Grant CHE-0840494.

4.9. References

- (1) Bondi, A. *J. Phys. Chem.* **1964**, *68*, 441-451.
- (2) Simon, A. *Angew. Chem. Int. Ed.* **1983**, *22*, 95-113.
- (3) van der Waals, J. D. *Nobel Lectures, Physics 1901-1921*; Elsevier Publishing Company: New York, 1967.
- (4) Müller, U. *Inorganic structural chemistry*; 2nd ed.; Wiley: Chichester, England ; Hoboken, NJ, 2007.
- (5) Levy, O.; Jahnátek, M.; Chepulskii, R. V.; Hart, G. L. W.; Curtarolo, S. *J. Am. Chem. Soc.* **2010**, *133*, 158-163.
- (6) Wang, H.; Wang, F.; Jones, K.; Miller, G. J. *Inorg. Chem.* **2011**, *50*, 12714-12723.
- (7) Wendorff, M.; Röhr, C. *Z. Anorg. Allg. Chem.* **2011**, *637*, 1013-1023.
- (8) Deringer, V. L.; Goerens, C.; Esters, M.; Dronskowski, R.; Fokwa, B. P. T. *Inorg. Chem.* **2012**, *51*, 5677-5685.
- (9) Lin, Q.; Smetana, V.; Miller, G. J.; Corbett, J. D. *Inorg. Chem.* **2012**, *51*, 8882-8889.

- (10) Osters, O.; Nilges, T.; Schöneich, M.; Schmidt, P.; Rothballer, J.; Pielnhofer, F.; Wehrich, R. *Inorg. Chem.* **2012**, *51*, 8119-8127.
- (11) Samal, S. L.; Lin, Q.; Corbett, J. D. *Inorg. Chem.* **2012**, *51*, 9395-9402.
- (12) Smetana, V.; Miller, G. J.; Corbett, J. D. *Inorg. Chem.* **2012**, *51*, 7711-7721.
- (13) Crivello, J.-C.; Breidi, A.; Joubert, J.-M. *Inorg. Chem.* **2013**, *52*, 3674-3686.
- (14) Khatun, M.; Stoyko, S. S.; Mar, A. *Inorg. Chem.* **2013**, *52*, 3148-3158.
- (15) Samal, S. L.; Gulo, F.; Corbett, J. D. *Inorg. Chem.* **2013**, *52*, 2697-2704.
- (16) Pöttgen, R. *Z. Anorg. Allg. Chem.* **2014**.
- (17) Emami, H.; Souques, R.; Crivello, J.-C.; Cuevas, F. *J. Solid State Chem.* **2013**, *198*, 475-484.
- (18) Shoko, E.; Kearley, G. J.; Peterson, V. K.; Mutka, H.; Koza, M. M.; Yamaura, J.-i.; Hiroi, Z.; Thorogood, G. J. *arXiv ePrints* **2013**.
- (19) Yzambart, G.; Bellec, N.; Nasser, G.; Jeannin, O.; Roisnel, T.; Fourmigué, M.; Auban-Senzier, P.; Íñiguez, J.; Canadell, E.; Lorcy, D. *J. Am. Chem. Soc.* **2012**, *134*, 17138-17148.
- (20) Sung, N. H.; Roh, C. J.; Kang, B. Y.; Cho, B. K. *J. Appl. Phys.* **2012**, *111*, 07-117.
- (21) Huang, W.-Y.; Yoshimura, F.; Ueda, K.; Shimomura, Y.; Sheu, H.-S.; Chan, T.-S.; Chiang, C.-Y.; Zhou, W.; Liu, R.-S. *Chem. Mater.* **2014**, *26*, 2075.
- (22) Lue, C. S.; Wong, S. F.; Huang, J. Y.; Hsieh, H. L.; Liao, H. Y.; Ramachandran, B.; Kuo, Y. K. *J. Appl. Phys.* **2013**, *113*, 013710.
- (23) Nam, G.; Jeon, J.; Kim, Y.; Kang, S. K.; Ahn, K.; You, T.-S. *J. Solid State Chem.* **2013**, *205*, 10-20.
- (24) Wang, P. L.; Kolodiaznyy, T.; Yao, J.; Mozharivskyj, Y. *J. Am. Chem. Soc.* **2012**, *134*, 1426-1429.
- (25) Zhao, H. J.; Ren, W.; Chen, X. M.; Bellaiche, L. *J. Phys.: Condens. Matter* **2013**, *25*, 385604.
- (26) Ishida, S.; Nakajima, M.; Liang, T.; Kihou, K.; Lee, C.-H.; Iyo, A.; Eisaki, H.; Kakeshita, T.; Tomioka, Y.; Ito, T.; Uchida, S.-i. *J. Am. Chem. Soc.* **2013**, *135*, 3158-3163.
- (27) Lehr, G. J.; Morelli, D. T.; Jin, H.; Heremans, J. P. *J. Appl. Phys.* **2013**, *114*, 223712.

- (28) Demirel, S.; Avci, S.; Altin, E.; Altin, S.; Yakinci, M. E. *Ceram. Int.* **2014**, *40*, 5217-5222.
- (29) Fredrickson, D. C. *J. Am. Chem. Soc.* **2011**, *133*, 10070-10073.
- (30) Fredrickson, D. C. *J. Am. Chem. Soc.* **2012**, *134*, 5991-5999.
- (31) Stacey, T. E.; Fredrickson, D. C. *Dalton Trans.* **2012**, *41*, 7801-7813.
- (32) Engelkemier, J.; Berns, V. M.; Fredrickson, D. C. *J. Chem. Theory Comput.* **2013**, *9*, 3170-3180.
- (33) Nielsen, O. H.; Martin, R. M. *Phys. Rev. B* **1985**, *32*, 3780-3791.
- (34) Godfrey, M. J. *Phys. Rev. B* **1988**, *37*, 10176-10183.
- (35) Ziesche, P.; Gräfenstein, J.; Nielsen, O. H. *Phys. Rev. B* **1988**, *37*, 8167-8178.
- (36) Filippetti, A.; Fiorentini, V. *Phys. Rev. B* **2000**, *61*, 8433-8442.
- (37) Treglia, G. In *Stress and strain in epitaxy; theoretical concepts, measurements, and applications*; Elsevier Science B.V.: 2001, p 119-150.
- (38) Rogers, C. L.; Rappe, A. M. *Phys. Rev. B* **2002**, *65*, 224117/224111-224117/224118.
- (39) Hadler, A. B.; Harris, N. A.; Fredrickson, D. C. *J. Am. Chem. Soc.* **2013**, *135*, 17369-17378.
- (40) Berns, V. M.; Fredrickson, D. C. *Inorg. Chem.* **2013**.
- (41) Fulfer, B. W.; McAlpin, J. D.; Engelkemier, J.; McCandless, G. T.; Prestigiacomo, J.; Stadler, S.; Fredrickson, D. C.; Chan, J. Y. *Chem. Mater.* **2014**, *26*, 1170-1179.
- (42) Hirshfeld, F. L. *Theoret. Chim. Acta* **1977**, *44*, 129-138.
- (43) Buschow, K. H. J.; Van Der Goot, A. S.; Birkhan, J. *J. Less Common Met.* **1969**, *19*, 433-436.
- (44) Kleber, W. *Krist. Technik* **1967**, *2*, 13-14.
- (45) Cerný, R.; François, M.; Yvon, K.; Jaccard, D.; Walker, E.; Petříček, V.; Císarová, I.; Nissen, H. U.; Wessicken, R. *J. Phys.: Condens. Matter* **1996**, *8*, 4485.
- (46) Černý, R.; Guénee, L.; Wessicken, R. *J. Solid State Chem.* **2003**, *174*, 125-131.
- (47) Giovannini, M.; Pasero, R.; De Negri, S.; Saccone, A. *Intermetallics* **2008**, *16*, 399-405.

- (48) Gottlieb-Schönmeyer, S.; Brühne, S.; Ritter, F.; Assmus, W.; Balanetsky, S.; Feuerbacher, M.; Weber, T.; Steurer, W. *Intermetallics* **2009**, *17*, 6-10.
- (49) Gonze, X.; Rignanese, G.-m.; Verstraete, M.; Beuken, J.-m.; Pouillon, Y.; Caracas, R.; Raty, J.-y.; Olevano, V.; Bruneval, F.; Reining, L.; Godby, R.; Onida, G.; Hamann, D. R.; Allan, D. C. *Z. Kristallogr.* **2005**, *220*, 558-562.
- (50) Gonze, X.; Amadon, B.; Anglade, P.-M.; Beuken, J.-M.; Bottin, F.; Boulanger, P.; Bruneval, F.; Caliste, D.; Caracas, R.; Côté, M.; Deutsch, T.; Genovese, L.; Ghosez, P.; Giantomassi, M.; Goedecker, S.; Hamann, D. R.; Hermet, P.; Jollet, F.; Jomard, G.; Leroux, S.; Mancini, M.; Mazevet, S.; Oliveira, M. J. T.; Onida, G.; Pouillon, Y.; Rangel, T.; Rignanese, G.-M.; Sangalli, D.; Shaltaf, R.; Torrent, M.; Verstraete, M. J.; Zerah, G.; Zwanziger, J. W. *Comput. Phys. Commun.* **2009**, *180*, 2582-2615.
- (51) Goedecker, S.; Teter, M.; Hutter, J. *Phys. Rev. B* **1996**, *54*, 1703-1710.
- (52) Hartwigsen, C.; Goedecker, S.; Hutter, J. *Phys. Rev. B* **1998**, *58*, 3641-3662.
- (53) Momma, K.; Izumi, F. *J. Appl. Crystallogr.* **2011**, *44*, 1272-1276.
- (54) Oliveira, M. J. T.; Nogueira, F. *Comput. Phys. Commun.* **2008**, *178*, 524-534.
- (55) Okabe, A.; Sugihara, K.; Chiu, S. N. *Spatial tessellations : concepts and applications of Voronoi diagrams*; 2nd ed.; Wiley: Chichester; New York, 2000.
- (56) Bader, R. F. W. *Atoms in molecules: a quantum theory*; Oxford University Press: Oxford, England, 1994.
- (57) Wood, E. A.; Compton, V. B. *Acta Crystallogr.* **1958**, *11*, 429-433.
- (58) Palenzona, A.; Manfrinetti, P. *J. Less Common Met.* **1982**, *85*, 307-312.
- (59) Greenwood, N.; Earnshaw, A. In *Chemistry of the Elements*; 2 ed.; Butterworth-Heinemann: Oxford, UK, 1997.
- (60) Bergerhoff, G.; Brown, I. D. In *Crystallographic Databases*; Allen, F. H., Bergerhoff, Sievers, R., Eds.; International Union of Crystallography: Chester, 1987.
- (61) Belsky, A.; Hellenbrandt, M.; Karen, V. L.; Luksch, P. *Acta Crystallogr. B* **2002**, *58*, 364-369.
- (62) Samson, S. *Nature* **1962**, *195*, 259-262.
- (63) Samson, S. *Acta Crystallogr.* **1965**, *220*, 401-413.

- (64) Samson, S. *Acta Crystallogr.* **1967**, 23, 586-600.
- (65) Andersson, S. *Acta Crystallogr. B* **1980**, 36, 2513-2516.
- (66) Cenxual, K.; Parthé, E.; Waterstrat, R. M. *Acta Crystallogr. C* **1986**, 42, 261-266.
- (67) Yang, Q.-B.; Andersson, S.; Stenberg, L. *Acta Crystallogr. B* **1987**, 43, 14-16.
- (68) Fredrickson, D. C.; Lee, S.; Hoffmann, R. *Angew. Chem., Int. Ed.* **2007**, 46, 1958-1976.
- (69) Berns, V. M.; Stacey, T. E.; Sapiro, M.; Fredrickson, D. C. *Eur. J. Inorg. Chem.* **2011**, 2011, 3936-3949.
- (70) Stacey, T. E.; Fredrickson, D. C. *Inorg. Chem.* **2013**.
- (71) Henkelman, G. A., A.; Jónsson, H. *Comput. Mater. Sci.* **2006**, 36, 254-360.
- (72) Sanville, E.; Kenny, S. D.; Smith, R.; Henkelman, G. J. *Comput. Chem.* **2007**, 28, 899-908.
- (73) Tang, W.; Sanville, E.; Henkelman, G. J. *Phys. Condens. Matter* **2009**, 21, 084204/084201-084204/084207.
- (74) Raub, C. J.; Hamilton, D. C. *J. Less-Common Metals* **1964**, 6, 486-488.
- (75) Haucke, W. Z. *Anorg. Allg. Chem.* **1940**, 244, 17-22.
- (76) Dronskowski, R.; Bloechl, P. E. *J. Phys. Chem.* **1993**, 97, 8617-8624.
- (77) Dwight, A. E. *Trans. Am. Soc. Met.* **1961**, 53, 479-500.
- (78) Joseph, R. R.; Gschneidner, K. A., Jr. *Scr. Met.* **1968**, 2, 631-634.
- (79) Pearson, W. B. *Acta Crystallogr., Sect. B* **1968**, 24, 7-9.

Chapter 5.

Chemical Pressure Schemes for the Prediction of Soft Phonon Modes:

A Chemist's Guide to the Vibrations of Solid State Materials

*This chapter has been published under an open access license as an ACS Editors' Choice article: Engelkemier, J.; Fredrickson, D. C. *Chem. Mater.* **2016**, 28, 3171-3183. Although not authors, B. J. Kilduff and Y. Guo were influential in the development of the ionic profile method described in this chapter.*

5.1. Abstract

The vibrational modes of inorganic materials play a central role in determining their properties, as is illustrated by the importance of phonon-electron coupling in superconductivity, phonon scattering in thermoelectric materials, and soft phonon modes in structural phase transitions. However, the prediction and control of these vibrations requires an understanding of how crystal structure and the stiffness of interatomic interactions are related. For compounds whose relationships between bonding and structure remain unclear, the elucidation of such structure-property relationships is immensely challenging. In this Chapter, we demonstrate how the Chemical Pressure (CP) approach can be used to draw visual and intuitive schemes relating the structure and vibrational properties of a solid state compound using the output of DFT calculations. We begin by illustrating how phonon band structures can validate the DFT-CP approach. For some intermetallic crystal structures, such as the Laves phases, the details of the packing

geometries make the resulting CP scheme very sensitive to assumptions about how space should be partitioned among the interatomic contacts. Using the Laves phase CaPd_2 as a model system, we demonstrate how the phonon band structure provides a reference against which the space-partitioning method can be refined. A key parameter that emerges is the ionicity of the crystal structure: the assumption of some electron transfer from the Ca to the Pd leads to a close agreement between the CP distribution and the major features of its phonon band structure. In particular, atomic motions along directions of positive CPs (indicative of overly short interatomic distances) contribute to high frequency modes, while those along negative CPs (corresponding to overly long distances) make up the lowest frequency modes. Finally, we apply this approach to Nb_3Ge and CaPd_5 , for which low-frequency phonon modes correlate with superconductivity and a rich variety of superstructures, respectively. Through these examples, CP analysis will emerge as a means of predicting the presence of soft phonon modes in a crystal structure, and a guide to how elemental substitutions will affect the frequencies of these modes.

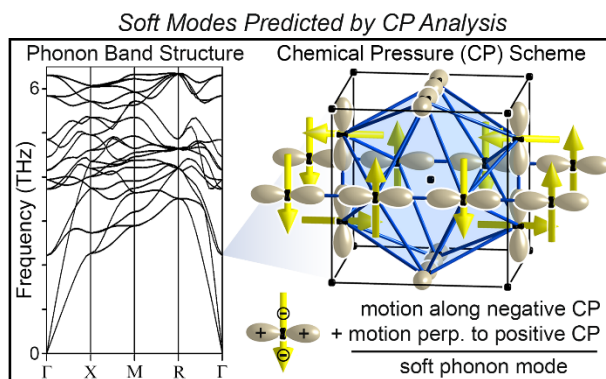


Figure 5.0. The low-frequency phonon modes of Cr_3Si type intermetallic compounds are connected to their critical temperatures, T_c 's, below which superconductivity is possible. Chemical Pressure (CP) analysis of the structure reveals chains of CP quadrupoles that predict lower phonon frequencies – and possibly higher T_c 's – through elemental substitutions that exacerbate the positive CP between the chains of atoms.

5.2. Introduction

Concepts relating structure and properties form the core inspiration behind the design of new materials. In thermoelectric materials, for example, the notion of a phonon-glass electron-crystal¹ predicts that the introduction of structural motifs that selectively scatter phonons over electrons will enhance a material's ability to exhibit an electrical voltage across a temperature gradient, and vice versa. This idea has led directly to the fruitful investigation of phases with rattling guest atoms, such as clathrates and stuffed skutterudites,²⁻⁶ as well as nanostructured materials whose domain boundaries serve to disrupt phonon-mediated thermal conductivity.^{7,8} For many solid state materials, however, a clear link between structure and properties remains a distant prospect. The need for such connections is especially pressing for metals and intermetallic phases, where electronic structures usually described in k -space must be bridged with specific structural moieties in physical space.

This disconnect is particularly evident for vibrational properties. The presence of soft phonon modes in intermetallics has been identified as an essential contributor to thermoelectric performance,⁹⁻¹⁴ superconductivity,¹⁵⁻¹⁷ unusual magnetic phenomena,^{18,19} magnetostriction,^{20,21} hydrogen diffusion,^{22,23} and structural phase transitions.²⁴⁻²⁸ However, few methods exist for directly tying the presence of these phonon modes (represented in k-space, using the same irreducible representations of the crystal symmetry as the electronic wavefunctions) to specific geometrical arrangements of atoms. In this Chapter, we will demonstrate how such relationships between structure and vibrational properties can be quickly and vividly derived using Density Functional Theory-Chemical Pressure (DFT-CP) analysis.

The DFT-CP method was originally developed to make sense of complex intermetallic structures whose formation appeared to be driven by conflicts between electronic and atomic size effects.²⁹⁻³² Following the concept of the quantum mechanical stress density,³³⁻³⁷ the approach converts the detailed output of the total DFT energy into spatially resolved maps of local pressure, which can be interpreted in terms of interatomic interactions. When applied to intermetallics, the DFT-CP analysis often reveals tense compromises in the atomic packing within crystal structures, in which various chemical pressures (CPs, local pressures induced by lattice constraints rather than an externally applied force) conflict in their desires for the structure to expand or contract (Figure 5.1). The tension can become so severe as to drive structural rearrangements, including the formation of the local icosahedral order in Bergman- and Tsai-type quasicrystal approximants,^{38,39} the incorporation of stuffing atoms by AuCu₃-type host lattices,⁴⁰ and the intergrowth of intermetallic and carbide domains in the Mn-Si-C system.⁴¹

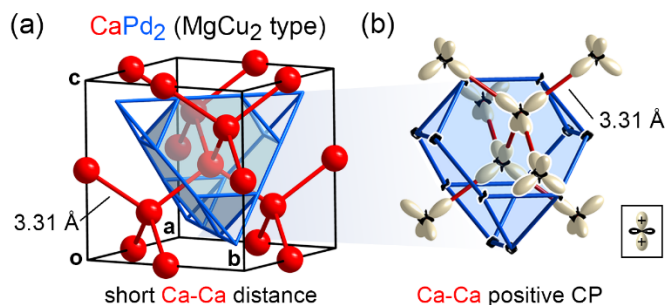


Figure 5.1. The MgCu₂-type Laves phase CaPd₂, a model system for the development of the DFT-Chemical Pressure (CP) method. (a) The cubic unit cell of CaPd₂. (b) The DFT-CP scheme previously calculated for this phase.³² Here, the CP distribution around each atom is represented as a surface: the sum of the pressures an atom experiences along any given direction from an atomic center is shown by the distance of the surface from its nucleus along that direction. White lobes represent positive CP (where expansion is favored locally), while black lobes represent negative CP (where contraction is desired).

As we will see in the following sections, the CP schemes that result from these analyses have implications that extend beyond the tendency for superstructure formation. Over a series of examples an intimate connection will take shape between a crystal structure's CP scheme and its phonon band structure. First, we will demonstrate how the phonon band structure of a material can be used to validate the DFT-CP approach, using the cubic Laves phase structure (Figure 5.1a) as a model system. Then, we explore the reverse process, in which CP schemes predict aspects of the phonon band structure for two other phases: the superconductor Nb₃Ge,⁴² whose soft phonon modes are implicated in the phase's relatively high T_c of 23 K;⁴³ and the CaCu₅ type phase CaPd₅,⁴⁴ whose CP scheme provides the basis for a broad structural chemistry.

From these results, a self-consistency between phonon frequencies and CP lobes will emerge in which the phonon band structure provides a reference for the optimization of the DFT-CP approach and, in turn, the CP scheme offers a visual and chemically intuitive representation of the system's vibrational properties.

5.3. The CaPd₂ model system

Our original motivation for considering a link between the CP scheme of a compound and its phonon band structure was to rigorously test the physical relevance of our interpretation of the CP method's results. As illustrated in Figure 5.2, the raw output of a CP calculation consists of a spatially resolved map of local pressures, the average over which gives the net macroscopic pressure experienced by the compound (usually zero for a geometrically optimized structure). For most intermetallics, the major features in these maps are intense, overall positive pressures near the atomic cores and a relatively homogeneous negative pressure spread throughout the interstitial spaces. The interpretation of such maps in terms of interatomic interactions then involves dividing the continuous three-dimensional CP maps into discrete domains belonging to the interatomic contacts (Figures 5.2a and 5.2b).

For many compounds, such as CaCu₅-type and Cr₃Si-type phases, the CP schemes obtained from the method are largely insensitive to how we divide space between interatomic contacts. In other cases, however, the situation is less clear-cut, and care must be taken to ensure the division is physically realistic.

Particularly problematic have been the Laves phases, such as the MgCu₂-type compound CaPd₂ (Figure 5.1a). AB₂ Laves phases are classically described as tetrahedrally close-packed. In the MgCu₂ type, this dense packing is built from a diamond network of A atoms (red) that is interpenetrated by a second diamond network built from vertex-sharing tetrahedra of B atoms (blue).

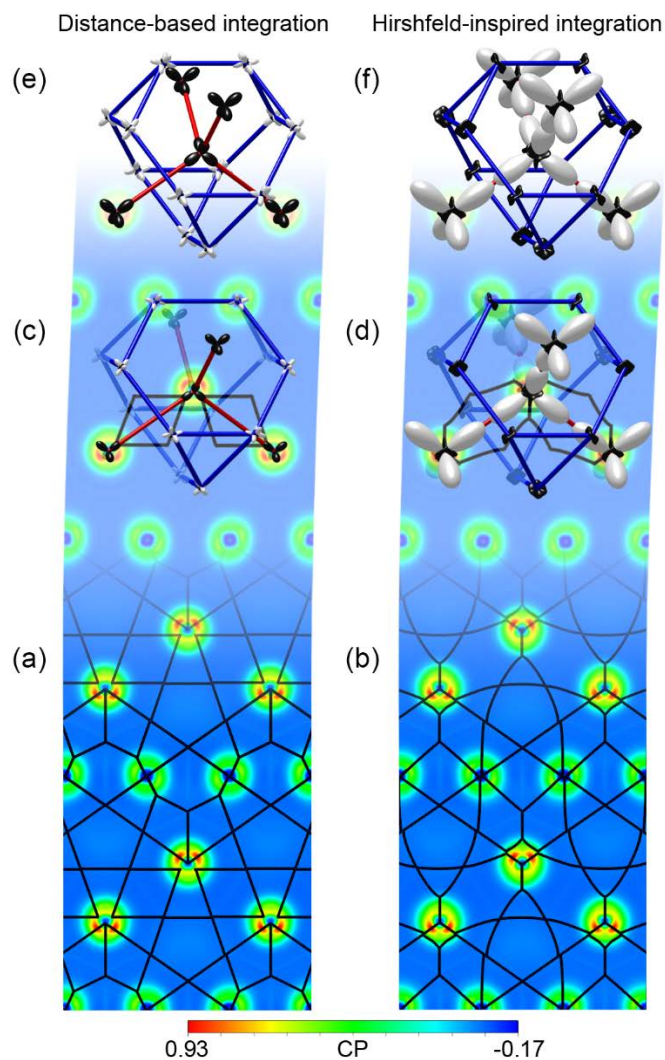


Figure 5.2. Construction of chemical pressure (CP) schemes from the raw CP maps calculated for CaPd_2 , using different methods for dividing space between interatomic contacts. (a)-(b) A cross-section of the CP map of CaPd_2 with borders outlined in black for the geometric contact volumes and Hirshfeld-inspired contact volumes. Pressure units for color map: atomic units. (c)-(d) The CP schemes obtained from projecting the average pressures within the contact volumes onto low-order real spherical harmonics, shown here in the context of the raw CP map. Dark gray lines indicate the borders around two Ca-Ca contact volumes. (e)-(f) The resulting CP schemes shown separately from the map. See the caption to Figure 5.1 for plotting conventions. Adapted from Ref. 32 with the permission of the American Chemical Society.

In terms of sphere packing, this arrangement produces an intriguing frustration that makes this structure an excellent model system for the development of the DFT-CP method. If the nearest neighbors on the B sublattice are viewed as touching each other, limits become imposed on the space of the A atoms. At the A:B radius ratio of $\sqrt{3}/2$, neighboring A atoms come into contact with each other, and the inclusion of larger A atoms would require stretching the B-B distances. At no radius ratio do the A and B spheres touch without sphere overlap in the A or B sublattices.

In the phase CaPd_2 , this tension is clearly present: The Ca:Pd radius ratio in CaPd_2 , calculated from empirical metallic radii, is 1.44, 66% larger than $\sqrt{3}/2$.⁴⁵ This size mismatch leads to Ca-Ca distances of only 3.31 Å – quite short compared to 3.94 Å for the sum of the metallic radii.⁴⁶ These unusual distances suggest that large internal stress between neighboring Ca contacts arises from the conflict between the space requirements of the Ca atoms and the optimal Ca-Pd and Pd-Pd bonding distances.

While the packing frustration in this compound seems fairly straightforward from a geometrical perspective, seeing this effect in a CP scheme requires care in how the space of the structure is divided between interatomic contacts (Figure 5.2). Perhaps the simplest approach is to divide the CP map into regions according to which pair of atoms each grid point is closest to (the geometric contact volume method). Our early testing of this approach resulted in reasonable and insightful CP schemes for a number of structures,^{31,38,40} but a quite unexpected scheme for CaPd_2 (Figure 5.2e): the signs and directionality of the CP lobes tell of Ca-Ca distances that are too long (black lobes between Ca atoms) and Pd-Pd distances that are too short (white lobes between Pd atoms).³²

An examination of the contact volumes constructed for the phase (Figures 5.2a and 5.2c) revealed that this effect had its origin in the neglect of the differing sizes of the atoms.³² Around each Ca atom, the

contacts to its Pd neighbors are somewhat shorter than its Ca neighbors. This situation leads to more of the volume around the Ca neighbors, including the strong positive pressures in their core regions (colored green and red in the CP maps of Figure 5.2), being assigned to Ca-Pd contact volumes rather than Ca-Ca ones. However, while the Ca-Ca distances are longer on an absolute scale, the situation appears very different when we consider the typical ranges of Ca-Ca and Ca-Pd distances. Factoring in the larger atomic radius of Ca, the Ca-Ca distance is quite short relative to those observed in other phases (while the Ca-Pd distance is fairly typical). As such it seems that the Ca-Ca contacts are underrepresented in the purely distance-based division of space into contact volumes.

To counter this effect, we recently developed an integration scheme that takes into account that a larger atom should have a more far-reaching influence on its surroundings than a smaller one,³² inspired by the Hirshfeld approach to the calculation of atomic charges from an electron density distribution.⁴⁷ Radial electron density profiles of free atoms are first mapped onto every atomic center in a structure. Then each voxel is assigned to the two atoms whose free atom electron density profiles are the highest at that point. Since the profiles for elements with larger atoms naturally decay with distance from the nucleus more slowly, the influence of larger atoms extends further than those of smaller atoms (compare the gray outlines in Figures 5.2c and 5.2d).

After introducing this more physically-motivated process for dividing up space, we obtained the CP scheme in Figure 5.2f. The dominant features in the plot are long white lobes pointing along the Ca-Ca contacts, indicative of positive pressures acting between the Ca atoms. This driving force for the expansion of the structure is counteracted by smaller black features directed into the spaces between the Ca and Pd atoms. The CP scheme thus recovers our expectations from the short Ca-Ca distances.

One concern, however, is the circular nature of this development, in which empirical models are guiding the decision of whether an interpretation of a first principles result is reasonable. Is there another way that we could validate and refine the DFT-CP method without recourse to tables of atomic radii? Herein, we will see that the examination of the vibrational modes of a structure opens one such avenue.

5.4. Connecting chemical pressure to vibrational properties

Let's begin by examining more closely how the idea of local pressures acting between atoms can be connected to vibrational properties. The basis for our discussion is the typical energy vs. distance curve for an interatomic interaction as shown in Figure 5.3a, with one small variation to adapt this plot to CP analysis: rather than using distance as the dependent variable, we use the volume of space assigned to that pair of atoms in the structure, such as one of the contact volumes illustrated in Figure 5.2.

The ideal separation of the atoms is represented by an energy minimum. As the space between the atoms decreases relative to this ideal, the system encounters a steep energetic penalty, resulting from Pauli repulsion between the electrons on the two atoms and Coulombic repulsion between the nuclei. Distances longer than the optimal length are also unfavorable, although the energetic cost for stretching a contact in this way increases comparatively slowly, as the system asymptotically approaches complete dissociation.

A local pressure experienced in such an interatomic interaction can be obtained by taking the negative derivative of energy with respect to the volume allocated by the system to the interaction ($V_{contact}$), i.e. local pressure = $-\partial E/\partial V_{contact}$. At short ranges, this local pressure is positive, reflecting the favorability of allowing the structure to expand. As the atoms are moved apart, the local pressure becomes negative, reaching a minimum at the inflection point in the $E(V_{contact})$ curve. It then weakens as the atoms become increasingly

independent of each other. Consequently, positive pressure consistently indicates a repulsive interaction, whereas negative pressures are more nebulous: they could be soothed by either contraction or elongation of interatomic distances.

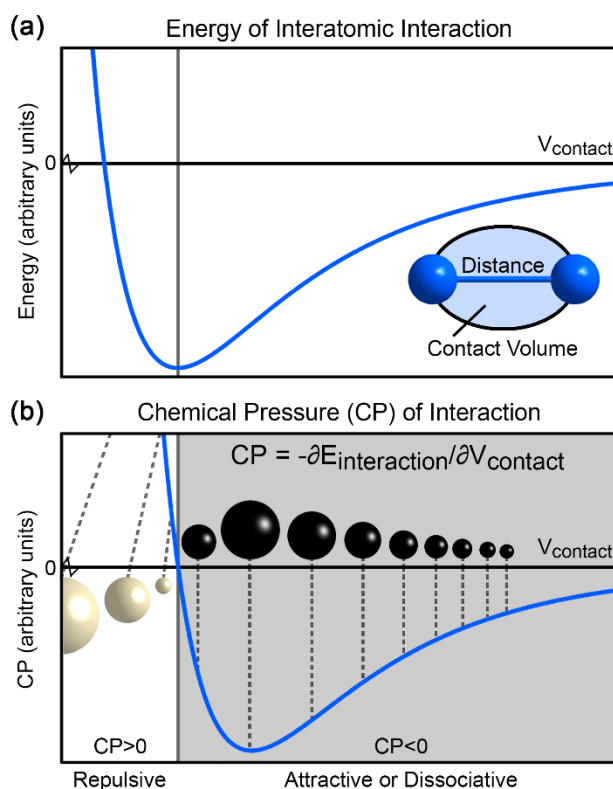


Figure 5.3. The chemical pressure concept interpreted in terms of the essentially universal potential energy curve for interatomic interactions. (a) The interaction energy as a function of the volume shared between the two atoms (V_{contact}), with a contact volume shown schematically as an inset. When the relative interatomic distances are held constant, each contact volume scales with the distance between the two atoms that share it. (b) The negative derivative of the energy, illustrating the connection between DFT energy and chemical pressure. Black and white spheres are used to emphasize the connection between points on the CP vs. V_{contact} curve and the lobes of the CP surfaces used elsewhere in this Chapter.

As mentioned above, this relationship between the forces acting on contacts that are longer or shorter than the ideal should have consequences for the vibrational properties of a structure. When an atom is held at its equilibrium position by positive CPs, motions of the atom against any of those pressures will be sharply resisted by the nearly exponential rise in energy along that direction. Vibrations involving such displacements would be expected to have relatively high frequencies, with larger positive pressures corresponding to increased stiffness in the modes.

Atoms held in place by opposing negative pressures, on the other hand, experience a very different potential energy surface. Moving an atom along a negative CP to shorten an overly-long contact should not face as high a degree of resistance from the opposing negative CP, as its pull should become weaker with increasing distance (once the inflection point in the E vs. $V_{contact}$ curve is passed). Thus vibrational modes with components along directions of negative CP are expected to be soft. In the following sections, we will see that – with some physically motivated adjustments to the CP integration method – these expectations are borne out by comparisons of the CP schemes for three intermetallic structures: the CaPd_2 model system, the superconductor Nb_3Ge , and CaPd_5 , whose CP scheme underlies a diverse structural chemistry.

5.5. Calibration of the CP integration scheme

Now that we have considered the qualitative connection between the CP scheme and vibrational properties for an interatomic interaction, we are in a position to test this relationship. We begin in Figure 5.4 (left) with the calculation of the phonon band structure for CaPd_2 , whose CP scheme we illustrated before in Figure 5.2. The phonon frequencies stretch from 0 THz for the acoustic modes at Γ to just over

8 THz (mid-infrared), and run through reciprocal space in a complex pattern of bands, one for each of the 18 positional degrees of freedom of the 6 atoms in the primitive unit cell.

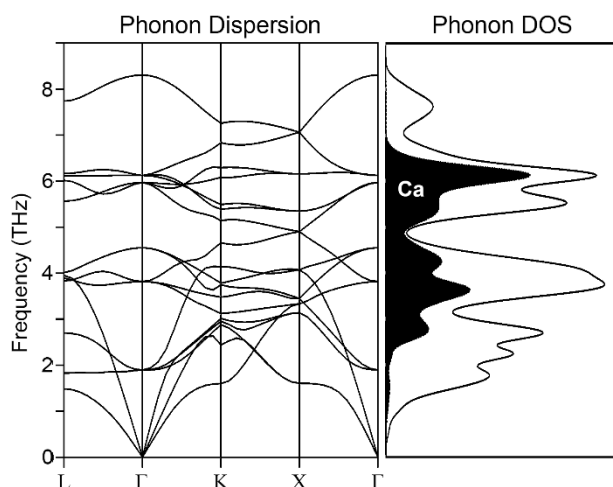


Figure 5.4. The LDA-DFT phonon band structure and density of states (DOS) of CaPd_2 . The contributions of the Ca motions to the DOS are shaded in black, with the remainder corresponding to the Pd displacements. Note that motion of Pd atoms dominates the lowest and highest frequencies in the density of states.

A general sense for how vibrations involving the various interaction types in the system (Ca-Ca, Ca-Pd, and Pd-Pd) are distributed over these frequencies is available from the Density of States (DOS) of the band structure. The projected DOS for the Ca atoms (Figure 5.3 right, shaded in black) appears concentrated in the center of the distribution, straddling a deep minimum at about 5 THz and stretching from approximately 2 to 7 THz. Few contributions from the Ca atoms to the DOS occur either above or below this range, indicating that vibrations along the Ca-Pd and Ca-Ca interactions are mostly restricted to these frequencies. The remainder of the phonon DOS derives from motions of the Pd atoms, leading to

the conclusion that both the lowest and highest frequency modes in the structure are associated almost exclusively with the Pd sublattice.

Using the considerations of the previous section, we can now compare these results to the expectations derived from the CP scheme of CaPd_2 (Figure 5.2f). The key features of the CP scheme are large positive pressures between the Ca atoms, negative pressures along the Ca-Pd contacts, and essentially zero pressure between the Pd atoms. This suggests that the force constants should increase in the order of Ca-Pd < Pd-Pd < Ca-Ca. Also given the smaller mass of Ca over Pd, we would expect that the highest frequency modes would involve mainly Ca-Ca contacts.

The phonon DOS distribution, however, gives quite a different ordering of frequencies: soft Pd-Pd modes < Ca-Pd, Ca-Ca modes < hard Pd-Pd modes. This difference clearly indicates that there is a problem with the current CP scheme of CaPd_2 . For example, it is difficult to see how the highest frequency phonon modes could be dominated by Pd atoms when their CP features are entirely negative or neutral. Evidently, some adjustment to the method is necessary to bring the CP scheme in line with the phonon band structure.

One place where refinements to the method are possible is in the use of electron density profiles for isolated atoms to model the influence of each atom on its surroundings. These profiles neglect the inevitable differences in the electronic structure of an atom that result from moving it from empty space to a condensed phase environment. These differences are perhaps most significant for cases where atoms of disparate electronegativities are combined, as in CaPd_2 , because it ignores the effects of ionic charge transfer. For CaPd_2 , a Bader charge analysis⁴⁸ gives charges of +1.33 and -0.66 for Ca and Pd, respectively.

Thus our use of neutral electron density profiles for cationic Ca and anionic Pd likely over- and underestimate their effective sizes, respectively.

To explore how these charges might affect the CP analysis, we carried out all-electron DFT calculations on free Ca and Pd ions with a range of charges, running from zero to the full Bader charges of CaPd_2 . As seen in Figure 5.5, the introduction of charges to the free atoms has systematic effects on the radial electron density profiles. Removing electrons from Ca atoms leads to the contraction of their profiles, since the remaining electrons feel a stronger pull toward the nucleus. This should then decrease the extent of its spatial influence in the interpretation of the CP map. For Pd atoms, adding electrons to create anionic character leads to the reverse: the expansion of the profile, which would create a longer-range influence in the CP map.

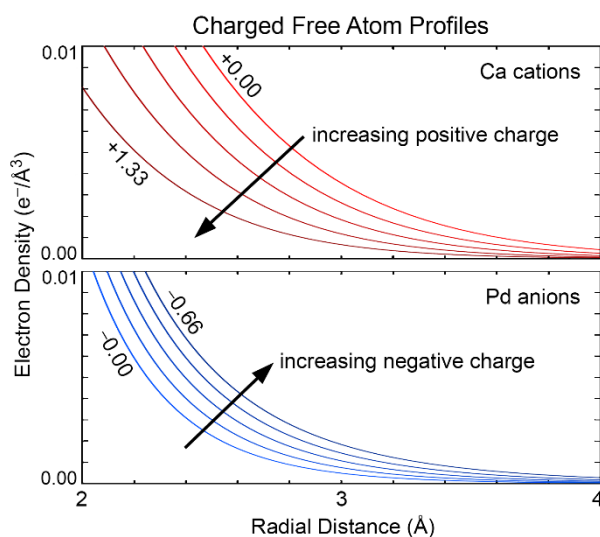


Figure 5.5. The effect of charge on the electron density profiles for Ca and Pd used in the Hirshfeld-inspired CP integration scheme. (a) The introduction of positive charge on the Ca atom causes the profile to decay more quickly with distance from the nucleus. (b) Making the Pd anionic has the opposite effect, making its profile more diffuse.

In Figure 5.6a, we explore how using these charged electron density profiles in the interpretation of the CP map influences the resulting CP scheme. Upon introducing a small degree of ionicity (25% of the Bader charges), the distribution of positive and negative CPs is nearly unchanged; the major effect is the growth of negative CPs along the Ca-Pd contacts. As we increase the ionicity to 50%, this trend continues and is joined by the appearance of positive CPs along the Pd-Pd contacts. Going to 75%, however, creates a sudden change: the positive Ca-Ca CP lobes of the previous images have been replaced by equally large negative lobes.

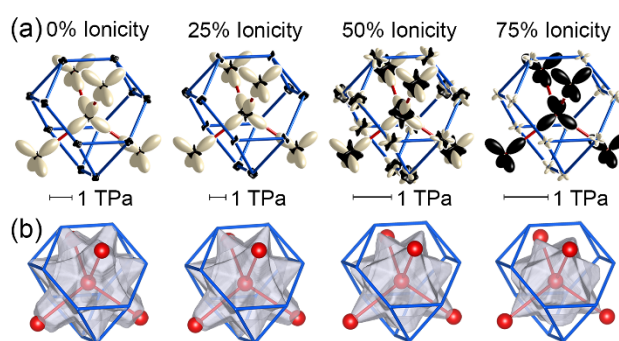


Figure 5.6. The role played by ionic charge in the integrated CP scheme of CaPd₂. (a) CP schemes calculated for CaPd₂ using electron density profiles of Ca and Pd ions with charges ranging from 0% to 75% of those obtained from a Bader analysis of the phase. Note the drastic change in the results between ionicity values of 50% and 75%. (b) The sum of all contact volumes around the central Ca atom for the same series of ionicity values. Critical differences in the CP scheme correlate with the differing extents that these volumes reach into the core regions of the neighboring atoms.

This progression of CP schemes can be understood from a simple comparison of the contact volumes at each ionicity value (Figure 5.6b). Shown in gray is the boundary surface of the sum of the contact volumes between the central Ca atom and its neighbors. Without any ionicity applied to the profiles, the

volume completely extends to envelop a quarter-share of the cores of the Ca neighbors and a substantial portion of those of the Pd neighbors. As a result, the positive pressures concentrated near atomic cores are being dominated by contact volumes involving Ca atoms. It is unsurprising then that no positive CP is seen along Pd-Pd contacts here.

As the ionicity is increased, the Ca atom's shrinking range of influence is evident in the contact volumes. At the 25% ionicity level, the boundaries have been pulled in slightly toward the central Ca atom, leading to a qualitatively similar but smaller domain. This contraction continues as we move to 50%, where the surface has receded to the point that it no longer fully surrounds the Pd centers. Pd-Pd positive pressures thus start to appear in the CP scheme. By 75% ionicity, the Ca cation has become effectively so small that its contact volumes do not even reach to the centers of the other Ca atoms. The Ca-Ca and Ca-Pd contact volumes both capture only the negative background pressures in the spaces between atoms and essentially none of the positive pressure associated with the neighbors' cores; the resulting CP scheme is similar to that obtained earlier using geometric contact volumes (Figure 5.2e).

Comparison of these CP scheme results to the phonon DOS distribution offers the opportunity to assign an effective ionicity to the CaPd_2 structure. The order of phonon frequencies in Figure 5.4 followed as: soft Pd-Pd motions < Ca-Pd, Ca-Ca motions < hard Pd-Pd motions. In choosing an ionicity which matches this arrangement, it appears that including too much and too little ionicity leads to opposite problems. For example, the use of high ionicity predicts that the Ca-Ca vibrations will have extremely low frequencies, while the low ionicity CP scheme suggests that the Ca-Ca motions will have high frequencies. Some intermediate value of the ionicity could then be expected to balance these two extremes. The best fit with our expectations from the phonon spectrum would then lie somewhere between 50% and 75% of

the total Bader charges. By scanning that region more closely, we found that the agreement is optimized in this case for an ionicity level of 55% (Figure 5.7a).

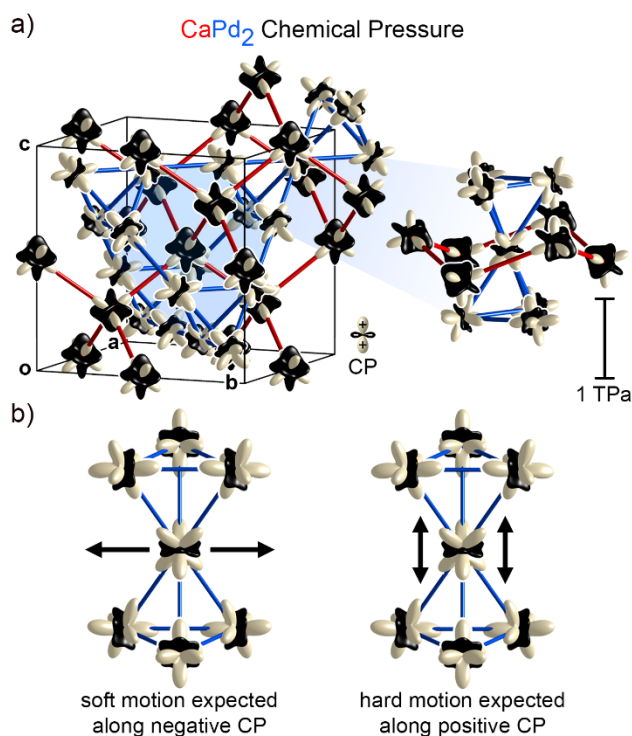


Figure 5.7. The CP scheme of CaPd_2 obtained using an ionicity calibrated against the phonon DOS distribution (55% of the total Bader charges). (a) The unit cell, highlighting the coordination environment of a single Pd atom. (b) Predictions of the soft and hard motions of the Pd atoms derived from the CP scheme.

This final CP scheme makes it clear how Pd motions can dominate both the softest and hardest phonon modes in the DOS: each Pd atom exhibits spatially separated positive and negative CP features. In view of Figure 5.7b, the positive CP lobes appear on each Pd atom directed toward its Pd neighbors above and below, while the negative CP contributions occur as a belt that wraps around the equator of the CP surface, corresponding to interactions with the Ca neighbors. The perpendicular orientations of these

opposite pressures are suggestive of strong anisotropy in the vibrational motions of the Pd atoms, with vertical motions in Figure 5.7b contributing to high-frequency modes, and perpendicular motions belonging to low-frequency ones. In the next section, we will see how these and similar considerations can be used to make sense of the 18 phonon bands of the system.

5.6. Chemical Pressure in the interpretation of phonon frequencies

Now that we have calibrated CaPd₂'s DFT-CP scheme against the general features of its phonon DOS, let's examine how the CP scheme elucidates the individual phonon modes of the phase. As a first step, it is useful to compare the phonon DOS and band structure (Figure 5.4) to see which modes are needed to form a representative set. The vibrations at the Γ -point (0 0 0) are particularly advantageous in this regard: not only do they transform as irreducible representations of the full point symmetry of the structure, but also their frequencies align well with the major peaks in the DOS curve. As such, we will focus our discussion on how the atomic motions in these modes compare with the features of the CP scheme.

To make this comparison, we plot in Figure 5.8 the atomic motions for the optical modes at Γ , with the relative motions of the atoms indicated with yellow arrows. These arrows are overlaid on the CP scheme of the phase, so that the direction of motion can be easily correlated with the CP lobes along those directions. First in the band structure at Γ is a triply-degenerate set at 0 THz. These modes are the Γ -component of the acoustic bands, corresponding to the translation of the whole crystal along the a , b , and c axes; as such these modes are not shown in the figure.

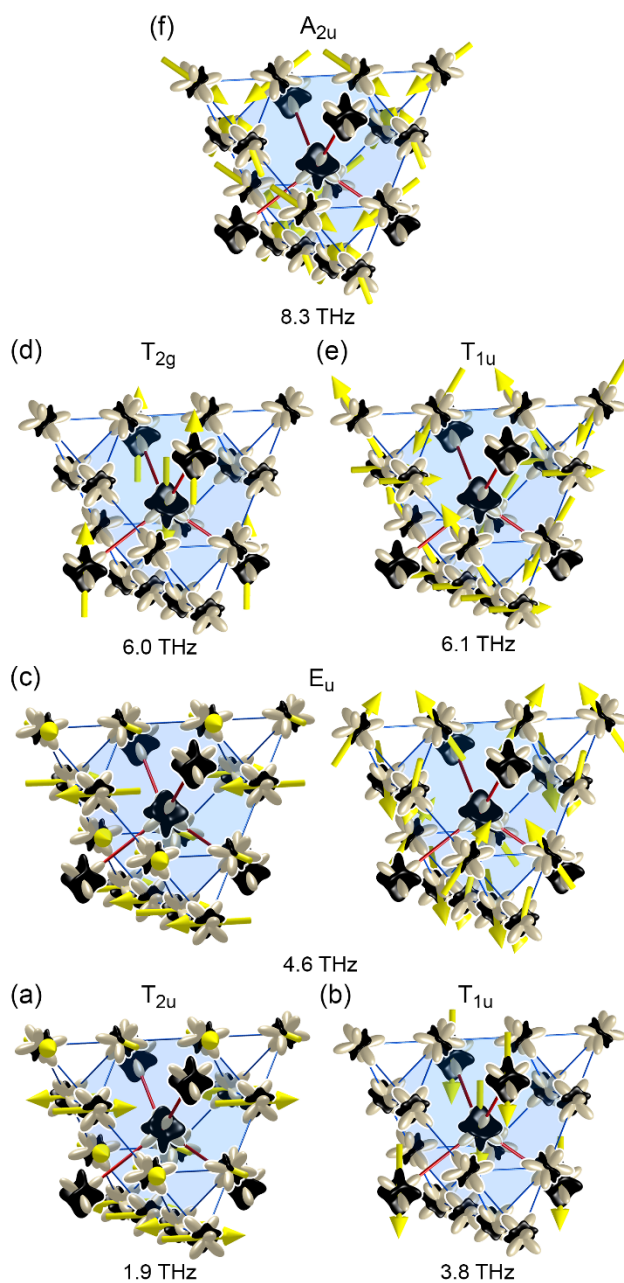


Figure 5.8. The movement of the atoms in CaPd_2 for each of the optical modes at Γ , overlaid onto the CP scheme. The direction and relative amplitudes of the atomic motions are shown by yellow arrows. Note that in the low-frequency modes (a-c) the arrows align exclusively with negative CP features, whereas they become increasingly directed along positive CP features in the higher-frequency modes (d-f). For clarity, motions whose relative amplitudes are smaller than the yellow arrow heads of the vectors have been omitted.

The first non-trivial vibrations are the three optical modes (Figure 5.8a) at 1.9 THz. These vibrations involve motions exclusively of the Pd atoms, as is anticipated by the DOS. The relative motions here can be easily interpreted when we recall that the Pd sublattice is formed from a diamond network of vertex-sharing Pd₄ tetrahedra. This vibrational mode corresponds to the twisting of this network through coupled rotations of the Pd₄ tetrahedra around the *a*, *b*, and *c* lattice vectors.

The location of this mode near the bottom of the band structure can be understood from the alignment of the motions with the CP features of the Pd atoms: the displacements of the individual Pd atoms are along directions of negative CP, soothing some of the overly long Ca-Pd contacts. In addition, these motions are almost orthogonal to the Pd atoms' positive CP lobes; the coupled rotation of the Pd₄ tetrahedra leads to essentially no added strain on the overly-compressed Pd-Pd contacts.

The next three optical modes (Figure 5.8b) at 3.8 THz also exhibit motions only along directions of negative CP: the entire Ca sublattice moves in lockstep along *a*, *b*, or *c* inside a nearly fixed Pd framework (which in fact undergoes a small, uniform counter-motion too small to represent clearly in the plot). These moderately soft modes prevent any already short Ca-Ca distances from contracting and push Ca atoms toward Pd atoms that are overly distant in the equilibrium geometry. The placement of these modes at a higher frequency than the previous set is likely due to the smaller mass of the Ca atoms.

The third set of optical modes (Figure 5.8c) at 4.6 THz is two-fold degenerate and corresponds to two linearly-independent ways of shearing the tetrahedra of the Pd sublattice. In each case, the Pd atoms move along directions of negative pressure, which by itself gives these modes a low frequency, as in the 1.9 THz modes. However, the choreography between neighboring Pd atoms is less elegant here: In the course of travelling along the negative CP directions, some Pd-Pd contacts are contracted.

The character of the phonon modes changes substantially on going from these first three optical frequencies to the fourth at 6.0 THz (Figure 5.8d). The three-fold degenerate modes at this frequency consist of the out-of-phase version of Ca-sublattice motions of Figure 5.8b. Rather than moving in concert, Ca atoms in every other layer along a , b , or c (one for each of the three different members of the degenerate set) are moving in opposite directions inside of a nearly motionless Pd framework. While these motions occur along directions of negative pressure around the Ca atoms, leading to the shortening of some Ca-Pd distances, these motions also have strong components parallel to the positive CP lobes along the Ca-Ca contacts. In fact, linear combinations of these modes can be taken to create ones in which the primary motion is the oscillation of individual Ca-Ca contacts.

At a slightly higher frequency of 6.1 THz, the penultimate triplet of modes mainly involves motions within the Pd sublattice (Figure 5.8e). Here, two Pd atoms in each tetrahedron move in an out-of-phase fashion toward the tetrahedral center, while the remaining two shift in response. The placement of this mode near the top of the phonon band structure can be rationalized by this being the first one in which the displacements of some of the Pd atoms have strong components along positive CP lobes.

The correlation of motions along positive CPs with high frequencies is strikingly illustrated by the last mode at 8.3 THz (Figure 5.8f), which in fact is the highest frequency vibration in the whole band structure. All four Pd atoms in each tetrahedral unit simultaneously oscillate toward or away from the center of the tetrahedron. When they move together into the center, each Pd atom moves along the vector corresponding to the sum of three positive CP lobes on that side of the atom. Similar painful collisions are also encountered on the opposite swing of the vibration when the Pd₄ unit expands: the expansion of one

tetrahedron correlates with the contraction of the four neighbors connected through vertex-sharing in the network.

In summary, the CP scheme of CaPd_2 provides a simple framework for understanding the phonon modes at the Γ point (Figure 5.9). The lowest frequency vibrations correspond to atomic motions that move along directions of negative pressure without significantly squeezing contacts marked by positive CPs. The hardest modes, in contrast, are those that involve atoms moving against positive CPs. Intermediate frequencies in the band structure represent cases where the relationship between the motions and negative or positive CP features is less straightforward. An intriguing correlation here with the DOS features is that the pseudogap at about 5 THz coincides with the separation between lower and higher frequency modes whose major motions are along negative and positive CP features, respectively. This situation mirrors the frequent appearance of bandgaps or pseudogaps in electronic structures at the transitions between bonding and antibonding states.

The CP scheme for CaPd_2 at this point serves as the basis for a simple relationship between its crystal structure and vibrational properties. The packing is frustrated by both the Pd-Pd and Ca-Ca contacts being forced to be shorter than their ideal distances as the structure struggles to provide sufficiently short distances for the Ca-Pd contacts. This leads to the Pd_4 tetrahedra and Ca diamond network being fairly rigid, as distortions of them would lead to enhanced positive pressures along the Pd-Pd and Ca-Ca contacts. However, modes that can shrink some Ca-Pd distances without straining these rigid units are soft, including the coupled rotations of the Pd_4 tetrahedra (in ways reminiscent of the coupled rotations of octahedra in perovskites⁴⁹⁻⁵¹) and the rattling of the Ca sublattice as a whole in the space provided by the Pd sublattice.

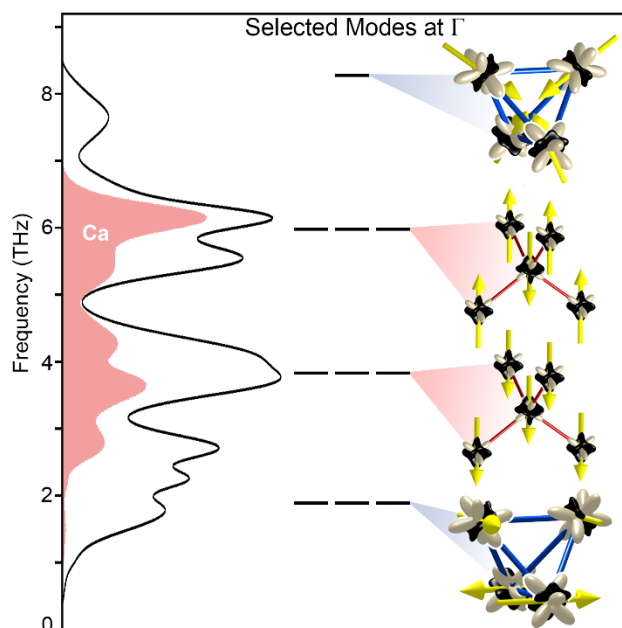


Figure 5.9. The major features of the phonon DOS of CaPd_2 interpreted in terms of the compound's CP scheme and selected phonon modes at the Γ point. Note that the deep pseudogap at ca. 5 THz coincides with the transition between modes with atomic motions along negative CP features and those whose motions exacerbate positive CPs.

This example illustrates the potential of CP analysis to derive structure-property relationships for intermetallic phases. This result in itself, however, is a little cyclical in that the CP scheme was calibrated to reflect certain aspects of the phonon DOS distribution. In the next two sections, we will demonstrate how this approach can be extended to two additional examples without further adjustments to the CP analysis (using simply an ionicity level of 50%): a high-temperature superconductor and a simple structure type whose CP scheme forms the basis for a broad structural diversity. In both of these systems, we will again see soft phonon modes arising from CP distributions that place positive and negative CP features perpendicular to each other, to create d-orbital-like distributions that might be referred to as *CP quadrupoles*.

5.7. Application to the superconductor Nb₃Ge

In our above analysis of CaPd₂, we saw how a CP scheme can provide a visual link between the structural features of a compound and its vibrational properties. One area in which such a connection could support materials design is superconductivity. Phonon-electron coupling plays a key role in this phenomenon, as is formulated in the BCS model,^{52,53} since this coupling allows for the correlated motion of electrons across a material. In the McMillan equation derived from the BCS model, the strength of this coupling is related directly to the phonon DOS: the coupling strength is inversely proportional to the expected mean squared phonon frequency, $\langle\omega^2\rangle$.^{54,55} The presence of low-frequency modes should then influence the potential for superconductivity. To demonstrate how these low-frequency modes are anticipated with CP analysis, we consider the Cr₃Si-type (A15) phase Nb₃Ge, whose T_c of 23 K is one of the highest observed for intermetallic compounds.⁵⁶⁻⁵⁸

Its crystal structure can be described as a body-centered cubic array of Ge atoms, which are surrounded by distorted icosahedra built from the crossing of Nb chains that run along the faces of the unit cell (Figure 5.10). The CP scheme of this compound directly connects these structural features to expectations about where different atomic motions should contribute to the phonon spectrum. The positive pressures within the scheme are localized along the Nb chains, indicating that the Nb-Nb distance of 2.53 Å (in the LDA-DFT optimized structure) is overly short for the degree of bonding between the atoms. This driving force for the expansion of the structure is countered by negative CPs at the remaining near-neighbor contacts, both the Nb-Ge interactions and the remaining Nb-Nb ones.

Overall, the CP distribution around the Nb atoms bears a close similarity to what we saw before in the Pd atoms of CaPd₂: positive CP lobes extend in opposite directions while negative CP features lie in the

perpendicular plane, creating a function reminiscent of a d_{z^2} atomic orbital that reflects a strong quadrupole component to the CP distribution around the Nb atom. As before, this pattern can be expected to underlie low-frequency vibrations (Figure 5.10a): motions of the Nb atom in the direction of negative CP serve not only to shorten some overly-long Nb-Nb or Nb-Ge contacts but also to allow the atom to slide away from its overly close Nb neighbors in the same chain.

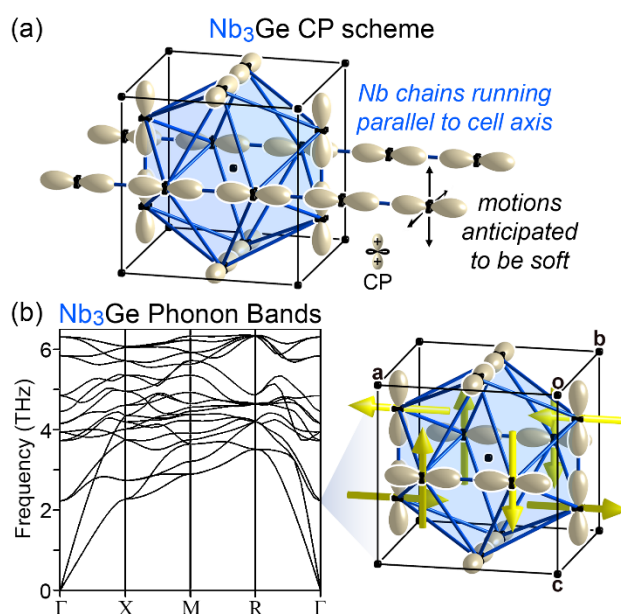


Figure 5.10. The connection between vibrational properties and structure revealed for the Cr_3Si -type superconductor Nb_3Ge using CP analysis. (a) The CP scheme of Nb_3Ge (at an ionicity level of 50%) with schematic illustrations of low-energy atomic motions that it anticipates. (b) The LDA-DFT phonon band structure of Nb_3Ge , along with an illustration of the softest optical mode at Γ overlaid on the CP scheme.

These expectations are borne out by the LDA-DFT phonon band structure (Figure 5.10b), where one optical phonon frequency stands out as being 1.5 THz lower than all others at the Γ point. Overlaying the

atomic displacement vectors for this mode on the CP scheme reveals exactly the anticipated motions. In this three-fold degenerate vibrational level, the Nb atoms vibrate in a transverse fashion relative to the Nb chains, with the motions of Nb neighbors being out-of-phase with each other. For some of the chains, the displacements occur within the faces of the unit cell and predominately lead to transitory stabilization of some overly long Nb-Nb contacts, as occurs in the (010) planes for the mode in Figure 5.10b. In other chains, the motions are perpendicular to the cell faces, as in the (100) planes in Figure 5.10b, along the Nb-Ge negative CPs.

The low frequency vibrational modes of Nb₃Ge can thus be traced to the crowding of the Nb atoms in the chains running along the *a*, *b*, and *c* axes, which prevents the optimization of other interatomic interactions in the structure. This result provides a new interpretation of the role the Nb chains play in the superconductivity of the phase. Whereas previous researchers focused on the influence of short Nb-Nb distances in the electronic DOS distribution,^{58,59} the DFT-CP analysis reveals that they also directly shape the soft phonon modes of the compound.

The visual nature of the CP schemes offers suggestions for how the frequency of these low-lying modes could be influenced by perturbations to the structure. Consider, for example, elemental substitution. Sn atoms are isoelectronic with Ge atoms, but are about 0.18 Å larger in terms of covalent radius. Replacing the Ge atoms in the structure with Sn atoms would lead to Nb-Sn contacts that are less over-extended relative to their original Nb-Ge ones. This CP relief would in turn place less strain on the Nb chains, weakening a key factor in the low frequency of the transverse Nb chain vibrations. In fact, an LDA-DFT phonon band structure on Nb₃Sn indicates that the frequency of these modes is 2.81 THz, 0.59

THz higher than those of Nb₃Ge. Given the desirability of small $\langle\omega^2\rangle$ values for superconductivity, it is not surprising that the T_c of Nb₃Sn is then lower than that of Nb₃Ge: 18 vs. 23 K.^{43,60}

There are, of course, some limits on how soft a phonon mode can get; such softening also enhances a phase's susceptibility to structural phase transitions. Indeed, Nb₃Ge itself is a metastable compound prepared through methods such as chemical vapor deposition,^{61,62} and several other Cr₃Si-type superconductors were found to undergo a martensitic cubic-to-tetragonal phase transition near their critical temperatures.^{63,64} Taken to the extreme, a phonon mode can become so soft that its force constant becomes negative, leading to the frequency being imaginary. Here, following a phonon mode is energetically downhill, meaning that the formation of a superstructure is favorable. In the next section, we will see such a case, illustrating how the dynamic instability of a simple CaCu₅-type structure points towards a diverse structural chemistry.

5.8. Phonons in the CaCu₅ type: a precursor to structural complexity

One of the first applications of the DFT-CP approach was to explain how atomic size effects in CaCu₅-type structures give rise to a wide range of structural derivatives. In that prior work, the structural diversity in these systems was traced to the relief of large negative pressure features the Ca atoms would experience in the hypothetical CaCu₅-type phases CaAg₅ and CaCd₅. Since over the course of this Chapter we have seen a relationship emerge between negative CP and soft-phonon modes, one might wonder to what extent the structural diversity derived from the CaCu₅ type can be connected to its phonon band structure. In this last case study, we will explore this possibility.

The CaCu_5 structure type, exemplified here by CaPd_5 (Figure 5.11a), is built from the alternation of Pd kagome nets and Pd honeycomb nets along the c axis. This alternation leads to a Pd sublattice based on vertex-sharing trigonal bipyramids. The Ca atoms reside in the hexagonal channels that result from this arrangement, each within an 18-coordinate cage of six Pd atoms above, six below, and six in the same plane.

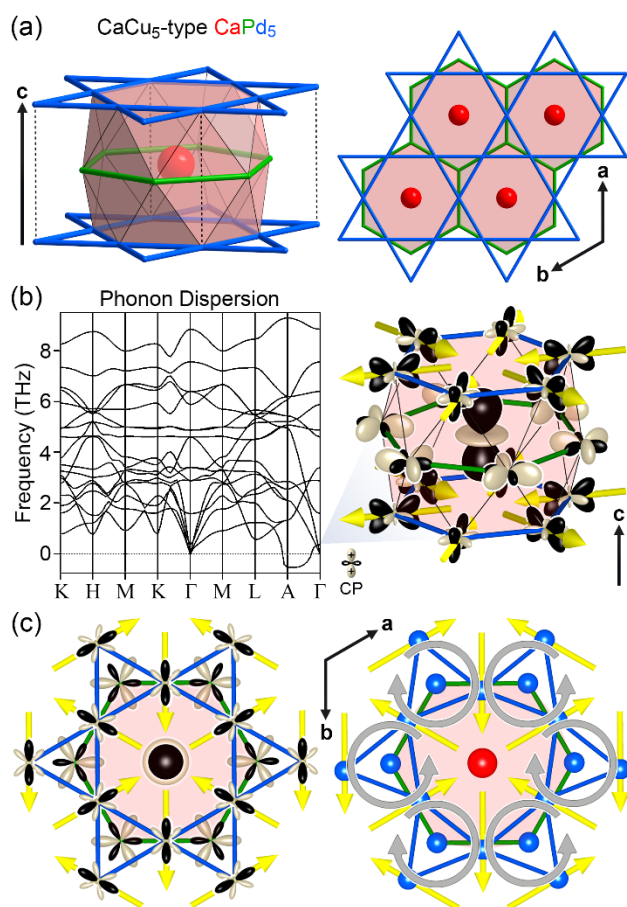


Figure 5.11. Structure-properties relationships derived from CP analysis of the CaCu_5 -type phase CaPd_5 . (a) The crystal structure of CaPd_5 . (b) The phonon band structure reveals an extremely soft phonon mode at Γ (whose frequency becomes imaginary between Γ and A in the Brillouin zone). (c) Overlaying the atomic motions of this soft mode on the CP scheme shows that the coupled rotation of the triangles in the kagome net allow the Pd atoms to travel along directions of negative pressure without straining the overly-short contacts within those triangles.

An intense CP scheme results from this arrangement: the Ca atoms are held in place by equally strong negative pressures to the Pd atoms above and below (see the large black lobes pointing up and down along c in Figure 5.11b). Contraction of the lattice is prevented by positive Ca-Pd pressures along the in-plane contacts, weaker positive CPs between the Pd atoms in the kagome layers, and essentially optimized interactions between the Pd layers.

The CP surfaces on these atoms highlight two motions that should be especially facile: the displacement of the Ca atom up or down along c would allow relief of the negative CPs in the direction of motion while bringing the Ca further from its overly-close Pd neighbors in the plane. Another easy motion would be for a Pd atom in the kagome network to follow one of its CP lobes by moving into the hexagonal opening between the Ca atoms, particularly if the vibration is coupled to that of other Pd atoms in the kagome net to avoid collisions along the Pd-Pd positive CPs.

Between these two possibilities of the Ca or Pd atoms moving, the latter would be predicted to contribute to lower frequencies due to the larger weight of the atoms. In fact, at the Γ point, the first optical phonon modes involving the Pd motion in the kagome net appear at 0.37 THz, just barely above the 0 THz acoustic modes. As is illustrated in Figure 5.11c, this mode corresponds to the coordinated rotation of the Pd triangles in the kagome net. Over the course of this vibration, each Pd atom moves along its axis of maximum negative CP, without the Pd-Pd contacts being significantly affected. The impact of this motion on the Ca atoms is profound: during each swing of the vibration, the symmetry between the six Pd atoms of the kagome net hexagons is broken to create a triangle of three close Pd neighbors for each Ca atom and three more distant ones; these near and distant Pd atoms then switch during the opposite swing.

This motion replaces six overly-long Ca-Pd contacts with three shorter ones, soothing the CPs on the Ca atoms.

This mode becomes even softer if we move away from the Γ point. On following the band from Γ to A ($0\ 0\ \frac{1}{2}$), we see the phonon frequency drop until it reaches $0.53i$ THz (represented as a negative number on the plot) at A. Here, the motions within each kagome layer are identical to those at the Γ point, with the only difference being that the oscillations in the neighboring layers along c are now out-of-phase. The imaginary frequency for this mode arises from the force constant being negative, indicating that following this motion away from the starting geometry is actually stabilizing. These results suggest that any experimentally observed CaCu₅-type CaPd₅ structure would be dynamically unstable at 0 K but could possibly be stabilized by entropic effects at higher temperatures.

The nature of these low frequency modes is closely connected to the observed structural derivatives of the CaCu₅ type that exist in the Ca-Ag and Ca-Cd systems, where the small size of the Ca atoms relative to their coordination environments in the CaCu₅ type would be exacerbated. In Ca₂Ag₇, the large negative CPs on the Ca atoms are relieved by dividing the CaCu₅ type into slabs such that the slab interfaces replace hexagons of Ag atoms above or below the Ca atoms with pairs of Ag atoms at a nearly ideal distance.^{29,30} The Ca coordination environments in Ca₁₄Cd₅₁ are stabilized in a similar way, with hexagons being replaced by Cd pairs or triangles.³⁹ These structural transformations mirror the formation of triangles from hexagons in the low-frequency phonon mode of CaPd₅, though in these cases the stoichiometries are also affected as Ag or Cd atoms are ejected from the structure relative to the original 1:5 stoichiometry.

In summary, a comparison of the CP scheme and phonon spectrum of CaPd₅ reveals how a packing frustration in this structure gives rise to an extremely soft vibrational mode. The character of this mode

hints at the ways in which the local structure of this compound responds to elemental substitutions that intensify the structure's CP scheme. Particularly, on moving from the Ca-Pd to the Ca-Ag or Ca-Cd system, the CaPd_5 structure gives way to the more complicated Ca_2Ag_7 and $\text{Ca}_{14}\text{Cd}_{51}$ structures whose Ca coordination environments have collapsed from 18-coordinate in the CaCu_5 type to 13-, 14-, or 15-coordinate. The shapes for these newly formed polyhedra show strong similarities to the deformations created by the low-frequency mode of CaPd_5 .

5.9. Conclusions

This Chapter has focused on developing a unified picture for two different aspects of solid state structures that are intimately connected but rarely studied together: the driving forces shaping the crystal structure of a material and the factors relating these structures to vibrational properties. We began by proposing that the phonon band structure of a material can serve as a reference for validating the DFT-CP method, a theoretical approach developed for explaining the complex structures of intermetallic phases. The validation of the CP scheme for CaPd_2 then led us to the importance of properly accounting for the ionicity of a crystal structure in dividing the DFT-CP maps between interatomic interactions. Once this calibration was accomplished, the CP schemes of phases such as CaPd_2 , Nb_3Ge , and CaPd_5 opened paths to the interpretation of their phonon modes in terms of local interactions.

Over the course of this work, the ionicity of a system was identified as a key parameter for obtaining physically meaningful CP schemes. It will be interesting to explore how the incorporation of this physical effect can enhance the applicability of the DFT-CP analysis to a broad range of solid state systems. In our applications thus far, we have found that an ionicity value of 50% of the Bader charges typically yields

physically meaningful results (which may be connected to the Bader charge analyses' tendency to overestimate charges⁶⁵). When applying this approach to new systems, however, it will be useful to test the dependence of the CP results on the value of this parameter. In most cases that we have examined, this dependence is slight, but where sharp changes are encountered (as in CaPd_2), comparisons with phonon band structures can serve as a guide.

Another emerging theme of this Chapter has been the ability of a compound's CP scheme to serve as a guide to its phonon frequencies. In particular, atomic motions that move along directions of negative CP without shortening contacts with positive CPs contribute to low-frequency modes, while motions along positive CP features correspond to the highest frequency modes. One situation particularly suited to soft motions is the presence of atomic CP distributions with large quadrupole ($l = 2$) components, such that the surfaces resemble d-orbitals with positive and negative CP features at right angles to each other. In these cases, motions along negative CPs offer not only the temporary contraction of overly-long distances, but also the potential to reduce positive CPs, as was seen with particular clarity in Nb_3Ge .

The importance of these $l=2$ components offers a simple approach to designing low-frequency phonon modes, and perhaps promoting phonon-mediated properties: one can screen crystal structures for those whose CP features show strong quadrupole components, then carry out site substitutions to exacerbate the tension inherent in the CP scheme. For example, replacement of Ge atoms in Nb_3Ge with smaller Si ones should lead to greater conflict between Nb-Nb repulsion and Nb-main group attraction, which would then soften the transverse vibrations along the Nb chains. In fact, the expectation is in-line with the as-of-yet unconfirmed prediction that the T_c of a defect-free Cr_3Si -type Nb_3Si phase could be as high as 35 K.⁶⁶

Overall, the case studies presented here illustrate how CP analysis can provide a conceptual link between the intriguing crystal structures of intermetallic phases and their physical properties. We are looking forward to seeing how this approach can bring new insights to other solid state phenomena involving motions of atoms within crystal structures, such as the plasticity of metals and thermal conductivity.

5.10. Technical procedures

DFT energy map generation. DFT-optimized structures and energies were obtained for CaPd_2 , Nb_3Ge , and CaPd_5 with the Abinit program,⁶⁷⁻⁶⁹ using the Teter 93 LDA exchange-correlation functional⁷⁰ and Hartwigsen-Goedecker-Hutter norm-conserving pseudopotentials.⁷¹ The semicore potential was chosen for Ca because previous experience has shown that the valence-only pseudopotential is not always sufficient, particularly when Ca is significantly cationic.

The three structures were optimized using a two-step procedure: first the ion positions were released in a fixed unit cell, then all geometrical parameters were relaxed simultaneously. Single point energy calculations were performed at the optimized volume and with isotropically expanded and contracted unit cells. The total volume range was 5% of the equilibrium unit cell volume, although the final CP scheme is rarely affected by the exact range as long as it is sufficiently large to avoid errors from numerical noise in the DFT calculations. For each single point calculation, 3D voxel grids of the kinetic energy density, electron density, and local components of the Kohn-Sham potential were output to be used as input data for DFT-CP analysis.

In setting the parameters for the Abinit calculations, the energy cut-offs were chosen such that the energy of formation of the compounds was converged to less than 4 meV per atom, and k-point grids were checked for convergence with respect to the final CP schemes. Additional technical details about the Abinit calculations, such as the specific k-point grids, energy cut-offs, and the coordinates of the optimized geometries, are given in the Supporting Information.

Chemical Pressure map generation. DFT-CP analysis was carried out with our DFT-CP package. The *CPmap* module was used to first combine the potential and density maps from Abinit into total energy maps for the three individual unit cell volumes. Then a chemical pressure map was calculated by taking the negative difference in energy of each voxel between the expanded-volume energy map and the contracted-volume energy map, divided by the difference in voxel volumes. Core unwarping (with tricubic interpolation) was applied to the chemical pressure map to correct for the slight change in absolute position of the voxels relative to the ion cores in the different maps.

Next the *CPintegrate* module was employed to divide the pressure map into contact volumes between atoms, using the Hirshfeld-inspired method as described in the Chapter. The average pressure was taken within each contact volume, and then each atom's contributions to all of the contact volumes around it was projected onto low order, real spherical harmonic functions (up to $l \leq 4$) centered on that atom. Using too few spherical harmonic functions (generally $l \leq 2$) will limit the level of detail that can be resolved from the chemical pressure maps, but using too many functions (generally $l > 6$) complicate the visualization of the CP distributions. The CP scheme plots were prepared by our Matlab application, Figuretool. Contact volume surfaces were visualized with Vesta.⁷²

Calculation of phonon frequencies. For comparison of phonon modes with the expectations of the CP schemes, the phonon band structures of CaPd₂, Nb₃Ge, and CaPd₅ were calculated using the linear response method implemented in the Abinit package.⁷³ First a high-quality wavefunction file was generated at the DFT-optimized geometry, using a Γ -centered k-point grid. The linear response of every atom in all three directions was found by a non-self-consistent calculation at a single q-point (reciprocal space for phonons). One such calculation was performed for a q-point corresponding to each k-point in the reference calculation. The Abinit utilities *mrgddb* and *anaddb* were used to derive the force constants from the linear response calculations. The phonon mode figures were created in Matlab with Figuretool.

Creation of free ion profiles. To obtain atomic charges for the generation of free ion profiles – used by the *CPmap* and *CPintegrate* modules for core unwarping and contact volume determination, respectively – a separate set of calculations was carried out with DFT using the Vienna Ab initio Simulation Package (VASP).^{74,75} GGA-PAW potentials⁷⁶ provided with the package were used for geometry optimization and charge analysis in the high precision mode. Core electron densities were output by VASP and used as reference input by the Bader program,⁷⁷⁻⁸⁰ with which the charge analysis was performed.

Once the total Bader charges were determined for each element in the structure (using an average over the two symmetry-distinct Pd sites in CaPd₂, whose charges were very similar), radial electron density profiles were generated by the Atomic Pseudopotential Engine (APE)⁸¹ for neutral atoms, ions at the full Bader charges, and ions at charges between these two extremes. For highly charged free anions, the convergence of the all-electron DFT wavefunctions was not always stable, but this could sometimes be addressed by turning using linear mixing or lowering the mixing parameter. However, we found that the

profiles calculated with a mixing parameter lower than about 0.03 were unreliable. Additional details are available in the Supporting Information.

Acknowledgements

We thank Yiming Guo, Katerina Hilleke, Daniel Kikuchi, Brandon Kilduff, and Vincent Yannello for insightful conversations regarding CP analysis. We also gratefully acknowledge the financial support of the National Science Foundation (NSF) through Grant DMR-1508496. This research involved calculations using computer resources supported by NSF grant CHE-0840494.

5.11. References

- (1) Slack, G. A. In *Thermoelectric Handbook*; Rowe, M., Ed.; CRC Press: Boca Raton, 1995, p 407.
- (2) Nolas, G. S.; Weakley, T. J. R.; Cohn, J. L. *Chem. Mater.* **1999**, *11*, 2470.
- (3) Nolas, G. S.; Kaeser, M.; Littleton, R. T.; Tritt, T. M. *Appl. Phys. Lett.* **2000**, *77*, 1855.
- (4) Nolas, G. S.; Lin, X.; Martin, J.; Beekman, M.; Wang, H. *J. Electron. Mater.* **2009**, *38*, 1052.
- (5) Mi, J.-L.; Christensen, M.; Nishibori, E.; Iversen, B. B. *Phys. Rev. B* **2011**, *84*, 064114.
- (6) Pailhès, S.; Euchner, H.; Giordano, V. M.; Debord, R.; Assy, A.; Gomès, S.; Bosak, A.; Machon, D.; Paschen, S.; de Boissieu, M. *Phys. Rev. Lett.* **2014**, *113*, 025506.
- (7) Higgins, J. M.; Schmitt, A. L.; Guzei, I. A.; Jin, S. *J. Am. Chem. Soc.* **2008**, *130*, 16086.
- (8) Vineis, C. J.; Shakouri, A.; Majumdar, A.; Kanatzidis, M. G. *Adv. Mater.* **2010**, *22*, 3970.
- (9) Kim, S. I.; Lee, K. H.; Mun, H. A.; Kim, H. S.; Hwang, S. W.; Roh, J. W.; Yang, D. J.; Shin, W. H.; Li, X. S.; Lee, Y. H.; Snyder, G. J.; Kim, S. W. *Science* **2015**, *348*, 109.

- (10) Zhao, L.-D.; Lo, S.-H.; Zhang, Y.; Sun, H.; Tan, G.; Uher, C.; Wolverton, C.; Dravid, V. P.; Kanatzidis, M. G. *Nature* **2014**, *508*, 373.
- (11) Zeier, W. G.; Pei, Y.; Pomrehn, G.; Day, T.; Heinz, N.; Heinrich, C. P.; Snyder, G. J.; Tremel, W. *J. Am. Chem. Soc.* **2013**, *135*, 726.
- (12) Xiao, C.; Xu, J.; Cao, B.; Li, K.; Kong, M.; Xie, Y. *J. Am. Chem. Soc.* **2012**, *134*, 7971.
- (13) Schmitt, D. C.; Haldolaarachchige, N.; Xiong, Y.; Young, D. P.; Jin, R.; Chan, J. Y. *J. Am. Chem. Soc.* **2012**, *134*, 5965.
- (14) Biswas, K.; He, J.; Blum, I. D.; Wu, C.-I.; Hogan, T. P.; Seidman, D. N.; Dravid, V. P.; Kanatzidis, M. G. *Nature* **2012**, *489*, 414.
- (15) Schwarz, U.; Wosylus, A.; Rosner, H.; Schnelle, W.; Ormeci, A.; Meier, K.; Baranov, A.; Nicklas, M.; Leipe, S.; Müller, C. J.; Grin, Y. *J. Am. Chem. Soc.* **2012**, *134*, 13558.
- (16) Duman, S.; Tütüncü, H. M. *J. Appl. Phys.* **2012**, *111*, 033514.
- (17) Xie, Y.; Oganov, A. R.; Ma, Y. *Phys. Rev. Lett.* **2010**, *104*, 177005.
- (18) Thalmeier, P. *J. Phys. C: Solid State Phys.* **1984**, *17*, 4153.
- (19) Paolasini, L.; Hennion, B.; Panchula, A.; Myers, K.; Canfield, P. *Phys. Rev. B* **1998**, *58*, 12125.
- (20) Feder, D.; Nowik, I. *J. Magn. Magn. Mater.* **1979**, *12*, 149.
- (21) Seh, M.; Nowik, I. *J. Magn. Magn. Mater.* **1981**, *22*, 239.
- (22) Atteberry, J. E.; Leisure, R. G.; Foster, K.; Skripov, A. V. *J. Phys.: Condens. Matter* **2004**, *16*, 8421.
- (23) Mazzolai, G.; Coluzzi, B.; Biscarini, A.; Mazzolai, F. M.; Tuissi, A.; Agresti, F.; Principi, G.; Lo Russo, S. *Mater. Sci. Eng., A* **2009**, *521–522*, 139.
- (24) Chu, F.; Pope, D. P.; Siegl, R. In *Alloy Modeling and Design*; Stocks, G. M., Turchi, P. E. A., Eds.; TMS: Warrendale, 1994, p 249.
- (25) Thoma, D. J.; Chu, F.; Wills, J. M.; Mitchell, T. E. *Mat. Res. Soc. Symp. Proc.* **1997**, *460*, 689.
- (26) Chu, F.; Thoma, D. J.; Mitchell, T. E.; Lin, C. L.; Šob, M. *Philos. Mag. B* **1998**, *77*, 121.

- (27) Euchner, H.; Mihalkovič, M.; Gähler, F.; Johnson, M. R.; Schober, H.; Rols, S.; Suard, E.; Bosak, A.; Ohhashi, S.; Tsai, A. P.; Lidin, S.; Gomez, C. P.; Custers, J.; Paschen, S.; de Boissieu, M. *Phys. Rev. B* **2011**, *83*, 144202.
- (28) Štrof, J.; Pavlů, J.; Wdowik, U. D.; Buršík, J.; Šob, M.; Vřešťál, J. *Calphad* **2014**, *44*, 62.
- (29) Fredrickson, D. C. *J. Am. Chem. Soc.* **2011**, *133*, 10070.
- (30) Fredrickson, D. C. *J. Am. Chem. Soc.* **2012**, *134*, 5991.
- (31) Engelkemier, J.; Berns, V. M.; Fredrickson, D. C. *J. Chem. Theory Comput.* **2013**, *9*, 3170.
- (32) Berns, V. M.; Engelkemier, J.; Guo, Y.; Kilduff, B. J.; Fredrickson, D. C. *J. Chem. Theory Comput.* **2014**, *10*, 3380.
- (33) Nielsen, O. H.; Martin, R. M. *Phys. Rev. B* **1985**, *32*, 3780.
- (34) Ziesche, P.; Gräfenstein, J.; Nielsen, O. H. *Phys. Rev. B* **1988**, *37*, 8167.
- (35) Godfrey, M. J. *Phys. Rev. B* **1988**, *37*, 10176.
- (36) Filippetti, A.; Fiorentini, V. *Phys. Rev. B* **2000**, *61*, 8433.
- (37) Rogers, C. L.; Rappe, A. M. *Phys. Rev. B* **2002**, *65*, 224117.
- (38) Berns, V. M.; Fredrickson, D. C. *Inorg. Chem.* **2013**, *52*, 12875.
- (39) Berns, V. M.; Fredrickson, D. C. *Inorg. Chem.* **2014**, *53*, 10762.
- (40) Fulfer, B. W.; McAlpin, J. D.; Engelkemier, J.; McCandless, G. T.; Prestigiacomo, J.; Stadler, S.; Fredrickson, D. C.; Chan, J. Y. *Chem. Mater.* **2014**, *26*, 1170.
- (41) Fredrickson, R. T.; Guo, Y.; Fredrickson, D. C. *J. Am. Chem. Soc.* **2016**, *138*, 248.
- (42) Carpenter, J. H.; Searcy, A. W. *J. Am. Chem. Soc.* **1956**, *78*, 2079.
- (43) Testardi, L. R.; Wernick, J. H.; Royer, W. A. *Solid State Commun.* **1974**, *15*, 1.
- (44) Mejbar, J.; Notin, M. *Scr. Metall. Mater.* **1990**, *24*, 1697.
- (45) Dwight, A. E. *Trans. Am. Soc. Met.* **1961**, *53*, 479.

- (46) Greenwood, N. N.; Earnshaw, A. *Chemistry of the Elements*; 2nd ed.; Butterworth-Heinemann: Oxford, 1997.
- (47) Hirshfeld, F. L. *Theoret. Chim. Acta* **1977**, *44*, 129.
- (48) Bader, R. F. W.; Henneker, W. H.; Cade, P. E. *J. Chem. Phys.* **1967**, *46*, 3341.
- (49) Glazer, A. *Acta Crystallogr. B* **1972**, *28*, 3384.
- (50) Benedek, N. A.; Fennie, C. J. *J. Phys. Chem. C* **2013**, *117*, 13339.
- (51) Li, X.; Benedek, N. A. *Chem. Mater.* **2015**, *27*, 2647.
- (52) Bardeen, J.; Cooper, L. N.; Schrieffer, J. R. *Phys. Rev.* **1957**, *108*, 1175.
- (53) Bardeen, J.; Cooper, L. N.; Schrieffer, J. R. *Phys. Rev.* **1957**, *106*, 162.
- (54) McMillan, W. L. *Phys. Rev.* **1968**, *167*, 331.
- (55) Dynes, R. C. *Solid State Commun.* **1972**, *10*, 615.
- (56) Tsuei, C. C. *Phys. Rev. B* **1978**, *18*, 6385.
- (57) Kwo, J.; Orlando, T. P.; Beasley, M. R. *Phys. Rev. B* **1981**, *24*, 2506.
- (58) Stewart, G. R. *Physica C* **2015**, *514*, 28.
- (59) Weger, M. *Rev. Mod. Phys.* **1964**, *36*, 175.
- (60) Geller, S.; Matthias, B. T.; Goldstein, R. *J. Am. Chem. Soc.* **1955**, *77*, 1502.
- (61) Haruki, K.; Kyoji, T. *Jpn. J. Appl. Phys.* **1977**, *16*, 2037.
- (62) Asano, T.; Tanaka, Y.; Tachikawa, K. *Cryogenics* **1985**, *25*, 503.
- (63) Batterman, B. W.; Barrett, C. S. *Phys. Rev. Lett.* **1964**, *13*, 390.
- (64) Weger, M.; Goldberg, I. B. In *Solid State Physics*; Ehrenreich, H., Seitz, F., David, T., Eds.; Academic Press: Cambridge, 1974; Vol. 28.
- (65) Fonseca Guerra, C.; Handgraaf, J.-W.; Baerends, E. J.; Bickelhaupt, F. M. *J. Comput. Chem.* **2004**, *25*, 189.

- (66) Geller, S. *Appl. Phys.* **1975**, 7, 321.
- (67) Gonze, X.; Beuken, J. M.; Caracas, R.; Detraux, F.; Fuchs, M.; Rignanese, G. M.; Sindic, L.; Verstraete, M.; Zerah, G.; Jollet, F.; Torrent, M.; Roy, A.; Mikami, M.; Ghosez, P.; Raty, J. Y.; Allan, D. C. *Comput. Mater. Sci.* **2002**, 25, 478.
- (68) Gonze, X.; Rignanese, G. M.; Verstraete, M.; Beuken, J. M.; Pouillon, R.; Caracas, R.; Jollet, F.; Torrent, M.; Zerah, G.; Mikami, M.; Ghosez, P.; Veithen, M.; Raty, J. Y.; Olevano, V.; Bruneval, F.; Reining, L.; Godby, R.; Onida, G.; Hamann, D. R.; Allan, D. C. *Z. Kristallogr.* **2005**, 220, 558.
- (69) Gonze, X.; Amadon, B.; Anglade, P. M.; Beuken, J. M.; Bottin, F.; Boulanger, P.; Bruneval, F.; Caliste, D.; Caracas, R.; Côté, M.; Deutsch, T.; Genovese, L.; Ghosez, P.; Giantomassi, M.; Goedecker, S.; Hamann, D. R.; Hermet, P.; Jollet, F.; Jomard, G.; Leroux, S.; Mancini, M.; Mazevet, S.; Oliveira, M. J. T.; Onida, G.; Pouillon, Y.; Rangel, T.; Rignanese, G. M.; Sangalli, D.; Shaltaf, R.; Torrent, M.; Verstraete, M. J.; Zerah, G.; Zwanziger, J. W. *Computer Phys. Comm.* **2009**, 180, 2582.
- (70) Goedecker, S.; Teter, M.; Hutter, J. *Phys. Rev. B* **1996**, 54, 1703.
- (71) Hartwigsen, C.; Goedecker, S.; Hutter, J. *Phys. Rev. B* **1998**, 58, 3641.
- (72) Momma, K.; Izumi, F. *J. Appl. Crystallogr.* **2011**, 44, 1272.
- (73) Giannozzi, P.; de Gironcoli, S.; Pavone, P.; Baroni, S. *Phys. Rev. B* **1991**, 43, 7231.
- (74) Kresse, G.; Furthmüller, J. *Phys. Rev. B* **1996**, 54, 11169.
- (75) Kresse, G.; Furthmüller, J. *Comput. Mater. Sci.* **1996**, 6, 15.
- (76) Kresse, G.; Joubert, D. *Phys. Rev. B* **1999**, 59, 1758.
- (77) Henkelman, G.; Arnaldsson, A.; Jónsson, H. *Comput. Mater. Sci.* **2006**, 36, 354.
- (78) Sanville, E.; Kenny, S. D.; Smith, R.; Henkelman, G. *J. Comp. Chem.* **2007**, 28, 899.
- (79) Tang, W.; Sanville, E.; Henkelman, G. *J. Phys.: Condens. Matter* **2009**, 21, 084204.
- (80) Yu, M.; Trinkle, D. R. *J. Chem. Phys.* **2011**, 134, 064111.
- (81) Oliveira, M. J. T.; Nogueira, F. *Comput. Phys. Commun.* **2008**, 178, 524.

Chapter 6.

Electronic and Chemical Pressure Effects on the Stability Range of Intermetal-

lic Intergrowths: Pushing the Limits of the HoCoGa₅ Type with ScTGa₅

(T = Fe, Co, Ni)

This chapter is in preparation for publication: Engelkemier, J.; Green, L.; McDougald, R. N.; Chan, J. Y.; Fredrickson, D. C. Engelkemier and Fredrickson contributed the theoretical and structural analyses. Synthesis, crystallography, and resistance measurements are by Green, McDougald, and Chan.

6.1. Abstract

The immense structural diversity of Ln-T-E systems (Ln = lanthanide or similar early d-block element, T = transition metal, E = p-block element) offers opportunities for the observation of intriguing physical properties (e.g. magnetically mediated superconductivity and heavy fermion effects) but also the challenge of understanding how their structures can be guided for the optimization of these properties. In this Chapter, we explore the factors stabilizing one member of this family: the HoCoGa₅ structure type, comprising AuCu₃-type LnGa₃ slabs intergrown with fluorite-type TGa₂ layers. We begin by probing the boundaries of its stability range through the growth and characterization of single crystals of ScTGa₅ (T = Fe, Co, Ni), where Sc represents the smallest possible Ln-like atom, and the series over T provides variability in terms of electron count. After confirming that these compounds adopt the HoCoGa₅ type and exhibit metallic

conductivity, we analyze their electronic structure using density functional theory (DFT) and DFT-calibrated Hückel calculations. Through these analyses, the observed electron count range of the HoCoGa₅ type is explained in terms of the 18-*n* rule, with *n* = 6 for the Sc atoms and *n* = 2 for the T sites. To account for the stability range with respect to atomic size, we carried out DFT-Chemical Pressure (DFT-CP) analysis on ScNiGa₅. Its CP scheme displays negative pressures between the Ga atoms resulting from stretching of the Ga sublattice to accommodate the space requirements of the Sc and T atoms, which is consistent with HoCoGa₅-type gallides only being observed when the Ln and T sites are occupied by relatively small atoms. From these conclusions, transitions to the related BaMg₄Si₃ and Ce₂NiGa₁₀ structure types at the edges of the HoCoGa₅-type stability range are rationalized, demonstrating how the 18-*n* bonding scheme and CP concept can be used together to guide our understanding of Ln-T-E systems.

6.2. Introduction

Since Hume-Rothery's foundational work on metals and alloys, it has been understood that the same factors govern the structures of both molecular and intermetallic compounds: electron counts, atomic sizes, and electronegativity differences.¹ However, while the steric, electronic, and electrostatic requirements of different molecular geometries are relatively well-understood, most metallic structures represent a larger challenge. Empirical observations often correlate the appearance of individual crystal structures to particular ranges of atomic size ratios and electron concentrations, as can be concisely represented with structure maps. One goal of designing metallic structures is to understand how the features of these structures lead to their locations in such maps. In this Chapter, we will illustrate how combining experiment

with recently developed theoretical methods can bring this understanding to a ternary structure of importance for its ability to support superconductivity: the HoCoGa_5 type.

This structure type is one of a multitude that arises in Ln-T-E systems (Ln = lanthanide or similar early d-block element, T = transition metal, E = p-block element), which represent some of the richest sources of truly ternary phases (where various elements have distinct coordination environments).² For example, the phase diagram for Sc-Co-Ga, one of the systems to be considered here, lists 15 separate ternary compounds – treacherous waters for those who would seek to navigate it with chemical principles.

And yet, there are prospects of unique physical properties that might be revealed if the ability to guide the structures of these phases is acquired: the homologous series $\text{Ce}_m\text{TIn}_{3m+2}$ (T = Co, Rh, Ir) has already offered novel mechanisms of superconductivity. Their structures can be viewed in terms of simple intergrowths of m -unit cell thick slabs of AuCu₃-type CeIn_3 with single layers of fluorite-type (or PtHg₂-type) TIn_2 layers. The CeIn_3 ³ ($m = \infty$) end member was the first Ce-based magnetically mediated superconductor to be discovered ($T_N = 10$ K; $T_c = 2.3$ K).^{4,5} CeCoIn_5 ⁶ and CeIrIn_5 ⁷ ($m = 1$) are ambient superconductors below 2.3 K and 0.4 K, respectively,^{8,9} while the isostructural CeRhIn_5 ⁷ is superconducting under applied pressure ($T_c = 2.1$ K).¹⁰ Antiferromagnetic Ce_2RhIn_8 ¹¹ ($m = 2$), meanwhile, is likewise superconducting under applied pressure with a T_c of 2 K.¹² Open questions are what factors stabilize the different members of the series, and to what extent the details of the intergrowth influence their properties.

The analogous gallides have not been as thoroughly explored for superconductivity, in part because there are no known Ce-containing homologues. For instance, while the HoCoGa_5 -type structure ($m = 1$) forms for indides with practically all lanthanides, the corresponding gallides have been observed only for the late lanthanides. The formation of gallides with the Ho_2CoGa_8 -structure type ($m = 2$) appears to be

similarly restricted.¹³ This inability to realize a whole series of gallium analogues to the $\text{Ln}_m\text{TIn}_{3m+2}$ series – not to mention the trends in properties that they might exhibit – highlights the need for understanding of how atomic size and electron count together influence the stability of intermetallic structures.

In this Chapter, we present a combined experimental and theoretical exploration of the stability range of the HoCoGa_5 type. First we report single crystal structure solutions and electrical resistivity measurements for ScTGa_5 ($\text{T} = \text{Fe}, \text{Co}, \text{Ni}$), which extends the range of HoCoGa_5 -type gallides that have been structurally characterized. Through the identity of the T element, we also synthetically scan the structural stability with respect to electron concentration.

We then present the results of two separate but complimentary theoretical methods: reversed approximation Molecular Orbital (raMO) analysis to explain the observed electron count range in terms of the $18-n$ rule,^{14,15} and Density Functional Theory-Chemical Pressure (DFT-CP) analysis¹⁶⁻¹⁸ to understand the effect of atomic size on the stability range of the rare earth elements. Finally, we make connections with other, more complex gallides and elucidate the competing factors that mark the boundaries of stability for each structure type, using the principles gleaned from examining the simpler HoCoGa_5 -type phases.

6.3. Experimental

Synthesis. Single crystals of ScTGa_5 ($\text{T} = \text{Fe}, \text{Co}, \text{Ni}$) were made from their constituent elements by the self-flux growth method. Metals with lower melting points, such as gallium, can be used as the flux material, which enables metals with higher melting points to dissolve at lower temperatures.¹⁹⁻²² Sc (granules, 99.9%), T = Fe, Co, Ni (powder, 99.98%), and Ga (shot, 99.999%) were used as received. Sc, T, and

Ga were placed in an alumina crucible in a molar ratio of 1:1:20, topped with a second, inverted alumina crucible containing quartz wool, backfilled with about $\frac{1}{3}$ atm of Ar, and sealed in a fused silica tube. The sealed vessels were heated to 1150 °C at a rate of 50 °C/h and held at that temperature for 72 hours, then cooled to 550 °C at a rate of 4 °C/h. Samples were then removed from the furnace, inverted, and centrifuged in order to separate the excess Ga flux from the single crystals. Residual Ga flux on the surface of the single crystals was removed by repeated sonication in hot water.

Structure determination. Single crystal X-ray diffraction data were collected on single crystal fragments of ScTGa_5 ($T = \text{Fe, Co, Ni}$). The fragments were cut into suitable sizes and mounted on glass fibers using a two-part epoxy. Data sets were collected on a Bruker D8 Quest Kappa single crystal X-ray diffractometer equipped with an I μ S microfocus Mo $K\alpha_1$ radiation source ($\lambda = 0.71073 \text{ \AA}$) operating at 50 kV and 1 mA, a HELIOS optics monochromator, and a CMOS detector. The collected data were corrected for absorption using the Bruker program SADABS (multi-scan method). Each dataset was indexed to a primitive tetragonal cell with dimensions of $a \approx 4.1 \text{ \AA}$ and $c \approx 6.6 \text{ \AA}$.

The systematic absences were consistent with the $P4/mmm$ space group of the HoCoGa_5 structure type. Initial models of the crystal structure were first obtained using SIR2008 (part of the IL MILIONE structure determination and refinement package)²³ and refined using SHELXL2014.²⁴

After examining the data sets collected for each of the ScTGa_5 analogues, large disagreeable reflections were identified in the refinement files for the model of the Fe analogue. Therefore, we chose to use the OMIT command to remove five reflections from the ScFeGa_5 model, which resulted in a model statically similar to that of ScCoGa_5 and ScNiGa_5 . The single crystal X-ray diffraction data collection and refined parameters for ScTGa_5 ($T = \text{Fe, Co, Ni}$) are provided in Table 6.1. The atomic positions, Wyckoff site

symmetries, and atomic displacement parameters for the samples are given in Table 6.2. Table 6.3 contains selected interatomic distances.

Table 6.1. Crystallographic parameters for ScTGa₅ (T = Fe, Co, Ni); Space group: *P4/mmm*, Z=1

	ScFeGa ₅	ScCoGa ₅	ScNiGa ₅
<i>a</i> (Å)	4.1367(7)	4.1290(11)	4.1466(6)
<i>c</i> (Å)	6.64220(17)	6.6034(16)	6.492(2)
<i>V</i> (Å ³)	113.66(4)	112.58(7)	111.63(5)
crystal size (mm ³)	0.2 × 0.3 × 0.4	0.04 × 0.1 × 0.1	0.06 × 0.08 × 0.3
temperature (K)	298(2)	298(2)	298(2)
θ range (deg)	3.1 – 30.6	3.1 – 30.5	4.9 – 30.6
μ (mm ⁻¹)	33.48	34.26	35.05
no. of collected reflections	1207	912	783
no. of unique reflections	130	135	134
<i>R</i> _{int}	0.064	0.055	0.057
<i>h</i>	-5 ≤ <i>h</i> ≤ 5	-4 ≤ <i>h</i> ≤ 5	-5 ≤ <i>h</i> ≤ 5
<i>k</i>	-4 ≤ <i>k</i> ≤ 5	-5 ≤ <i>k</i> ≤ 4	-4 ≤ <i>k</i> ≤ 5
<i>l</i>	-9 ≤ <i>l</i> ≤ 9	-9 ≤ <i>l</i> ≤ 6	-9 ≤ <i>l</i> ≤ 9
$\Delta\rho_{\max}$ (e Å ⁻³)	4.03	2.98	2.20
$\Delta\rho_{\min}$ (e Å ⁻³)	-3.90	-1.57	-4.00
GoF	1.27	1.21	1.21
extinction coefficient	0.99(11)	0.39(3)	0.48(4)
<i>R</i> ₁ (<i>F</i>) for $F_o^2 > 2\sigma(F_o^2)$ ^a	0.046	0.030	0.040
<i>R</i> _w (<i>F</i> _o ²) ^b	0.121	0.077	0.086

$$^a R_1 = \frac{\sum ||F_o| - |F_c||}{\sum |F_o|}$$

$$^b wR_2 = [\sum w(F_o^2 - F_c^2)^2 / \sum w(F_o^2)^2]^{1/2}$$

Elemental analysis. Single crystals of ScTGa₅ (T = Fe, Co, Ni) were characterized by electron dispersive spectroscopy (EDS) using a LEO 1530 VP SEM equipped with an EDAX detector operating with an accelerating voltage of 19 kV and a working distance of 11.3 mm. Multiple crystals from each batch were

examined. Spectra were integrated for 45 seconds, the results from 4 spots on the single crystal were averaged, and atomic ratios were normalized to scandium. The elemental compositions of samples are as follows: Sc_{1.00(2)}Fe_{0.95(2)}Ga_{4.48(1)}, Sc_{1.00(1)}Co_{1.06(5)}Ga_{4.65(2)}, and Sc_{1.00(2)}Ni_{1.33(3)}-Ga_{4.56(3)}. The disagreement between the structure models refined against the single crystal X-ray diffraction data and the EDS data are attributed to the semiquantitative nature of EDS measurements.

Table 6.2. Atomic positions and lattice parameters

atom	<i>x</i>	<i>y</i>	<i>z</i>
Sc 1 <i>a</i>	0	0	0
T 1 <i>b</i>	0	0	½
Ga1 1 <i>c</i>	½	½	0
Ga2 4 <i>i</i>	0	½	<i>z</i> Ga2
compound	<i>a</i> (Å)	<i>c</i> (Å)	<i>z</i> Ga2
ScFeGa ₅	4.1367(7)	6.64220(17)	0.30336(13)
ScCoGa ₅	4.1290(11)	6.6034(16)	0.30308(9)
ScNiGa ₅	4.1466(6)	6.492(2)	0.29752(13)

Table 6.3. Selected interatomic distances (Å)

	ScFeGa ₅	ScCoGa ₅	ScNiGa ₅
within cuboctahedron			
Ga1-Ga2	2.8876(7)	2.8754(7)	2.8336(8)
Sc-Ga1 (×4)	2.9251(5)	2.9196(8)	2.9321(4)
Sc-Ga2 (×8)	2.8876(7)	2.8754(7)	2.8336(8)
within rectangular prism			
Ga2-Ga2 (<i>c</i> -axis)	2.6123(17)	2.6006(14)	2.6290(19)
Ga2-Ga2 (<i>ab</i> -plane)	2.9251(5)	2.9196(8)	2.9321(4)
T-Ga2 (×8)	2.4462(6)	2.4399(6)	2.4549(6)
between cuboctahedra and rectangular prism			
Sc-T	3.3211(1)	3.3017(8)	3.246(1)

Physical properties. Single crystals of ScTGa_5 ($T = \text{Fe, Co, Ni}$) were selected for electrical resistance measurements, which were carried out on a Quantum Design Physical Property Measurement System (PPMS) with current applied in the *ab*-plane of the sample. Data were collected over a temperature range of 2 to 290 K. Temperature dependent resistance measurements were performed using a four-probe configuration. Electrical contacts were made by attaching platinum wires to the samples with silver epoxy.

Electronic structure calculations. Geometry optimizations of ScTGa_5 ($T = \text{Fe, Co, Ni}$) were performed with Density Functional Theory (DFT), using the Vienna Ab initio Simulation Package (VASP)^{25,26} for reversed approximation Molecular Orbital (raMO) analysis and ABINIT²⁷⁻²⁹ for DFT-Chemical Pressure (CP) analysis. The optimizations were performed in two steps: first the atomic positions were relaxed in a fixed unit cell, and then all structural parameters were allowed to change simultaneously.

VASP was used in the high-precision mode with the GGA-Projector Augmented Wave (PAW) potentials^{30,31} provided with the package. Single-point energy calculations were performed in the optimized geometries to obtain electronic band structures and projected density of states (DOS) curves. Hückel parameters were calibrated to the DFT output with the eHtuner program.³² These parameters were used in simple Hückel calculations with YAeHMOP to generate Hamiltonian matrices. Then, raMO analysis and visualization were performed in MATLAB using our Figuretool application.

To generate each CP scheme, three single-point energy calculations were performed, using ABINIT with norm-conserving Hartwigsen-Goedecker-Hutter pseudopotentials³³ and the Teter 93 LDA exchange-correlational functional.³⁴ One of these calculation was performed at an isotropically expanded unit cell volume, one at the optimized volume, and one at an isotropically contracted volume. For each

one, the components of the total Kohn-Sham potential, the electron density, and kinetic energy were output, from which CP maps were generated within the Fredrickson group CP package. The CP schemes were visualized in MATLAB with our Figuretool application. Further computational details for each procedure, such as optimized geometries, k-point grids, energy cutoffs, total energies, Bader charges, and ionic profiles (generated by the Atomic Pseudopotential Engine)³⁵ are provided in Appendix D.

6.4. Results and discussion

Crystal growth and characterization. Using the self-flux method with excess Ga, large crystals were obtained with sizes ranging from 1 to 5 mm across (Figure 6.1). The crystals were silver-colored with a metallic sheen. Elemental analysis of the crystals harvested with Energy Dispersive X-ray Spectroscopy confirmed compositions consistent with the targeted ScTGa_5 ($T = \text{Fe, Co, Ni}$) phases. Based on the mass of the crystals obtained, the reaction yields were approximately 75%, 30%, and 15% for the Co, Ni, and Fe analogues, respectively.



Figure 6.1. A photograph of a large flux-grown crystal of ScCoGa_5 .

Crystal structures of ScTGa_5 ($T = \text{Fe}, \text{Co}, \text{Ni}$). After selecting suitably sized fragments of the ScTGa_5 crystals, we collected single crystal X-ray diffraction data sets on them to confirm the structures of these compounds. As is reported in the Sc-T-Ga phase diagrams, our structure refinements found all three phases crystallize in the tetragonal HoCoGa_5 -structure type with space group $P4/mmm$.^{13,36} This structure can be simply visualized in terms of an intergrowth of slabs of the common AuCu_3 and fluorite structure types (Figure 6.2): single unit cell-thick slabs of the AuCu_3 -type ScGa_3 slabs of $\text{Sc}@Ga_{12/4}$ cuboctahedra are interwoven in a 1:1 ratio with fluorite-type TGa_2 layers of edge-sharing $\text{T}@Ga_{4/2}$ rectangular prisms.

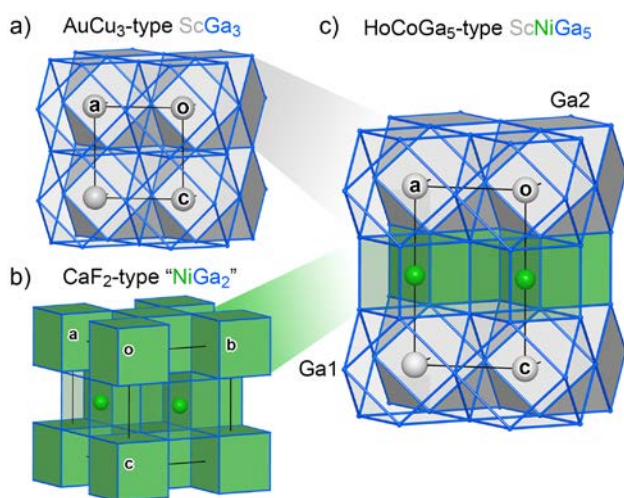


Figure 6.2. The crystal structures of ScTGa_5 ($T = \text{Fe}, \text{Co}, \text{Ni}$), depicted as an intergrowth of AuCu_3 -type and fluorite-type slabs. (a) ScGa_3 in the AuCu_3 type. (b) A hypothetical fluorite-type NiGa_2 phase. (c) The HoCoGa_5 -type structure of ScNiGa_5 .

The four symmetry-distinct sites of the structures can be understood from this intergrowth picture (Table 6.1). The positions of the Sc and T sites are fixed by symmetry at the centers of the Ga cuboctahedra and rectangular prisms, respectively. The Ga1 site, meanwhile, represents the Ga atoms in the middle

of the AuCu_3 -type slabs occurring at the centers of the (001) faces of the unit cell. Finally, the Ga2 site defines the square nets of Ga atoms at the “interface” of the cuboctahedra and the rectangular prisms.

The z coordinate of the Ga2 site is the only parameter not fixed by symmetry and, together with the c lattice parameter, controls the thicknesses of the AuCu_3 - and fluorite-type slabs. Across the series $T = \text{Fe}$, Co , and Ni , the c parameter and Ga2 z coordinate conspire to create a slight contraction of the cuboctahedra along the c -axis (evidenced by the longer Sc-Ga1 distances in Table 6.3 compared to Sc-Ga2 distances) with the heights going from 4.03 Å to 4.00 Å to 3.86 Å. As thickness of the fluorite-type slab is essentially constant at 2.614(14) Å, this contraction of the ScGa_3 layers leads to a similar contraction in the Sc-T distances between slabs (contacts that will be important in our bonding analysis later) from 3.32 Å to 3.30 Å to 3.24 Å.

The interatomic distances for the remaining contacts are in accord with those observed for related phases. The eight Sc-Ga2 interatomic distances are comparable to Sc-Ga distances of binary compounds like ScGa ,³⁷ ScGa_2 ,³⁸ and ScGa_3 ³⁹ (2.85-2.90 Å), but the four Sc-Ga1 distances are slightly longer. T-Ga distances are also typical of bond lengths in binary phases, such as FeGa_3 ,^{40,41} CoGa_3 ,⁴⁰ and NiGa_3 ⁴² (2.36-2.49 Å).

Electrical Properties. The temperature-dependent in-plane electrical resistance measurements for ScTGa_5 ($T = \text{Fe}$, Co , Ni) are given in Figure 6.3. In all three cases, the measured resistance rises with increasing temperature, a signature of metallic conductivity. The residual resistance of ScFeGa_5 , however, is almost twice that of the Co and Ni analogues. This observation, along with the low synthetic yield and the higher crystallographic R-factor (Table 6.1), indicates that the crystals of ScFeGa_5 are of poorer quality.

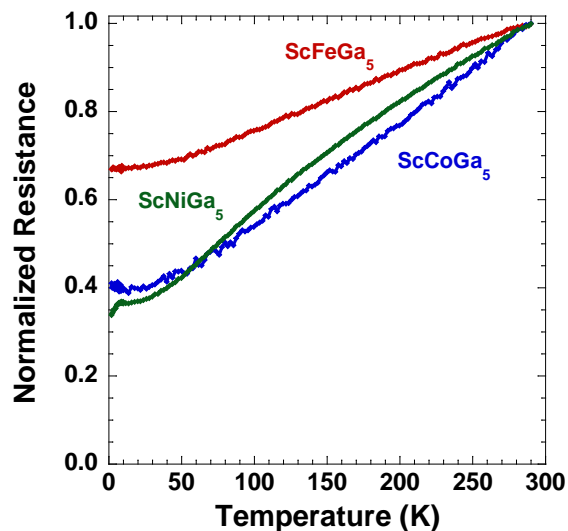


Figure 6.3. Normalized electrical resistance as a function of temperature for the ScTGa_5 ($T = \text{Fe, Co, Ni}$) series. All three show typical metallic behavior.

Preliminary electronic structure analysis. Now that we have confirmed the crystal structures of these ScTGa_5 phases, we are in a position to explore the factors stabilizing their structure type using electronic structure calculations. Their GGA-DFT density of states (DOS) distributions offer important clues here (Figure 6.4). For each ScTGa_5 phase, the Fermi energy (E_F) lies near a pseudogap at ca. -7 eV, just above a dense collection of T d-based states. The non-zero DOS value at the E_F for all three compounds is consistent with their metallic conductivity, while the presence of the pseudogap is suggestive of a role for valence electron concentration in their stability. The E_F for the $T = \text{Fe, Co, and Ni}$ phases lies at the base, middle, and top of the pseudogaps, respectively, consistent with a rigid-band picture for the phases. As such, ScCoGa_5 appears to be the most optimized of the three at 27 electrons per formula unit (3 for Sc + 9 for Co + 3×5 for Ga).

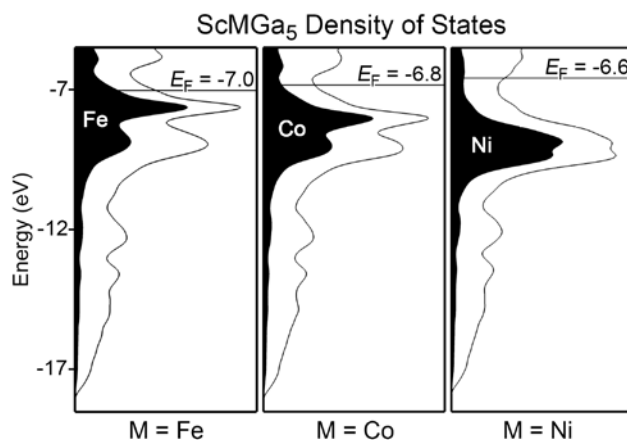


Figure 6.4. Electronic density of states (DOS) of ScTGa_5 ($T = \text{Fe, Co, Ni}$). The projected T component of the DOS is shaded in black. As the valence electron count increases, the Fermi energy goes from the bottom of the pseudogap for $T = \text{Fe}$, to the middle for $T = \text{Co}$, and to the top of it for $T = \text{Ni}$.

Electron counting using the 18- n rule. A simple rationale for the appearance of the pseudogap near this electron count is offered by 18- n rule recently demonstrated to underlie the ideal valence electron counts for many transition metal-containing intermetallics.¹⁵ In this bonding scheme, each transition metal atom (in this case both the Sc and T atoms, as we will see below) is envisioned as requiring 18- n electrons to achieve closed shell electron configurations, where n is the number of electron pairs that the transition metal atom shares covalently with its transition metal neighbors. From this perspective, the main group (E) atoms are viewed as contributing electrons to transition metal-centered orbitals, unless specific E-E contacts are identified as being non-interacting with the transition metal sites.

An advantage of the 18- n approach is that, like the Zintl concept, it can be applied through an examination of the structure, even without an electronic structure calculation. For example, in the case of ScCoGa_5 , the total valence electron count of 27 falls far short of the $2 \times 18 = 36$ electrons necessary for both

Sc and Co atoms to have 18 electron configurations on their own ($n = 0$). Just as carbon can form four covalent bonds to satisfy the octet rule, however, ScCoGa_5 might still be able to achieve an ideal electron count through the sharing of electron pairs along Sc-Sc, Sc-Co, or Co-Co contacts ($n > 0$). The typical mechanism by which this occurs is the isolobal bond, functioning with same nodal character as covalent σ and π transition metal-transition metal bonds, but with substantial delocalization over bridging E atoms.

The HoCoGa_5 -type structure of the ScTGa_5 phases offers several opportunities for such isolobal bonds to form. We'll consider ScCoGa_5 as a specific example. Each Sc and Co atom has a six Sc/Co neighbors within a radius of 4.2 Å in a flattened octahedral arrangement (Figure 6.5). For the Co atoms, four of these neighbors are other Co atoms in the TGa_2 layers at a distance of 4.13 Å, a distance that is long even for a Co-Co isolobal bond. However, the remaining two neighbors, Sc atoms in the ScGa_3 slabs above and below along c , are only 3.30 Å away and are supported by four Ga atoms – an arrangement highly conducive to isolobal bonding. From this geometrical analysis, the T atoms can be assigned as $n=2$, requiring 16 electrons for a filled 18-electron configuration.

For the Sc atoms, the coordination by Sc and Co is similar, with two Sc-Co contacts each along c , and four neighbors perpendicular to c at a distance of 4.13 Å. While this 4.13 Å distance was long enough for us to discount the possibility of Co-Co interaction, the metallic radius of Sc is 0.37 Å larger than Co's. Indeed, our earlier theoretical investigations generalizing the 18- n rule revealed that isolobal bonds are present at corresponding contacts in AuCu_3 -type ScGa_3 . In ScCoGa_5 , we thus consider the Sc atoms to have $n=6$.

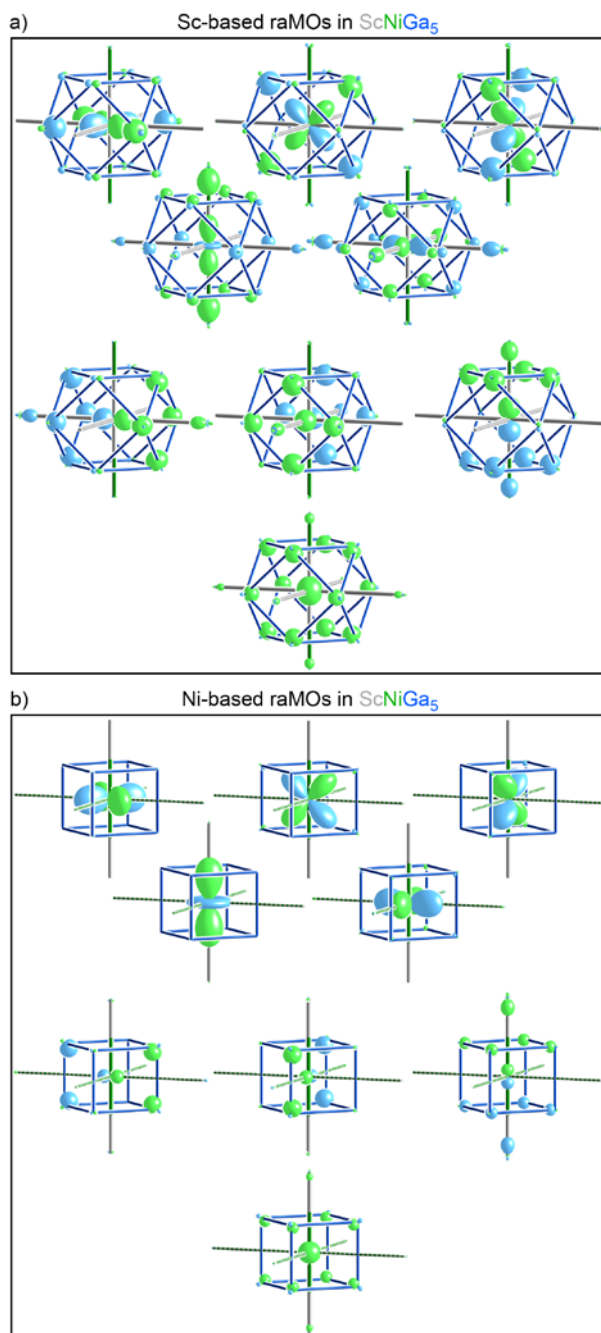


Figure 6.5. The reversed approximation Molecular Orbitals (raMOs) for ScNiGa₅ generated to reproduce the s, p, and d valence atomic orbitals of a Sc or Ni atom. (a) Reproduction of the nine Sc s, p, d orbitals. Note the bonding contributions from the Sc neighbors in the s, p_x, p_y, d_{z²}, and d_{x²-y²} raMOs, and from the two Ni neighbors along the c-axis in the s, p_z, and d_{z²} raMOs. (b) The corresponding raMOs for a Ni atom in the structure. Almost no contributions are visible from neighboring Ni atoms, but bonding overlap occurs with the Sc neighbors along the c-axis in the s and p_z raMOs.

Combining our analyses for the Sc and Co atoms, we obtain an ideal 18- n electron count for ScCoGa₅ of $(18 - 6 \text{ for Sc}) + (18 - 2 \text{ for Co}) = 28$ total electrons per formula unit. This is $\frac{1}{2}$ electron per Sc/Co atom higher than the total electron count for ScCoGa₅, but it matches the total electron count for ScNiGa₅ where the E_F lies at the top of the pseudogap in its DOS curve (Figure 6.4). In contrast, ScFeGa₅ falls short of the ideal by 1 electron per transition metal atom, which helps to explain why its E_F falls below the pseudogap.

Confirmation of the 18- n picture using the reversed approximation Molecular Orbital (raMO) analysis. We can test this bonding picture against the electronic structure of these phases using the reversed approximation Molecular Orbital (raMO) method, a recently developed theoretical technique. It works by using the occupied crystal orbitals from a DFT-calibrated Hückel calculation as the basis set for the calculation of a simple, local MO diagram hypothesized to play a role in the electronic structure. The more closely the resulting raMOs reproduce the model MOs, the better that model characterizes the compound's bonding.

For filled 18- n electron configurations, a useful model MO diagram is the set of nine s, p, and d atomic orbital levels of the transition metal atom. In Figure 6.5, we show the raMO reconstructions of these orbitals for a Sc and a Ni atom in ScNiGa₅, where the phase's electron count matches that predicted by the 18- n rule.

For both the Sc and Ni atoms, the nodal characters of each of the s, p, and d atomic orbitals are well-represented, indicating that an electron pair is associated with each of these functions. The raMOs differ, however, in terms of how localized each is to the central orbital that served to template its construction.

All of the Sc raMOs, as well as the Ni s and p ones appear delocalized through the coordination environment of the central atom, with positive orbital overlaps highlighting stabilizing interactions. These features show how the electron pairs assigned formally to the central atom in terms of 18- n rule counting are actively involved in bonding. The d orbitals on Ni, on the other hand, are highly localized with very little density on any other atoms, as expected for the nearly core-like character of the d orbitals of T atoms.

The bonding contributions from Sc or Ni neighbors in several of these raMOs are suggestive of isolobal bonds being present. This possibility can be explored further by attempting to localize the raMOs along specific Sc-Sc or Sc-Ni contacts through linear combinations. Given the octahedral arrangements of the Sc/Ni-Sc/Ni contacts, this localization is conveniently possible by making sp^3d^2 hybrids of the raMOs on the Sc or Ni sites (Figure 6.6).

Through this process, six isolobal bonds are generated on the Sc site (two Ni-Sc and four Sc-Sc) and two Ni-Sc isolobal bonds on the Ni site. These functions follow closely our earlier conclusions of the Sc and Ni atoms being $n=6$ and $n=2$ centers, respectively, in the structure. The conclusion that $ScNiGa_5$ is at an ideal electron count is in reasonable agreement with the position of the pseudogaps in the DOS distributions of the $ScTGa_5$ phases in Figure 6.4. The DOS minimum in these plots appears to occur somewhere between 27 ($T = Co$) and 28 ($T = Ni$) electrons per formula unit.

We are now in a position to generalize this bonding picture to the larger family of $HoCoGa_5$ -type phases. To do this, we performed a survey of the gallides and indides adopting this structure type in the Inorganic Crystal Structure Database,⁴³⁻⁴⁵ leaving out those containing actinide elements (Figure 6.7). Of the compounds found in this search, $ScFeGa_5$ is the only one that deviates from the ideal electron count

of 28 per formula unit by as much as 1 electron per Ln/T atom. The HoCoGa₅-type thus shows a strong adherence to the 18-*n* rule.

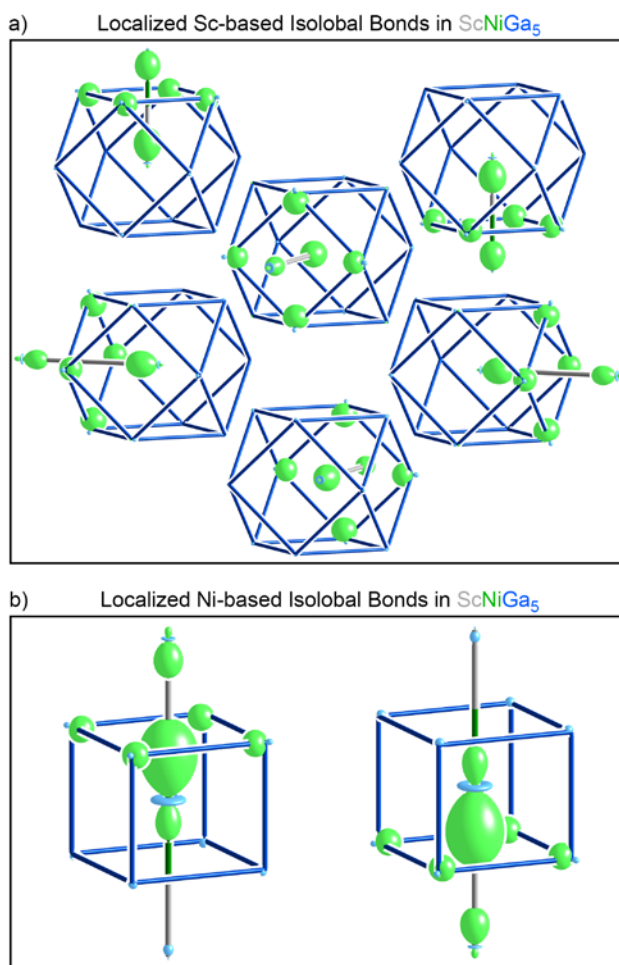


Figure 6.6. Localized isolobal bonding functions in ScNiGa₅ generated from linear combinations of the raMOs in Figure 6.5.

(a) Six Sc-based isolobal bonds, two with Ni and four with its Sc neighbors through the square faces of the cuboctahedral coordination by Ga atoms. (b) Two isolobal bonds between Ni and its Sc neighbors along the *c*-axis.

Atomic size stability range explored through DFT-Chemical Pressure (DFT-CP) analysis. In

Figure 6.7, another trend is apparent that cannot be easily explained in terms of electron count: while HoCoGa₅-type indides form for a wide range of Ln and T elements, the gallides are limited to 3d transition metals and smaller lanthanide elements, trends that seem to have more to do with atomic size than electron count.

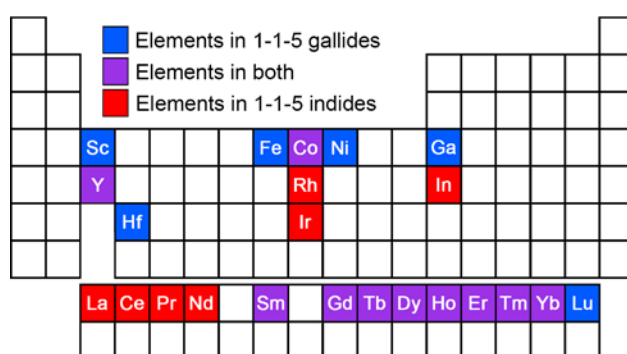


Figure 6.7. The elements occurring in HoCoGa₅-type gallides (blue), indides (red), or both (purple). Gallides have only been reported in combination with smaller lanthanides or early d-block elements, whereas indium compounds can incorporate both smaller and larger rare earth atoms, as well as larger transition metals. Actinide-containing phases have been excluded as our theoretical results cannot be easily extrapolated to such compounds.

Clues to how atomic sizes may influence the favorability of the HoCoGa₅ type can be found in our earlier CP analysis⁴⁶ of the Y₄PdGa₁₂ structure type, which can accommodate larger transition metal atoms into the octahedral holes of a AuCu₃-like YGa₃ network (Figure 6.2a). A hypothetical “YGa₃” phase was found to be destabilized by stretching of the Ga-Ga interactions due to the relatively large size of the Y atoms. Filling 1/4 of the octahedral holes with a transition metal provided relief in this situation by replacing

some of the overly-long Ga-Ga contacts with nearly ideal T-Ga ones, and creating shorter Ga-Ga distances in neighboring unstuffed octahedra through compression as the T atoms were accommodated. Perhaps similar stresses are at work in HoCoGa₅-type gallides.

Figure 6.8 shows the calculated CP scheme for ScNiGa₅. As anticipated from the earlier results on the Y₄PdGa₁₂ type, we see negative pressures (black lobes) distributed along all Ga-Ga atoms, suggesting that their distances are stretched relative to their ideal values. The origin of this stretching of the Ga sublattice is evident in the CP features of both Ni (in green rectangular prisms) and Sc (in gray cuboctahedra). Ni and Sc experience positive CP along every direction (within the resolution of the plot, which includes components of the CP distribution from real spherical harmonics with $l \leq 4$).

This tension has clear implications for the stability range of the HoCoGa₅ type. Already in ScNiGa₅, where Sc and Ni are perhaps the smallest atoms to occupy their respective positions in HoCoGa₅-type gallides, these atoms are somewhat too large for their coordination environments. Substituting a larger element for either the Sc or the Ni atoms would exacerbate this conflict, eventually leading to this structure type losing out to other competing geometries.

Connections to broader structural chemistry. The expected tension to emerge for large Ln atoms in HoCoGa₅-type gallides provides a simple interpretation of a number of more complicated structures in Ln-T-Ga systems (Figure 6.9). One avenue for expanding the space around a large Ln atom without elongating Ga-Ga interatomic distances would be to simply add additional Ga atoms to increase the coordination number of the Ln atom. The BaMg₄Si₃-type phase LaPdGa₆⁴⁷ represents just such a mechanism: the vertex-sharing Ga atom in the plane of the Ln atoms in the HoCoGa₅ type (Figure 6.9a) has been replaced by a Ga-Ga dumbbell that straddles the lanthanide layer (Figure 6.9b). La atoms are surrounded by 16

nearly equidistant Ga neighbors in a coordination polyhedron resembling that of Ba atoms in the BaAl_4 type, rather than 12 in a cuboctahedron. This expanded polyhedron appears much better adapted to occupation by a large atom.

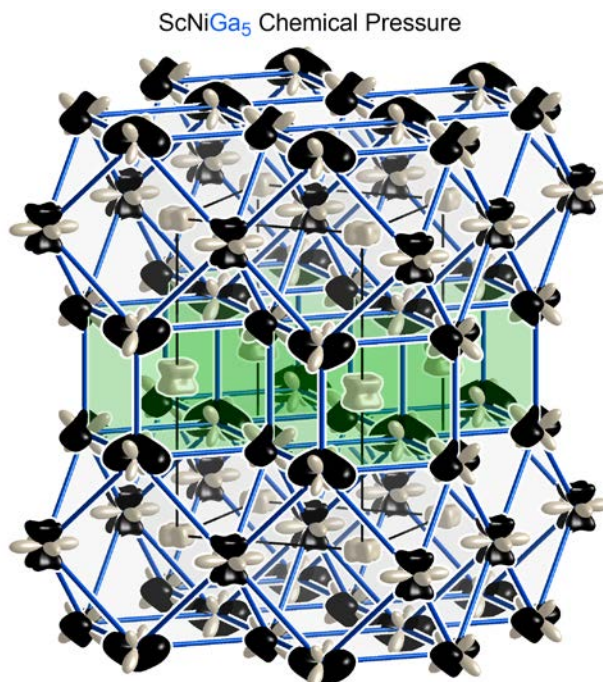


Figure 6.8. The chemical pressure (CP) scheme for ScNiGa_5 . On each atom, a radial lobe representing the sums of the local pressures experienced along each direction. The surfaces are presented in black where the pressures are negative (calling for the contraction of the structure), and white for directions along which the pressures are positive (pushing toward expansion of the structure). Negative CPs between the Ga atoms and positive CPs emanating from the Sc and Ga atoms (centering the green and gray polyhedra) signal tension between strained Ga-Ga bonds and overly dense coordination environments for the Sc/Ni atoms. Substituting a larger atom onto either the Sc or Ni site would increase this tension.

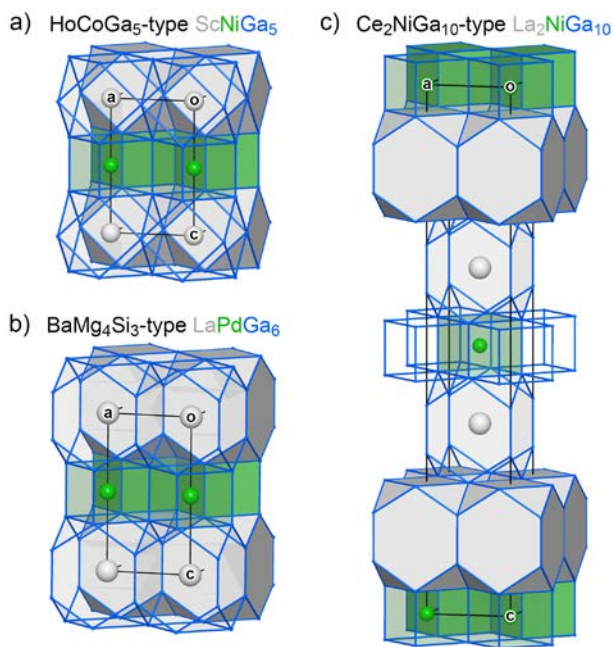


Figure 6.9. Derivatives of the HoCoGa_5 type accommodating large Ln atoms. (a) The HoCoGa_5 -type structure of ScNiGa_5 , shown for comparison. (b) The BaMg_4Si_3 -type structure of LaPdGa_6 . (c) The $\text{Ce}_2\text{NiGa}_{10}$ -type structure of $\text{La}_2\text{NiGa}_{10}$.

Of course, such a change in coordination environment and composition is not without electronic repercussions. The isolobal bond that would exist between Pd and La in the HoCoGa_5 type is broken in the LaPdGa_6 structure because of the extra distance between the atoms. Thus, the ideal $18-n$ count is raised from 28 electrons (with $n = 2$ for Pd and 6 for La) in the HoCoGa_5 type to 32 ($n = 0$ for Pd, 4 for La) in LaPdGa_6 . This increase in ideal electron count is nearly accommodated by the addition of one Ga atom per formula unit, with the electron count from the stoichiometry being 31 electrons.

Another alternate structure accommodating larger Ln atoms is exemplified by the $\text{Ce}_2\text{NiGa}_{10}$ -type $\text{La}_2\text{NiGa}_{10}$ ⁴⁸ (Figure 6.9c). Once again, the cuboctahedron is replaced by a more expansive 16 coordinate cage, but now the slabs of Ln-centered polyhedra in the LaPdGa_6 structure have doubled in thickness to

create larger regions of the BaAl_4 structure type in $\text{La}_2\text{NiGa}_{10}$. The electron counting for this phase follows closely that of LaPdGa_6 as the number of La and T neighbors for the sites is unchanged: $n=4$ for La and $n=0$ for Pd. These values predict an ideal electron count of 46 per formula unit, which matches that given by the stoichiometry.

It may be somewhat surprising that Ga-Ga bonding has not entered into our electron counting, especially for the Ga-rich layer in $\text{La}_2\text{NiGa}_{10}$. As in many other structures following the $18-n$ rule, these compound's Ln-Ga and T-Ga interactions are so extensive that no Ga-Ga contacts are isolated from Ln or T atoms. In examining compounds with higher Ga content, however, such as those adopting the $\text{Ce}_2\text{CuGa}_{12}$ type,⁴⁹ we would need to search for additional electrons assigned to the Ga sublattices.

Our conclusions regarding the factors stabilizing HoCoGa_5 gallides and these more complex structures can be summarized in a structure map. In Figure 6.10, we plot the occurrence of these structures as a function of valence electron concentration (electrons per Ln/T atom) and the 3+ radius of the Ln element it contains. The known HoCoGa_5 -type phases and the $m=2$ members of the $\text{Ln}_m\text{TGa}_{3m+2}$ homologous series it is part of appear here in the lower left side of the map, corresponding to low electron concentrations and small Ln atoms. The $\text{Ce}_2\text{CuGa}_{12}$ - and BaMg_4Si_3 -type phases, on the other hand, occur at the upper left, where larger Ln atoms are able to occupy the larger 16-coordinate cages, and higher electron concentrations support the smaller number of isolobal bonds possible in these structures.

This structure map also provides a context for viewing the three ScTGa_5 compounds characterized in this Chapter. They significantly extend the observed boundary of stability for the HoCoGa_5 type: by $\frac{1}{2}$ of an electron per Ln/T atom in each direction, and by more than 0.1 Å in terms of ionic radius of the Ln element (excepting HfNiGa_5 ,⁵⁰ whose structure was inferred from powder). The exceptional flexibility of

the ScTGa₅ series may be connected to the small radius of its Sc atoms: the small size of Sc may allow closer Ga-Ga contacts desired by the CP scheme of the HoCoGa₅ type than could be attained in analogues with larger Ln atoms. In turn, this reduced strain could add to the tolerance of the structure to non-ideal electron counts.

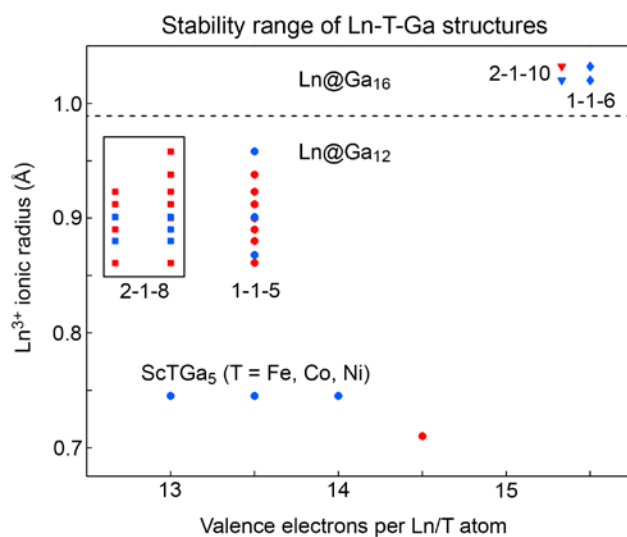


Figure 6.10. The stability range of Ln-T gallides based on the size of the Ln atom and valence electron concentration (electron count per Ln/T atom). Reported HoCoGa₅-type phases are represented by circles, BaMg₄Si₃-type phases by triangles, and Ce₂NiGa₁₀-type phases by diamonds. Squares are for Ho₂CoGa₈-type compounds, the $m = 2$ member of the homologous series of which the HoCoGa₅ type is the $m = 1$ member. Red symbols indicate when structures were assigned without refinement of the atomic parameters against diffraction data. The upper right of the plot, corresponding to high electron count and large Ln atoms, is occupied by the structural derivatives that replace Ln-centered cuboctahedra with larger Ga cages. The three ScTGa₅ phases studied in this Chapter represent extremes in electron count and atomic size for the HoCoGa₅ type.

6.5. Conclusions

In this Chapter, we have explored the factors shaping the stability range of the HoCoGa_5 type as a point of entry into the broader structural chemistry of Ln-T-E phases (Ln = lanthanide or early d-block element, T = transition metal, E = p-block main group element). We began with the growth of crystals of the ScTGa_5 (T = Fe, Co, Ni) phases at the edge of this stability range, and confirmation of their HoCoGa_5 type structures and metallic conductivity. Theoretical calculations were then applied to elucidating the roles that valence electron concentration and atomic sizes play in these compounds. From these analyses, we traced the stability range of the HoCoGa_5 -type gallides to filling of $18-n$ electron configurations on the Ln and T atoms, and a tension between overly long Ga-Ga contacts and the size requirements of the Ln and T atoms. The latter effect provides a rationale for the absence of Ga analogues to the Ce-T-In series of superconductors, as well as for the alternative structures observed with larger coordination environments for the Ln atoms.

The bonding picture for the Ln-T-E phases described here extends the applicability of the $18-n$ rule, which has so far mainly been applied to binary compounds. At the same time, these compounds raise an intriguing question concerning the various ways that the Ln atoms are incorporated into the $18-n$ bonding scheme. In this case, the Ln atoms appear as $18-n$ electron centers that participate in isolobal bonds, much as was found for early and mid-block transition metals in the AuCu_3 and TiAl_3 structure types.^{15,51} In other compounds, however, such as $\text{Gd}_{13}\text{Fe}_{10}\text{C}_{13}$ ⁵² and GdCoSi_2 ,⁵³ the Ln atoms are viewed as electron donors to T-based $18-n$ electron configurations. Determining the circumstances under which the Ln atoms take on these different roles could be an exciting subject for future research.

Another possible research direction is to explore how the insights derived here can be applied to the design of new compounds. For example, can phases with Ga₁₂ cuboctahedra centered by larger Ln atoms be stabilized? Such a structure would need a mechanism to compensate for the severely over-extended Ga-Ga contacts within the cuboctahedra. One possibility is offered by the Sm₄Co₃Ga₁₂ structure type,⁵⁴ in which some T atoms occupy the octahedral holes in AuCu₃-type slabs of a Ho₂CoGa₈-type framework. However, from the work of Slater et al. on the stability range of this structure type,⁵⁵ it seems that more extensive insertion of interstitials may be necessary to open the cuboctahedra enough to accommodate La or Ce.

Acknowledgements

We gratefully acknowledge financial support from the National Science Foundation (NSF) through grants DMR-1508496 (work at UW-Madison) and DMR-1360863 (work at UT at Dallas). This work also used computer resources supported by NSF grant CHE-0840494.

6.6. References

- (1) Hume-Rothery, W.; Raynor, G. V. *The structure of metals and alloys*; 4th ed.; Institute of Metals: London, 1962.
- (2) Schmitt, D. C.; Drake, B. L.; McCandless, G. T.; Chan, J. Y. *Acc. Chem. Res.* **2015**, *48*, 612-618.
- (3) Vogel, R.; Klose, H. Z. *Metallkd* **1954**, *45*, 633-638.
- (4) Walker, I. R.; Grosche, F. M.; Freye, D. M.; Lonzarich, G. G. *Physica C* **1997**, *282-287*, Part 1, 303-306.

- (5) Mathur, N. D.; Grosche, F. M.; Julian, S. R.; Walker, I. R.; Freye, D. M.; Haselwimmer, R. K. W.; Lonzarich, G. G. *Nature* **1998**, *394*, 39-43.
- (6) Kal'ichak, Y. M.; Zaremba, V. I.; Baranyak, V. M.; Bruskov, V. A.; Zavali, P. Y. *Izvestiya Akademii Nauk: Metall* **1989**, 213-215.
- (7) Moshopoulou, E. G.; Fisk, Z.; Sarrao, J. L.; Thompson, J. D. *J. Solid State Chem.* **2001**, *158*, 25-33.
- (8) Zhou, B. B.; Misra, S.; da Silva Neto, E. H.; Aynajian, P.; Baumbach, R. E.; Thompson, J. D.; Bauer, E. D.; Yazdani, A. *Nat. Phys.* **2013**, *9*, 474-479.
- (9) Petrovic, C.; Movshovich, R.; Jaime, M.; Pagliuso, P. G.; Hundley, M. F.; Sarrao, J. L.; Fisk, Z.; Thompson, J. D. *EPL* **2001**, *53*, 354.
- (10) Hegger, H.; Petrovic, C.; Moshopoulou, E. G.; Hundley, M. F.; Sarrao, J. L.; Fisk, Z.; Thompson, J. D. *Phys. Rev. Lett.* **2000**, *84*, 4986-4989.
- (11) Moshopoulou, E. G.; Ibberson, R. M.; Sarrao, J. L.; Thompson, J. D.; Fisk, Z. *Acta Crystallogr. Sect. B* **2006**, *62*, 173-189.
- (12) Nicklas, M.; Sidorov, V. A.; Borges, H. A.; Pagliuso, P. G.; Petrovic, C.; Fisk, Z.; Sarrao, J. L.; Thompson, J. D. *Phys. Rev. B* **2003**, *67*, 020506.
- (13) Grin, Y. N.; Yarmolyuk, Y. P.; Gladyshevskij, E. I. *Kristallografiya* **1979**, *24*, 242-246.
- (14) Yannello, V. J.; Fredrickson, D. C. *Inorg. Chem.* **2014**, *53*, 10627-10631.
- (15) Yannello, V. J.; Fredrickson, D. C. *Inorg. Chem.* **2015**, *54*, 11385-11398.
- (16) Fredrickson, D. C. *J. Am. Chem. Soc.* **2012**, *134*, 5991-5999.
- (17) Engelkemier, J.; Berns, V. M.; Fredrickson, D. C. *J. Chem. Theory Comput.* **2013**, *9*, 3170-3180.
- (18) Berns, V. M.; Engelkemier, J.; Guo, Y.; Kilduff, B. J.; Fredrickson, D. C. *J. Chem. Theory Comput.* **2014**, *10*, 3380-3392.
- (19) Canfield, P. C.; Fisk, Z. *Philos. Mag. B* **1992**, *65*, 1117-1123.
- (20) Kanatzidis, M. G.; Pöttgen, R.; Jeitschko, W. *Angew. Chem. Int. Ed.* **2005**, *44*, 6996-7023.
- (21) Thomas, E. L.; Millican, J. N.; Okudzeto, E. K.; Chan, J. Y. *Comments Inorg. Chem.* **2006**, *27*, 1-39.

- (22) Phelan, W. A.; Menard, M. C.; Kangas, M. J.; McCandless, G. T.; Drake, B. L.; Chan, J. Y. *Chem. Mater.* **2012**, *24*, 409-420.
- (23) Burla, M. C.; Caliendo, R.; Camalli, M.; Carrozzini, B.; Cascarano, G. L.; De Caro, L.; Giacovazzo, C.; Polidori, G.; Siliqi, D.; Spagna, R. J. *Appl. Crystallogr.* **2007**, *40*, 609-613.
- (24) Sheldrick, G. *Acta Crystallogr. Sect. C* **2015**, *71*, 3-8.
- (25) Kresse, G.; Furthmüller, J. *Phys. Rev. B* **1996**, *54*, 11169-11186.
- (26) Kresse, G.; Furthmüller, J. *Comput. Mater. Sci.* **1996**, *6*, 15-50.
- (27) Gonze, X.; Beuken, J. M.; Caracas, R.; Detraux, F.; Fuchs, M.; Rignanese, G. M.; Sindic, L.; Verstraete, M.; Zerah, G.; Jollet, F.; Torrent, M.; Roy, A.; Mikami, M.; Ghosez, P.; Raty, J. Y.; Allan, D. C. *Comput. Mater. Sci.* **2002**, *25*, 478-492.
- (28) Gonze, X. *Z. Kristallogr. - Cryst. Mater.* **2005**, *220*, 558.
- (29) Gonze, X.; Amadon, B.; Anglade, P. M.; Beuken, J. M.; Bottin, F.; Boulanger, P.; Bruneval, F.; Caliste, D.; Caracas, R.; Côté, M.; Deutsch, T.; Genovese, L.; Ghosez, P.; Giantomassi, M.; Goedecker, S.; Hamann, D. R.; Hermet, P.; Jollet, F.; Jomard, G.; Leroux, S.; Mancini, M.; Mazevet, S.; Oliveira, M. J. T.; Onida, G.; Pouillon, Y.; Rangel, T.; Rignanese, G. M.; Sangalli, D.; Shaltaf, R.; Torrent, M.; Verstraete, M. J.; Zerah, G.; Zwanziger, J. W. *Comput. Phys. Commun.* **2009**, *180*, 2582-2615.
- (30) Blöchl, P. E. *Phys. Rev. B* **1994**, *50*, 17953-79.
- (31) Kresse, G.; Joubert, D. *Phys. Rev. B* **1999**, *59*, 1758-1775.
- (32) Stacey, T. E.; Fredrickson, D. C. *Dalton Trans.* **2012**, *41*, 7801-7813.
- (33) Hartwigsen, C.; Goedecker, S.; Hutter, J. *Phys. Rev. B* **1998**, *58*, 3641-3662.
- (34) Goedecker, S.; Teter, M.; Hutter, J. *Phys. Rev. B* **1996**, *54*, 1703-1710.
- (35) Oliveira, M. J. T.; Nogueira, F. *Comput. Phys. Commun.* **2008**, *178*, 524-534.
- (36) Zhu, X.; Lu, W.; Ning, W.; Qu, Z.; Li, L.; Qi, T. F.; Cao, G.; Petrovic, C.; Zhang, Y. *J. Alloys Compd.* **2013**, *578*, 543-546.
- (37) Schob, O.; Parthe, E. *Acta Crystallogr.* **1965**, *19*, 214-224.
- (38) Belyavina, N.; Markiv, V. *Vestn. Kiev. Univ. Fiz.* **1980**, 15-17.

- (39) Dwight, A. E. In Proc. 7th Rare Earth Res. Conf. 1969; Vol. 1, p 273-282.
- (40) Schubert, K.; Breimer, H.; Gohle, R.; Lukas, H. L.; Meissner, H. G.; Stolz, E. *Naturwissenschaften* **1958**, *45*, 360-361.
- (41) Lu, H.-S.; Liang, C.-K. *Wuli Xuebao* **1965**, *21*, 849-57.
- (42) Hellner, E. Z. *Metallkd* **1950**, *41*, 480.
- (43) Bergerhoff, G.; Hundt, R.; Sievers, R.; Brown, I. D. J. *Chem. Inf. Comput. Sci.* **1983**, *23*, 66-69.
- (44) Bergerhoff, G.; Brown, I. D. In Crystallographic Databases; Allen, F. H., Bergerhoff, Sievers, R., Eds.; International Union of Crystallography: Chester, 1987, p 77-95.
- (45) Belsky, A.; Hellenbrandt, M.; Karen, V. L.; Luksch, P. *Acta Crystallogr. B* **2002**, *58*, 364-369.
- (46) Fulfer, B. W.; McAlpin, J. D.; Engelkemier, J.; McCandless, G. T.; Prestigiacomo, J.; Stadler, S.; Fredrickson, D. C.; Chan, J. Y. *Chem. Mater.* **2014**, *26*, 1170-1179.
- (47) Macaluso, R. T.; Nakatsuji, S.; Lee, H.; Fisk, Z.; Moldovan, M.; Young, D. P.; Chan, J. Y. *J. Solid State Chem.* **2003**, *174*, 296-301.
- (48) Yarmolyuk, Y. P.; Grin, Y. N.; Rozhdestvenskaya, I. V.; Usov, O. A.; Kuz'min, A. M.; Bruskov, V. A.; Gladyshevskii, E. I. *Sov. Phys. Crystallogr.* **1982**, *27*, 599-600.
- (49) Cho, J. Y.; Millican, J. N.; Capan, C.; Sokolov, D. A.; Moldovan, M.; Karki, A. B.; Young, D. P.; Aronson, M. C.; Chan, J. Y. *Chem. Mater.* **2008**, *20*, 6116-6123.
- (50) Markiv, V. Y.; Belyavina, N. N. *Russ. Metall.* **1979**, *3*, 205-208.
- (51) Kilduff, B. J.; Yannello, V. J.; Fredrickson, D. C. *Inorg. Chem.* **2015**, *54*, 8103-8110.
- (52) Hadler, A. B.; Yannello, V. J.; Bi, W.; Alp, E. E.; Fredrickson, D. C. *J. Am. Chem. Soc.* **2014**, *136*, 12073-12084.
- (53) Vinokur, A. I.; Fredrickson, D. C. *Inorg. Chem.* **2016**, accepted, DOI: <http://dx.doi.org/10.1021/acs.inorgchem.6b00724>.
- (54) Jia, Y.; Belin, C.; Tillard, M.; Lacroix-Orio, L.; Zitoun, D.; Feng, G. *Inorg. Chem.* **2007**, *46*, 4177-4186.
- (55) Slater, B. R.; Bie, H.; Gaultois, M. W.; Stoyko, S. S.; Mar, A. *Eur. J. Inorg. Chem.* **2011**, 3896-3903.

Appendix A.

Supporting Information for Chapter 2:

First-Principles Elucidation of Atomic Size Effects Using DFT-Chemical Pressure Analysis: Origins of $\text{Ca}_{36}\text{Sn}_{23}$'s Long-Period Superstructure

The specific information given in this Chapter came from the work of Engelkemier, but contributions were made by both Berns and Engelkemier, particularly for the conclusions presented in Section A.1.

A.1. Treatment of the $P_{\text{remainder}}$ components

One question encountered in the development of the DFT-CP analysis is to what extent each of the terms of the DFT total energy can be mapped to an energy grid. The energetic terms contributing to $P_{\text{remainder}}$ in Equation 2.4 all share the feature that they are not easily represented as an integral of an energy density over the unit cell volume. However, in principle some of these terms can be divided to some degree across a structure. Consider the E_{α} component of E_{total} . This component of the total energy represents the difference in the stability provided to a homogeneous electron gas by the ion cores and the simple Coulomb potentials used in the calculation of E_{Ewald} :

$$\begin{aligned}
E_a &= \left(\sum_j^{N_{\text{ions}}} \iiint_{\text{all space}} V_{\text{local},j}(\vec{r} - \vec{r}_{\text{ion},j}) - \frac{Z_j}{|\vec{r} - \vec{r}_{\text{ion},j}|} dV \right) \frac{N_{\text{electrons}}}{V_{\text{cell}}} \\
&= \left(\sum_j^{N_{\text{ions}}} \alpha_j \right) \frac{N_{\text{electrons}}}{V_{\text{cell}}}
\end{aligned} \tag{A.1}$$

As is evident from the above equation, the E_a contribution can be decomposed into a sum over terms corresponding to individual ions, which could then be mapped to the positions of these ions in space. The effort required to achieve this using the ABINIT program is minimal: the α_j values for Equation A.1 are given in the ABINIT output file for each pseudopotential with the label “epsatm.” The atomic contributions to E_a are then obtained by multiplying the corresponding α_j values by the average electron density for the unit cell.

Similar considerations apply to E_{nonlocal} , which is built up from a sum of terms resulting from the differential screening of s-, p-, d- and f- type orbital character around the individual ion cores in the system. While this is difficult to represent as a continuous function in 3D space, it should certainly be possible to distribute E_{nonlocal} appropriately among the atoms of the structure. A more complicated procedure is necessary here than for E_a . One begins by running a self-consistent field calculation on the structure of interest to obtain the ground state electron density and wavefunctions. Then holding fixed this electron density, the wavefunctions, and their occupancies, one goes atom by atom through the structure and calculates the total energy resulting when each ion core is placed alone in the unit cell in the midst of this electronic structure. The E_{nonlocal} term listed in the output for each atom then corresponds to the contribution from that atom to the nonlocal energy for the full structure. An annotated ABINIT input file for performing this procedure is provided in Section A.2.

Once the E_a and $E_{nonlocal}$ energies are resolved into atomic contributions, this information can be incorporated in the DFT-CP analysis by distributing these atomic terms among the voxel energies ($E_{voxel,n}$'s) of Equation 2.3. Here, we follow the argument of Filippetti and Fiorentini¹ that the nonlocal energies are associated with the ion core regions, and as such can be localized to the space close to their corresponding nuclei. For each atom, we count the voxels that occur within a fixed radius of the nuclear position, and partition the atomic E_a and $E_{nonlocal}$ equally across these voxels. The specific value of the radius should have no effect on the results of the CP analysis as long as the volume it encloses does not cross the boundaries of the atomic cells used in the integration of the CP map, at least when isotropic core component averaging is used.

In this way, the E_a and $E_{nonlocal}$ components of the DFT total energy can be moved from the $E_{remainder}$ term of Equation 2.2 into the grid of voxel energies. Their incorporation into the pressure map then occurs naturally through the differentiation of the energy grid with respect to volume (Equation 2.4). At this point, $P_{remainder}$ contains only contributions from the Ewald energy and the band occupancy smearing energy.

As the band occupancy smearing energy is not localizable to any particular points in space, it is reasonable to treat this unmapped pressure as homogeneously distributed across the unit cell. E_{Ewald} , on the other hand, represents the electrostatic energy of a homogeneous electron gas surrounding an array of point charges, which involves both the total energy of all the ions interacting with the homogenous electron gas as well as a converging sum of the Coulomb repulsion between every pair of ions in an infinite crystal lattice, shown in Equation A.2. The Ewald energy has the form:²

$$E_{Ewald} \propto \sum_{i \neq j} \frac{q_i q_j}{|r_i - r_j|} = \sum_{i \neq j} \left(\frac{q_i q_j \operatorname{erfc}(\eta |r_i - r_j|)}{|r_i - r_j|} \right) + \sum_{i \neq j} \left(\frac{q_i q_j \operatorname{erf}(\eta |r_i - r_j|)}{|r_i - r_j|} \right) \quad (\text{A.2})$$

In this equation, the divergent summation over the Coulombic interactions between charges in a lattice is decomposed into a short range and long range components, which are best treated in real and reciprocal space, respectively. The parameter η determines how steeply the short range interactions are extinguished with increasing distance (r), with the distance cut-off of the short range component roughly corresponding to $\eta \times r = 2.0$. Once an η value is chosen, the short range ion-ion portion of E_{Ewald} is attributed to pairs of atoms, and the corresponding pressures can be applied to the contact volumes described in the main text.

We have now described how the largest energy components contributing to $P_{remainder}$ can be resolved spatially. In what ways does such a mapping influence the results of a DFT-CP analysis? In Figure A.1, we plot CP anisotropy surfaces for Ca_5Sn_3 with different combinations of $P_{remainder}$ terms included in the CP map, using the contact volume integration scheme. Two different pseudopotentials for Ca are used: the images in the left column were generated from calculations using the semicore Ca potential, while those on the right we made using the valence-only potential. E_a and $E_{nonlocal}$ energies were mapped to spheres of radius 0.3 \AA around the nuclear positions, while an η value of 0.25 a_0^{-1} (corresponding to a cut-off distance of about 8 a_0 or 4.2 \AA) was used for the short-range E_{Ewald} contributions.

All versions of the semicore calculations, including Figure 2.6c, show essentially identical results, regardless of which additional terms are mapped. This high correspondence can be understood in that the semicore Ca pseudopotential, which explicitly models 10 electrons as valence as compared to 2 electrons in the valence-only pseudopotential, nearly completely captures the true core-electron effects of an all-

electron calculation in the vicinity of the Ca. In this case, the short-range Ewald repulsion between Ca cores is high and the $E_{nonlocal}$ and E_a corrections are small.

The invariance of the semicore Ca results to the mapping of $P_{remainder}$ terms suggests that a reliable picture of the pressures at work in the hypothetical Ca_5Sn_3 structure has been obtained. From a practical point of view, then, we can judge the value of mapping the $P_{remainder}$ terms by their ability to bring agreement between the semicore Ca picture and that obtained with the valence-only Ca pseudopotential. In other words, the mapping the remainder terms is useful if they correct for any missing core effects from using a smoother, valence-only pseudopotential. Somewhat surprisingly, this appears to not be the case. Moving down the valence-only results from Figures A.1a, to A.1b, to A.1c, and finally to Figure 2.6c, we see that the correspondence to the semicore picture increases as fewer $P_{remainder}$ terms are mapped.

Why would this be? There are, in fact, good physical reasons why mapping the remainder terms could be problematic. The short-range E_{Ewald} pressure depends heavily on the choice of η value, which introduces a large ambiguity into the CP results. There is also an inherent ambiguity in the E_a and $E_{nonlocal}$ terms as well. While we have shown how to distribute these pressures to individual atoms, we have no way of determining their spatial directionality. Rather than arbitrarily mapping these values isotropically into the core regions, it seems more valid to treat them homogeneously across the entire unit cell.

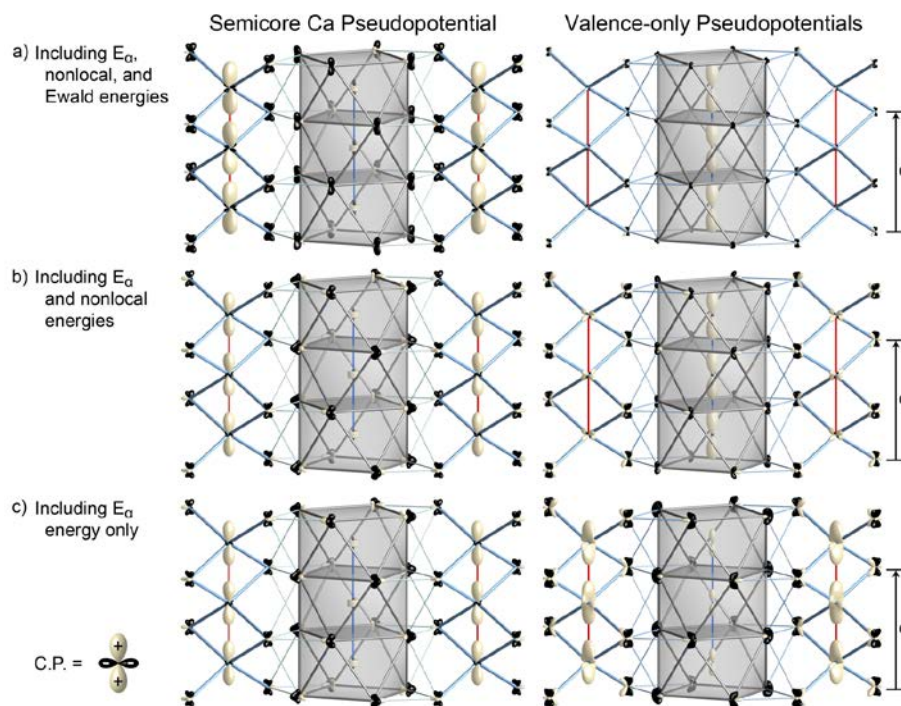


Figure A.1. The CP distribution around each atom is shown as a radial plot. See Figure 2.6 for details. The scale in the three semi-core results is set to 150. For the valence-only plots, the scale of (a) is 1250 and the scales of (b) and (c) are both 2500.

A.2. ABINIT input file for the calculation of nonlocal energies atom by atom

!CaSSn3 first nonlocal calculation for the conventional unit cell.

!Changes for the nonlocal calculation:

```

natom 1           !Only one atom is placed in the cell at a time.
ndtset 32        !There is a separate calculation for each atom.
nsym 1          !The symmetry is set to P1.
ntypat 2
znucl 20 50
typat1 1        !The first 20 calculations are for Ca atoms.
typat2 1
typat3 1
typat4 1
typat5 1
typat6 1
typat7 1

```

typat8 1
 typat9 1
 typat10 1
 typat11 1
 typat12 1
 typat13 1
 typat14 1
 typat15 1
 typat16 1
 typat17 1
 typat18 1
 typat19 1
 typat20 1
 typat21 2
 typat22 2
 typat23 2
 typat24 2
 typat25 2
 typat26 2
 typat27 2
 typat28 2
 typat29 2
 typat30 2
 typat31 2
 typat32 2

!The final 12 calculations are for Sn atoms.

!The fractional coordinates of each atom for separate calculations:

xred1	0.5000000000	0.0000000000	0.2499999992
xred2	0.5000000000	0.0000000000	0.7499999803
xred3	0.0000000000	0.5000000000	0.7499999803
xred4	0.0000000000	0.5000000000	0.2499999992
xred5	0.4159988753	0.2844270151	0.5000000000
xred6	0.2155730038	0.9159988377	0.0000000000
xred7	0.7155730218	0.4159988753	0.5000000000
xred8	0.0840011616	0.7844270151	0.5000000000
xred9	0.5840011616	0.2844270151	0.0000000000
xred10	0.9159988377	0.2155730038	0.5000000000
xred11	0.4159988753	0.7155730218	0.0000000000
xred12	0.2155730038	0.0840011616	0.5000000000
xred13	0.7155730218	0.5840011616	0.0000000000

xred14	0.7844270151	0.9159988377	0.5000000000
xred15	0.0840011616	0.2155730038	0.0000000000
xred16	0.5840011616	0.7155730218	0.5000000000
xred17	0.7844270151	0.0840011616	0.0000000000
xred18	0.2844270151	0.5840011616	0.5000000000
xred19	0.9159988377	0.7844270151	0.0000000000
xred20	0.2844270151	0.4159988753	0.0000000000
xred21	0.5000000000	0.5000000000	0.2499999992
xred22	0.0000000000	0.0000000000	0.2499999992
xred23	0.5000000000	0.5000000000	0.7499999803
xred24	0.0000000000	0.0000000000	0.7499999803
xred25	0.3427017685	0.8427018053	0.5000000000
xred26	0.1572982504	0.3427017685	0.5000000000
xred27	0.8427018053	0.3427017685	0.0000000000
xred28	0.8427018053	0.6572982315	0.5000000000
xred29	0.3427017685	0.1572982504	0.0000000000
xred30	0.6572982315	0.1572982504	0.5000000000
xred31	0.1572982504	0.6572982315	0.0000000000
xred32	0.6572982315	0.8427018053	0.0000000000

!The total charge in the unit cell for each calculation:

charge1 -86

charge2 -86

charge3 -86

charge4 -86

charge5 -86

charge6 -86

charge7 -86

charge8 -86

charge9 -86

charge10 -86

charge11 -86

charge12 -86

charge13 -86

charge14 -86

charge15 -86

charge16 -86

charge17 -86

charge18 -86

charge19 -86

!The first 20 calculations involve a

!single Ca atom in a unit cell with

!the surrounding electronic structure

!arising from 20 Ca and 12 Sn atoms.

!The total number of electrons is

!20*2 + 12*4 = 88 electrons. The one

!Ca ion has a charge of +2, which makes

!the total charge in the cell -86.

```

charge20 -86
charge21 -84      !The last 12 calculations involve a
charge22 -84      !single Sn atom with a charge of +4,
charge23 -84      !making the total cell charge -84.
charge24 -84
charge25 -84
charge26 -84
charge27 -84
charge28 -84
charge29 -84
charge30 -84
charge31 -84
charge32 -84

```

!The charge and kpoint distribution is held fixed:

```

getwfk 1          !The wavefunction is read in from a
prtwf 0           !previous calculation.
getden 1          !The electron density is read in
prtden 0         !from a previous calculation.
nstep 0          !The wavefunctions are not updated.
kptopt 0         !The kpoints are specified explicitly
nkpt 12         !from the previous SCF calculation.
kpt 0.125000000 0.125000000 0.062500000
      0.375000000 0.125000000 0.062500000
      0.375000000 0.375000000 0.062500000
      0.125000000 0.125000000 0.187500000
      0.375000000 0.125000000 0.187500000
      0.375000000 0.375000000 0.187500000
      0.125000000 0.125000000 0.312500000
      0.375000000 0.125000000 0.312500000
      0.375000000 0.375000000 0.312500000
      0.125000000 0.125000000 0.437500000
      0.375000000 0.125000000 0.437500000
      0.375000000 0.375000000 0.437500000
wtk 0.062500000 0.125000000 0.062500000
      0.062500000 0.125000000 0.062500000
      0.062500000 0.125000000 0.062500000
      0.062500000 0.125000000 0.062500000

```

```

!These parameters are left unchanged:
acell  1.8897261329  1.8897261329  1.8897261329 Bohr
rprim  12.1986207140  0.0000000000  0.0000000000
        0.0000000000  12.1986207140  0.0000000000
        0.0000000000  0.0000000000  5.9549405940
ecut   30.000000 Hartree
tsmear 0.0050000 Hartree
toldfe 0.0000000367493254 Hartree
occopt 3
nband  108
ngfft  120 120 60

```

```

!Changes for the second nonlocal calculation:
!getwfk 3          !The wavefunction and density are read in for
!getden 3          !the second volume of the CP calculation.

```

A.3. Optimized structures, total energies, and breakdowns of total pressures by energy terms

Table A.1. Unit cell parameters for the VASP optimized structures of Ca_5Sn_3 and $\text{Ca}_{36}\text{Sn}_{23}$

	Ca_5Sn_3	$\text{Ca}_{36}\text{Sn}_{23}$
<i>a</i>	12.1864342798648764	12.1519878572427977
<i>c</i>	5.9489916024459149	22.1713863342970328

Table A.2. Reduced coordinates for atoms in VASP optimized structure of Ca_5Sn_3

Atom type	<i>x</i>	<i>y</i>	<i>z</i>
Ca	0.5	0	0.25
Ca	0.5	0	0.75
Ca	0	0.5	0.75
Ca	0	0.5	0.25
Ca	0.415999	0.284427	0.5
Ca	0.215573	0.915999	0
Ca	0.715573	0.415999	0.5
Ca	0.084001	0.784427	0.5
Ca	0.584001	0.284427	0
Ca	0.915999	0.215573	0.5
Ca	0.415999	0.715573	0
Ca	0.215573	0.084001	0.5
Ca	0.715573	0.584001	0
Ca	0.784427	0.915999	0.5
Ca	0.084001	0.215573	0
Ca	0.584001	0.715573	0.5

Ca	0.784427	0.084001	0
Ca	0.284427	0.584001	0.5
Ca	0.915999	0.784427	0
Ca	0.284427	0.415999	0
Sn	0.5	0.5	0.25
Sn	0	0	0.25
Sn	0.5	0.5	0.75
Sn	0	0	0.75
Sn	0.342702	0.842702	0.5
Sn	0.157298	0.342702	0.5
Sn	0.842702	0.342702	0
Sn	0.842702	0.657298	0.5
Sn	0.342702	0.157298	0
Sn	0.657298	0.157298	0.5
Sn	0.157298	0.657298	0
Sn	0.657298	0.842702	0

Table A.3. Reduced coordinates for atoms in VASP optimized structure of $\text{Ca}_{36}\text{Sn}_{23}$

Atom type	x	y	z
Ca	0.944181	0.788422	0.908049
Ca	0.211578	0.944181	0.908049
Ca	0.055819	0.211578	0.908049
Ca	0.288422	0.444181	0.908049
Ca	0.444181	0.711578	0.091951
Ca	0.555819	0.288422	0.091951
Ca	0.288422	0.444181	0.091951
Ca	0.711578	0.555819	0.091951
Ca	0.711578	0.555819	0.908049
Ca	0.444181	0.711578	0.908049
Ca	0.555819	0.288422	0.908049
Ca	0.211578	0.944181	0.091951
Ca	0.944181	0.788422	0.091951
Ca	0.788422	0.055819	0.091951
Ca	0.788422	0.055819	0.908049
Ca	0.055819	0.211578	0.091951
Ca	0.912902	0.784767	0.631103
Ca	0.215232	0.912902	0.631103
Ca	0.087098	0.215232	0.631103
Ca	0.784767	0.087098	0.631103
Ca	0.412902	0.715232	0.368897
Ca	0.587098	0.284768	0.368897
Ca	0.284768	0.412902	0.368897
Ca	0.715232	0.587098	0.368897
Ca	0.412902	0.715232	0.631103
Ca	0.587098	0.284768	0.631103
Ca	0.215232	0.912902	0.368897

Ca	0.912902	0.784767	0.368897
Ca	0.784767	0.087098	0.368897
Ca	0.087098	0.215232	0.368897
Ca	0.284768	0.412902	0.631103
Ca	0.715232	0.587098	0.631103
Ca	0.787273	0.923357	0.760904
Ca	0.076643	0.787273	0.760904
Ca	0.212727	0.076643	0.760904
Ca	0.923357	0.212727	0.760904
Ca	0.287273	0.576643	0.239096
Ca	0.712727	0.423356	0.239096
Ca	0.423356	0.287273	0.239096
Ca	0.576643	0.712727	0.239096
Ca	0.287273	0.576643	0.760904
Ca	0.712727	0.423356	0.760904
Ca	0.076643	0.787273	0.239096
Ca	0.787273	0.923357	0.239096
Ca	0.923357	0.212727	0.239096
Ca	0.212727	0.076643	0.239096
Ca	0.423356	0.287273	0.760904
Ca	0.576643	0.712727	0.760904
Ca	0.416731	0.282083	0.5
Ca	0.217917	0.083269	0.5
Ca	0.916731	0.217917	0.5
Ca	0.583269	0.717917	0.5
Ca	0.782083	0.916731	0.5
Ca	0.083269	0.782083	0.5
Ca	0.717917	0.416731	0.5
Ca	0.282083	0.583269	0.5
Ca	0.834569	0.334569	0
Ca	0.334569	0.165431	0
Ca	0.165431	0.665431	0
Ca	0.665431	0.834569	0
Ca	0.5	0	0.872466
Ca	0.5	0	0.127534
Ca	0	0.5	0.127534
Ca	0	0.5	0.872466
Ca	0.5	0	0.721301
Ca	0.5	0	0.278699
Ca	0	0.5	0.278699
Ca	0	0.5	0.721301
Ca	0.5	0	0.571767
Ca	0	0.5	0.428233
Ca	0.5	0	0.428233
Ca	0	0.5	0.571767
Sn	0.153331	0.653331	0.638892
Sn	0.653331	0.846669	0.638892
Sn	0.846669	0.346669	0.638892

Sn	0.653331	0.846669	0.361108
Sn	0.846669	0.346669	0.361108
Sn	0.346669	0.153331	0.361108
Sn	0.153331	0.653331	0.361108
Sn	0.346669	0.153331	0.638892
Sn	0.303398	0.196602	0.869386
Sn	0.696602	0.803398	0.869386
Sn	0.696602	0.803398	0.130614
Sn	0.303398	0.196602	0.130614
Sn	0.803398	0.303398	0.869386
Sn	0.196602	0.696602	0.869386
Sn	0.196602	0.696602	0.130614
Sn	0.803398	0.303398	0.130614
Sn	0.662822	0.162822	0.783678
Sn	0.662822	0.162822	0.216322
Sn	0.837178	0.662822	0.216322
Sn	0.337178	0.837178	0.216322
Sn	0.837178	0.662822	0.783678
Sn	0.162822	0.337178	0.783678
Sn	0.162822	0.337178	0.216322
Sn	0.337178	0.837178	0.783678
Sn	0.843035	0.656965	0.5
Sn	0.343035	0.843035	0.5
Sn	0.156965	0.343035	0.5
Sn	0.656965	0.156965	0.5
Sn	0.912088	0.587912	0
Sn	0.587912	0.087912	0
Sn	0.412088	0.912088	0
Sn	0.087912	0.412088	0
Sn	0.5	0.5	0.164275
Sn	0.5	0.5	0.835725
Sn	0	0	0.835725
Sn	0	0	0.164275
Sn	0.5	0.5	0.301163
Sn	0	0	0.698837
Sn	0.5	0.5	0.698837
Sn	0	0	0.301163
Sn	0.5	0.5	0.433748
Sn	0	0	0.433748
Sn	0.5	0.5	0.566252
Sn	0	0	0.566252
Sn	0.5	0.5	0
Sn	0	0	0

Table A.4. Data on the total energies and pressure components of structures considered (atomic units)

	Ca ₅ Sn ₃ (valence-only Ca)	Ca ₅ Sn ₃ (semicore Ca)	Ca ₃₆ Sn ₂₃
total energy (ABINIT)	-58.757676168	-778.16450094	-221.67674155
total energy (VASP)	-4.499800907		-16.869428852
kinetic E pressure	0.0036552	0.003576	0.00354703
local psp E pressure	0.0016288	0.037223	0.00165429
Hartree E pressure	-0.000597	-0.0125	-0.00060361
exchange-correlation E pressure	-0.000832	-0.00135	-0.00083634
Ewald E pressure	-0.003587	-0.02925	-0.00361534
-kT × entropy pressure	3.99E-06	4.25E-06	0.00000386
psp core E pressure	0.0011493	0.002326	0.00117043
nonlocal psp E pressure	-0.001513	7.58E-06	-0.00141023
total pressure	-9.2E-05	3.17E-05	-0.00008991

A.4. References

- (1) Filippetti, A.; Fiorentini, V. *Phys. Rev. B* **2000**, *61*, 8433.
- (2) Martin, R. M. *Electronic structure: basic theory and practical methods*; 1st ed.; Cambridge University Press: Cambridge, UK ; New York, 2008.

Appendix B.

Supporting Information for Chapter 4:

Progress in Visualizing Atomic Size Effects with DFT-Chemical Pressure

Analysis: From Isolated Atoms to Trends in AB₅ Intermetallics

The specific information presented here came from the work of Berns, but contributions were made by all authors, especially for the theoretical analyses of the structures shown in Figures 4.2 and 4.3. Section B.3 was primarily the work of Berns. Section B.4 was primarily the work of Guo.

B.1. Detailed Technical Procedures

The geometrical optimization of each structure was carried out in two steps: first the ionic positions were relaxed in a fixed unit cell, and then all structural parameters were released. Energy cutoffs for the planewave basis were set sufficiently high to converge the energy of formation to less than 0.5 meV/atom. Monkhorst-Pack k-point grids¹ were constructed by specifying the `ngkpt` input parameter or by using the `prtkpt` utility. Unless otherwise specified, semicore HGH potentials² (when available) were used for all atoms, with the exception of Pd, for which the valence-only version is most comparable to the semicore pseudopotentials of Cu, Ag and Au. Further details regarding the calculations are given in Table B.1, while the optimized structural parameters are listed in Tables B.2-B.11.

Once the optimizations were complete, three single-point calculations were performed over a span of 3% about the optimal unit cell volume to prepare the electron densities, potentials, and kinetic energy densities needed for the creation of CP maps. The voxel spacing in the CP maps were derived from the fast Fourier transform grids used in the ABINIT calculations. The DFT-CP software is based on two programs used to calculate the CP maps, as well as integrate and project the CP distribution around each atom. *CPmap* generates the CP maps from the ABINIT single point calculations, and including the grid unwarping procedure described in the main text. The Hirshfeld-inspired integration scheme is implemented in the *CPintegrate* program, which was used to project the CP map onto real spherical harmonics ($l \leq 5$) centered at the atomic positions.

Table B.1. Computational parameters and total energies

Structure ^a	Energy cutoff	Number of unique k-points	FFT grid	Total energy
Isolated Ca (SC)	35 Ha	1	150 × 150 × 150	-36.640997 Ha
Isolated Ca (VO)	35 Ha	1	150 × 150 × 150	-0.668313 Ha
Isolated La	40 Ha	1	150 × 150 × 150	-31.592133 Ha
Isolated Cu	45 Ha	1	120 × 120 × 120	-46.910665 Ha
Isolated Pd	40 Ha	1	150 × 150 × 150	-28.799283 Ha
Isolated Cd	35 Ha	1	150 × 150 × 150	-45.998438 Ha
Isolated Au	80 Ha	1	150 × 150 × 150	-33.160002 Ha
Isolated Ga (SC)	80 Ha	1	150 × 150 × 150	-74.004191 Ha
Isolated Ga (VO)	80 Ha	1	150 × 150 × 150	-2.149122 Ha
SrAg ₅	50 Ha	15	150 × 150 × 120	-215.769000 Ha
La ₅ Sn ₃	40 Ha	4	108 × 108 × 108	-339.327910 Ha
Ni ₃ C	80 Ha	60	80 × 80 × 80	-234.948791 Ha
NbGa ₃	50 Ha	18	75 × 75 × 75	-12.047973 Ha
CaCu ₅ (CaCu ₅ -type)	85 Ha	15	150 × 150 × 120	-277.195271 Ha
CaCu ₅ (AuBe ₅ -type)	85 Ha	10	150 × 150 × 150	-1108.722801 Ha
CaAu ₅ (CaCu ₅ -type)	30 Ha	15	150 × 150 × 120	-203.316309 Ha
CaAu ₅ (AuBe ₅ -type)	30 Ha	10	120 × 120 × 120	-813.277045 Ha

^a“Isolated” refers to a single atom placed in the center of a 10 Å cubic unit cell. See Tables B.2 and B.3.

B.2. Structural parameters

Table B.2. Unit cell parameters for DFT-optimized structures (converted to conventional cells)

Structure	a	b	c	α	β	γ
All isolated atoms	10.00000 Å	10.00000 Å	10.00000 Å	90°	90°	90°
SrAg ₅	5.55915 Å	5.55915 Å	4.54145 Å	90°	90°	120°
La ₅ Sn ₃	12.59205 Å	12.59205 Å	6.17215 Å	90°	90°	90°
Ni ₃ C	4.49667 Å	4.49667 Å	12.71836 Å	90°	90°	120°
NbGa ₃	3.68337 Å	3.68337 Å	8.52030 Å	90°	90°	90°
CaCu ₅ (CaCu ₅ -type)	4.97267 Å	4.97267 Å	3.97010 Å	90°	90°	120°
CaCu ₅ (AuBe ₅ -type)	6.88885 Å	6.88885 Å	6.88885 Å	90°	90°	90°
CaAu ₅ (CaCu ₅ -type)	5.48234 Å	5.48234 Å	4.63381 Å	90°	90°	120°
CaAu ₅ (AuBe ₅ -type)	7.71309 Å	7.71309 Å	7.71309 Å	90°	90°	90°

Table B.3. Atomic coordinates for all single-atom calculations

Element	x	y	z
any	0.50000	0.50000	0.50000

Table B.4. Atomic coordinates for ABINIT-optimized SrAg₅ structure

Element	x	y	z
Sr	0.00000	0.00000	0.00000
Ag	0.33333	0.66667	0.00000
Ag	0.66667	0.33333	0.00000
Ag	0.50000	0.50000	0.50000
Ag	0.00000	0.50000	0.50000
Ag	0.50000	0.00000	0.50000

Table B.5. Atomic coordinates for ABINIT-optimized La₅Sn₃ structure (conventional cell)

Element	x	y	z
La	0.08563	0.21856	0.00000
La	0.58563	0.71856	0.50000
La	0.00000	0.50000	0.25000
La	0.50000	0.00000	0.75000
La	0.78144	0.08563	0.00000
La	0.28144	0.58563	0.50000
La	0.50000	0.00000	0.25000
La	0.00000	0.50000	0.75000
La	0.91437	0.21856	0.50000
La	0.41437	0.71856	0.00000
La	0.41437	0.28144	0.50000
La	0.91437	0.78144	0.00000
La	0.28144	0.41437	0.00000
La	0.78144	0.91437	0.50000
La	0.21856	0.08563	0.50000
La	0.71856	0.58563	0.00000

La	0.71856	0.41437	0.50000
La	0.21856	0.91437	0.00000
La	0.58563	0.28144	0.00000
La	0.08563	0.78144	0.50000
Sn	0.15987	0.65987	0.00000
Sn	0.65987	0.15987	0.50000
Sn	0.00000	0.00000	0.25000
Sn	0.50000	0.50000	0.75000
Sn	0.34013	0.15987	0.00000
Sn	0.84013	0.65987	0.50000
Sn	0.34013	0.84013	0.50000
Sn	0.84013	0.34013	0.00000
Sn	0.15987	0.34013	0.50000
Sn	0.65987	0.84013	0.00000
Sn	0.00000	0.00000	0.75000
Sn	0.50000	0.50000	0.25000

Table B.6. Atomic coordinates for ABINIT-optimized NbGa₃ structure (conventional cell)

Element	x	y	z
Nb	0.00000	0.00000	0.00000
Nb	0.50000	0.50000	0.50000
Ga	0.00000	0.00000	0.50000
Ga	0.50000	0.50000	0.00000
Ga	0.00000	0.50000	0.25000
Ga	0.50000	0.00000	0.75000
Ga	0.50000	0.00000	0.25000
Ga	0.00000	0.50000	0.75000

Table B.7. Atomic coordinates for VASP-optimized Ni₃C structure (conventional cell)

Element	x	y	z
Ni	0.33333	0.00000	0.25000
Ni	0.66667	0.00000	0.75000
Ni	0.00000	0.33333	0.25000
Ni	0.00000	0.66667	0.75000
Ni	0.66667	0.66667	0.25000
Ni	0.33333	0.33333	0.75000
Ni	0.00000	0.33333	0.08333
Ni	0.33333	0.33333	0.58333
Ni	0.66667	0.66667	0.41667
Ni	0.66667	0.00000	0.58333
Ni	0.33333	0.00000	0.41667
Ni	0.00000	0.66667	0.58333
Ni	0.66667	0.66667	0.08333
Ni	0.00000	0.66667	0.91667
Ni	0.33333	0.00000	0.08333
Ni	0.33333	0.33333	0.91667
Ni	0.00000	0.33333	0.41667
Ni	0.66667	0.00000	0.91667

C	0.00000	0.00000	0.00000
C	0.00000	0.00000	0.50000
C	0.66667	0.33333	0.33333
C	0.66667	0.33333	0.83333
C	0.33333	0.66667	0.66667
C	0.33333	0.66667	0.16667

Table B.8. Atomic coordinates for ABINIT-optimized CaCu_5 structure (CaCu_5 -type)

Element	x	y	z
Ca	0.00000	0.00000	0.00000
Cu	0.33333	0.66667	0.00000
Cu	0.66667	0.33333	0.00000
Cu	0.50000	0.50000	0.50000
Cu	0.00000	0.50000	0.50000
Cu	0.50000	0.00000	0.50000

Table B.9. Atomic coordinates for ABINIT-optimized CaCu_5 structure (AuBe_5 -type)

Element	x	y	z
Ca	0.00000	0.00000	0.00000
Ca	0.50000	0.50000	0.00000
Ca	0.00000	0.50000	0.50000
Ca	0.50000	0.00000	0.50000
Cu	0.25000	0.25000	0.25000
Cu	0.62500	0.62500	0.62500
Cu	0.75000	0.75000	0.25000
Cu	0.37500	0.37500	0.62500
Cu	0.75000	0.25000	0.75000
Cu	0.37500	0.62500	0.37500
Cu	0.25000	0.75000	0.75000
Cu	0.62500	0.37500	0.37500
Cu	0.12500	0.12500	0.62500
Cu	0.87500	0.87500	0.62500
Cu	0.87500	0.12500	0.37500
Cu	0.12500	0.87500	0.37500
Cu	0.62500	0.12500	0.12500
Cu	0.37500	0.87500	0.12500
Cu	0.37500	0.12500	0.87500
Cu	0.62500	0.87500	0.87500
Cu	0.12500	0.62500	0.12500
Cu	0.87500	0.37500	0.12500
Cu	0.87500	0.62500	0.87500
Cu	0.12500	0.37500	0.87500

Table B.10. Atomic coordinates for ABINIT-optimized CaAu₅ structure (CaCu₅-type)

Element	x	y	z
Ca	0.00000	0.00000	0.00000
Au	0.33333	0.66667	0.00000
Au	0.66667	0.33333	0.00000
Au	0.50000	0.50000	0.50000
Au	0.00000	0.50000	0.50000
Au	0.50000	0.00000	0.50000

Table B.11. Atomic coordinates for ABINIT-optimized CaAu₅ structure (AuBe₅-type)

Element	x	y	z
Ca	0.00000	0.00000	0.00000
Ca	0.50000	0.50000	0.00000
Ca	0.00000	0.50000	0.50000
Ca	0.50000	0.00000	0.50000
Au	0.25000	0.25000	0.25000
Au	0.62500	0.62500	0.62500
Au	0.75000	0.75000	0.25000
Au	0.37500	0.37500	0.62500
Au	0.75000	0.25000	0.75000
Au	0.37500	0.62500	0.37500
Au	0.25000	0.75000	0.75000
Au	0.62500	0.37500	0.37500
Au	0.12500	0.12500	0.62500
Au	0.87500	0.87500	0.62500
Au	0.87500	0.12500	0.37500
Au	0.12500	0.87500	0.37500
Au	0.62500	0.12500	0.12500
Au	0.37500	0.87500	0.12500
Au	0.37500	0.12500	0.87500
Au	0.62500	0.87500	0.87500
Au	0.12500	0.62500	0.12500
Au	0.87500	0.37500	0.12500
Au	0.87500	0.62500	0.87500
Au	0.12500	0.37500	0.87500

B.3. Discussion of the prevalence of highly positive CP features in the atomic core regions that are oriented between internuclear vectors, rather than along them

In Figure 4.4f, strong chemical pressure features are observed in the core regions of the Ca atoms. The directionality of these features would suggest that they arise from interatomic interactions, but they are

awkwardly oriented along the boundaries between contact volumes. This is in fact a specific example of an interesting trend that we have observed for a variety of phases, which we will now explore. In Figure B.1, we show isosurfaces of the CP maps generated for a series of structures, with the isosurface level set to a sufficiently high level that only the most intense, positive pressure features are visible. For all of the structures shown, the isosurfaces reveal lobes that are directed into interstitial spaces rather than along the interatomic contacts.

For CaPd_2 (Figure B.1a), the tetrapod of white pressure isosurfaces around each calcium atom point not to the nearest calcium neighbor, but to the centers of the triangular faces of the surrounding Pd truncated tetrahedron. This is echoed in Figure B.1b, where similar four-pronged pressures on the elemental silicon point into the interstices. On CrGa_4 in the PtHg_4 type^{3,4} (Figure B.1c), the octahedral arrangement of lobes around the Cr atoms appears to suggest positive pressures along Cr-Cr contacts, but the 5.5 Å bond length suggests this is quite far from a too-close contact ($2 \times d_{\text{Cr}} = 2 \times 1.28 = 2.56$ Å). Finally, the niobium atom in NbGa_3 ⁵ (Figure B.1d) exhibits these pressure features oriented toward the top and bottom square faces of a cuboctahedron of gallium atoms. These features point out of the *ab* plane of the Nb atom, in which the closest Nb-Ga contacts occur (2.65 Å vs 2.86 Å for out-of-plane contacts). What is the source of these features of the chemical pressure maps?

A straightforward approach to investigating the origins of these features is to plot the contributions to the CP maps from specific terms in the total energy. For simplicity, we will pursue this approach here with just for elemental silicon, though the same could be carried out for all of the structures depicted in Figure 4.1.

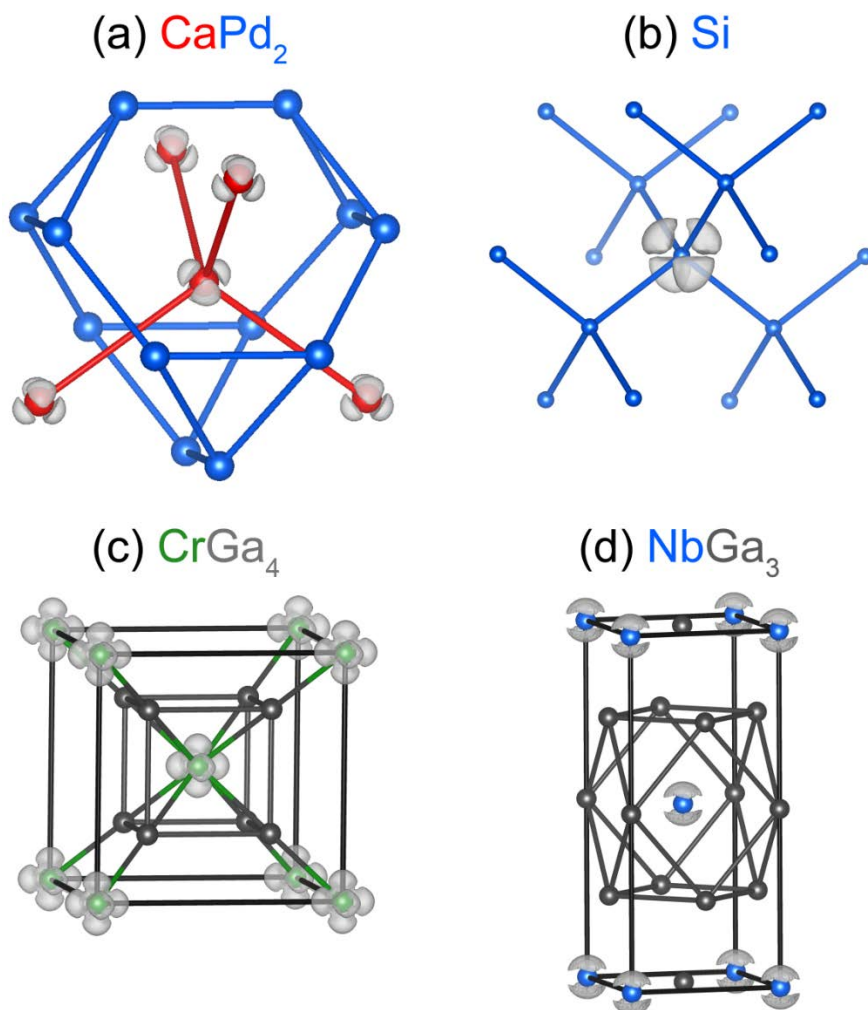


Figure B.1. Positive chemical pressure is shown for a series of solid state structures. (a) CaPd_2 in the MgCu_2 -type Laves phase at an isosurface value of 0.075 a.u. This is a 3-dimensional plot of the strongest positive features seen in Figure 4.4f. These positive pressure features point not between atomic contacts, but rather to the void spaces in the structure. The same trend can be seen for (b) elemental Si, plotted at an isosurface value of 0.022 a.u., (c) CrGa_4 in the PtHg_4 type, plotted at 0.083, and (d) NbGa_3 in the TiAl_3 type, plotted at 0.085.

After examining separately each energetic contribution to the chemical pressure, we found that the major contribution to these positive pressure features was the local potential component of the total energy. In Figure B.2, we see the difference in the local potential on going from a slightly expanded

structure to a slightly contracted one. This is akin to computing only the local potential component of the chemical pressure, without multiplying by the electron density and dividing by the change in volume.

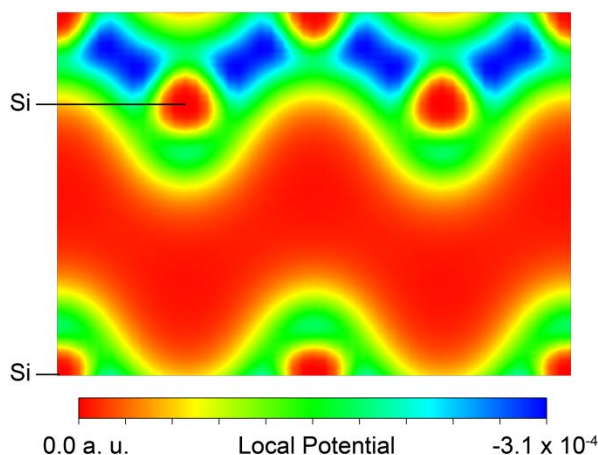


Figure B.2. The difference between the local potential surfaces of elemental silicon from the expanded unit cell volume to the contracted unit cell volume, corrected for distortion using CPmap. The (110) plane of the structure is depicted to capture the interatomic interactions.

We note first that this function is non-positive over the entire unit cell. This implies that the potential becomes universally more negative as the cell contracts, with nearly zero change far from the nuclei. The largest changes are, in fact, between silicon atoms, implying a drastic deepening of the potential on contraction of the unit cell, as is expected for a model of overlapping potential wells. As the atoms are forced closer together, the overlap of the potentials increases, and electrons in the middle ground experience a stronger interaction with both nuclei. This strongly negative component lies directly in line with interatomic contact. When calculating the chemical pressure, the local component depicted in Figure B.2 provides a severe negative component between atoms, which counteracts the strong positive features

normally present in the core of the atom. The positive core features remain unopposed in the other directions around an atomic center, with the net result being the appearance of relatively intense positive pressure features appearing in the core regions away from the interatomic vectors for strong interactions.

Figure B.3 shows the integrated results for the chemical pressure calculation on elemental silicon. Si-Si contacts are nearly optimal, with only small white lobes pointing between them. No longer do we see the high positive pressures observed in Figure B.1b; in their place are negative lobes, pointing to interstitial voids within the diamond framework, better reflecting our chemical intuition of this structure.

The integration step correctly disperses the strongly positive features (as seen in Figure 4.4f), resulting in interatomic pressures that well-represent the full interaction.

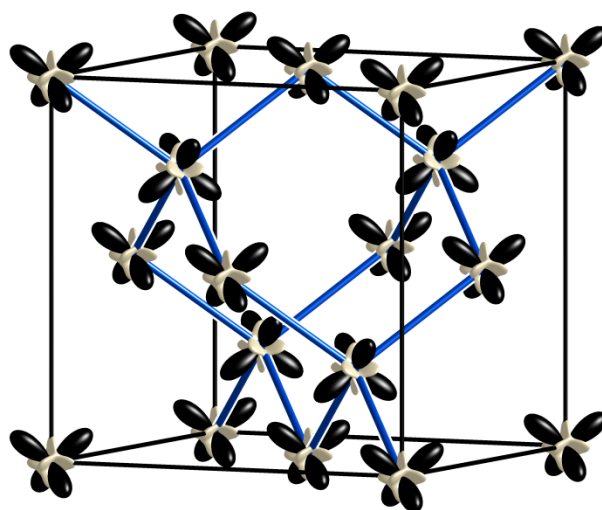


Figure B.3. The DFT-CP anisotropies calculated for elemental silicon. Pressures are near optimal between silicon atoms, as expected. Negative pressure features point towards void spaces in the structure.

B.4. Voxel volume calculation in distorted grid

Since the grid unwarping procedure leads to shifts of grid points relative to a uniform grid, the volume associated with each voxel is no longer constant. The calculation of the corrected voxel volumes is important for subsequent integration over the grids, but the computational cost for an exact calculation of voxel volumes can be prohibitive. Here we present the approximate calculation adopted in the *CPmap* program and demonstrate that it gives satisfyingly accurate results for small distortions of the grid.

In the following discussion, we use $(\mathbf{p}, \mathbf{q}, \mathbf{r}) \equiv (\mathbf{p} \times \mathbf{q}) \cdot \mathbf{r} \equiv \begin{vmatrix} p_x & p_y & p_z \\ q_x & q_y & q_z \\ r_x & r_y & r_z \end{vmatrix}$ to denote the triple product

of three-dimensional vectors $\mathbf{p}, \mathbf{q}, \mathbf{r}$.

For an undistorted grid, each voxel takes the shape of a parallelepiped, so its volume is simply given by

$$V_{\text{voxel}} = (\mathbf{a}_{\text{voxel}}, \mathbf{b}_{\text{voxel}}, \mathbf{c}_{\text{voxel}})$$

where $\mathbf{a}_{\text{voxel}}, \mathbf{b}_{\text{voxel}}, \mathbf{c}_{\text{voxel}}$ are the three edge vectors of the undistorted voxel parallelepiped. Here we take voxel 000 to be the voxel of interest, where 000 is its index $n_x n_y n_z$ in the voxel grid. If we consider the coordinates of its six direct neighbors, it can be seen that

$$r_{100} - r_{\bar{1}00} = 2\mathbf{a}_{\text{voxel}}, r_{010} - r_{0\bar{1}0} = 2\mathbf{b}_{\text{voxel}}, r_{001} - r_{00\bar{1}} = 2\mathbf{c}_{\text{voxel}}$$

So we can write its voxel volume as an expression of the coordinates of its neighbors:

$$\begin{aligned} V_{000} &= (\mathbf{a}_{\text{voxel}}, \mathbf{b}_{\text{voxel}}, \mathbf{c}_{\text{voxel}}) = \frac{1}{8}(2\mathbf{a}_{\text{voxel}}, 2\mathbf{b}_{\text{voxel}}, 2\mathbf{c}_{\text{voxel}}) \\ &= \frac{1}{8}(\mathbf{r}_{100} - \mathbf{r}_{\bar{1}00}, \mathbf{r}_{010} - \mathbf{r}_{0\bar{1}0}, \mathbf{r}_{001} - \mathbf{r}_{00\bar{1}}) \end{aligned} \tag{B.1}$$

As will be shown in the discussion below, Equation B.1 can also be applied to approximately to the distorted grid. We will see that this equation captures the essential effect of distortion of neighboring voxels on a voxel's volume, and also preserves (to first order) the sum of all voxel volumes as equal to the total unit cell volume.

Lemma. For a change in the position of any of the six direct neighbor voxels to 000, the first order change to V_{000} (as defined by Equation B.1) will be $\frac{1}{2} \Delta k \cdot V_{\text{voxel}}$, where Δk is the perturbation along the corresponding voxel edge vector away from 000. The other components of the displacement have only higher order effects.

Proof. In a distorted grid, any voxel may experience a perturbation $\Delta \mathbf{r}_{n_x, n_y, n_z}$, so we have

$$\begin{aligned} V'_{000} &= \frac{1}{8} ((r_{100} - r_{\bar{1}00}) + (\Delta r_{100} - \Delta r_{\bar{1}00}), (r_{010} - r_{0\bar{1}0}) + (\Delta r_{010} - \Delta r_{0\bar{1}0}), (r_{001} - r_{00\bar{1}}) + (\Delta r_{001} - \Delta r_{00\bar{1}})) \\ &= \frac{1}{8} (2\mathbf{a}_{\text{voxel}} + (\Delta r_{100} - \Delta r_{\bar{1}00}), 2\mathbf{b}_{\text{voxel}} + (\Delta r_{010} - \Delta r_{0\bar{1}0}), 2\mathbf{c}_{\text{voxel}} + (\Delta r_{001} - \Delta r_{00\bar{1}})) \quad (\text{B.2}) \end{aligned}$$

Since the triple product is linear with respect to each variable, an expansion of Equation B.2 gives

$$\begin{aligned} \Delta V_{000} &= V'_{000} - V_{000} \\ &= \frac{1}{8} [(\Delta r_{100} - \Delta r_{\bar{1}00}, 2\mathbf{b}_{\text{voxel}}, 2\mathbf{c}_{\text{voxel}}) + (2\mathbf{b}_{\text{voxel}}, \Delta r_{010} - \Delta r_{0\bar{1}0}, 2\mathbf{c}_{\text{voxel}}) + (2\mathbf{a}_{\text{voxel}}, 2\mathbf{b}_{\text{voxel}}, \Delta r_{001} - \Delta r_{00\bar{1}})] \\ &\quad + 2^{nd} \text{ and higher order terms} \\ &= \frac{1}{8} [(\Delta r_{100}, 2\mathbf{b}_{\text{voxel}}, 2\mathbf{c}_{\text{voxel}}) + (2\mathbf{b}_{\text{voxel}}, \Delta r_{010}, 2\mathbf{c}_{\text{voxel}}) + (2\mathbf{a}_{\text{voxel}}, 2\mathbf{b}_{\text{voxel}}, \Delta r_{001})] \\ &\quad - \frac{1}{8} [(\Delta r_{\bar{1}00}, 2\mathbf{b}_{\text{voxel}}, 2\mathbf{c}_{\text{voxel}}) + (2\mathbf{b}_{\text{voxel}}, \Delta r_{0\bar{1}0}, 2\mathbf{c}_{\text{voxel}}) + (2\mathbf{a}_{\text{voxel}}, 2\mathbf{b}_{\text{voxel}}, \Delta r_{00\bar{1}})] \\ &\quad + 2^{nd} \text{ and higher order terms} \quad (\text{B.3}) \end{aligned}$$

Here we focus only on the $\Delta \mathbf{r}_{100}$ term, since the other five terms can be treated with a similar approach.

If we rewrite $\Delta \mathbf{r}_{100}$ as a linear combination of the three voxel edge vectors, i.e.

$$\Delta \mathbf{r}_{100} = \Delta k_{100a} \mathbf{a}_{\text{voxel}} + \Delta k_{100b} \mathbf{b}_{\text{voxel}} + \Delta k_{100c} \mathbf{c}_{\text{voxel}}$$

the term becomes

$$\begin{aligned} \frac{1}{8} (\Delta \mathbf{r}_{100}, 2\mathbf{b}_{\text{voxel}}, 2\mathbf{c}_{\text{voxel}}) &= \frac{1}{8} (\Delta k_{100a} \mathbf{a}_{\text{voxel}} + \Delta k_{100b} \mathbf{b}_{\text{voxel}} + \Delta k_{100c} \mathbf{c}_{\text{voxel}}, 2\mathbf{b}_{\text{voxel}}, 2\mathbf{c}_{\text{voxel}}) \\ &= \frac{1}{8} (\Delta k_{100a} \mathbf{a}_{\text{voxel}}, 2\mathbf{b}_{\text{voxel}}, 2\mathbf{c}_{\text{voxel}}) = \frac{1}{2} \Delta k_{100a} \cdot V_{\text{voxel}} \end{aligned}$$

That is, for voxel 100, only a perturbation along the $\mathbf{a}_{\text{voxel}}$ direction has a first order effect on the voxel volume of $\frac{1}{2} \Delta k_{100a} \cdot V_{\text{voxel}}$, while perturbation along $\mathbf{b}_{\text{voxel}}$ and $\mathbf{c}_{\text{voxel}}$ has no effect (it only introduces a shearing of the parallelepiped, which does not affect its volume). ■

Proposition. The change in total volume of all voxels as calculated using Equation B.1 in a distorted grid is second order with respect to the distortion.

Proof. We will still focus our discussion on voxel 100. Following from the lemma above, we only need to consider a movement along the $\mathbf{a}_{\text{voxel}}$ direction. Such a perturbation will change the volume of voxel 000 by $\frac{1}{2} \Delta k_{100a} \cdot V_{\text{voxel}}$, but it also changes the volume of voxel 200 by $-\frac{1}{2} \Delta k_{100a} \cdot V_{\text{voxel}}$. Therefore the first order perturbations cancel out, so we are left with only the higher order terms in Equation B.3. It so follows that

$$\sum_{n_x, n_y, n_z} \Delta V_{n_x, n_y, n_z} = O(|\Delta \mathbf{r}_{n_x, n_y, n_z}|^2)$$

i.e. the change in total volume of all voxels in the unit cell is second order with respect to the distortion. ■

In all calculations carried out in this Article, the volumes of the voxels in the distorted grid add up to the unit cell volume within 0.00001 \AA^3 . This threshold can be adjusted in the source code if testing to higher precision is desired.

B.5. References

- (1) Monkhorst, H.; Pack, J. *Phys. Rev. B* **1976**, *13*, 5188-5192.
- (2) Hartwigsen, C.; Goedecker, S.; Hutter, J. *Phys. Rev. B* **1998**, *58*, 3641-3662.
- (3) Meissner, H.-G.; Schubert, K. *Z. Metallkd.* **1965**, *56*, 523-530.
- (4) Häussermann, U.; Viklund, P.; Boström, M.; Norrestam, R.; Simak, S. *Phys. Rev. B* **2001**, *63*.
- (5) Baron, V. V.; Myzenkova, L. F.; Savitskii, E. M.; Gladyshevskii, E. I. *Zh. Neorg. Khim.* **1964**, *9*, 2170-2173.

Appendix C.

Supporting Information for Chapter 5:

Chemical Pressure Schemes for the Prediction of Soft Phonon Modes: A

Chemist's Guide to the Vibrations of Solid State Materials

C.1. Technical details

Table C.1. Computational parameters and total energies for CP calculations with ABINIT

Structure	Energy cutoff	k-point vectors ^a	k-point shift	FFT grid	Total energy
CaPd ₂ (LDA)	75.00 Ha	4 4 -4 -4 4 -4 -4 4 4	0.5 0.5 0.5	128 × 128 × 128	-189.488440 Ha
Nb ₃ Ge (LDA)	40.00 Ha	5 0 0 0 5 0 0 0 5	0.0 0.0 0.0	72 × 72 × 72	-39.346400 Ha
CaPd ₅ (LDA)	80.00 Ha	5 0 0 0 5 0 0 0 6	0.0 0.0 0.5	96 × 96 × 80	-181.631403 Ha

^aThree vectors that define a real-space super-lattice whose reciprocal lattice defines the k-point grid

Table C.2. Computational parameters for response function calculations with ABINIT

Structure	Energy cutoff	k-point grid	k-point shift	FFT grid	q-points
CaPd ₂ (LDA)	75.00 Ha	5 × 5 × 5	0.0 0.0 0.0	80 × 80 × 80	10
Nb ₃ Ge (LDA)	40.00 Ha	5 × 5 × 5	0.0 0.0 0.0	60 × 60 × 60	10
CaPd ₅ (LDA)	80.00 Ha	5 × 5 × 7	0.0 0.0 0.0	80 × 80 × 72	20

Table C.3. Computational parameters and total energies for Bader calculations with VASP

Structure	Energy cutoff	k-point grid	FFT grid	Fine FFT grid ^a	Total energy
CaPd ₂ (PAW-GGA)	5.17 Ha	12 × 12 × 12	34 × 34 × 34	54 × 54 × 54	-29.076115 eV
Nb ₃ Ge (PAW-GGA)	5.19 Ha	20 × 20 × 20	32 × 32 × 32	54 × 54 × 54	-72.316164 eV
CaPd ₅ (PAW-GGA)	5.17 Ha	19 × 19 × 20	36 × 36 × 28	50 × 50 × 42	-30.297229 eV

^aThe second, finer FFT mesh around the atomic centers in the PAW method

C.2. Optimized structural parameters

Table C.4. Unit cell parameters for DFT-optimized structures (converted to conventional cell)

Structure	<i>a</i>	<i>b</i>	<i>c</i>	α	β	γ
CaPd ₂ (LDA)	7.56926 Å	7.56926 Å	7.56926 Å	90°	90°	90°
CaPd ₂ (PAW-GGA)	7.73955 Å	7.73955 Å	7.73955 Å	90°	90°	90°
Nb ₃ Ge (LDA)	5.05050 Å	5.05050 Å	5.05050 Å	90°	90°	90°
Nb ₃ Ge (PAW-GGA)	5.15611 Å	5.15611 Å	5.15611 Å	90°	90°	90°
CaPd ₅ (LDA)	5.25376 Å	5.25376 Å	4.38444 Å	90°	90°	120°
CaPd ₅ (PAW-GGA)	5.34490 Å	5.34490 Å	4.47471 Å	90°	90°	120°

Table C.5. Fractional atomic coordinates for the ABINIT-optimized CaPd₂ structure

Element	<i>x</i>	<i>y</i>	<i>z</i>
Ca	0.00000	0.00000	0.00000
Ca	0.50000	0.50000	0.00000
Ca	0.50000	0.00000	0.50000
Ca	0.00000	0.50000	0.50000
Ca	0.25000	0.25000	0.25000
Ca	0.75000	0.75000	0.25000
Ca	0.75000	0.25000	0.75000
Ca	0.25000	0.75000	0.75000
Pd	0.62500	0.62500	0.62500
Pd	0.12500	0.12500	0.62500
Pd	0.12500	0.62500	0.12500
Pd	0.62500	0.12500	0.12500
Pd	0.37500	0.37500	0.62500
Pd	0.87500	0.87500	0.62500
Pd	0.87500	0.37500	0.12500
Pd	0.37500	0.87500	0.12500
Pd	0.37500	0.62500	0.37500
Pd	0.87500	0.12500	0.37500
Pd	0.87500	0.62500	0.87500
Pd	0.37500	0.12500	0.87500
Pd	0.62500	0.37500	0.37500
Pd	0.12500	0.87500	0.37500
Pd	0.12500	0.37500	0.87500
Pd	0.62500	0.87500	0.87500

Table C.6. Fractional atomic coordinates for the VASP-optimized CaPd₂ structure

Element	x	y	z
Ca	0.00000	0.00000	0.00000
Ca	0.50000	0.50000	0.00000
Ca	0.50000	0.00000	0.50000
Ca	0.00000	0.50000	0.50000
Ca	0.25000	0.25000	0.25000
Ca	0.75000	0.75000	0.25000
Ca	0.75000	0.25000	0.75000
Ca	0.25000	0.75000	0.75000
Pd	0.62500	0.62500	0.62500
Pd	0.12500	0.12500	0.62500
Pd	0.12500	0.62500	0.12500
Pd	0.62500	0.12500	0.12500
Pd	0.37500	0.37500	0.62500
Pd	0.87500	0.87500	0.62500
Pd	0.87500	0.37500	0.12500
Pd	0.37500	0.87500	0.12500
Pd	0.37500	0.62500	0.37500
Pd	0.87500	0.12500	0.37500
Pd	0.87500	0.62500	0.87500
Pd	0.37500	0.12500	0.87500
Pd	0.62500	0.37500	0.37500
Pd	0.12500	0.87500	0.37500
Pd	0.12500	0.37500	0.87500
Pd	0.62500	0.87500	0.87500

Table C.7. Fractional atomic coordinates for the ABINIT-optimized Nb₃Ge structure

Element	x	y	z
Nb	0.25000	0.00000	0.50000
Nb	0.75000	0.00000	0.50000
Nb	0.50000	0.25000	0.00000
Nb	0.50000	0.75000	0.00000
Nb	0.00000	0.50000	0.25000
Nb	0.00000	0.50000	0.75000
Ge	0.00000	0.00000	0.00000
Ge	0.50000	0.50000	0.50000

Table C.8. Fractional atomic coordinates for the VASP-optimized Nb₃Ge structure

Element	x	y	z
Nb	0.25000	0.00000	0.50000
Nb	0.75000	0.00000	0.50000
Nb	0.50000	0.25000	0.00000
Nb	0.50000	0.75000	0.00000
Nb	0.00000	0.50000	0.25000
Nb	0.00000	0.50000	0.75000
Ge	0.00000	0.00000	0.00000

Ge	0.50000	0.50000	0.50000
----	---------	---------	---------

Table C.9. Fractional atomic coordinates for the ABINIT-optimized CaPd₅ structure

Element	x	y	z
Ca	0.00000	0.00000	0.00000
Pd	0.33333	0.66667	0.00000
Pd	0.66667	0.33333	0.00000
Pd	0.50000	0.00000	0.50000
Pd	0.00000	0.50000	0.50000
Pd	0.50000	0.50000	0.50000

Table C.10. Fractional atomic coordinates for the VASP-optimized CaPd₅ structure

Element	x	y	z
Ca	0.00000	0.00000	0.00000
Pd	0.33333	0.66667	0.00000
Pd	0.66667	0.33333	0.00000
Pd	0.50000	0.00000	0.50000
Pd	0.00000	0.50000	0.50000
Pd	0.50000	0.50000	0.50000

Appendix D.

Supporting Information for Chapter 6:

Electronic and Chemical Pressure Effects on the Stability Range of Intermetallic Intergrowths: Pushing the Limits of the HoCoGa₅ type with ScTGa₅ (T = Fe, Co, Ni) Phases

The additional theoretical details and supplementary analyses detailed in this chapter are the work of Engelkemier and Fredrickson.

D.1. Additional computational details

Table D.1. Computational parameters and total energies of CP calculations with Abinit

Structure	Energy cutoff	k-point grid	k-point shift			FFT grid	Total energy
ScFeGa ₅ (LDA)	155.00 Ha	6 × 6 × 4	0.5	0.5	0.5	108 × 108 × 108	-438.705286 Ha
ScCoGa ₅ (LDA)	155.00 Ha	6 × 6 × 4	0.5	0.5	0.5	108 × 108 × 108	-446.229264 Ha
ScNiGa ₅ (LDA)	155.00 Ha	6 × 6 × 4	0.5	0.5	0.5	108 × 108 × 108	-455.266418 Ha

Table D.2. Computational parameters of phonon calculations with Abinit

Structure	Energy cutoff	k-point grid	k-point shift			FFT grid	q-points
ScFeGa ₅ (LDA)	135.00 Ha	5 × 5 × 3	0.0	0.0	0.0	90 × 90 × 135	12
ScCoGa ₅ (LDA)	135.00 Ha	5 × 5 × 3	0.0	0.0	0.0	80 × 80 × 135	12
ScNiGa ₅ (LDA)	135.00 Ha	5 × 5 × 3	0.0	0.0	0.0	90 × 90 × 135	12

Table D.3. Computational parameters and total energies of raMO and Bader calculations with VASP

Structure	Energy cutoff	k-point grid	FFT grid	Fine FFT grid*	Total energy
ScFeGa ₅ (PAW-GGA)	5.10 Ha	20 × 20 × 14	28 × 28 × 42	40 × 40 × 70	-31.606136 eV
ScCoGa ₅ (PAW-GGA)	5.10 Ha	20 × 20 × 14	28 × 28 × 42	40 × 40 × 64	-30.838431 eV
ScNiGa ₅ (PAW-GGA)	5.10 Ha	20 × 20 × 14	28 × 28 × 40	42 × 42 × 70	-29.262343 eV

*The second, finer FFT-mesh around the atomic centers in the PAW method

D.2. Optimized structural parameters

Table D.4. Unit cell parameters for DFT-optimized structures

Structure	<i>a</i>	<i>b</i>	<i>c</i>	α	β	γ
ScFeGa ₅ (LDA)	4.05210 Å	4.05210 Å	6.49871 Å	90°	90°	90°
ScCoGa ₅ (LDA)	4.04393 Å	4.04393 Å	6.48028 Å	90°	90°	90°
ScNiGa ₅ (LDA)	4.06404 Å	4.06404 Å	6.48288 Å	90°	90°	90°
ScFeGa ₅ (PAW-GGA)	4.14168 Å	4.14168 Å	6.66943 Å	90°	90°	90°
ScCoGa ₅ (PAW-GGA)	4.13672 Å	4.13672 Å	6.64535 Å	90°	90°	90°
ScNiGa ₅ (PAW-GGA)	4.18788 Å	4.18788 Å	6.58447 Å	90°	90°	90°

Table D.5. Fractional atomic coordinates for the Abinit-optimized ScFeGa₅ structure

Element	<i>x</i>	<i>y</i>	<i>z</i>
Sc	0.00000	0.00000	0.00000
Fe	0.00000	0.00000	0.50000
Ga	0.50000	0.50000	0.00000
Ga	0.50000	0.00000	0.30339
Ga	0.00000	0.50000	0.30339
Ga	0.50000	0.00000	0.69661
Ga	0.00000	0.50000	0.69661

Table D.6. Fractional atomic coordinates for the VASP-optimized ScFeGa₅ structure

Element	<i>x</i>	<i>y</i>	<i>z</i>
Sc	0.00000	0.00000	0.00000
Fe	0.00000	0.00000	0.50000
Ga	0.50000	0.50000	0.00000
Ga	0.50000	0.00000	0.30477
Ga	0.00000	0.50000	0.30477
Ga	0.50000	0.00000	0.69523
Ga	0.00000	0.50000	0.69523

Table D.7. Fractional atomic coordinates for the Abinit-optimized ScCoGa₅ structure

Element	<i>x</i>	<i>Y</i>	<i>z</i>
Sc	0.00000	0.00000	0.00000
Co	0.00000	0.00000	0.50000

Ga	0.50000	0.50000	0.00000
Ga	0.50000	0.00000	0.30240
Ga	0.00000	0.50000	0.30240
Ga	0.50000	0.00000	0.69760
Ga	0.00000	0.50000	0.69760

Table D.8. Fractional atomic coordinates for the VASP-optimized ScCoGa₅ structure

Element	<i>x</i>	<i>y</i>	<i>z</i>
Sc	0.00000	0.00000	0.00000
Co	0.00000	0.00000	0.50000
Ga	0.50000	0.50000	0.00000
Ga	0.50000	0.00000	0.30348
Ga	0.00000	0.50000	0.30348
Ga	0.50000	0.00000	0.69652
Ga	0.00000	0.50000	0.69652

Table D.9. Fractional atomic coordinates for the Abinit-optimized ScNiGa₅ structure

Element	<i>x</i>	<i>y</i>	<i>z</i>
Sc	0.00000	0.00000	0.00000
Ni	0.00000	0.00000	0.50000
Ga	0.50000	0.50000	0.00000
Ga	0.50000	0.00000	0.29973
Ga	0.00000	0.50000	0.29973
Ga	0.50000	0.00000	0.70027
Ga	0.00000	0.50000	0.70027

Table D.10. Fractional atomic coordinates for the VASP-optimized ScNiGa₅ structure

Element	<i>x</i>	<i>y</i>	<i>z</i>
Sc	0.00000	0.00000	0.00000
Ni	0.00000	0.00000	0.50000
Ga	0.50000	0.50000	0.00000
Ga	0.50000	0.00000	0.29904
Ga	0.00000	0.50000	0.29904
Ga	0.50000	0.00000	0.70096
Ga	0.00000	0.50000	0.70096

D.3. Chemical Pressure calibration to phonon modes and density of states

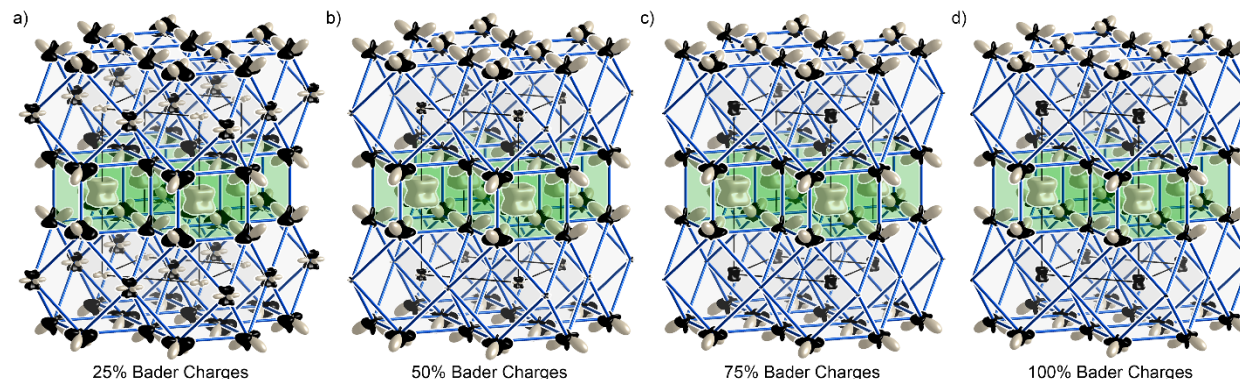


Figure D.1. The Chemical Pressure (CP) scheme for ScNiGa_5 using ionic electron density profiles of free atoms. Sc atoms center the light gray cuboctahedron. Ni atoms center the green rectangular prisms. Ga atoms are connected by blue lines. The length of a CP lobe emanating from an atom indicates the intensity of the CP along that direction. White lobes represent positive CP, calling for the expansion of the structure, and black lobes represent negative CP, calling for contraction. (a) The CP scheme at 25% of the total charges calculated by Bader analysis. The scheme is qualitatively the same as the 0% result presented in Chapter 6, but the positive CP on the Sc atoms has noticeably decreased, particularly along the c -axis. Also, the positive CP on the Ni sites has increased relative to Sc. (b) The CP scheme at 50% of the total Bader charges. Small positive pressures still exist between Sc atoms, but negative pressure has grown in, pointing toward the four Ga contacts above and below. The Sc sites become completely surrounded by negative CP in (c) and (d), which correspond to the CP scheme at 75% and 100% of the Bader charges, respectively. Because there is nothing in the phonon data to suggest that motions of Sc atoms along the c -axis are soft, the 0% CP scheme was chosen. In fact, the projected phonon DOS (Figure D.2) suggests that both Sc and Ni participate very little in the lower-frequency vibrations. See Figures D.3 and D.4 for further discussion.

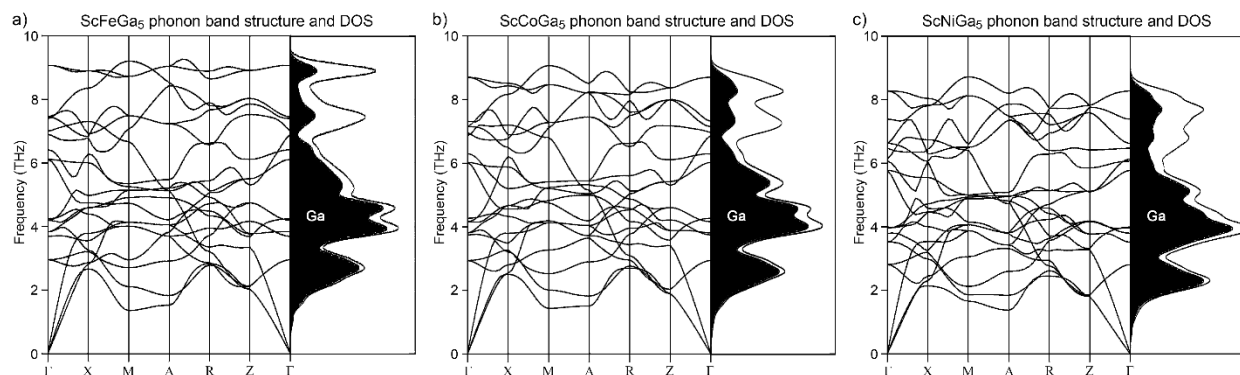


Figure D.2. The LDA-DFT phonon band structures and density of states (DOS) for ScTGa_5 ($T = \text{Fe}, \text{Co}, \text{Ni}$). For all three phases, the projected DOS (shaded in black) suggests that the movement of Ga atoms dominates the low-frequency phonon modes, which is in agreement with positive CP pointing in all directions on Sc and T sites and negative CP between Ga-Ga contacts in the 0% ionicity CP scheme (Figure 6.8).

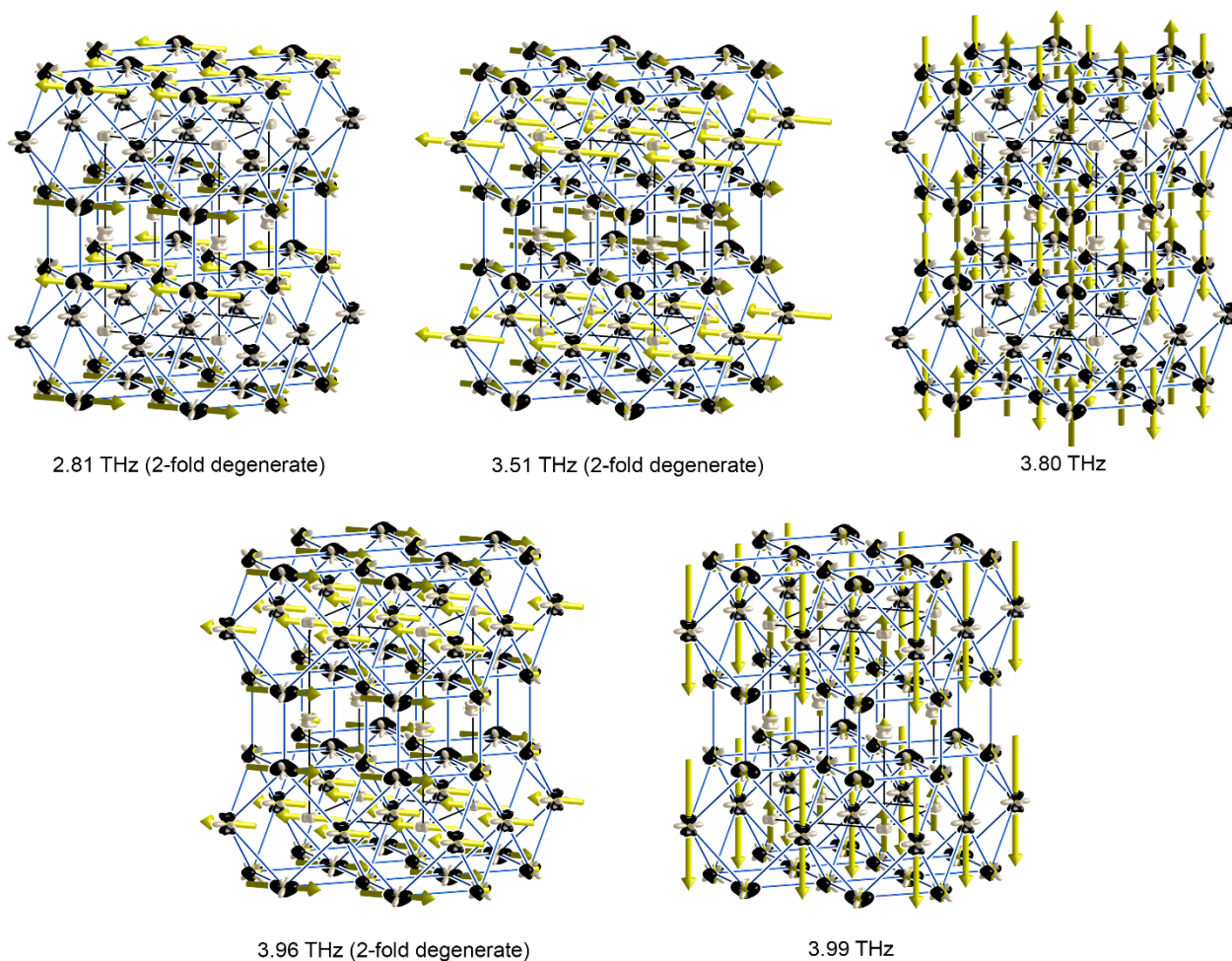


Figure D.3. The lower-frequency phonon modes calculated at the Γ point for ScNiGa_5 , plotted with the 0% ionicity CP scheme presented in Chapter 6. Ga atoms are connected by blue lines, Sc atoms center the cuboctahedra, and Ni atoms center the rectangular prisms. See Figure D.1 for CP plotting conventions. Yellow arrows represent the relative magnitude of motion among the atoms for a particular mode. Softer vibrations tend to correlate with motion along directions of high negative CP, especially when that motion is also orthogonal to positive CP (CP quadrupole). For example, Ga atoms move along negative CP into the holes of the fluorite-type layers in the mode at 2.81 THz. At 3.99 THz, even though some Sc and Ga atoms move closer along the c -axis, this mode demonstrates the principle of a CP quadrupole. Ga and Sc atoms in the same ab plane oscillate in opposite directions, relieving the positive CP in the plane while bring some Ga-Ga contacts closer together along c .

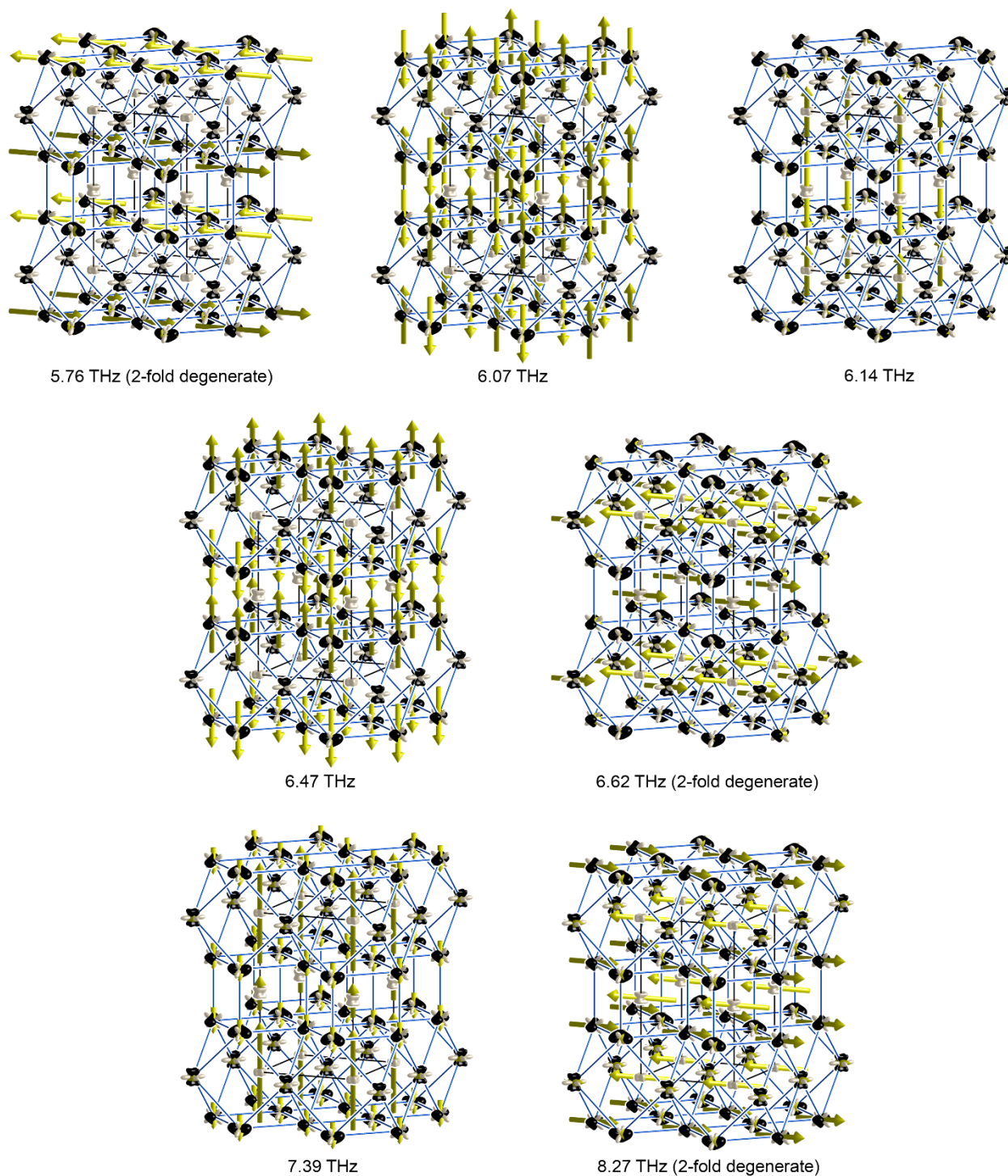


Figure D.4. The higher-frequency phonon modes calculated at the Γ point for ScNiGa_5 , plotted with the 0% ionicity CP scheme presented in Chapter 6. Ga atoms are connected by blue lines, Sc atoms center the cuboctahedra, and Ni atoms center the rectangular prisms. See Figure D.1 for CP plotting conventions. Yellow arrows represent the relative magnitude of motion among the atoms for a particular mode. Harder vibrations tend to correlate with motion along directions of positive CP. Evidence that there should be positive CP between interplanar Sc and Ga atoms is given by the modes at 5.76, 6.14, and 7.39 THz, in particular.

Appendix E.

Source code for the DFT-CP analysis package

The original DFT-CP analysis program was developed by Fredrickson. Engelkemier and Guo wrote later additions to the code. Guo was the primary developer of all the Core Unwarp and Map Integration functions. Engelkemier wrote most of the Symmetry, XC, and Main Helper functions, additionally organizing and annotating the code. Berns and Kilduff made essential contributions to the conceptual development of the DFT-CP method.

E.1. Annotated C code

```

/*
  CPmap, part of the Fredrickson Group DFT Chemical Pressure Package
  Copyright (C) 2012-2016 by the Fredrickson Group at University of Wisconsin

  This program is free software: you can redistribute it or modify it under the
  terms of the GNU General Public License as published by the Free Software
  Foundation, either version 3 of the License, or any later version.

  This program is distributed in the hope that it will be useful, but WITHOUT
  ANY WARRANTY; without even the implied warranty of MERCHANTABILITY or FITNESS
  FOR A PARTICULAR PURPOSE. See the GNU General Public License for more details.

  You should have received a copy of the GNU General Public License along with
  this program. If not, see <http://www.gnu.org/licenses/>.

  To cite DFT-Chemical Pressure or for further reading, see the following papers:
  V.M. Berns, J. Engelkemier, Y. Guo, B.J. Kilduff, D.C. Fredrickson. JCTC. 2014, 10, 3380-3392.
  J. Engelkemier, V.M. Berns, D.C. Fredrickson. J. Chem. Theory Comput. 2013, 9, 3170-3180.
  D.C. Fredrickson. J. Am. Chem. Soc. 2012, 134, 5991-5999.
*/

#include <stdlib.h>
#include <stdio.h>
#include <string.h>
#include <math.h>
#include <gsl/gsl_linalg.h>
#include <gsl/gsl_matrix.h>

```



```

double total[7][7][7][NIONMAX][NIONMAX], *** swj, *** swjk, *** wj[NEQVOX];
} vmap;

/* SUPPORT FUNCTIONS */

int ElementName(int Z, char * name) {
/* called by: PrintAverage, ReadProfile, SetBubbles */
/* calls: none */
const char * element[119] = {
    "&", "H", "He", "Li", "Be", "B", "C", "N", "O", "F", "Ne", "Na", "Mg", "Al", "Si", "P", "S", "Cl", "Ar",
    "K", "Ca", "Sc", "Ti", "V", "Cr", "Mn", "Fe", "Co", "Ni", "Cu", "Zn", "Ga", "Ge", "As", "Se", "Br", "Kr",
    "Rb", "Sr", "Y", "Zr", "Nb", "Mo", "Tc", "Ru", "Rh", "Pd", "Ag", "Cd", "In", "Sn", "Sb", "Te", "I", "Xe",
    "Cs", "Ba", "La", "Ce", "Pr", "Nd", "Pm", "Sm", "Eu", "Gd", "Tb", "Dy", "Ho", "Er", "Tm", "Yb", "Lu",
    "Hf", "Ta", "W", "Re", "Os", "Ir", "Pt", "Au", "Hg", "Tl", "Pb", "Bi", "Po", "At", "Rn",
    "Fr", "Ra", "Ac", "Th", "Pa", "U", "Np", "Pu", "Am", "Cm", "Bk", "Cf", "Es", "Fm", "Md", "No", "Lr",
    "Rf", "Db", "Sg", "Bh", "Hs", "Mt", "Ds", "Rg", "Cn", "Uut", "Fl", "Uup", "Lv", "Uus", "Uuo"};
if (Z>=0 && Z<119) strncpy(name, element[Z], 4);
else strncpy(name, "Un", 4);
return 0;
}

int FinishLine(FILE * fptr) {
/* called by: CoreCorrection, ReadProfile */
/* calls: none */
char check;
int cont=0;
while (cont==0) {
    check = fgetc(fptr);
    if (check==10 || check==EOF) cont = 1;
}
if (check==EOF) return 1;
else return 0;
}

int ReadLine(FILE * fptr, char * newstr) {
/* called by: CalcKineticTF, PressureContrib */
/* calls: none */
char check;
int cont=0, counter=0;
while (cont==0) {
    check = getc(fptr);
    if (check==10) cont = 1;
    else if (check==EOF) return 1;
    *(newstr+counter) = check;
    counter++;
}
*(newstr+counter-1) = 0;
return 0;
}

```

```

int Getkm(struct CrystData * gridin) {
    /* called by main */
    /* calls: none */
    double fa=0.0, fb=0.0, fc=0.0;
    fa = pow((gridin->cellb_y*gridin->cellc_z-gridin->cellb_z*gridin->cellc_y), 2)+
        pow((gridin->cellb_z*gridin->cellc_x-gridin->cellb_x*gridin->cellc_z), 2)+
        pow((gridin->cellb_x*gridin->cellc_y-gridin->cellb_y*gridin->cellc_x), 2);
    fb = pow((gridin->cellc_y*gridin->cella_z-gridin->cellc_z*gridin->cella_y), 2)+
        pow((gridin->cellc_z*gridin->cella_x-gridin->cellc_x*gridin->cella_z), 2)+
        pow((gridin->cellc_x*gridin->cella_y-gridin->cellc_y*gridin->cella_x), 2);
    fc = pow((gridin->cella_y*gridin->cellb_z-gridin->cella_z*gridin->cellb_y), 2)+
        pow((gridin->cella_z*gridin->cellb_x-gridin->cella_x*gridin->cellb_z), 2)+
        pow((gridin->cella_x*gridin->cellb_y-gridin->cella_y*gridin->cellb_x), 2);
    kam = (int)ceil(R_MAX/(gridin->volcell/sqrt(fa)));
    kbm = (int)ceil(R_MAX/(gridin->volcell/sqrt(fb)));
    kcm = (int)ceil(R_MAX/(gridin->volcell/sqrt(fc)));
    printf(" Using supercell range %d %d %d\n", kam, kbm, kcm);
    fprintf(cplog, "Supercell range: %d %d %d\n", kam, kbm, kcm);
    if(kam>3 || kbm>3 || kcm>3) {
        printf("\n BAD NEWS: Unit cell too small or distorted!\n");
        fprintf(cplog, "\nTerminated because an appropriate supercell could not be found\n");
        fprintf(cplog, "Suggestion: check your files or decrease R_MAX and recompile\n");
        errcount++;
        return 1;
    }
    return 0;
}

double Getwj(int atom, double dist) {
    /* called by: CoordSearch, CoreUnwarp */
    /* calls: none */
    int start=0;
    double xmax=0.0, xmin=0.0;
    start = (int)ceil((log(dist+1.0e-6)-logint[atom])/logslope[atom]);
    if (start<0) start = 0;
    while (start<prof_nmax[atom] && rprofile[atom][start]<dist) start++;
    while (rprofile[atom][start]>dist && start>0) start--;
    if (start==0) {
        if (rhoprofile[atom][0]<=0.0) {
            printf("\n BAD NEWS: Electron density profile for atom #%d is abnormal!\n", atom+1);
            fprintf(cplog, "\nTerminated because density=%f at dist=%f for atom #%d is <= 0\n",
                rhoprofile[atom][0], dist, atom+1);
            fprintf(cplog, "Suggestion: check your profiles for non-numerical data\n");
            errcount++;
            return -1000.0;
        } else return rhoprofile[atom][0];
    }
    else if (start>=prof_nmax[atom]) {
        printf("\n CAUTION: The atomic density profiles are too short! Continuing anyway...\n");
        fprintf(cplog, "WARNING: atomic radial density profile for atom #%d should be longer than
%.6e bohr\n", atom+1, dist);
        errcount++;
        return 0.0; /* assume no density at long distance */
    } else { /* interpolation between closest two points in radial profile */

```

```

    xmin = rhoprofile[atom][start];
    xmax = rhoprofile[atom][start+1];
    return (xmin*(rprofile[atom][start+1]-dist)+xmax*(dist-rprofile[atom][start]))/
        (rprofile[atom][start+1]-rprofile[atom][start]);
}
}

int Cart2Sph(double x, double y, double z, double * r, double * theta, double * phi) {
    /* called by: AverageContact */
    /* calls: none */
    *r = sqrt(x*x+y*y+z*z);
    if (*r>0.0) {
        *theta = acos(z / *r);
        if (fabs(sin(*theta))>0.0) {
            *phi = acos(x/(*r * sin(*theta)));
            if(x/(*r * sin(*theta))>1.0) *phi = acos(1.0);
            if(x/(*r * sin(*theta))<-1.0) *phi = acos(-1.0);
            if(y<0.0) *phi = -*phi;
        } else *phi = 0;
    } else {
        *phi = 0.0;
        *theta = 0.0;
    }
    return 0;
}

/* VOXEL GRID FUNCTIONS */

int FixEdges(struct CrystData * gridin) {
    /* called by: AverageContact, Bin2XSF, CalcVxc, CalcVxc1, CoreUnwarp, OutputXSF, SymmetrizeGrid
    */
    /* calls: none */
    int jx=0, jy=0, jz=0, gridx=0, gridy=0, gridz=0;
    for (jy=0; jy<=ngy; jy++) {
        for (jx=0; jx<=ngx; jx++) {
            gridin->grid[jx][jy][ngz] = gridin->grid[jx][jy][0];
        }
    }
    for (jz=0; jz<=ngz; jz++) {
        for (jx=0; jx<=ngx; jx++) {
            gridin->grid[jx][ngy][jz] = gridin->grid[jx][0][jz];
        }
    }
    for (jz=0; jz<=ngz; jz++) {
        for (jy=0; jy<=ngy; jy++) {
            gridin->grid[ngx][jy][jz] = gridin->grid[0][jy][jz];
        }
    }
    for (jz=0; jz<=ngz; jz++) {
        gridin->grid[ngx][ngy][jz] = gridin->grid[0][0][jz];
    }
    for (jy=0; jy<=ngy; jy++) {
        gridin->grid[ngx][jy][ngz] = gridin->grid[0][jy][0];
    }
}

```

```

    }
    for (jx=0; jx<=ngx; jx++) {
        gridin->grid[jx][ngy][ngz] = gridin->grid[jx][0][0];
    }
    gridin->grid[ngx][ngy][ngz] = gridin->grid[0][0][0];
    return 0;
}

double IntegrateGrid(struct CrystData * gridin) {
    /* called by: CalcCP, GridStats, MapEntot */
    /* calls: none */
    int jx=0, jy=0, jz=0;
    double sum=0.0;
    for (jz=0; jz<ngz; jz++) {
        for (jy=0; jy<ngy; jy++) {
            for (jx=0; jx<ngx; jx++) {
                sum += gridin->grid[jx][jy][jz];
            }
        }
    }
    return (sum*gridin->volvox);
}

int ShiftGrid(struct CrystData * gridin, double num, struct CrystData * gridout) {
    /* called by: CalcCP, CoreCorrection, GridStats */
    /* calls: none */
    int jx=0, jy=0, jz=0;
    gridout->volvox = gridin->volvox;
    for (jz=0; jz<=ngz; jz++) {
        for (jy=0; jy<=ngy; jy++) {
            for (jx=0; jx<=ngx; jx++) {
                gridout->grid[jx][jy][jz] = gridin->grid[jx][jy][jz]+num;
            }
        }
    }
    return 0;
}

int ScaleGrid(struct CrystData * gridin, double factor, struct CrystData * gridout) {
    /* called by: CalcCP, MapEntot */
    /* calls: none */
    int jx=0, jy=0, jz=0;
    gridout->volvox = gridin->volvox;
    for (jz=0; jz<=ngz; jz++) {
        for (jy=0; jy<=ngy; jy++) {
            for (jx=0; jx<=ngx; jx++) {
                gridout->grid[jx][jy][jz] = gridin->grid[jx][jy][jz]*factor;
            }
        }
    }
    return 0;
}

```

```

int PowerGrid(struct CrystData * gridin, int expon, struct CrystData * gridout) {
    /* called by: GridStats */
    /* calls: none */
    int jx=0, jy=0, jz=0;
    gridout->volvox = gridin->volvox;
    for (jz=0; jz<=ngz; jz++) {
        for (jy=0; jy<=ngy; jy++) {
            for (jx=0; jx<=ngx; jx++) {
                gridout->grid[jx][jy][jz] = pow(gridin->grid[jx][jy][jz], expon);
            }
        }
    }
    return 0;
}

int AddGrid(struct CrystData * gridin, struct CrystData * gridin2, struct CrystData * gridout) {
    /* called by: MapEntot */
    /* calls: none */
    int jx=0, jy=0, jz=0;
    gridout->volvox = gridin->volvox;
    for (jz=0; jz<=ngz; jz++) {
        for (jy=0; jy<=ngy; jy++) {
            for (jx=0; jx<=ngx; jx++) {
                gridout->grid[jx][jy][jz] = gridin->grid[jx][jy][jz]+gridin2->grid[jx][jy][jz];
            }
        }
    }
    return 0;
}

int SubtractGrid(struct CrystData * gridin, struct CrystData * gridin2, struct CrystData *
gridout) {
    /* called by: CalcCP, MapEntot */
    /* calls: none */
    int jx=0, jy=0, jz=0;
    gridout->volvox = gridin->volvox;
    for (jz=0; jz<=ngz; jz++) {
        for (jy=0; jy<=ngy; jy++) {
            for (jx=0; jx<=ngx; jx++) {
                gridout->grid[jx][jy][jz] = gridin->grid[jx][jy][jz]-gridin2->grid[jx][jy][jz];
            }
        }
    }
    return 0;
}

int MultiplyGrid(struct CrystData * gridin, struct CrystData * gridin2, struct CrystData *
gridout) {
    /* called by: MapEntot */
    /* calls: none */
    int jx=0, jy=0, jz=0;
    gridout->volvox = gridin->volvox;
    for (jz=0; jz<=ngz; jz++) {
        for (jy=0; jy<=ngy; jy++) {

```

```

        for (jx=0; jx<=ngx; jx++) {
            gridout->grid[jx][jy][jz] = gridin->grid[jx][jy][jz]*gridin2->grid[jx][jy][jz];
        }
    }
}
return 0;
}

int CopyStruct(struct CrystData * gridin, struct CrystData * gridout) {
    /* called by: CPcalc */
    /* calls: none */
    int i=0;
    gridout->cella_x = gridin->cella_x;
    gridout->cella_y = gridin->cella_y;
    gridout->cella_z = gridin->cella_z;
    gridout->cellb_x = gridin->cellb_x;
    gridout->cellb_y = gridin->cellb_y;
    gridout->cellb_z = gridin->cellb_z;
    gridout->cellc_x = gridin->cellc_x;
    gridout->cellc_y = gridin->cellc_y;
    gridout->cellc_z = gridin->cellc_z;
    gridout->nion = gridin->nion;
    gridout->volcell = gridin->volcell;
    gridout->volvox = gridin->volvox;
    for (i=0; i<gridin->nion; i++) {
        gridout->corerad[i] = gridin->corerad[i];
        gridout->xcart[i] = gridin->xcart[i];
        gridout->ycart[i] = gridin->ycart[i];
        gridout->zcart[i] = gridin->zcart[i];
        gridout->zatomic[i] = gridin->zatomic[i];
    }
    return 0;
}

int GridStats(struct CrystData * gridin, const char * str) {
    /* called by: main */
    /* calls: IntegrateGrid, PowerGrid, ShiftGrid */
    int jx=0, jy=0, jz=0, nvox=0;
    double min=1.0e7, max=-1.0e7, kurt=0.0, mean=0.0, sdev=0.0, skew=0.0, sum=0.0, var=0.0;
    for (jz=0; jz<ngz; jz++) {
        for (jy=0; jy<ngy; jy++) {
            for (jx=0; jx<ngx; jx++) {
                if (gridin->grid[jx][jy][jz]>max) max=gridin->grid[jx][jy][jz];
                if (gridin->grid[jx][jy][jz]<min) min=gridin->grid[jx][jy][jz];
            }
        }
    }
    nvox = ngx*ngy*ngz;
    sum = IntegrateGrid(gridin)/gridin->volvox;
    mean = sum/(double)nvox;
    ShiftGrid(gridin, -mean, &temp);
    PowerGrid(&temp, 2, &temp);
    sum = IntegrateGrid(&temp)/gridin->volvox;
}

```

```

var = sum/(double)(nvox-1);
sdev = sqrt(var);
ShiftGrid(gridin, -mean, &temp);
PowerGrid(&temp, 3, &temp);
sum = IntegrateGrid(&temp)/gridin->volvox;
skew = sum/(double)(nvox-1)/pow(sdev, 3);
ShiftGrid(gridin, -mean, &temp);
PowerGrid(&temp, 4, &temp);
sum = IntegrateGrid(&temp)/gridin->volvox;
kurt = sum/(double)(nvox-1)/pow(sdev, 4)-3;
sum = IntegrateGrid(gridin)/gridin->volvox;
fprintf(cplog, "%s:\n   voxel volume: %12.6f\n max voxel value: %12.6f\n min voxel value:
%12.6f\n   voxel sum: %12.6f\n   mean: %12.6f\n   variance: %12.6f\n
skewness: %12.6f\n   kurtosis: %12.6f\n\n",
    str, gridin->volvox, max, min, sum, mean, var, skew, kurt);
return 0;
}

```

```
/* SYMMETRY FUNCTIONS */
```

```

int SymAtoms(struct CrystData * gridin, struct SymMap * map) {
    /* Calls: none */
    /* called by: main */
    int check=0, i=0, j=0, k=0;
    double ax=gridin->cella_x, ay=gridin->cella_y, az=gridin->cella_z;
    double bx=gridin->cellb_x, by=gridin->cellb_y, bz=gridin->cellb_z;
    double cx=gridin->cellc_x, cy=gridin->cellc_y, cz=gridin->cellc_z;
    double det=0.0, xf=0.0, yf=0.0, zf=0.0, xf2=0.0, yf2=0.0, zf2=0.0;
    double coord_eqx[NIONMAX][100], coord_eqy[NIONMAX][100], coord_eqz[NIONMAX][100];
    for (i=0; i<NIONMAX; i++) map->nequiv[i] = 0;
    for (i=0; i<gridin->nion; i++) {
        for (j=0; j<gridin->nion; j++) {
            map->equiv[i][j] = 0;
        }
    }
    det = 1.0/(ax*by*cz-ax*cy*bz-bx*ay*cz+bx*cy*az+cx*ay*bz-cx*by*az);
    for (k=0; k<map->nsymel; k++) {
        for (i=0; i<gridin->nion; i++) {
            xf = det*((by*cz-cy*bz)*gridin->xcart[i]+(cx*bz-bx*cz)*gridin->ycart[i]+(bx*cy-
            cx*by)*gridin->zcart[i]);
            yf = det*((cy*az-ay*cz)*gridin->xcart[i]+(ax*cz-cx*az)*gridin->ycart[i]+(cx*ay-
            ax*cy)*gridin->zcart[i]);
            zf = det*((ay*bz-by*az)*gridin->xcart[i]+(bx*az-ax*bz)*gridin->ycart[i]+(ax*by-
            bx*ay)*gridin->zcart[i]);
            xf2 = xf*map->symrel[k][0][0]+yf*map->symrel[k][0][1]+zf*map->symrel[k][0][2]+map-
            >tions[k][0];
            yf2 = xf*map->symrel[k][1][0]+yf*map->symrel[k][1][1]+zf*map->symrel[k][1][2]+map-
            >tions[k][1];
            zf2 = xf*map->symrel[k][2][0]+yf*map->symrel[k][2][1]+zf*map->symrel[k][2][2]+map-
            >tions[k][2];
            while (xf2<0.0) { xf2 += 1.0; }
            while (fabs(xf2-1.0)<1.0e-6) { xf2 -= 1.0; }
            while (yf2<0.0) { yf2 += 1.0; }
            while (fabs(yf2-1.0)<1.0e-6) { yf2 -= 1.0; }

```

```

    while (zf2<0.0) { zf2 += 1.0; }
    while (fabs(zf2-1.0)<1.0e-6) { zf2 -= 1.0; }
    coord_eqx[i][k] = xf2;
    coord_eqy[i][k] = yf2;
    coord_eqz[i][k] = zf2;
}
}
for (i=0; i<gridin->nion; i++) {
    for (k=0; k<map->nsymel; k++) {
        for (j=0; j<gridin->nion; j++) {
            xf = det*((by*cz-cy*bz)*gridin->xcart[j]+(cx*bz-bx*cz)*gridin->ycart[j]+(bx*cy-
cx*by)*gridin->zcart[j]);
            yf = det*((cy*az-ay*cz)*gridin->xcart[j]+(ax*cz-cx*az)*gridin->ycart[j]+(cx*ay-
ax*cy)*gridin->zcart[j]);
            zf = det*((ay*bz-by*az)*gridin->xcart[j]+(bx*az-ax*bz)*gridin->ycart[j]+(ax*by-
bx*ay)*gridin->zcart[j]);
            if (fabs(coord_eqx[i][k]-xf)<0.01 && fabs(coord_eqy[i][k]-yf)<0.01 &&
fabs(coord_eqz[i][k]-zf)<0.01) {
                map->equiv[i][j] = 1;
            }
        }
    }
}
for (i=0; i<gridin->nion; i++) {
    for (j=0; j<gridin->nion; j++) {
        if (map->equiv[i][j]==1) map->nequiv[i]++;
    }
}
return 0;
}

int CheckSym(struct SymMap * map) {
    /* called by: SymmetrizeGrid */
    /* calls: none */
    char ngn[4];
    int i=0, j=0, halfflag[3], quartflag[3];
    for (i=0; i<map->nsymel; i++) {
        for (j=0; j<3; j++) {
            if (fabs(map->tnons[i][j]-0.5)<1.0e-10) halfflag[j] = 1;
            else if (fabs(map->tnons[i][j]-0.25)<1.0e-10) quartflag[j] = 1;
        }
    }
    for (j=0; j<3; j++) {
        if (j==0) strncpy(ngn, "ngx", 3);
        else if (j==1) strncpy(ngn, "ngy", 3);
        else if (j==2) strncpy(ngn, "ngz", 3);
        if (halfflag[j]==1 && quartflag[j]==1) fprintf(cplog, "%s FFT index must be divisible by
4\n", ngn);
        else if (quartflag[j]==1) fprintf(cplog, "%s FFT index must be divisible by 4 if it is
divisible by 2\n", ngn);
        else if (halfflag[j]==1) fprintf(cplog, "%s FFT index must be divisible by 2\n", ngn);
        else fprintf(cplog, "%s FFT index has no symmetry restrictions\n", ngn);
    }
    return 0;
}

```

```

int SymmetrizeGrid(struct CrystData * gridin, struct SymMap * map) {
    /* called by: CalcCP */
    /* calls: CheckSym, FixEdges */
    int flag=0, i=0, jx=0, jy=0, jz=0, jx2=0, jy2=0, jz2=0;
    double xf=0.0, yf=0.0, zf=0.0, xf2=0.0, yf2=0.0, zf2=0.0;
    double voxspacing_xf=0.0, voxspacing_yf=0.0, voxspacing_zf=0.0;
    voxspacing_xf = 1.0/(double)ngx;
    voxspacing_yf = 1.0/(double)ngy;
    voxspacing_zf = 1.0/(double)ngz;
    for (jz=0; jz<=ngz; jz++) {
        for (jy=0; jy<=ngy; jy++) {
            for (jx=0; jx<=ngx; jx++) {
                core.grid[jx][jy][jz] = 0.0; /* temp voxel counter */
            }
        }
    }
    for (i=0; i<map->nsymel; i++) {
        for (jz=0; jz<ngz; jz++) {
            zf = (double)jz/(double)ngz;
            for (jy=0; jy<ngy; jy++) {
                yf = (double)jy/(double)ngy;
                for (jx=0; jx<ngx; jx++) {
                    xf = (double)jx/(double)ngx;
                    xf2 = xf*map->symrel[i][0][0]+yf*map->symrel[i][0][1]+zf*map->symrel[i][0][2]+map->tnons[i][0];
                    yf2 = xf*map->symrel[i][1][0]+yf*map->symrel[i][1][1]+zf*map->symrel[i][1][2]+map->tnons[i][1];
                    zf2 = xf*map->symrel[i][2][0]+yf*map->symrel[i][2][1]+zf*map->symrel[i][2][2]+map->tnons[i][2];
                    jx2 = (int)(floor(xf2/voxspacing_xf+0.5));
                    jy2 = (int)(floor(yf2/voxspacing_yf+0.5));
                    jz2 = (int)(floor(zf2/voxspacing_zf+0.5));
                    while (jx2<0) { jx2 += ngx; }
                    while (jx2>=ngx) { jx2 -= ngx; }
                    while (jy2<0) { jy2 += ngy; }
                    while (jy2>=ngy) { jy2 -= ngy; }
                    while (jz2<0) { jz2 += ngz; }
                    while (jz2>=ngz) { jz2 -= ngz; }
                    core.grid[jx][jy][jz] += gridin->grid[jx2][jy2][jz2];
                    if (fabs(xf2/voxspacing_xf-0.5)<0.001) flag = 1;
                    else if (fabs(yf2/voxspacing_yf-0.5)<0.001) flag = 1;
                    else if (fabs(zf2/voxspacing_zf-0.5)<0.001) flag = 1;
                    if (flag==1) {
                        printf("\n BAD NEWS: FFT grid is incommensurate with symmetry operation %d!\n",
i+1);
                            CheckSym(&smap);
                            fprintf(cplog, "\nTerminated because FFT grid is not compatible with symmetry
operation %d\n", i+1);
                            fprintf(cplog, "Suggestion: re-run Abinit with another ngfft based on the
recommendations above\n");
                            fprintf(cplog, "Or re-run CP with symmetry restoration turned off (not
recommended)\n");
                            errcount++;
                            return 2;
                        }
                    }
                }
            }
        }
    }
}

```

```

    }
  }
}
for (jz=0; jz<ngz; jz++) {
  for (jy=0; jy<ngy; jy++) {
    for (jx=0; jx<ngx; jx++) {
      gridin->grid[jx][jy][jz] = core.grid[jx][jy][jz]/(double)map->nsmel;
    }
  }
}
FixEdges(gridin);
return 0;
}

/* I/O FUNCTIONS */

int Bin2XSF(char binname[STRMAX], struct CrystData * gridin, struct CrystData * gridin2) {
  /* called by: Den2XSF */
  /* calls: FixEdges */
  char codvsn[10], title[150];
  int bandtot=0, date=0, fform=0, headform=0, lmn_size=0, occopt_this=0;
  int intxc=0, istwfkv=0, ixc_this=0, i=0, jx=0, jy=0, jz=0, k=0;
  int natom=0, nbandv=0, ngfftx=0, ngffty=0, ngfftz=0, nkpt=0, npsp=0;
  int npwarrv=0, nspden=0, nspinor=0, nsppol=0, nsym=0, ntypat=0;
  int pertcase=0, pspcod=0, pspdat=0, pspso=0, pspxc=0, type=0, usepaw=0, usewvl=0;
  int so_psp[NIONMAX], symafm[100], symrel[3][3][100], typat[NIONMAX];
  double ax_star=0.0, ay_star=0.0, az_star=0.0, bx_star=0.0;
  double by_star=0.0, bz_star=0.0, cx_star=0.0, cy_star=0.0, cz_star=0.0;
  double cellvol=0.0, ecut=0.0, ecutdg=0.0, ecut_eff=0.0, ecutsm=0.0, eigen=0.0, etotal=0.0;
  double efermi=0.0, kptv=0.0, occ=0.0, qptnx=0.0, qptny=0.0, qptnz=0.0, residm=0.0;
  double rprimd_ax=0.0, rprimd_ay=0.0, rprimd_az=0.0, rprimd_bx=0.0;
  double rprimd_by=0.0, rprimd_bz=0.0, rprimd_cx=0.0, rprimd_cy=0.0, rprimd_cz=0.0;
  double stmbias=0.0, tphysel=0.0, tsmear=0.0, wtkv=0.0, x=0.0, y=0.0, z=0.0, zionpsp=0.0,
  znuclpsp=0.0;
  double nonlocalE_byatom[NIONMAX], nonlocalE_byatom_IM[NIONMAX], tnons[3][100],
  znucltypat[NIONMAX];
  FILE * fptr;
  fptr = fopen(binname, "rb+");
  if (fptr==NULL) {
    printf("\n BAD NEWS: File %s not found!\n", binname);
    fprintf(cplog, "\nTerminated because binary file %s not found\n", binname);
    fprintf(cplog, "Suggestion: check your Abinit files or input options\n");
    errcount++;
    return 1;
  }
  fread(&i, sizeof(int), 1, fptr);
  i = fread(codvsn, sizeof(char), 6, fptr);
  fread(&headform, sizeof(int), 1, fptr);
  fread(&fform, sizeof(int), 1, fptr);
  fread(&i, sizeof(int), 1, fptr);
  fread(&i, sizeof(int), 1, fptr);
  fread(&bandtot, sizeof(int), 1, fptr);

```

```

fread(&date, sizeof(int), 1, fptr);
fprintf(cplog, "Start date of %s: %d\n", binname, date);
fread(&intxc, sizeof(int), 1, fptr);
fread(&ixc_this, sizeof(int), 1, fptr);
ixc = ixc_this; /* global */
fread(&natom, sizeof(int), 1, fptr);
gridin->nion = natom;
fread(&ngfftx, sizeof(int), 1, fptr);
fread(&ngffty, sizeof(int), 1, fptr);
fread(&ngfftz, sizeof(int), 1, fptr);
if (ngx!=0 || ngy!=0 || ngz!=0) {
    if (ngx!=ngfftx || ngy!=ngffty || ngz!=ngfftz) {
        printf("\n BAD NEWS: Different numbers of voxels between datasets!\n");
        fprintf(cplog, "\nTerminated because not all FFT grids are equal\n");
        fprintf(cplog, "\nPrevious grid: %d %d %d, New grid for %s: %d %d %d\n",
            binname, ngx, ngy, ngz, ngfftx, ngffty, ngfftz);
        fprintf(cplog, "Suggestion: specify ngfft in Abinit input such that boxcut is ~2\n");
        errcount++;
        return 2;
    }
}
ngx = ngfftx; /* global */
ngy = ngffty; /* global */
ngz = ngfftz; /* global */
fread(&nkpt, sizeof(int), 1, fptr);
fread(&nspden, sizeof(int), 1, fptr);
fread(&nspinor, sizeof(int), 1, fptr);
fread(&nspol, sizeof(int), 1, fptr);
nspin = nspol; /* global */
if (nspinor!=1 || (nspin==2 && nspden!=2)) {
    printf("\n BAD NEWS: Spin-orbit coupling, non-scalar magnetism, or non-collinear magnetism
detected!\n");
    fprintf(cplog, "\nTerminated because nspinor=1, or nspol=2 and nspden is not 2\n");
    fprintf(cplog, "Suggestion: Check your files or re-run Abinit with different input
options\n");
    errcount++;
    return 3;
}
fread(&nsym, sizeof(int), 1, fptr);
smap.nsymel = nsym;
fread(&npsp, sizeof(int), 1, fptr);
fread(&ntypat, sizeof(int), 1, fptr);
fread(&occopt_this, sizeof(int), 1, fptr);
occopt =occopt_this; /* global */
fread(&pertcase, sizeof(int), 1, fptr);
fread(&usepaw, sizeof(int), 1, fptr);
fread(&ecut, sizeof(double), 1, fptr);
fread(&ecutdg, sizeof(double), 1, fptr);
fread(&ecutsm, sizeof(double), 1, fptr);
fread(&ecut_eff, sizeof(double), 1, fptr);
fread(&qptnx, sizeof(double), 1, fptr);
fread(&qptny, sizeof(double), 1, fptr);
fread(&qptnz, sizeof(double), 1, fptr);
fread(&rprimd_ax, sizeof(double), 1, fptr);

```

```

gridin->cella_x = rprimd_ax;
fread(&rprimd_ay, sizeof(double), 1, fptr);
gridin->cella_y = rprimd_ay;
fread(&rprimd_az, sizeof(double), 1, fptr);
gridin->cella_z = rprimd_az;
fread(&rprimd_bx, sizeof(double), 1, fptr);
gridin->cellb_x = rprimd_bx;
fread(&rprimd_by, sizeof(double), 1, fptr);
gridin->cellb_y = rprimd_by;
fread(&rprimd_bz, sizeof(double), 1, fptr);
gridin->cellb_z = rprimd_bz;
fread(&rprimd_cx, sizeof(double), 1, fptr);
gridin->cellc_x = rprimd_cx;
fread(&rprimd_cy, sizeof(double), 1, fptr);
gridin->cellc_y = rprimd_cy;
fread(&rprimd_cz, sizeof(double), 1, fptr);
gridin->cellc_z = rprimd_cz;
cellvol = (rprimd_ax*(rprimd_by*rprimd_cz-rprimd_bz*rprimd_cy)-rprimd_ay*
(rprimd_bx*rprimd_cz-rprimd_bz*rprimd_cx)+rprimd_az*(rprimd_bx*rprimd_cy-
rprimd_by*rprimd_cx));
gridin->volcell = cellvol;
gridin->volvox = cellvol/(ngx*ngy*ngz);
ax_star = 2*PI*(rprimd_by*rprimd_cz-rprimd_cy*rprimd_bz)/cellvol;
ay_star = -2*PI*(rprimd_bx*rprimd_cz-rprimd_cx*rprimd_bz)/cellvol;
az_star = 2*PI*(rprimd_bx*rprimd_cy-rprimd_cx*rprimd_by)/cellvol;
bx_star = 2*PI*(rprimd_cy*rprimd_az-rprimd_ay*rprimd_cz)/cellvol;
by_star = -2*PI*(rprimd_cx*rprimd_az-rprimd_ax*rprimd_cz)/cellvol;
bz_star = 2*PI*(rprimd_cx*rprimd_ay-rprimd_ax*rprimd_cy)/cellvol;
cx_star = 2*PI*(rprimd_ay*rprimd_bz-rprimd_by*rprimd_az)/cellvol;
cy_star = -2*PI*(rprimd_ax*rprimd_bz-rprimd_bx*rprimd_az)/cellvol;
cz_star = 2*PI*(rprimd_ax*rprimd_by-rprimd_bx*rprimd_ay)/cellvol;
fread(&stmbias, sizeof(double), 1, fptr);
fread(&tphysel, sizeof(double), 1, fptr);
fread(&tsmear, sizeof(double), 1, fptr);
fread(&usewvl, sizeof(int), 1, fptr);
fread(&i, sizeof(int), 1, fptr);
fread(&i, sizeof(int), 1, fptr);
for (i=0; i<nkpt; i++) fread(&istwfkv, sizeof(int), 1, fptr);
for (i=0; i<(nkpt*nsppol); i++) fread(&nbandv, sizeof(int), 1, fptr);
for (i=0; i<(nkpt); i++) fread(&npwarrv, sizeof(int), 1, fptr);
for (i=0; i<(npsp); i++) fread(&so_psp[i], sizeof(int), 1, fptr);
for (i=0; i<(nsym); i++) fread(&symafm[i], sizeof(int), 1, fptr);
for (i=0; i<(nsym); i++) {
    fread(&symrel[0][0][i], sizeof(int), 1, fptr);
    smap.symrel[i][0][0] = symrel[0][0][i];
    fread(&symrel[1][0][i], sizeof(int), 1, fptr);
    smap.symrel[i][1][0] = symrel[1][0][i];
    fread(&symrel[2][0][i], sizeof(int), 1, fptr);
    smap.symrel[i][2][0] = symrel[2][0][i];
    fread(&symrel[0][1][i], sizeof(int), 1, fptr);
    smap.symrel[i][0][1] = symrel[0][1][i];
    fread(&symrel[1][1][i], sizeof(int), 1, fptr);
    smap.symrel[i][1][1] = symrel[1][1][i];
    fread(&symrel[2][1][i], sizeof(int), 1, fptr);

```

```

    smap.symrel[i][2][1] = symrel[2][1][i];
    fread(&symrel[0][2][i], sizeof(int), 1, fptr);
    smap.symrel[i][0][2] = symrel[0][2][i];
    fread(&symrel[1][2][i], sizeof(int), 1, fptr);
    smap.symrel[i][1][2] = symrel[1][2][i];
    fread(&symrel[2][2][i], sizeof(int), 1, fptr);
    smap.symrel[i][2][2] = symrel[2][2][i];
}
for (i=0; i<(natom); i++) fread(&typat[i], sizeof(int), 1, fptr);
for (i=0; i<(nkpt); i++) {
    fread(&kptv, sizeof(double), 1, fptr);
    fread(&kptv, sizeof(double), 1, fptr);
    fread(&kptv, sizeof(double), 1, fptr);
}
for (i=0; i<bandtot; i++) fread(&occ, sizeof(double), 1, fptr);
for (i=0; i<nsym; i++) {
    fread(&tnons[0][i], sizeof(double), 1, fptr);
    smap.tnons[i][0] = tnons[0][i];
    fread(&tnons[1][i], sizeof(double), 1, fptr);
    smap.tnons[i][1] = tnons[1][i];
    fread(&tnons[2][i], sizeof(double), 1, fptr);
    smap.tnons[i][2] = tnons[2][i];
}
for (i=0; i<ntypat; i++) fread(&znucltypat[i], sizeof(double), 1, fptr);
for(i=0; i<natom; i++) {
    type = typat[i]-1;
    gridin->zatomic[i] = (int)znucltypat[type];
}
for (i=0; i<nkpt; i++) fread(&wtkv, sizeof(double), 1, fptr);
fread(&i, sizeof(int), 1, fptr);
for (k=0; k<npsp; k++) {
    fread(&i, sizeof(int), 1, fptr);
    fread(title, sizeof(char), 132, fptr);
    fread(&znuclpsp, sizeof(double), 1, fptr);
    fread(&zionpsp, sizeof(double), 1, fptr);
    fread(&pspsso, sizeof(int), 1, fptr);
    fread(&pspdatt, sizeof(int), 1, fptr);
    fread(&pspcod, sizeof(int), 1, fptr);
    fread(&pspxc, sizeof(int), 1, fptr);
    fread(&lmn_size, sizeof(int), 1, fptr);
    fread(&i, sizeof(int), 1, fptr);
}
if (usepaw==0) {
    fread(&i, sizeof(int), 1, fptr);
    fread(&residm, sizeof(double), 1, fptr);
    for (i=0; i<natom; i++) {
        fread(&x, sizeof(double), 1, fptr);
        fread(&y, sizeof(double), 1, fptr);
        fread(&z, sizeof(double), 1, fptr);
        gridin->xcart[i] = x*gridin->cella_x+y*gridin->cellb_x+z*gridin->cellc_x;
        gridin->ycart[i] = x*gridin->cella_y+y*gridin->cellb_y+z*gridin->cellc_y;
        gridin->zcart[i] = x*gridin->cella_z+y*gridin->cellb_z+z*gridin->cellc_z;
    }
}

```

```

fread(&etotal, sizeof(double), 1, fptr);
gridin->entot = etotal;
fread(&efermi, sizeof(double), 1, fptr);
fread(&i, sizeof(int), 1, fptr);
} else {
printf("\n BAD NEWS: PAW pseudopotential detected!\n");
fprintf(cplog, "\nTerminated because PAW pseudopotentials are not yet supported\n");
fprintf(cplog, "Suggestion: re-run Abinit with norm-conserving pseudopotentials\n");
errcount++;
return 4;
}
/* allocating memory for the voxel grid */
gridin->grid = (double***)malloc((ngx+1)*sizeof(double**));
for (jx=0; jx<=ngx; jx++) {
gridin->grid[jx] = (double**)malloc((ngy+1)*sizeof(double*));
for (jy=0; jy<=ngy; jy++) {
gridin->grid[jx][jy] = (double*)malloc((ngz+1)*sizeof(double));
}
}
if (nspin==2) {
gridin2->grid = (double***)malloc((ngx+1)*sizeof(double**));
for (jx=0; jx<=ngx; jx++) {
gridin2->grid[jx] = (double**)malloc((ngy+1)*sizeof(double*));
for (jy=0; jy<=ngy; jy++) {
gridin2->grid[jx][jy] = (double*)malloc((ngz+1)*sizeof(double));
}
}
}
/* reading in the voxel grid values */
fread(&i, sizeof(int), 1, fptr);
for (jz=0; jz<ngz; jz++) {
for (jy=0; jy<ngy; jy++) {
for (jx=0; jx<ngx; jx++) {
fread(&eigen, sizeof(double), 1, fptr);
gridin->grid[jx][jy][jz] = eigen;
}
}
}
}
FixEdges(gridin);
fread(&i, sizeof(int), 1, fptr);
if (nspin==2) {
fread(&i, sizeof(int), 1, fptr);
gridin2->volvox = gridin->volvox;
for (jz=0; jz<ngz; jz++) {
for (jy=0; jy<ngy; jy++) {
for (jx=0; jx<ngx; jx++) {
fread(&eigen, sizeof(double), 1, fptr);
gridin2->grid[jx][jy][jz] = eigen;
/* down density = total density - up density */
gridin->grid[jx][jy][jz] = gridin->grid[jx][jy][jz]-gridin2->grid[jx][jy][jz];
}
}
}
}
}

```

```

    FixEdges(gridin);
    FixEdges(gridin2);
    fread(&i, sizeof(int), 1, fptr);
}
fclose(fptr);
return 0;
}

int OutputXSF(FILE * fptr, struct CrystData * gridref, struct CrystData * gridout) {
    /* called by: main, CoreUnwarp, Den2XSF, MapEntot */
    /* calls: FixEdges */
    int i=0, jx=0, jy=0, jz=0, linecount=0;
    FixEdges(gridout);
    fprintf(fptr, " DIM-GROUP\n");
    fprintf(fptr, " 3 1\n");
    fprintf(fptr, " PRIMVEC\n");
    fprintf(fptr, "%20.14f %20.14f %20.14f\n", gridref->cella_x*R_BOHR, gridref->cella_y*R_BOHR,
gridref->cella_z*R_BOHR);
    fprintf(fptr, "%20.14f %20.14f %20.14f\n", gridref->cellb_x*R_BOHR, gridref->cellb_y*R_BOHR,
gridref->cellb_z*R_BOHR);
    fprintf(fptr, "%20.14f %20.14f %20.14f\n", gridref->cellc_x*R_BOHR, gridref->cellc_y*R_BOHR,
gridref->cellc_z*R_BOHR);
    fprintf(fptr, " PRIMCOORD\n");
    fprintf(fptr, "%12d 1\n", gridref->nion);
    for (i=0; i<gridref->nion; i++) fprintf(fptr, "%9d %20.14f %20.14f %20.14f\n",
gridref->zatomic[i], gridref->xcart[i]*R_BOHR, gridref->ycart[i]*R_BOHR, gridref->
zcart[i]*R_BOHR);
    fprintf(fptr, " ATOMS\n");
    for (i=0; i<gridref->nion; i++) fprintf(fptr, "%9d %20.14f %20.14f %20.14f\n",
gridref->zatomic[i], gridref->xcart[i]*R_BOHR, gridref->ycart[i]*R_BOHR, gridref->
zcart[i]*R_BOHR);
    fprintf(fptr, " BEGIN_BLOCK_DATAGRID3D\n");
    fprintf(fptr, " datagrids\n");
    fprintf(fptr, " DATAGRID_3D_DENSITY\n");
    fprintf(fptr, "%12d %12d %12d\n", ngx+1, ngy+1, ngz+1);
    fprintf(fptr, " 0.0 0.0 0.0\n");
    fprintf(fptr, "%20.14f %20.14f %20.14f\n", gridref->cella_x*R_BOHR, gridref->cella_y*R_BOHR,
gridref->cella_z*R_BOHR);
    fprintf(fptr, "%20.14f %20.14f %20.14f\n", gridref->cellb_x*R_BOHR, gridref->cellb_y*R_BOHR,
gridref->cellb_z*R_BOHR);
    fprintf(fptr, "%20.14f %20.14f %20.14f\n", gridref->cellc_x*R_BOHR, gridref->cellc_y*R_BOHR,
gridref->cellc_z*R_BOHR);
    for (jz=0; jz<=ngz; jz++) {
        for (jy=0; jy<=ngy; jy++) {
            for (jx=0; jx<=ngx; jx++) {
                linecount++;
                fprintf(fptr, " %20.14f", gridout->grid[jx][jy][jz]);
                if (linecount==6) {
                    fprintf(fptr, "\n");
                    linecount = 0;
                }
            }
        }
    }
    fprintf(fptr, " END_DATAGRID_3D\n");
}

```

```

    fprintf(fp, " END_BLOCK_DATAGRID3D\n");
    return 0;
}

int Den2XSF(char name[STRMAX], int num, char type[STRMAX], struct CrystData * gridin, struct
CrystData * gridin2) {
    /* called by: ReadAll, ReadGradient */
    /* calls: Bin2XSF, OutputXSF */
    char denfile[STRMAX], xsffile[STRMAX];
    int check=0;
    FILE * fp;
    snprintf(denfile, STRMAX, "%s_o_DS%d_%s", name, num, type);
    check = Bin2XSF(denfile, gridin, gridin2); /* always read from binary file */
    if (check!=0) return 1;
    if (printbin==1) {
        strncpy(xsffile, denfile, STRMAX);
        strcat(xsffile, ".xsf", STRMAX);
        fp = fopen(xsffile, "w");
        OutputXSF(fp, gridin, gridin);
        fclose(fp);
        if (nspin==2) {
            strncpy(xsffile, denfile, STRMAX);
            strcat(xsffile, "2.xsf", STRMAX);
            fp = fopen(xsffile, "w");
            OutputXSF(fp, gridin, gridin2);
            fclose(fp);
        }
    }
    return 0;
}

int ReadProfile(struct CrystData * gridin) {
    /* called by: CoreUnwarp */
    /* calls: ElementName, FinishLine */
    char element[STRMAX], profname[STRMAX];
    int i=0, j=0, k=0, stop[NIONMAX];
    FILE * fp;
    for (i=0; i<gridin->nion; i++) stop[i] = 0;
    for (i=0; i<gridin->nion; i++) {
        if (stop[i]==1) continue;
        ElementName(gridin->zatomic[i], element);
        if (smap.nequiv[i]>1) {
            fprintf(cplog, "Enter the name of the Hirshfeld profile for atom #%d (%s, %d equivalent
sites): ",
                i+1, element, smap.nequiv[i]);
        } else {
            fprintf(cplog, "Enter the name of the Hirshfeld profile for atom #%d (%s, %d site): ",
                i+1, element, smap.nequiv[i]);
        }
        retry_profile:
        if (smap.nequiv[i]>1) {
            printf(" Enter the name of the Hirshfeld profile for atom #%d (%s, %d equivalent sites):
",
                i+1, element, smap.nequiv[i]);

```

```

} else {
    printf(" Enter the name of the Hirshfeld profile for atom #d (%s, %d site): ",
        i+1, element, smap.nequiv[i]);
}
scanf("%s", profname);
fptr = fopen(profname, "r");
if (fptr==NULL) {
    printf(" Atomic radial density profile %s not found!\n", profname);
    printf(" Enter the name again or press ctrl-c to quit\n");
    goto retry_profile;
}
fprintf(cplog, "%s\n", profname);
for (j=i; j<gridin->nion; j++) {
    if (smap.equiv[i][j]!=1) continue;
    k = 0;
    while (FinishLine(fptr)==0) {
        fscanf(fptr, "%lf %lf", &rprofile[j][k], &rhoprofile[j][k]);
        k++;
        if (k==NPOINTMAX) {
            printf("\n BAD NEWS: Density profile %s is bigger than expected!\n", profname);
            fprintf(cplog, "\nTerminated because file %s is too long\n", profname);
            fprintf(cplog, "Suggestion: increase NPOINTMAX and recompile\n");
            errcount++;
            return 1;
        }
    }
    fclose(fptr);
    fptr = fopen(profname, "r");
    logint[j] = log(rprofile[j][0]);
    logslope[j] = (log(rprofile[j][k-1])-log(rprofile[j][0]))/((double)k-1.0);
    prof_nmax[j] = k;
    stop[j] = 1;
}
fclose(fptr);
}
return 0;
}

int OutputWeight(struct CrystData * gridin, struct ContactVol * map, struct CrystData * gridout)
{
    /* called by: main */
    /* calls: FixEdges, OutputXSF */
    char filename[STRMAX];
    int atom=0, i=0, jx=0, jy=0, jz=0;
    double tempcp=0.0;
    FILE * fptr;
    for(i=0; i<map->neighcount[jx][jy][jz]; i++) {
        printf(" Creating voxel weight map for atom %d\n", i+1);
        for(jz=0; jz<ngz; jz++) {
            for(jy=0; jy<ngy; jy++) {
                for(jx=0; jx<ngx; jx++) {
                    atom = map->ionmap[i][jx][jy][jz]&127;
                    tempcp = 0.5*(map->swj[jx][jy][jz]-map->wj[atom][jx][jy][jz])*map->wj[atom][jx][jy][jz];

```

```

        gridout->grid[jx][jy][jz] = tempcp/map->swjk[jx][jy][jz];
    }
}
}
FixEdges(gridout);
snprintf(filename, STRMAX, "%s-voxelweight-%d.xsf", cpoutname, i+1);
fptr = fopen(filename, "w");
OutputXSF(fptr, gridin, gridout);
fclose(fptr);
}
return 0;
}

/* CORE UNWARP FUNCTIONS */

double CubicInterpolation(double x, double y1, double y2, double y3, double y4) {
    /* called by: TricubicInterpolation */
    /* calls: none */
    double a=0.0, b=0.0, c=0.0, d=y2, apc=0.0, qapc=0.0;
    b = 0.5*(y1+y3)-y2;
    apc = 0.5*(y3-y1);
    qapc = 0.5*(y4-4*b-d);
    a = (qapc-apc)/3.0;
    c = apc-a;
    return (((a*x+b)*x+c)*x+d); /* y = ax^3+bx^2+cx+d */
}

double TricubicInterpolation(struct CrystData * gridin, struct CrystData * gridref, double x,
double y, double z) {
    /* called by: CoreUnwarp */
    /* calls: CubicInterpolation */
    int a1=0, a2=0, a3=0, a4=0, b1=0, b2=0, b3=0, b4=0, c1=0, c2=0, c3=0, c4=0;
    double xf=0.0, yf=0.0, zf=0.0, y1=0.0, y2=0.0, y3=0.0, y4=0.0, y11=0.0, y12=0.0, y13=0.0,
y14=0.0, y21=0.0;
    double y22=0.0, y23=0.0, y24=0.0, y31=0.0, y32=0.0, y33=0.0, y34=0.0, y41=0.0, y42=0.0,
y43=0.0, y44=0.0;
    double delta=0.0, interpvalue=0.0, voxspacing_xf=0.0, voxspacing_yf=0.0, voxspacing_zf=0.0;
    gsl_matrix * xf_to_r = gsl_matrix_alloc(3, 3);
    gsl_vector * rf = gsl_vector_alloc(3);
    gsl_vector * rcart = gsl_vector_alloc(3);
    /* convert cartesian x, y, z to fractional xf, yf, zf */
    gsl_matrix_set(xf_to_r, 0, 0, gridref->cella_x);
    gsl_matrix_set(xf_to_r, 0, 1, gridref->cellb_x);
    gsl_matrix_set(xf_to_r, 0, 2, gridref->cellc_x);
    gsl_matrix_set(xf_to_r, 1, 0, gridref->cella_y);
    gsl_matrix_set(xf_to_r, 1, 1, gridref->cellb_y);
    gsl_matrix_set(xf_to_r, 1, 2, gridref->cellc_y);
    gsl_matrix_set(xf_to_r, 2, 0, gridref->cella_z);
    gsl_matrix_set(xf_to_r, 2, 1, gridref->cellb_z);
    gsl_matrix_set(xf_to_r, 2, 2, gridref->cellc_z);
    gsl_vector_set(rcart, 0, x);
    gsl_vector_set(rcart, 1, y);
    gsl_vector_set(rcart, 2, z);

```

```

gsl_linalg_HH_solve(xf_to_r, rcart, rf);
xf = gsl_vector_get(rf, 0);
yf = gsl_vector_get(rf, 1);
zf = gsl_vector_get(rf, 2);
gsl_matrix_free(xf_to_r);
gsl_vector_free(rf);
gsl_vector_free(rcart);
/* translate xf, yf, zf into central unit cell */
xf -= floor(xf);
yf -= floor(yf);
zf -= floor(zf);
if (xf>0.999999) xf = 0.0;
if (yf>0.999999) yf = 0.0;
if (zf>0.999999) zf = 0.0;
/* determine voxels around xf, yf, zf */
voxspacing_xf = 1.0/(double)ngx;
voxspacing_yf = 1.0/(double)ngy;
voxspacing_zf = 1.0/(double)ngz;
a2 = (int)(xf/voxspacing_xf);
a1 = (a2-1+ngx)%ngx;
a3 = (a2+1+ngx)%ngx;
a4 = (a2+2+ngx)%ngx;
b2 = (int)(yf/voxspacing_yf);
b1 = (b2-1+ngy)%ngy;
b3 = (b2+1+ngy)%ngy;
b4 = (b2+2+ngy)%ngy;
c2 = (int)(zf/voxspacing_zf);
c1 = (c2-1+ngz)%ngz;
c3 = (c2+1+ngz)%ngz;
c4 = (c2+2+ngz)%ngz;
delta = (xf-(double)a2*voxspacing_xf)/voxspacing_xf;
y11 = CubicInterpolation(delta, gridin->grid[a1][b1][c1], gridin->grid[a2][b1][c1],
    gridin->grid[a3][b1][c1], gridin->grid[a4][b1][c1]);
y12 = CubicInterpolation(delta, gridin->grid[a1][b1][c2], gridin->grid[a2][b1][c2],
    gridin->grid[a3][b1][c2], gridin->grid[a4][b1][c2]);
y13 = CubicInterpolation(delta, gridin->grid[a1][b1][c3], gridin->grid[a2][b1][c3],
    gridin->grid[a3][b1][c3], gridin->grid[a4][b1][c3]);
y14 = CubicInterpolation(delta, gridin->grid[a1][b1][c4], gridin->grid[a2][b1][c4],
    gridin->grid[a3][b1][c4], gridin->grid[a4][b1][c4]);
y21 = CubicInterpolation(delta, gridin->grid[a1][b2][c1], gridin->grid[a2][b2][c1],
    gridin->grid[a3][b2][c1], gridin->grid[a4][b2][c1]);
y22 = CubicInterpolation(delta, gridin->grid[a1][b2][c2], gridin->grid[a2][b2][c2],
    gridin->grid[a3][b2][c2], gridin->grid[a4][b2][c2]);
y23 = CubicInterpolation(delta, gridin->grid[a1][b2][c3], gridin->grid[a2][b2][c3],
    gridin->grid[a3][b2][c3], gridin->grid[a4][b2][c3]);
y24 = CubicInterpolation(delta, gridin->grid[a1][b2][c4], gridin->grid[a2][b2][c4],
    gridin->grid[a3][b2][c4], gridin->grid[a4][b2][c4]);
y31 = CubicInterpolation(delta, gridin->grid[a1][b3][c1], gridin->grid[a2][b3][c1],
    gridin->grid[a3][b3][c1], gridin->grid[a4][b3][c1]);
y32 = CubicInterpolation(delta, gridin->grid[a1][b3][c2], gridin->grid[a2][b3][c2],
    gridin->grid[a3][b3][c2], gridin->grid[a4][b3][c2]);
y33 = CubicInterpolation(delta, gridin->grid[a1][b3][c3], gridin->grid[a2][b3][c3],
    gridin->grid[a3][b3][c3], gridin->grid[a4][b3][c3]);

```

```

y34 = CubicInterpolation(delta, gridin->grid[a1][b3][c4], gridin->grid[a2][b3][c4],
    gridin->grid[a3][b3][c4], gridin->grid[a4][b3][c4]);
y41 = CubicInterpolation(delta, gridin->grid[a1][b4][c1], gridin->grid[a2][b4][c1],
    gridin->grid[a3][b4][c1], gridin->grid[a4][b4][c1]);
y42 = CubicInterpolation(delta, gridin->grid[a1][b4][c2], gridin->grid[a2][b4][c2],
    gridin->grid[a3][b4][c2], gridin->grid[a4][b4][c2]);
y43 = CubicInterpolation(delta, gridin->grid[a1][b4][c3], gridin->grid[a2][b4][c3],
    gridin->grid[a3][b4][c3], gridin->grid[a4][b4][c3]);
y44 = CubicInterpolation(delta, gridin->grid[a1][b4][c4], gridin->grid[a2][b4][c4],
    gridin->grid[a3][b4][c4], gridin->grid[a4][b4][c4]);
delta = (yf-b2*voxspeacing_yf)/voxspeacing_yf;
y1 = CubicInterpolation(delta, y11, y21, y31, y41);
y2 = CubicInterpolation(delta, y12, y22, y32, y42);
y3 = CubicInterpolation(delta, y13, y23, y33, y43);
y4 = CubicInterpolation(delta, y14, y24, y34, y44);
delta = (zf-(double)c2*voxspeacing_zf)/voxspeacing_zf;
interpvalue = CubicInterpolation(delta, (double)y1, (double)y2, (double)y3, (double)y4);
return interpvalue;
}

int CoreUnwarp(struct CrystData * gridinup, struct CrystData * gridin, struct CrystData *
gridindn, struct CrystData * gridoutup, struct CrystData * gridoutdn) {
    /* called by: main */
    /* calls: FixEdges, Getwj, OutputXSF, ReadProfile, TricubicInterpolation */
    char str[STRMAX];
    int atom=0, check=0, count=0, ngcount=0, ngp=0, ngp0=0;
    int i=0, jx=0, jy=0, jz=0, jx1=0, jy1=0, jz1=0, jx2=0, jy2=0, jz2=0, ka=0, kb=0, kc=0;
    double dist=0.0, encoeurup=0.0, encoeurdn=0.0, endelta=0.0, wfrac=0.0, wsum=0.0;
    double upscale=0.0, dnscale=0.0, dxnewup=0.0, dynewup=0.0, dznewup=0.0, dxnewdn=0.0,
    dynewdn=0.0, dznewdn=0.0;
    double volnew=0.0, voltotup=0.0, voltotdn=0.0, xtran=0.0, ytran=0.0, ztran=0.0;
    double voxcenter_x=0.0, voxcenter_y=0.0, voxcenter_z=0.0, xc=0.0, yc=0.0, zc=0.0, xf=0.0,
    yf=0.0, zf=0.0;
    double xdist1=0.0, ydist1=0.0, zdist1=0.0, xdist2=0.0, ydist2=0.0, zdist2=0.0, xdist3=0.0,
    ydist3=0.0, zdist3=0.0;
    FILE * fptr;
    for (jz=0; jz<=ngz; jz++) {
        for (jy=0; jy<=ngy; jy++) {
            for (jx=0; jx<=ngx; jx++) {
                core.grid[jx][jy][jz] = 0.0; /* placeholder grid */
                pothi.grid[jx][jy][jz] = 0.0; /* placeholder grid */
                potlo.grid[jx][jy][jz] = 0.0; /* placeholder grid */
                temp.grid[jx][jy][jz] = 0.0; /* placeholder grid */
            }
        }
    }
    upscale = pow(gridinup->volvox/gridin->volvox, ONETHIRD)-1.0;
    dnscale = pow(gridindn->volvox/gridin->volvox, ONETHIRD)-1.0;
    fprintf(cplog, "Began core unwarping\n");
    printf(" Interpolating between %d x %d x %d = %d voxels\n", ngx, ngy, ngz, ngx*ngy*ngz);
    fprintf(cplog, "Interpolated %d x %d x %d = %d voxels\n", ngx, ngy, ngz, ngx*ngy*ngz);
    printf("0%%");
    fflush(stdout);
    /* for every voxel in the unit cell */

```

```

for (jz=0; jz<ngz; jz++) {
  /* xf, yf, zf fractional coordinates */
  zf = (double)jz/(double)ngz;
  for (jy=0; jy<ngy; jy++) {
    yf = (double)jy/(double)ngy;
    for (jx=0; jx<ngx; jx++) {
      xf = (double)jx/(double)ngx;
      /* voxel centers in cartesian coordinates */
      voxcenter_x = xf*gridin->cella_x+yf*gridin->cellb_x+zf*gridin->cellc_x;
      voxcenter_y = xf*gridin->cella_y+yf*gridin->cellb_y+zf*gridin->cellc_y;
      voxcenter_z = xf*gridin->cella_z+yf*gridin->cellb_z+zf*gridin->cellc_z;
      /* prints percent completion */
      ngcount++;
      ngp = ngcount*100/(ngx*ngy*ngz);
      if (ngp!=ngp0) {
        printf("\r%d%%", ngp);
        fflush(stdout);
      }
      ngp0 = ngp;
      /* for every unit cell in the supercell */
      hmap.neighcount = 0;
      wsum = 0.0;
      for (ka=-kam; ka<=kam; ka++) {
        for (kb=-kbn; kb<=kbn; kb++) {
          for (kc=-kcn; kc<=kcn; kc++) {
            /* for every atom in cartesian coordinates */
            for (atom=0; atom<gridin->nion; atom++) {
              xc = gridin->xcart[atom]+ka*gridin->cella_x+kb*gridin->cellb_x+kc*gridin-
>cellc_x;
              yc = gridin->ycart[atom]+ka*gridin->cella_y+kb*gridin->cellb_y+kc*gridin-
>cellc_y;
              zc = gridin->zcart[atom]+ka*gridin->cella_z+kb*gridin->cellb_z+kc*gridin-
>cellc_z;

              dist = sqrt((voxcenter_x-xc)*(voxcenter_x-xc)+(voxcenter_y-yc)*
(voxcenter_y-yc)+(voxcenter_z-zc)*(voxcenter_z-zc));
              /* if voxel is close enough to translated atom */
              if (dist<R_MAX) {
                /* determine hirshfeld-like weight for atom */
                count = hmap.neighcount;
                hmap.wj[count] = Getwj(atom, dist);
                if (hmap.wj[count]==-1000.0) return 1;
                wsum += hmap.wj[count];
                hmap.atomid[count] = atom;
                hmap.xcart[count] = xc;
                hmap.ycart[count] = yc;
                hmap.zcart[count] = zc;
                hmap.neighcount++;
                if (hmap.neighcount==NEQVOX) {
                  printf("\n BAD NEWS: The number of nearby atoms exceeds %d!\n", NEQVOX);
                  fprintf(cplog, "\nTerminated because the number of atoms near voxel %d %d %d
is larger than %d\n",
                    jx, jy, jz, NEQVOX);
                  fprintf(cplog, "Suggestion: increase NEQVOX or decrease R_MAX and
recompile\n");
                  errcount++;

```

```

        return 2;
    }
}
}
}
}
}
/* determine shift in voxel position for expanded and contracted datasets */
dxnewup = 0.0;
dynewup = 0.0;
dznewup = 0.0;
dxnewdn = 0.0;
dynewdn = 0.0;
dznewdn = 0.0;
/* for a voxel near an atomic nuclei, wfrac=1 for that atom and dxnewup is the
   x-vector between the equilibrium voxel center and the upscaled voxel such that
   xnewup = equilibrium voxel position (cf. JCTC 2014, Eq 6) */
for (i=0; i<hmap.neighcount; i++) {
    wfrac = hmap.wj[i]/wsum; /* cf. JCTC 2014, Eq 8 */
    if(wsum==0.0) {
        printf("\n BAD NEWS: A grid voxel was not interpolated!\n");
        fprintf(cplog, "\nTerminated because sum of hirshfeld-like atomic weights for voxel
%d %d %d = zero\n", jx, jy, jz);
        fprintf(cplog, "Suggestion: check the atomic density profiles or increase R_MAX and
recompile\n");
        errcount++;
        return 4;
    }
    /* vector distance between each voxel center and nearby atoms (cf. delta_r in Eq 7)
       as a hirshfeld-weighted sum of each atom's influence, scaled either up or down
       for the expanded or contracted dataset, respectively */
    dxnewup += wfrac*(hmap.xcart[i]-voxcenter_x)*upscale;
    dynewup += wfrac*(hmap.ycart[i]-voxcenter_y)*upscale;
    dznewup += wfrac*(hmap.zcart[i]-voxcenter_z)*upscale;
    dxnewdn += wfrac*(hmap.xcart[i]-voxcenter_x)*dnscale;
    dynewdn += wfrac*(hmap.ycart[i]-voxcenter_y)*dnscale;
    dznewdn += wfrac*(hmap.zcart[i]-voxcenter_z)*dnscale;
    /* hirshfeld charge analysis */
    hmap.chg[hmap.atomid[i]] += wfrac*gridin->grid[jx][jy][jz]*gridin->volvox;
}
/* expanded-volume cartesian voxel position plus the hirshfeld-weighted correction (cf.
JCTC 2014, Eq 9a) */
xnewup[jx][jy][jz] = xf*gridinup->cella_x+yf*gridinup->cellb_x+zf*gridinup-
>cellc_x+dxnewup;
ynewup[jx][jy][jz] = xf*gridinup->cella_y+yf*gridinup->cellb_y+zf*gridinup-
>cellc_y+dynewup;
znewup[jx][jy][jz] = xf*gridinup->cella_z+yf*gridinup->cellb_z+zf*gridinup-
>cellc_z+dznewup;
/* new interpolated energy at shifted voxel center */
pothi.grid[jx][jy][jz] = TricubicInterpolation(gridoutup, gridinup,
xnewup[jx][jy][jz], ynewup[jx][jy][jz], znewup[jx][jy][jz]);
/* cf. JCTC 2014, Eq 9b */
xnewdn[jx][jy][jz] = xf*gridindn->cella_x+yf*gridindn->cellb_x+zf*gridindn-
>cellc_x+dxnewdn;

```

```

        ynewdn[jx][jy][jz] = xf*gridindn->cella_y+yf*gridindn->cellb_y+zf*gridindn-
>cellc_y+dynewdn;
        znewdn[jx][jy][jz] = xf*gridindn->cella_z+yf*gridindn->cellb_z+zf*gridindn-
>cellc_z+dznewdn;
        potlo.grid[jx][jy][jz] = TricubicInterpolation(gridoutdn, gridindn,
        xnewdn[jx][jy][jz], ynewdn[jx][jy][jz], znewdn[jx][jy][jz]);
    }
}
}
printf(" Finished\n");
/* reassign voxels with interpolated energies and shifted-grid volumes */
for (jz=0; jz<ngz; jz++) {
    for (jy=0; jy<ngy; jy++) {
        for (jx=0; jx<ngx; jx++) {
            xtran = 0;
            ytran = 0;
            ztran = 0;
            /* jx1 and jx2 are neighboring voxel indices to jx */
            jx1 = (jx==0)? (xtran = 1, ngx-1) : (jx-1);
            jy1 = (jy==0)? (ytran = 1, ngy-1) : (jy-1);
            jz1 = (jz==0)? (ztran = 1, ngz-1) : (jz-1);
            jx2 = (jx==ngx-1)? (xtran = 1, 0) : (jx+1);
            jy2 = (jy==ngy-1)? (ytran = 1, 0) : (jy+1);
            jz2 = (jz==ngz-1)? (ztran = 1, 0) : (jz+1);
            /* assuming insignificant change in angles, the new volume of a voxel is
            based on the shifted distance between neighboring voxel centers */
            xd1st1 = xnewup[jx2][jy][jz]-xnewup[jx1][jy][jz]+xtran*gridinup->cella_x;
            ydist1 = ynewup[jx2][jy][jz]-ynewup[jx1][jy][jz]+xtran*gridinup->cella_y;
            zdist1 = znewup[jx2][jy][jz]-znewup[jx1][jy][jz]+xtran*gridinup->cella_z;
            xd1st2 = xnewup[jx][jy2][jz]-xnewup[jx][jy1][jz]+ytran*gridinup->cellb_x;
            ydist2 = ynewup[jx][jy2][jz]-ynewup[jx][jy1][jz]+ytran*gridinup->cellb_y;
            zdist2 = znewup[jx][jy2][jz]-znewup[jx][jy1][jz]+ytran*gridinup->cellb_z;
            xd1st3 = xnewup[jx][jy][jz2]-xnewup[jx][jy][jz1]+ztran*gridinup->cellc_x;
            ydist3 = ynewup[jx][jy][jz2]-ynewup[jx][jy][jz1]+ztran*gridinup->cellc_y;
            zdist3 = znewup[jx][jy][jz2]-znewup[jx][jy][jz1]+ztran*gridinup->cellc_z;
            volnew = 0.125*(xd1st1*(ydist2*zdist3-ydist3*zdist2)+xd1st2*
            (ydist3*zdist1-ydist1*zdist3)+xd1st3*(ydist1*zdist2-ydist2*zdist1));
            voltotup += volnew;
            core.grid[jx][jy][jz] = volnew;
            /* divide by old volume and subtract old energy to replace their values,
            cf. the numerator of Eq 10 in JCTC 2014 */
            endelta = pothi.grid[jx][jy][jz]*(volnew/gridinup->volvox)-gridoutup->grid[jx][jy][jz];
            gridoutup->grid[jx][jy][jz] += endelta;
            encoreup -= endelta;
            xd1st1 = xnewdn[jx2][jy][jz]-xnewdn[jx1][jy][jz]+xtran*gridindn->cella_x;
            ydist1 = ynewdn[jx2][jy][jz]-ynewdn[jx1][jy][jz]+xtran*gridindn->cella_y;
            zdist1 = znewdn[jx2][jy][jz]-znewdn[jx1][jy][jz]+xtran*gridindn->cella_z;
            xd1st2 = xnewdn[jx][jy2][jz]-xnewdn[jx][jy1][jz]+ytran*gridindn->cellb_x;
            ydist2 = ynewdn[jx][jy2][jz]-ynewdn[jx][jy1][jz]+ytran*gridindn->cellb_y;
            zdist2 = znewdn[jx][jy2][jz]-znewdn[jx][jy1][jz]+ytran*gridindn->cellb_z;
            xd1st3 = xnewdn[jx][jy][jz2]-xnewdn[jx][jy][jz1]+ztran*gridindn->cellc_x;
            ydist3 = ynewdn[jx][jy][jz2]-ynewdn[jx][jy][jz1]+ztran*gridindn->cellc_y;
            zdist3 = znewdn[jx][jy][jz2]-znewdn[jx][jy][jz1]+ztran*gridindn->cellc_z;
            volnew = 0.125*(xd1st1*(ydist2*zdist3-ydist3*zdist2)+xd1st2*

```

```

        (ydist3*zdist1-ydist1*zdist3)+xdist3*(ydist1*zdist2-ydist2*zdist1));
    voltotdn += volnew;
    temp.grid[jx][jy][jz] = volnew;
    endelta = potlo.grid[jx][jy][jz]*(volnew/gridindn->volvox)-gridoutdn->grid[jx][jy][jz];
    gridoutdn->grid[jx][jy][jz] += endelta;
    encoredn -= endelta;
    }
}
}
fprintf(cplog, "Interpolated unit cell vol: %.6e, %.6e\n", voltotup, voltotdn);
if (fabs(gridinup->volcell-voltotup)>1.0e-5 || fabs(gridindn->volcell-voltotdn)>1.0e-5) {
    printf("\n CAUTION: Interpolated unit cell volume has changed a lot! Continuing
    anyway...\n");
    fprintf(cplog, "WARNING: interpolated unit cell volumes: %f and %f\n", voltotup, voltotdn);
    fprintf(cplog, "                real cell volumes: %f and %f\n", gridinup->volcell,
    gridindn->volcell);
    errcount++;
}
fprintf(cplog, "\n");
/* record total change in average map value */
en_core[0] = encoreup;
en_core[2] = encoredn;
FixEdges(gridoutup);
FixEdges(gridoutdn);
for (i=0; i<gridin->nion; i++) fprintf(cplog, "Hirshfeld charge on atom %d: %.6e\n", i+1,
hmap.chg[i]);
fprintf(cplog, "\n");
if (printhmap==1) { /* output voxel map of new volumes */
    FixEdges(&core);
    snprintf(str, STRMAX, "%s-upvox.xsf", cpoutname);
    fptr = fopen(str, "w");
    OutputXSF(fptr, gridin, &core);
    fclose(fptr);
    FixEdges(&temp);
    snprintf(str, STRMAX, "%s-dnvox.xsf", cpoutname);
    fptr = fopen(str, "w");
    OutputXSF(fptr, gridin, &temp);
    fclose(fptr);
}
return 0;
}

/* XC FUNCTIONS */

int ReadGradient() {
    /* called by: IdentifyXC */
    /* calls: Den2XSF */
    fprintf(cplog, "\n");
    Den2XSF(abinitname, dshi, "GDEN1", &gdenhi1, &gdenhi4);
    Den2XSF(abinitname, dshi, "GDEN2", &gdenhi2, &gdenhi5);
    Den2XSF(abinitname, dshi, "GDEN3", &gdenhi3, &gdenhi6);
    Den2XSF(abinitname, dseq, "GDEN1", &gdeneq1, &gdeneq4);
    Den2XSF(abinitname, dseq, "GDEN2", &gdeneq2, &gdeneq5);
}

```

```

Den2XSF(abinitname, dseq, "GDEN3", &gdeneq3, &gdeneq6);
Den2XSF(abinitname, dslo, "GDEN1", &gdenlo1, &gdenlo4);
Den2XSF(abinitname, dslo, "GDEN2", &gdenlo2, &gdenlo5);
Den2XSF(abinitname, dslo, "GDEN3", &gdenlo3, &gdenlo6);
if (errcount!=0) return 1;
return 0;
}

int IdentifyXC(int id) {
  /* called by: main */
  /* calls: ReadGradient */
  /* list of one-to-one equivalent Abinit to LibXC functional IDs */
  int abinit2libxc[43] = { 0,20,10,0,0,0,0,0,0,0,0,101130,101,0,0,0,
    161,162,0,0,0,0,0,0,0,163,164,0,0,0,0,0,0,0,0,0,0,0,0 };
  int check=0, i=0, isgga=0;
  xc_func_type func;
  xcpot[0] = 0;
  xcpot[1] = 0;
  if (id==0) {
    printf("\n BAD NEWS: No exchange-correlation potential detected!\n", abinitout);
    fprintf(cplog, "\nTerminated because ixc=0\n");
    fprintf(cplog, "Suggestion: re-run Abinit with a different ixc or turn off exch-corr
mapping\n");
    errcount++;
    return 1;
  } else if (id>42) {
    printf("\n BAD NEWS: Invalid exchange-correlation potential detected!\n", abinitout);
    fprintf(cplog, "\nTerminated because ixc=%d > 42 is not defined by Abinit\n", ixc);
    fprintf(cplog, "Suggestion: check Abinit files for discrepancies\n");
    errcount++;
    return 2;
  } else if (id>0 && abinit2libxc[id]==0) {
    printf("\n BAD NEWS: Exchange-correlation potential not supported!\n", abinitout);
    fprintf(cplog, "\nTerminated because ixc=%d is not supported by CPpackage\n", ixc);
    fprintf(cplog, "Suggestion: re-run Abinit with a different ixc or contact the Fredrickson
Group\n");
    errcount++;
    return 3;
  } else {
    if (id<0) { /* not a built-in Abinit functional */
      xcpot[0] = -1*id/1000; /* remove lowest three digits */
      xcpot[1] = -1*id-(xcpot[0]*1000); /* remove highest three digits */
    } else {
      xcpot[0] = abinit2libxc[id]/1000;
      xcpot[1] = abinit2libxc[id]-(xcpot[0]*1000);
    }
  }
  for (i=0; i<2; i++) {
    if (i==0 && xcpot[0]==0) continue; /* only three digits */
    if (nspin==2) check = xc_func_init(&func, xcpot[i], XC_POLARIZED);
    else check = xc_func_init(&func, xcpot[i], XC_POLARIZED);
    if (check!=0) {
      printf("\n BAD NEWS: Unrecognized XC functional!\n");
      fprintf(cplog, "\nTerminated because LibXC does not support the exchange-correlation
functional: %d\n", xcpot[i]);
    }
  }
}

```

```

        fprintf(cplog, "Suggestion: re-run Abinit with different ixc input\n");
        errcount++;
        return 4;
    }
    isgga = xc_family_from_id(xcpot[i], NULL, NULL);
    switch (isgga) {
        case XC_FAMILY_LDA:
            xc_func_end(&func);
            break; /* do not need electron density gradient */
        default:
            check = ReadGradient();
            if (check!=0) return 5;
            xc_func_end(&func);
            goto bottom; /* initialize gradient files only once */
    }
}
}
bottom:
return 0;
}
}

int CoreCorrection(struct CrystData * gridin, struct CrystData * coreout) {
    /* called by: MapEntot */
    /* calls: FinishLine, ShiftGrid */
    char pspfile[STRMAX], str[200];
    int check=0, i=0, jx=0, jy=0, jz=0, jx1=0, jy1=0, jz1=0, k=0, stop=0;
    int lloc=0, lmax_this=0, mmax=0, pspcod=0, pspxc=0, r2well=0;
    int neps_atomvalues=0, zint=0, zused[120], zvalues[NIONMAX];
    double core_elec=0.0, fchrg=0.0, fraction=0.0, rchrg=0.0;
    double core_r[500][120], core_rho[500][120], ddrho=0.0, drho=0.0, rho_core=0.0;
    double dl=0.0, d2=0.0, delta=0.0, distsq=0.0, rmax[120], z=0.0, zion[NIONMAX];
    double xf=0.0, yf=0.0, zf=0.0, voxcenter_x=0.0, voxcenter_y=0.0, voxcenter_z=0.0;
    FILE * fptr1;
    FILE * fptr2;
    for (i=0; i<120; i++) zused[i] = 0;
    fptr1 = fopen(abinitout, "r");
    if (fptr1==NULL) {
        printf("\n BAD NEWS: File %s not found!\n", abinitout);
        fprintf(cplog, "\nTerminated because file %s not found\n", abinitout);
        fprintf(cplog, "Suggestion: check your Abinit files or input options\n");
        errcount++;
        return 1;
    }
    while (stop==0) {
        check = fscanf(fptr1, "%s", str);
        if (check==EOF) stop = 1;
        if (strncmp(str, "pspini:", 7)==0) {
            fscanf(fptr1, "%s %s %s %s %s %s %s", str, str, str, str, str, str, str, pspfile);
            FinishLine(fptr1);
            FinishLine(fptr1);
            FinishLine(fptr1);
            fscanf(fptr1, "%s", str);
            fscanf(fptr1, "%lf %lf", &z, &zion[neps_atomvalues]);

```

```

zvalues[neps_atomvalues] = (int)z;
zint = (int)z;
FinishLine(fptrl);
fscanf(fptrl, "%d %d %d %d %d %d", &pspcod, &pspxc, &lmax_this, &lloc, &mmax, &r2well);
FinishLine(fptrl);
fscanf(fptrl, "%lf %lf", &rchrg, &fchrg);
rmax[zint] = rchrg;
FinishLine(fptrl);
if (fchrg!=0.0) {
    fprintf(cplog, "Core correction detected on Z=%d pseudopotential\n", zint);
    fprintf(cplog, "Reading core density from %s, lmax=%d, mmax=%d\n", pspfile, lmax_this,
mmax);
    zused[zint] = 1;
    fptr2 = fopen(pspfile, "r");
    if (fptr2==NULL) {
        printf("\n BAD NEWS: File %s not found!\n", pspfile);
        fprintf(cplog, "\nTerminated because file %s not found\n", pspfile);
        fprintf(cplog, "Suggestion: check your Abinit files or input options\n");
        errcount++;
        return 2;
    }
    for (i=0; i<18; i++) FinishLine(fptr2);
    for (i=0; i<lmax_this+1; i++) {
        FinishLine(fptr2);
        for (k=0; k<mmax; k++) FinishLine(fptr2);
    }
    for (i=1; i<mmax+1; i++) {
        fscanf(fptr2, "%lf %lf %lf %lf", &core_r[i][zint], &core_rho[i][zint], &drho, &addrho);
    }
    fclose(fptr2);
    core_r[0][zint] = 0.0;
    core_rho[0][zint] = core_rho[0][zint];
    fprintf(cplog, "r_max = %.6e angstrom\n", rmax[zint]*R_BOHR);
}
}
}
fclose(fptrl);
coreout->volvox = gridin->volvox;
ShiftGrid(gridin, 0.0, coreout); /* copies gridin grid onto coreout grid */
for (i=0; i<gridin->nion; i++) {
    zint = gridin->zatomic[i];
    if (zused[zint]==1) {
        for (jz=-ngz+1)/2; jz<ngz+(ngz+1)/2; jz++) {
            zf = (double)jz/(double)ngz;
            for (jy=-ngy+1)/2; jy<ngy+(ngy+1)/2; jy++) {
                yf = (double)jy/(double)ngy;
                for (jx=-ngx+1)/2; jx<ngx+(ngx+1)/2; jx++) {
                    xf = (double)jx/(double)ngx;
                    voxcenter_x = (xf)*gridin->cella_x+(yf)*gridin->cellb_x+(zf)*gridin->cellc_x;
                    voxcenter_y = (xf)*gridin->cella_y+(yf)*gridin->cellb_y+(zf)*gridin->cellc_y;
                    voxcenter_z = (xf)*gridin->cella_z+(yf)*gridin->cellb_z+(zf)*gridin->cellc_z;
                    distsq = sqrt((voxcenter_x-gridin->xcart[i])*(voxcenter_x-gridin->xcart[i])+
(voxcenter_y-gridin->ycart[i])*(voxcenter_y-gridin->ycart[i])+
(voxcenter_z-gridin->zcart[i])*(voxcenter_z-gridin->zcart[i]));
                }
            }
        }
    }
}

```



```

        denom = B1*r_s+B2*pow(r_s, 2)+B3*pow(r_s, 3)+B4*pow(r_s, 4);
        gridout->grid[jx][jy][jz] = -numer/denom;
    }
}
}
FixEdges(gridout);
return 0;
}

int CalcVxc(struct CrystData * gridin, struct CrystData * gridin2, int dsnum, struct CrystData *
gridout, struct CrystData *gridout2) {
    /* called by: MapEntot */
    /* calls: FixEdges */
    int check=0, i=0, id=0, jx=0, jy=0, jz=0;
    double grad[1], gradx=0.0, grady=0.0, gradz=0.0, energy[1], sden[2];
    xc_func_type func;
    for (jz=0; jz<ngz; jz++) {
        for (jy=0; jy<ngy; jy++) {
            for (jx=0; jx<ngx; jx++) {
                gridout->grid[jx][jy][jz] = 0.0;
                if (nspin==2) gridout2->grid[jx][jy][jz] = 0.0;
            }
        }
    }
}
if (nspin==1 && xcpot[0]==0 && xcpot[1]==20) { /* default Teter93 LDA functional */
    CalcVxc1(gridin, gridout);
    return 0;
}
for (i=0; i<2; i++) {
    if (i==0 && xcpot[0]==0) continue; /* only three digits */
    else if (nspin==2) xc_func_init(&func, xcpot[i], XC_POLARIZED);
    else xc_func_init(&func, xcpot[i], XC_UNPOLARIZED);
    id = xc_family_from_id(xcpot[i], NULL, NULL);
    switch (id) {
        case XC_FAMILY_LDA:
            for (jz=0; jz<ngz; jz++) {
                for (jy=0; jy<ngy; jy++) {
                    for (jx=0; jx<ngx; jx++) {
                        if (nspin==2) {
                            sden[0] = gridin2->grid[jx][jy][jz]; /* alpha density */
                            sden[1] = gridin->grid[jx][jy][jz]; /* beta density */
                            xc_lda_exc(&func, 1, sden, energy);
                            gridout2->grid[jx][jy][jz] += energy[0];
                        } else {
                            xc_lda_exc(&func, 1, &gridin->grid[jx][jy][jz], energy);
                            gridout->grid[jx][jy][jz] += energy[0];
                        }
                    }
                }
            }
        }
    }
    break;
    case XC_FAMILY_GGA:
    case XC_FAMILY_HYB_GGA:
        for (jz=0; jz<ngz; jz++) {

```

```

for (jy=0; jy<ngy; jy++) {
  for (jx=0; jx<ngx; jx++) {
    if(dsnum==dshi) {
      if (nspin==2) { // spin-polarized GGA results in wrong total energy
        sden[0] = gridin2->grid[jx][jy][jz];
        sden[1] = gridin->grid[jx][jy][jz];
        gradx = gdenhi4.grid[jx][jy][jz];
        grady = gdenhi5.grid[jx][jy][jz];
        gradz = gdenhi6.grid[jx][jy][jz];
        grad[0] = gradx*gradx+grady*grady+gradz*gradz;
        xc_gga_exc(&func, 1, sden, &grad[0], &energy[0]);
        gridout2->grid[jx][jy][jz] += energy[0];
      } else {
        gradx = gdenhi1.grid[jx][jy][jz];
        grady = gdenhi2.grid[jx][jy][jz];
        gradz = gdenhi3.grid[jx][jy][jz];
        grad[0] = gradx*gradx+grady*grady+gradz*gradz;
        xc_gga_exc(&func, 1, &gridin->grid[jx][jy][jz], &grad[0], &energy[0]);
        gridout->grid[jx][jy][jz] += energy[0];
      }
    }
  }
  else if(dsnum==dseq) {
    if (nspin==2) {
      sden[0] = gridin2->grid[jx][jy][jz];
      sden[1] = gridin->grid[jx][jy][jz];
      gradx = gdeneq4.grid[jx][jy][jz];
      grady = gdeneq5.grid[jx][jy][jz];
      gradz = gdeneq6.grid[jx][jy][jz];
      grad[0] = gradx*gradx+grady*grady+gradz*gradz;
      xc_gga_exc(&func, 1, sden, &grad[0], &energy[0]);
      gridout2->grid[jx][jy][jz] += energy[0];
    } else {
      gradx = gdeneq1.grid[jx][jy][jz];
      grady = gdeneq2.grid[jx][jy][jz];
      gradz = gdeneq3.grid[jx][jy][jz];
      grad[0] = gradx*gradx+grady*grady+gradz*gradz;
      xc_gga_exc(&func, 1, &gridin->grid[jx][jy][jz], &grad[0], &energy[0]);
      gridout->grid[jx][jy][jz] += energy[0];
    }
  }
  else if(dsnum==dsl0) {
    if (nspin==2) {
      sden[0] = gridin2->grid[jx][jy][jz];
      sden[1] = gridin->grid[jx][jy][jz];
      gradx = gdenlo4.grid[jx][jy][jz];
      grady = gdenlo5.grid[jx][jy][jz];
      gradz = gdenlo6.grid[jx][jy][jz];
      grad[0] = gradx*gradx+grady*grady+gradz*gradz;
      xc_gga_exc(&func, 1, sden, &grad[0], &energy[0]);
      gridout2->grid[jx][jy][jz] += energy[0];
    } else {
      gradx = gdenlo1.grid[jx][jy][jz];
      grady = gdenlo2.grid[jx][jy][jz];

```

```

        gradz = gdenlo3.grid[jx][jy][jz];
        grad[0] = gradx*gradx+grady*grady+gradz*gradz;
        xc_gga_exc(&func, 1, &gridin->grid[jx][jy][jz], &grad[0], &energy[0]);
        gridout->grid[jx][jy][jz] += energy[0];
    }
} /* grad[0] = square of vector magnitude of electron density gradient */
}
}
}
break;
default:
    printf("\n BAD NEWS: Unrecognized XC functional!\n");
    fprintf(cplog, "\nTerminated because the XC potential was not recognized as an LDA or GGA
functional\n");
    fprintf(cplog, "Suggestion: re-run Abinit with a different XC functional or check that
ixc=%d is correct\n", xcpot[i]);
    errcount++;
    return 1;
}
xc_func_end(&func);
}
FixEdges(gridout);
return 0;
}

```

```
/* MAP CALCULATION FUNCTIONS */
```

```

int CalcKineticTF(struct CrystData * gridin, int dsnum, struct CrystData * gridout) {
    /* called by: MapEntot */
    /* calls: ReadLine */
    char line[500], str1[30], str2[30], str3[30];
    int check=0, i=0, jx=0, jy=0, jz=0, stop=0;
    double E_core[dsnum], E_entropy[dsnum], E_ewald[dsnum], E_hartree[dsnum], E_int[dsnum];
    double E_kinetic[dsnum], E_locPsp[dsnum], E_nlPsp[dsnum], E_total[dsnum], E_xc[dsnum];
    double normKE=0;
    FILE * fptr;
    fptr = fopen(abinitout, "r");
    if (fptr==NULL) {
        printf("\n BAD NEWS: File %s not found!\n", abinitout);
        fprintf(cplog, "\nTerminated because file %s not found\n", abinitout);
        fprintf(cplog, "Suggestion: check your Abinit files or input options\n");
        errcount++;
        return 1;
    }
    while (stop==0) {
        check = ReadLine(fptr, line);
        if (check==1) {
            printf("\n BAD NEWS: Energy data in %s not found!\n", abinitout);
            fprintf(cplog, "\nTerminated because total free energy list #%d not found in %s\n", i+1,
abinitout);
            fprintf(cplog, "Suggestion: check %s or check if data matches format in CPpackage source
code\n", abinitout);
            errcount++;
        }
    }
}

```

```

    return 2;
}
if (strcmp(line, "Components of total free energy (in Hartree) :", 47)==0) {
    fscanf(fptr, "%s %s %s %lf", str1, str2, str3, &E_kinetic[i]);
    fscanf(fptr, "%s %s %s %lf", str1, str2, str3, &E_hartree[i]);
    fscanf(fptr, "%s %s %s %lf", str1, str2, str3, &E_xc[i]);
    fscanf(fptr, "%s %s %s %lf", str1, str2, str3, &E_ewald[i]);
    fscanf(fptr, "%s %s %s %lf", str1, str2, str3, &E_core[i]);
    fscanf(fptr, "%s %s %s %lf", str1, str2, str3, &E_locPsp[i]);
    fscanf(fptr, "%s %s %s %lf", str1, str2, str3, &E_nlPsp[i]);
    fscanf(fptr, "%s %s %s %lf", str1, str2, str3, &E_int[i]);
    fscanf(fptr, "%s %s %lf", str1, str2, &E_entropy[i]);
    fscanf(fptr, "%s %s %lf", str1, str2, &E_total[i]);
    i++;
}
if (i==dsnum) stop = 1;
}
fclose(fptr);
for (jz=0; jz<ngz; jz++) {
    for (jy=0; jy<ngy; jy++) {
        for (jx=0; jx<ngx; jx++) {
            normKE += pow(gridin->grid[jx][jy][jz], 5.0/3.0)*gridin->volvox;
        }
    }
}
for (jz=0; jz<=ngz; jz++) {
    for (jy=0; jy<=ngy; jy++) {
        for (jx=0; jx<=ngx; jx++) {
            gridout->grid[jx][jy][jz] = E_kinetic[dsnum-1]*(pow(gridin->grid[jx][jy][jz],
5.0/3.0)/normKE);
        }
    }
}
return 0;
}

```

```

int MapEntot(struct CrystData * denin, struct CrystData * denin2, struct CrystData * kdenin,
struct CrystData * kdenin2, struct CrystData * potin, struct CrystData * potin2, struct CrystData
* vhxcin, struct CrystData * vhxcin2, struct CrystData * vhain, struct CrystData * vhain2, int
dsnum, double vol, struct CrystData * etout) {

```

```

    /* called by: main */
    /* calls: AddGrid, CalcKineticTF, CalcVxc, CoreCorrection, IntegrateGrid, MultiplyGrid,
OutputXSF, ScaleGrid, SubtractGrid */
    char enfile[STRMAX];
    int check=0, jx=0, jy=0, jz=0;
    double integ1=0.0, integ2=0.0;
    FILE * fptr;
    core.volvox = vol;
    core2.volvox = vol;
    temp.volvox = vol;
    temp2.volvox = vol;
    vxc.volvox = vol;
    vxc2.volvox = vol;
    fprintf(cplog, " Cell volume DS%d: %20.14f\n", dsnum, denin->volcell);

```

```

    if (nspin==2) fprintf(cplog, " Electron count: %20.14f\n",
IntegrateGrid(denin)+IntegrateGrid(denin2));
    else fprintf(cplog, " Electron count: %20.14f\n", IntegrateGrid(denin));\

    if (mapkin==2) {
        kdenin->volvox = vol;
        if (nspin==2) {
            AddGrid(denin, denin2, &temp);
            check = CalcKineticTF(&temp, dsnum, kdenin);
        } else check = CalcKineticTF(denin, dsnum, kdenin);
        if (check!=0) return 1;
    }
}
if (mapkin==1 || mapkin==2) {
    if (nspin==2 && mapkin!=2) p_kin[dsnum-1] = IntegrateGrid(kdenin)+IntegrateGrid(kdenin2);
    else p_kin[dsnum-1] = IntegrateGrid(kdenin);
    fprintf(cplog, " Kinetic energy: %20.14f\n", p_kin[dsnum-1]);
}

SubtractGrid(potin, vhxcin, potin);
if (nspin==2) {
    SubtractGrid(potin2, vhxcin2, potin2);
    AddGrid(potin, potin2, potin); /* combine up and down pot from here on */
}
if (maploc!=1) {
    SubtractGrid(potin, potin, potin);
    if (nspin==2) SubtractGrid(potin2, potin2, potin2);
}
if (nspin==2) {
    AddGrid(denin, denin2, &temp2);
    MultiplyGrid(potin, &temp2, &temp);
} else MultiplyGrid(potin, denin, &temp); /* temp is vden here */
p_loc[dsnum-1] = IntegrateGrid(&temp);
fprintf(cplog, " V_local energy: %20.14f\n", p_loc[dsnum-1]);

if (mapxc==1) { /* Vxc = epsilon(r) where Exc[rho] = integ(epsilon(r)*rho(r))dV */
    check = CoreCorrection(denin, &core); /* for psuedopotentials with nonlinear core correction
*/
    if (check!=0) return 2;
    if (nspin==2) {
        check = CoreCorrection(denin2, &core2);
        if (check!=0) return 2;
    }
    check = CalcVxc(&core, &core2, dsnum, &vxc, &vxc2);
    if (check!=0) return 3;
} else {
    SubtractGrid(&vxc, &vxc, &vxc);
    if (nspin==2) SubtractGrid(&vxc2, &vxc2, &vxc2);
}

if (maphart==1) {
    ScaleGrid(vhain, 0.5, vhain);
    AddGrid(potin, vhain, potin);
    if (nspin==2) {
        ScaleGrid(vhain2, 0.5, vhain2);

```

```

    AddGrid(potin, vhain2, potin);
}
} else {
    SubtractGrid(vhain, vhain, vhain);
    if (nspin==2) SubtractGrid(vhain2, vhain2, vhain2);
}
if (nspin==2) {
    AddGrid(denin, denin2, &temp2);
    MultiplyGrid(vhain2, &temp2, &temp); /* vhain1 is empty */
} else MultiplyGrid(vhain, denin, &temp);
p_hart[dsnum-1] = IntegrateGrid(&temp);
fprintf(cplog, " Hartree energy: %20.14f\n", p_hart[dsnum-1]);

if (nspin==2) {
    AddGrid(&core, &core2, &temp2);
    MultiplyGrid(&temp2, &vxc2, &temp);
} else MultiplyGrid(&core, &vxc, &temp); /* core = denin for HGH pseudopotentials */
p_xc[dsnum-1] = IntegrateGrid(&temp);
fprintf(cplog, "Exch-corr energy: %20.14f\n", p_xc[dsnum-1]);
if (p_xc[dsnum-1]!=p_xc[dsnum-1]) { /* undefined number */
    printf("\n BAD NEWS: The electron density is sometimes negative!\n");
    fprintf(cplog, "\nTerminated because of negative values in the electron density file\n");
    fprintf(cplog, "Suggestion: re-run Abinit with higher ecut or less empty space in the unit
cell\n");
    errcount++;
    return 3;
}

if (nspin==2) {
    AddGrid(denin, denin2, &temp2);
    MultiplyGrid(potin, &temp2, potin);
} else MultiplyGrid(potin, denin, potin); /* Vden(r) = V(r)*rho(r) potential energy density */
AddGrid(potin, &temp, potin); /* full potential including exchange-correlation */
fprintf(cplog, "Potential energy: %20.14f\n", IntegrateGrid(potin));
if (maploc==1 && IntegrateGrid(potin)>0.0) {
    printf("\n BAD NEWS: The potential energy is positive!\n");
    fprintf(cplog, "\nTerminated because total potential energy from DS%d is positive\n", dsnum);
    fprintf(cplog, "Suggestion: check your Abinit files for inconsistencies\n");
    errcount++;
    return 4;
}

if (mapkin==1 || mapkin==2) AddGrid(kdenin, potin, potin); /* total energy density */
if (nspin==2 && mapkin==1) AddGrid(kdenin2, potin, potin);
ScaleGrid(potin, denin->volvox, etotout); /* etot = grid of total voxel energies */
fprintf(cplog, "Total map energy: %20.14f\n\n", IntegrateGrid(etotout));
if (printen==1) {
    snprintf(enfile, STRMAX, "%s-emap%d.xsf", cpoutname, dsnum);
    fptr = fopen(enfile, "w");
    OutputXSF(fptr, denin, etotout);
    fclose(fptr);
}
return 0;
}

```

```

double PressureContrib(struct CrystData * gridinup, struct CrystData * gridin, struct CrystData *
gridindn, double pin_kin, double pin_loc, double pin_hart, double pin_xc, double * p_entropy,
double * p_mapcore, double * pout_nonloc, double * pout_ewald, double * pout_ealpha, double *
pout_kin, double * pout_loc, double * pout_hart, double * pout_xc) {
    /* called by: CalcCP */
    /* calls: ReadLine */
    char check=0, i=0, line[500], stop=0, str1[30], str2[30], str3[30];
    double dV=0.0, pin_map=0.0, pin_nonmap=0.0, pin_tot=0.0;
    double p_mapped=0.0, p_nonmapped=0.0, p_total=0.0;
    double E_core[3], E_entropy[3], E_ewald[3], E_hartree[3], E_int[3];
    double E_kinetic[3], E_locpsp[3], E_nonlocpsp[3], E_total[3], E_xc[3];
    FILE * fptr;
    fptr = fopen(abinitout, "r");
    if (fptr==NULL) {
        printf("\n BAD NEWS: File %s not found!\n", abinitout);
        fprintf(cplog, "\nTerminated because file %s not found\n", abinitout);
        fprintf(cplog, "Suggestion: check your files and input options\n");
        errcount++;
        return 0.0;
    }
    while (stop==0) {
        check = ReadLine(fptr, line);
        if (check==1) {
            printf("\n BAD NEWS: Energy data in %s not found!\n", abinitout);
            fprintf(cplog, "\nTerminated because total free energy list #d not found in %s\n", i+1,
abinitout);
            fprintf(cplog, "Suggestion: check %s or check if data matches format in CPpackage source
code\n", abinitout);
            errcount++;
            return 0.0;
        }
        if (strncmp(line, " Components of total free energy (in Hartree) :", 47)==0) {
            fscanf(fptr, "%s %s %s %lf", str1, str2, str3, &E_kinetic[i]);
            fscanf(fptr, "%s %s %s %lf", str1, str2, str3, &E_hartree[i]);
            fscanf(fptr, "%s %s %s %lf", str1, str2, str3, &E_xc[i]);
            fscanf(fptr, "%s %s %s %lf", str1, str2, str3, &E_ewald[i]);
            fscanf(fptr, "%s %s %s %lf", str1, str2, str3, &E_core[i]);
            fscanf(fptr, "%s %s %s %lf", str1, str2, str3, &E_locpsp[i]);
            fscanf(fptr, "%s %s %s %lf", str1, str2, str3, &E_nonlocpsp[i]);
            if (occopt==3) {
                fscanf(fptr, "%s %s %s %lf", str1, str2, str3, &E_int[i]);
                fscanf(fptr, "%s %s %lf", str1, str2, &E_entropy[i]);
            }
            fscanf(fptr, "%s %s %lf", str1, str2, &E_total[i]);
            i++;
        }
    }
    if (i==3) stop = 1;
}
fclose(fptr);
dV = gridindn->volcell-gridinup->volcell; /* negative sign */
*pout_kin = (E_kinetic[0]-E_kinetic[2])/dV;
*pout_hart = (E_hartree[0]-E_hartree[2])/dV;
*pout_xc = (E_xc[0]-E_xc[2])/dV;
*pout_ewald = (E_ewald[0]-E_ewald[2])/dV;
*pout_ealpha = (E_core[0]-E_core[2])/dV;

```

```

*pout_loc = (E_locpsp[0]-E_locpsp[2])/dV;
*pout_nonloc = (E_nonlocpsp[0]-E_nonlocpsp[2])/dV;
*p_entropy = (E_entropy[0]-E_entropy[2])/dV;
*p_mapcore = (en_core[0]-en_core[2])/dV;
printf("\n -----SUMMARY OF CP PRESSURE CONTRIBUTIONS-----\n");
fprintf(cplog, "-----SUMMARY OF CP PRESSURE CONTRIBUTIONS-----\n");
printf(" Mapped Contributions          ABINIT          CPmap\n");
fprintf(cplog, "Mapped Contributions          ABINIT          CPmap\n");
if (mapkin==1 || mapkin==2) {
    printf("          kinetic E pressure %12.8f %12.8f\n", *pout_kin, pin_kin);
    fprintf(cplog, "          kinetic E pressure %12.8f %12.8f\n", *pout_kin, pin_kin);
    p_mapped += *pout_kin;
    pin_map += pin_kin;
}
if (maploc==1) {
    printf("          local psp E pressure %12.8f %12.8f\n", *pout_loc, pin_loc);
    fprintf(cplog, "          local psp E pressure %12.8f %12.8f\n", *pout_loc, pin_loc);
    p_mapped += *pout_loc;
    pin_map += pin_loc;
}
if (maphart==1) {
    printf("          Hartree E pressure %12.8f %12.8f\n", *pout_hart, pin_hart);
    fprintf(cplog, "          Hartree E pressure %12.8f %12.8f\n", *pout_hart, pin_hart);
    p_mapped += *pout_hart;
    pin_map += pin_hart;
}
if (mapxc==1) {
    printf("          exch-corr E pressure %12.8f %12.8f\n", *pout_xc, pin_xc);
    fprintf(cplog, "          exch-corr E pressure %12.8f %12.8f\n", *pout_xc, pin_xc);
    p_mapped += *pout_xc;
    pin_map += pin_xc;
}
if (mapcore==1) {
    printf("          -restore core E pressure same as -> %12.8f\n", -*p_mapcore);
    fprintf(cplog, "          -restore core E pressure same as -> %12.8f\n", -*p_mapcore);
    p_mapped += -*p_mapcore;
    pin_map += -*p_mapcore;
}
printf(" -----\n");
fprintf(cplog, "-----\n");
printf("          Total mapped pressure %12.8f %12.8f\n", p_mapped, pin_map);
fprintf(cplog, "          Total mapped pressure %12.8f %12.8f\n", p_mapped, pin_map);
printf(" Non-mapped Contributions\n");
fprintf(cplog, "Non-mapped Contributions\n");
if (mapcore == 1) {
    printf("          restore core E pressure same as -> %12.8f\n", *p_mapcore);
    fprintf(cplog, "          restore core E pressure same as -> %12.8f\n", *p_mapcore);
    p_nonmapped += *p_mapcore;
    pin_nonmap += *p_mapcore;
}
if (mapkin!=1 && mapkin!=2) {
    printf("          kinetic E pressure %12.8f <- same as\n", *pout_kin);
    fprintf(cplog, "          kinetic E pressure %12.8f <- same as\n", *pout_kin);
}

```

```

    p_nonmapped += *pout_kin;
    pin_nonmap += *pout_kin;
}
if (maploc!=1) {
    printf("          local psp E pressure %12.8f  <- same as\n", *pout_loc);
    fprintf(cplog, "          local psp E pressure %12.8f  <- same as\n", *pout_loc);
    p_nonmapped += *pout_loc;
    pin_nonmap += *pout_loc;
}
if (maphart!=1) {
    printf("          Hartree E pressure %12.8f  <- same as\n", *pout_hart);
    fprintf(cplog, "          Hartree E pressure %12.8f  <- same as\n", *pout_hart);
    p_nonmapped += *pout_hart;
    pin_nonmap += *pout_hart;
}
if (mapxc!=1) {
    printf("          exch-corr E pressure %12.8f  <- same as\n", *pout_xc);
    fprintf(cplog, "          exch-corr E pressure %12.8f  <- same as\n", *pout_xc);
    p_nonmapped += *pout_xc;
    pin_nonmap += *pout_xc;
}
printf("          non-mapped Ewald E pressure %12.8f  <- same as\n", *pout_ewald);
fprintf(cplog, "          non-mapped Ewald E pressure %12.8f  <- same as\n", *pout_ewald);
p_nonmapped += *pout_ewald;
pin_nonmap += *pout_ewald;
printf("          psp core E pressure %12.8f  <- same as\n", *pout_ealpha);
fprintf(cplog, "          psp core E pressure %12.8f  <- same as\n", *pout_ealpha);
p_nonmapped += *pout_ealpha;
pin_nonmap += *pout_ealpha;
printf("          nonlocal psp E pressure %12.8f  <- same as\n", *pout_nonloc);
fprintf(cplog, "          nonlocal psp E pressure %12.8f  <- same as\n", *pout_nonloc);
p_nonmapped += *pout_nonloc;
pin_nonmap += *pout_nonloc;
if (occopt==3) {
    printf("          -kt*entropy pressure %12.8f  <- same as\n", *p_entropy);
    fprintf(cplog, "          -kt*entropy pressure %12.8f  <- same as\n", *p_entropy);
    p_nonmapped += *p_entropy;
    pin_nonmap += *p_entropy;
}
printf(" -----\n");
fprintf(cplog, " -----\n");
printf("          Total non-mapped pressure %12.8f %12.8f\n\n", p_nonmapped, pin_nonmap);
fprintf(cplog, "          Total non-mapped pressure %12.8f %12.8f\n\n", p_nonmapped, pin_nonmap);
p_total = (E_total[0]-E_total[2])/dV;
pin_tot = pin_map+pin_nonmap;
printf(" Total Pressure          %12.8f %12.8f\n", p_total, pin_tot);
fprintf(cplog, "Total Pressure          %12.8f %12.8f\n", p_total, pin_tot);
printf(" -----\n");
fprintf(cplog, " -----\n");
if (fabs((p_total-pin_tot))>1.0e-5) {
    printf("\n BAD NEWS: Pressures from Abinit and CP disagree!\n");
    fprintf(cplog, "\nTerminated because pressures from Abinit and CPmap disagree\n");
    fprintf(cplog, "Suggestion: check your files for odd behavior\n");
}

```

```

    errcount++;
    return 0.0;
}
return pin_tot;
}

int CalcCP(struct CrystData * denin_up, struct CrystData * denin, struct CrystData * denin_dn,
struct CrystData * etotin_up, struct CrystData * etotin_dn, struct CrystData * cpout) {
    /* called by: main */
    /* calls: CopyStruct, IntegrateGrid, PressureContrib, ScaleGrid, ShiftGrid, SubtractGrid,
SymmetrizeGrid */
    char cpfile[STRMAX];
    int check=0, i=0, stop=0, voxtot=ngx*ngy*ngz;
    double dV=0.0, hart=0.0, kin=0.0, loc=0.0, ptot=0.0, xc=0.0;
    double p_check=0.0, p_entropy=0.0, p_mapcore=0, p_remain=0.0;
    FILE * fptr;
    CopyStruct(denin, cpout); /* copies geometric information */
    dV = etotin_dn->volvox-etotin_up->volvox; /* smaller minus larger because p = -dE/dV */
    SubtractGrid(etotin_up, etotin_dn, cpout); /* cpout is energy difference here */
    cpout->volvox = (etotin_up->volvox+etotin_dn->volvox)/2.0;
    ScaleGrid(cpout, 1.0/dV, cpout);
    p_remain = IntegrateGrid(cpout)/(cpout->volvox*voxtot);
    if (mapcore==1 && mapsym==1) {
        printf(" Restoring symmetry after interpolation\n");
        check = SymmetrizeGrid(cpout, &smap);
        if (check!=0) return 1;
        p_check = IntegrateGrid(cpout)/(cpout->volvox*voxtot);
        if (fabs(p_remain-p_check)>1.0e-12) {
            fprintf(cplog, "WARNING: total pressure changed after symmetrization\n");
            fprintf(cplog, " before: %20.14f\n", p_remain);
            fprintf(cplog, " after: %20.14f\n", p_check);
            errcount++;
            if (fabs(p_remain-p_check)<1.0e-5) printf("\n CAUTION: Total pressure has changed!
Continuing anyway...\n");
            else {
                printf("\n BAD NEWS: Total pressure has changed!\n");
                fprintf(cplog, "\nTerminated because symmetrization caused a change in pressure\n");
                fprintf(cplog, "Suggestion: check Abinit outfile for correct nsym, symrel, and tnons\n");
                return 2;
            }
        }
    }
}
fprintf(cplog, "          dV/volume: %.6e\n", -dV/cpout->volvox);
fprintf(cplog, "CP before mapping: %.6e\n\n", p_remain);
p_kin[3] = p_kin[0]-p_kin[2];
p_loc[3] = p_loc[0]-p_loc[2];
p_hart[3] = p_hart[0]-p_hart[2];
p_xc[3] = p_xc[0]-p_xc[2];
kin = p_kin[3]/(dV*voxtot);
loc = p_loc[3]/(dV*voxtot);
hart = p_hart[3]/(dV*voxtot);
xc = p_xc[3]/(dV*voxtot);
ptot = PressureContrib(denin_up, denin, denin_dn, kin, loc, hart, xc, &p_entropy, &p_mapcore,
&p_nonloc[3], &p_ewald[3], &p_ealph[3], &p_kin[3], &p_loc[3], &p_hart[3], &p_xc[3]);

```

```

if (ptot==0.0) return 3;
if (rescp==3 && mapcore==1) p_remain = p_mapcore;
else if (rescp==3) p_remain = 0.0;
else if (rescp==2) {
    p_remain = -1.0*IntegrateGrid(cpout)/(cpout->volvox*voxtot);
    fprintf(cplog, "Homogenous background pressure = %.6e\n", p_remain);
} else if (rescp==1) {
    p_remain = 0.0;
    if (mapkin!=1 && mapkin!=2) p_remain += p_kin[3];
    if (maploc!=1) p_remain += p_loc[3];
    if (maphart!=1) p_remain += p_hart[3];
    if (mapxc!=1) p_remain += p_xc[3];
    if (mapcore==1) p_remain += p_mapcore;
    p_remain += p_entropy+p_ewald[3]+p_nonloc[3]+p_ealph[3];
}
ShiftGrid(cpout, p_remain, cpout);
p_remain = IntegrateGrid(cpout)/(cpout->volvox*voxtot);
printf(" Average CP of map = %.6e au\n", p_remain);
printf("           = %.6e GPa\n\n", p_remain*AU2GPA);
fprintf(cplog, "Average CP = %.6e au\n", p_remain);
fprintf(cplog, "           = %.6e GPa\n\n", p_remain*AU2GPA);
if (fabs(ptot-p_remain)>1.0e-5) {
    printf(" BAD NEWS: Average mapped pressure does not match DFT results!\n");
    fprintf(cplog, "\nTerminated because averaged mapped pressure does not match total in Abinit
outfile\n");
    fprintf(cplog, "Suggestion: check the Abinit outfile and potentials for odd behavior\n");
    errcount++;
    return 4;
}
snprintf(cpfile, STRMAX, "%s-CP.xsf", cpoutname);
fptr = fopen(cpfile, "w");
OutputXSF(fptr, denin, cpout);
fclose(fptr);
printf(" CP file %s is finished\n\n", cpfile);
return 0;
}

```

```

/* MAP INTEGRATION FUNCTIONS */

```

```

int SetBubbles(struct CrystData * gridin) {
    /* called by: main */
    /* calls: ElementName */
    char element[STRMAX];
    int i=0, j=0, stop[NIONMAX];
    for (i=0; i<gridin->nion; i++) {
        if (stop[i]==1) continue;
        ElementName(gridin->zatomic[i], element);
        if (smap.nequiv[i]>1) {
            fprintf(cplog, "Enter a core radius for atom #%d in Angstrom (%s, %d equivalent sites): ",
                i+1, element, smap.nequiv[i]);
        } else {
            fprintf(cplog, "Enter a core radius for atom #%d in Angstrom (%s, %d site): ",
                i+1, element, smap.nequiv[i]);
        }
    }
}

```

```

}
retry_radius:
if (smap.nequiv[i]>1) {
    printf(" Enter a core radius for atom #%d in Angstrom (%s, %d equivalent sites): ",
        i+1, element, smap.nequiv[i]);
} else {
    printf(" Enter a core radius for atom #%d in Angstrom (%s, %d site): ",
        i+1, element, smap.nequiv[i]);
}
scanf("%lf", gridin->corerad[i]);
if (gridin->corerad[i]<0.0) {
    printf(" Invalid input. Please try again\n");
    goto retry_radius;
}
fprintf(cplog, "%f Angstrom = %f bohr\n", gridin->corerad[i], gridin->corerad[i]/R_BOHR);
gridin->corerad[i] = gridin->corerad[i]/R_BOHR;
for (j=i; j<gridin->nion; j++) {
    if (smap.equiv[i][j]!=1) continue;
    gridin->corerad[j] = gridin->corerad[i];
    stop[j] = 1;
}
}
return 0;
}

int CoordSearch(struct CrystData * gridin, struct ContactVol * map) {
    /* called by: main */
    /* calls: Getwj */
    int atom=0, atom2=0, atom3[NEQVOX], index=0, i=0, j=0, jx=0, jy=0, jz=0;
    int ka1=0, kb1=0, kc1=0, ka2=0, kb2=0, kc2=0, ka3[NEQVOX], kb3[NEQVOX], kc3[NEQVOX];
    int ka=0, kb=0, kc=0, check[NEQVOX], ngcount=0, ngp=0, ngp0=0, voxtot=ngx*ngy*ngz;
    double dist=0.0, dmax=0.0, voxcenter_x=0.0, voxcenter_y=0.0, voxcenter_z=0.0;
    double wj_temp[NEQVOX], wmax=0.0, wmax2=0.0, xf=0.0, yf=0.0, zf=0.0, xc=0.0, yc=0.0, zc=0.0;
    printf("0%%");
    fflush(stdout);
    /* every voxel in the unit cell */
    for (jz=0; jz<ngz; jz++) {
        /* fractional coordinates */
        zf = (double)jz/(double)ngz;
        for (jy=0; jy<ngy; jy++) {
            yf = (double)jy/(double)ngy;
            for (jx=0; jx<ngx; jx++) {
                xf = (double)jx/(double)ngx;
                /* cartesian coordinates */
                voxcenter_x = xf*gridin->cella_x+yf*gridin->cellb_x+zf*gridin->cellc_x;
                voxcenter_y = xf*gridin->cella_y+yf*gridin->cellb_y+zf*gridin->cellc_y;
                voxcenter_z = xf*gridin->cella_z+yf*gridin->cellb_z+zf*gridin->cellc_z;
                for (i=0; i<NIONMAX; i++) check[i] = 0;
                map->neighcount[jx][jy][jz] = 0;
                map->neighcount2[jx][jy][jz] = 0;
                map->swj[jx][jy][jz] = 0.0;
                map->swjk[jx][jy][jz] = 0.0;
                wmax=0.0;
            }
        }
    }
}

```



```

    atom3[i] = map->ionmap[i][jx][jy][jz]&127;
    wj_temp[i] = map->wj[i][jx][jy][jz];
}
/* all pairs of atoms identified above near voxel jx, jy, jz */
for (i=0; i<map->neighcount2[jx][jy][jz]; i++) {
    ka1=ka3[i];
    kb1=kb3[i];
    kc1=kc3[i];
    atom=atom3[i];
    for (j=i+1; j<map->neighcount2[jx][jy][jz]; j++) {
        ka2=ka3[j];
        kb2=kb3[j];
        kc2=kc3[j];
        atom2=atom3[j];
        /* if the weight product of the two atoms is within tolerance */
        if (wj_temp[i]*wj_temp[j]>=wmax*wmax2*(1.0-tolerance)) {
            /* record individual atom information if not recorded before */
            if (check[i]==0) {
                check[i] = 1;
                index = map->neighcount[jx][jy][jz];
                map->neighkey[index][jx][jy][jz] = i;
                map->ionmap[index][jx][jy][jz] = ((ka1+3)<<13)+((kb1+3)<<10)+((kc1+3)<<7)+atom;
                map->swj[jx][jy][jz] += wj_temp[i];
                map->swjk[jx][jy][jz] += wj_temp[i]*wj_temp[i];
                map->neighcount[jx][jy][jz]++;
            }
            if (check[j]==0) {
                check[j] = 1;
                index = map->neighcount[jx][jy][jz];
                map->neighkey[index][jx][jy][jz] = j;
                map->ionmap[index][jx][jy][jz] = ((ka2+3)<<13)+((kb2+3)<<10)+((kc2+3)<<7)+atom2;
                map->swj[jx][jy][jz] += wj_temp[j];
                map->swjk[jx][jy][jz] += wj_temp[j]*wj_temp[j];
                map->neighcount[jx][jy][jz]++;
            }
        }
        /* determines longest atom-to-voxel distance for the log file */
        xc = gridin->xcart[atom]+ka1*gridin->cella_x+kb1*gridin->cellb_x+kc1*gridin-
>cellc_x;
        yc = gridin->ycart[atom]+ka1*gridin->cella_y+kb1*gridin->cellb_y+kc1*gridin-
>cellc_y;
        zc = gridin->zcart[atom]+ka1*gridin->cella_z+kb1*gridin->cellb_z+kc1*gridin-
>cellc_z;
        dist = sqrt((voxcenter_x-xc)*(voxcenter_x-xc)+(voxcenter_y-yc)*(voxcenter_y-yc)+
            (voxcenter_z-zc)*(voxcenter_z-zc));
        if (dist>dmax) dmax = dist;
        xc = gridin->xcart[atom2]+ka2*gridin->cella_x+kb2*gridin->cellb_x+kc2*gridin-
>cellc_x;
        yc = gridin->ycart[atom2]+ka2*gridin->cella_y+kb2*gridin->cellb_y+kc2*gridin-
>cellc_y;
        zc = gridin->zcart[atom2]+ka2*gridin->cella_z+kb2*gridin->cellb_z+kc2*gridin-
>cellc_z;
        dist = sqrt((voxcenter_x-xc)*(voxcenter_x-xc)+(voxcenter_y-yc)*(voxcenter_y-yc)+
            (voxcenter_z-zc)*(voxcenter_z-zc));
        if (dist>dmax) dmax = dist;
    }
}

```

```

    }
  }
  /* S(wj*wk)=1/2*S(wj)^2-S(wj^2); faster than looping through all j*k atom combinations */
  map->swjk[jx][jy][jz] = 0.5*(map->swj[jx][jy][jz]*map->swj[jx][jy][jz]-map-
>swjk[jx][jy][jz]);
  }
}
}
fprintf(cpllog, "Longest contact within %.2lf bohr was %.2lf bohr away\n", R_MAX, dmax);
fprintf(cpllog, "Adjust R_MAX and recompile to improve accuracy/speed as necessary\n", R_MAX,
dmax);
printf(" Finished\n");
return 0;
}

```

```

int AssignContact(struct ContactVol * map, struct CrystData * gridin) {
  /* called by: main */
  /* calls: none */
  int atom=0, atom2=0, index=0, index2=0, ngcount=0, ngp=0, ngp0=0, voxtot=ngx*ngy*ngz;
  int i=0, j=0, k=0, jx=0, jy=0, jz=0, ka=0, kb=0, kc=0, ka1=0, kb1=0, kc1=0, ka2=0, kb2=0,
kc2=0;
  double coeff=0.0, denom=0.0, numer=0.0, wmax=0.0, wmax2=0.0;
  for (i=0; i<7; i++) {
    for (j=0; j<7; j++) {
      for (k=0; k<7; k++) {
        for (atom=0; atom<gridin->nion; atom++) {
          for (atom2=0; atom2<gridin->nion; atom2++) {
            map->count[i][j][k][atom][atom2] = 0.0;
            map->total[i][j][k][atom][atom2] = 0.0;
          }
        }
      }
    }
  }
  printf("0%%");
  fflush(stdout);
  for (jz=0; jz<ngz; jz++) {
    for (jy=0; jy<ngy; jy++) {
      for (jx=0; jx<ngx; jx++) {
        ngcount++;
        ngp = ngcount*100/voxtot;
        if (ngp!=ngp0) {
          printf("\r%d%%", ngp);
          fflush(stdout);
        }
        ngp0 = ngp;
        wmax = -200.0;
        wmax2 = -100.0;
        for (i=0; i<map->neighcount2[jx][jy][jz]; i++) {
          if (wmax<map->wj[i][jx][jy][jz]) {
            wmax2 = wmax;
            wmax = map->wj[i][jx][jy][jz];
          } else if (wmax2<map->wj[i][jx][jy][jz]) wmax2 = map->wj[i][jx][jy][jz];
        }
      }
    }
  }
}

```

```

/* every possible pair of atoms identified by CoordSearch */
for (i=0; i<map->neighcount[jx][jy][jz]; i++) {
    kal = (map->ionmap[i][jx][jy][jz]>>13&7)-3;
    kbl = (map->ionmap[i][jx][jy][jz]>>10&7)-3;
    kcl = (map->ionmap[i][jx][jy][jz]>>7&7)-3;
    atom = map->ionmap[i][jx][jy][jz]&127;
    index = map->neighkey[i][jx][jy][jz];
    for (j=i+1; j<map->neighcount[jx][jy][jz]; j++) {
        ka2 = (map->ionmap[j][jx][jy][jz]>>13&7)-3;
        kb2 = (map->ionmap[j][jx][jy][jz]>>10&7)-3;
        kc2 = (map->ionmap[j][jx][jy][jz]>>7&7)-3;
        atom2 = map->ionmap[j][jx][jy][jz]&127;
        index2 = map->neighkey[j][jx][jy][jz];
        if (map->wj[index][jx][jy][jz]*map->wj[index2][jx][jy][jz]>=wmax*wmax2*(1.0-
tolerance)) {
            /* weight of ions i*j compared to sum of all weight products at voxel jx, jy, jz */
            coeff = map->wj[index][jx][jy][jz]*map->wj[index2][jx][jy][jz]/map-
>swjk[jx][jy][jz];
            /* sum of each ion pair's total weight contributions within the supercell */
            map->count[ka2-kal+3][kb2-kbl+3][kc2-kcl+3][atom][atom2] += coeff;
            /* as map->count but weighted by the pressure at each voxel */
            map->total[ka2-kal+3][kb2-kbl+3][kc2-kcl+3][atom][atom2] += coeff*gridin-
>grid[jx][jy][jz];
        }
    }
}
}
}
}
}
printf(" Finished\n");
/* every pair of atoms */
for (atom=0; atom<gridin->nion; atom++) {
    for (atom2=atom; atom2<gridin->nion; atom2++) {
        /* every cell in the supercell */
        for (ka=-kam; ka<=kam; ka++) {
            for (kb=-kbm; kb<=kbm; kb++) {
                for (kc=-kcm; kc<=kcm; kc++) {
                    if (atom==atom2 && ka==0 && kb==0 && kc==0) continue; /* skip self interaction */
                    numer = map->total[ka+3][kb+3][kc+3][atom][atom2]+map->total[-ka+3][-kb+3][-
kc+3][atom2][atom];
                    denom = map->count[ka+3][kb+3][kc+3][atom][atom2]+map->count[-ka+3][-kb+3][-
kc+3][atom2][atom];
                    /* total CP contribution of every ion pair / total number of voxels within their
influence */
                    map->average[ka+3][kb+3][kc+3][atom][atom2] = (denom==0.0)? 0.0 : numer/denom;
                    map->average[-ka+3][-kb+3][-kc+3][atom2][atom] = (denom==0.0)? 0.0 : numer/denom;
                }
            }
        }
    }
}
return 0;
}

```

```

int AverageContact(struct ContactVol * map, struct CrystData * gridin, struct CrystData *
gridout) {
    /* called by: main */
    /* calls: Cart2Sph, FixEdges */
    int i=0, j=0, jx=0, jy=0, jz=0, ka=0, kb=0, kc=0, ka2=0, kb2=0, kc2=0, l=0, m=0, voxcount=0;
    int atom=0, atom2=0, index=0, index2=0, ngccount=0, ngp=0, ngp0=0, voxtot=ngx*ngy*ngz;
    double coeff=0.0, cosmphi[L_MAX], sinmphi[L_MAX], tempcp=0.0, wmax=0.0, wmax2=0.0;
    double costheta=0.0, voxel_r=0.0, voxel_theta=0.0, voxel_phi=0.0, Y00=0.0;
    double voxcenter_x=0.0, voxcenter_y=0.0, voxcenter_z=0.0, xf=0.0, yf=0.0, zf=0.0;
    for (i=0; i<gridin->nion; i++) {
        gridout->voxcount[i] = 0;
        gridout->intCP[i] = 0;
        for (l=0; l<10; l++) {
            for (m=0; m<l+1; m++) {
                gridout->intYlm[i][l][2*m] = 0.0;
                gridout->intYlm[i][l][2*m+1] = 0.0;
            }
        }
    }
    Y00 = gsl_sf_legendre_sphPlm(0,0,0);
    printf("0%%");
    fflush(stdout);
    for (jz=0; jz<ngz; jz++) {
        zf = (double)jz/(double)ngz;
        for (jy=0; jy<ngy; jy++) {
            yf = (double)jy/(double)ngy;
            for (jx=0; jx<ngx; jx++) {
                xf = (double)jx/(double)ngx;
                ngccount++;
                ngp = ngccount*100/voxtot;
                if (ngp!=ngp0) {
                    printf("\r%d%%", ngp);
                    fflush(stdout);
                }
                ngp0 = ngp;
                tempcp = 0.0;
                for (i=0; i<map->neighcount[jx][jy][jz]; i++) {
                    ka = (map->ionmap[i][jx][jy][jz]>>13&7)-3;
                    kb = (map->ionmap[i][jx][jy][jz]>>10&7)-3;
                    kc = (map->ionmap[i][jx][jy][jz]>>7&7)-3;
                    atom = map->ionmap[i][jx][jy][jz]&127;
                    index = map->neighkey[i][jx][jy][jz];
                    for (j=i+1; j<map->neighcount[jx][jy][jz]; j++) {
                        ka2 = (map->ionmap[j][jx][jy][jz]>>13&7)-3;
                        kb2 = (map->ionmap[j][jx][jy][jz]>>10&7)-3;
                        kc2 = (map->ionmap[j][jx][jy][jz]>>7&7)-3;
                        atom2 = map->ionmap[j][jx][jy][jz]&127;
                        index2 = map->neighkey[j][jx][jy][jz];
                        /* weighted sum of CP from all ion pairs */
                        tempcp += map->wj[index][jx][jy][jz]*map->wj[index2][jx][jy][jz]*
                            map->average[ka2-ka+3][kb2-kb+3][kc2-kc+3][atom][atom2];
                    }
                }
            }
        }
    }
}

```



```

int PrintAverage(struct CrystData * gridin, struct CrystData * gridout) {
    /* called by: main */
    /* calls: ElementName */
    char element[10];
    int atom=0;
    double average=0.0;
    for(atom=0; atom<gridin->nion; atom++) {
        average = gridout->intCP[atom]/gridout->voxcount[atom];
        ElementName(gridin->zatomic[atom], element);
        printf(" Atom %d (%s) Integration Results\n", atom+1, element);
        printf(" around point (%.2f, %.2f, %.2f) Angstrom\n", gridin->xcart[atom]*R_BOHR,
            gridin->ycart[atom]*R_BOHR, gridin->zcart[atom]*R_BOHR);
        printf(" average over: %9.0f voxels\n", gridout->voxcount[atom]);
        printf(" l=0 coefficient: %+.2e a.u.\n", gridout->intYlm[atom][0][0]/gridout-
>voxcount[atom]);
        printf(" net pressure: %+.2e a.u.\n", average);
        printf(" %+.22.2f GPa\n\n", average*AU2GPA);
        fprintf(cplog, "Atom %d (%s) Integration Results\n", atom+1, element);
        fprintf(cplog, "around point (%.2f, %.2f, %.2f) Angstrom\n", gridin->xcart[atom]*R_BOHR,
            gridin->ycart[atom]*R_BOHR, gridin->zcart[atom]*R_BOHR);
        fprintf(cplog, "average over: %9.0f voxels\n", gridout->voxcount[atom]);
        fprintf(cplog, "l=0 coefficient: %+.2e a.u.\n", gridout->intYlm[atom][0][0]/gridout-
>voxcount[atom]);
        fprintf(cplog, "net pressure: %+.2e a.u.\n", average);
        fprintf(cplog, "%+.22.2f GPa\n\n", average*AU2GPA);
    }
    return 0;
}

int PrintCoeff(struct CrystData * gridin, struct CrystData * gridout) {
    /* called by: main */
    /* calls: none */
    char filename[STRMAX];
    int atom=0, l=0, m=0;
    FILE * fptr;
    strncpy(filename, cpoutname, STRMAX);
    strncat(filename, "-coeff", STRMAX);
    fptr = fopen(filename, "w");
    for(atom=0; atom<gridin->nion; atom++) {
        fprintf(fptr, "l_%dm_%d= %20.14f\n", 0, 0, gridout->intYlm[atom][0][0]/gridout-
>voxcount[atom]);
        for(l=1; l<lmax+1; l++) {
            fprintf(fptr, "l_%dm_%dp= %20.14f\n", l, 0, gridout->intYlm[atom][l][0]/gridout-
>voxcount[atom]);
            for(m=1; m<l+1; m++) {
                fprintf(fptr, "l_%dm_%dp= %20.14f\n", l, m, gridout->intYlm[atom][l][2*m-1]/gridout-
>voxcount[atom]);
                fprintf(fptr, "l_%dm_%dm= %20.14f\n", l, m, gridout->intYlm[atom][l][2*m]/gridout-
>voxcount[atom]);
            }
        }
    }
    fclose(fptr);
    return 0;
}

```

```

/* MAIN HELPER FUNCTIONS */

int SetOptions() {
    /* called by: main */
    /* calls: none */
    int ds_option=0, i=0;
    fprintf(cplog, "Selected custom options:\n");
    fprintf(cplog, "Mapped following energy terms: ");
    printf(" Map kinetic energy? [1=Yes] [2=Thomas-Fermi] ");
    scanf("%d", &mapkin);
    if (mapkin==1) fprintf(cplog, "kinetic ");
    else if (mapkin==2) fprintf(cplog, "Thomas-Fermi kinetic ");
    printf(" Map local energy?           [1=Yes] ");
    scanf("%d", &maploc);
    if (maploc==1) fprintf(cplog, "local ");
    printf(" Map Hartree energy?         [1=Yes] ");
    scanf("%d", &maphart);
    if (maphart==1) fprintf(cplog, "hartree ");
    printf(" Map exchange-correlation energy? [1=Yes] ");
    scanf("%d", &mapxc);
    if (mapxc==1) fprintf(cplog, "exchange-correlation");
    printf(" Use core unwarping (recommended)? [1=Yes] ");
    scanf("%d", &mapcore);
    if (mapcore==1) {
        printf(" Restore symmetry (recommended)? [1=Yes] ");
        scanf("%d", &mapsym);
    }
    fprintf(cplog, "\n");
    if (mapsym==1 && mapcore==1) fprintf(cplog, "With hirshfeld-inspired core unwarping and symmetry restoration\n");
    else if (mapsym==1) fprintf(cplog, "With hirshfeld-inspired core unwarping\n");
    retrycp:
    printf(" Add unmapped pressure homogeneously? [1=Yes] ");
    scanf("%d", &rescp);
    if (rescp!=1) {
        printf(" Subtract it homogeneously instead? [2=Yes] ");
        scanf("%d", &rescp);
    }
    if (rescp!=1 && rescp!=2) {
        printf(" Ignore it instead (not recommended)? [3=Yes] ");
        scanf("%d", &rescp);
    }
    if (rescp!=1 && rescp!=2 && rescp!=3) {
        printf(" Invalid option. Please choose again\n");
        goto retrycp;
    }
    fprintf(cplog, "Choice to handle remaining pressure = %d\n", rescp);
    retryscheme:
    printf(" Partition scheme? [1=Hirshfeld] [2=Distance] ");
    scanf("%d", &scheme);
    if (scheme!=1 && scheme!=2) {
        printf(" Invalid choice. Please try again\n");
        goto retryscheme;
    }
}

```

```

retrytolerance:
printf(" Percent tolerance?           [1=Default] ");
scanf("%lf", &tolerance);
if (tolerance<0.0 || tolerance>100.0) {
    printf(" Tolerance out of bounds. Please try again\n");
    goto retrytolerance;
} else tolerance = tolerance/100.0;
fprintf(cplog, "Scheme=%d with l_max=%d and tolerance=%.2f%% was used\n", scheme, lmax,
tolerance*100.0);
retrylmax:
printf(" Max l for spherical harmonics?   [6=Default] ");
scanf("%d", &lmax);
if (lmax<=0) {
    printf(" Invalid input. Please choose again\n");
    goto retrylmax;
} else if (lmax>L_MAX) {
    printf("\n BAD NEWS: Max l=%d is higher than expected!\n", lmax);
    fprintf(cplog, "\nTerminated because Max l=%d is >= than L_MAX=%d\n", lmax, L_MAX);
    fprintf(cplog, "Suggestion: increase the value of L_MAX and recompile\n");
    errcount++;
    return 1;
}
if (scheme==2) {
    printf(" Enter core 'bubble' radii?           [1=Yes] ");
    scanf("%d", &isradii);
}
printf(" Use datasets other than 1 through 3? [1=Yes] ");
scanf("%d", &ds_option);
if (ds_option==1) {
    printf(" Enter the number of the expanded dataset:   ");
    scanf("%d", &dshi);
    printf(" Enter the number of the equilibrium dataset: ");
    scanf("%d", &dseq);
    printf(" Enter the number of the contracted dataset:   ");
    scanf("%d", &dslo);
    fprintf(cplog, "Datasets DS%d, DS%d, DS%d were used\n", dshi, dseq, dslo);
}
printf(" Output potential maps as XSF files? [1=Yes] ");
scanf("%d", &printbin);
printf(" Output total energy maps?           [1=Yes] ");
scanf("%d", &printen);
if (mapcore==1) {
    printf(" Output map of new voxel volumes?       [1=Yes] ");
    scanf("%d", &printhmap);
}
printf(" Output voxel weight maps?           [1=Yes] ");
scanf("%d", &printvmap);
if (printbin==1) fprintf(cplog, "XSF files from binary potential files were output\n");
if (printen==1) fprintf(cplog, "Intermediate energy maps were output\n");
if (printhmap==1) fprintf(cplog, "Interpolated voxel maps were output\n");
if (printvmap==1) fprintf(cplog, "Voxel weight maps were output\n");
fprintf(cplog, "\n");
printf("\n");
return 0;

```

```

}

int ReadAll() {
    /* called by: main */
    /* calls: Den2XSF */
    Den2XSF(abinitname, dshi, "DEN", &denhi, &denhi2);
    Den2XSF(abinitname, dseq, "DEN", &deneq, &deneq2);
    Den2XSF(abinitname, dslo, "DEN", &denlo, &denlo2);
    if (mapkin==1) {
        Den2XSF(abinitname, dshi, "KDEN", &kdenhi, &kdenhi2);
        Den2XSF(abinitname, dseq, "KDEN", &kdeneq, &kdeneq2);
        Den2XSF(abinitname, dslo, "KDEN", &kdenlo, &kdenlo2);
    }
    Den2XSF(abinitname, dshi, "POT", &pothi, &pothi2);
    Den2XSF(abinitname, dseq, "POT", &poteq, &poteq2);
    Den2XSF(abinitname, dslo, "POT", &potlo, &potlo2);
    Den2XSF(abinitname, dshi, "VHA", &vhahi, &vhahi2);
    Den2XSF(abinitname, dseq, "VHA", &vhaeq, &vhaeq2);
    Den2XSF(abinitname, dslo, "VHA", &vhalo, &vhalo2);
    Den2XSF(abinitname, dshi, "VHXC", &vhxchi, &vhxchi2);
    Den2XSF(abinitname, dseq, "VHXC", &vhxceq, &vhxceq2);
    Den2XSF(abinitname, dslo, "VHXC", &vhxclo, &vhxclo2);
    fprintf(cplog, "\n");
    if (errcount!=0) return 1;
    volhi = denhi.volvox; /* global */
    voleq = deneq.volvox; /* global */
    vollo = denlo.volvox; /* global */
    return 0;
}

int ErrorCheck(double vol1, double vol2, double vol3) {
    /* called by: main */
    /* calls: none */
    int d1=0, d2=0, d3=0, d4=0, d5=0, d6=0, d7=0, d8=0;
    int d9=0, d10=0, d11=0, d12=0, d13=0, d14=0, d15=0;
    if (NIONMAX < deneq.nion) {
        printf("\n BAD NEWS: Too many atoms!\n");
        fprintf(cplog, "\nTerminated because nion (%d) > NIONMAX (%d)\n", deneq.nion, NIONMAX);
        fprintf(cplog, "Suggestion: increase NIONMAX and recompile CPpackage\n");
        errcount++;
        return 1;
    } else if (vol1<=vol2 || vol2<=vol3) {
        printf("\n BAD NEWS: Negative or no change in volume!\n");
        fprintf(cplog, "\nTerminated because change in volume is not positive\n");
        fprintf(cplog, "DS1 vol=%20.14f \nDS2 vol=%20.14f \nDS3 vol=%20.14f\n", vol1, vol2, vol3);
        fprintf(cplog, "Suggestion: check Abinit input file for discrepancies\n");
        errcount++;
        return 2;
    } else if (denhi.nion!=deneq.nion || deneq.nion!=denlo.nion) {
        printf("\n BAD NEWS: Unequal number of atoms between Abinit datasets!\n");
        fprintf(cplog, "\nTerminated because number of atoms is not equal\n");
        fprintf(cplog, "DS1 nion=%d, DS2 nion=%d, DS3 nion=%d\n", denhi.nion, deneq.nion,
denlo.nion);
        fprintf(cplog, "Suggestion: check your files for discrepancies\n");
    }
}

```

```

    errcount++;
    return 3;
}
return 0;
}

int AllocAll(double vol1, double vol2, double vol3) {
    /* called by: main */
    /* calls: none */
    int gridx=ngx+1, gridy=ngy+1, gridz=ngz+1, jx=0, jy=0;
    core.grid = (double***)malloc(gridx*sizeof(double**));
    cp.grid = (double***)malloc(gridx*sizeof(double**));
    cp_Y.grid = (double***)malloc(gridx*sizeof(double**));
    etothi.grid = (double***)malloc(gridx*sizeof(double**));
    etoteq.grid = (double***)malloc(gridx*sizeof(double**));
    etotlo.grid = (double***)malloc(gridx*sizeof(double**));
    temp.grid = (double***)malloc(gridx*sizeof(double**));
    vxc.grid = (double***)malloc(gridx*sizeof(double**));
    if (mapcore==1) {
        xnewup = (double***)malloc(gridx*sizeof(double**));
        ynewup = (double***)malloc(gridx*sizeof(double**));
        znewup = (double***)malloc(gridx*sizeof(double**));
        xnewdn = (double***)malloc(gridx*sizeof(double**));
        ynewdn = (double***)malloc(gridx*sizeof(double**));
        znewdn = (double***)malloc(gridx*sizeof(double**));
    }
    if (mapkin==2) {
        kdenhi.grid = (double***)malloc(gridx*sizeof(double**));
        kdeneq.grid = (double***)malloc(gridx*sizeof(double**));
        kdenlo.grid = (double***)malloc(gridx*sizeof(double**));
    }
    if (nspin==2) {
        core2.grid = (double***)malloc(gridx*sizeof(double**));
        temp2.grid = (double***)malloc(gridx*sizeof(double**));
        vxc2.grid = (double***)malloc(gridx*sizeof(double**));
    }
    for (jx=0; jx<gridx; jx++) {
        core.grid[jx] = (double**)malloc(gridy*sizeof(double*));
        cp.grid[jx] = (double**)malloc(gridy*sizeof(double*));
        cp_Y.grid[jx] = (double**)malloc(gridy*sizeof(double*));
        etothi.grid[jx] = (double**)malloc(gridy*sizeof(double*));
        etoteq.grid[jx] = (double**)malloc(gridy*sizeof(double*));
        etotlo.grid[jx] = (double**)malloc(gridy*sizeof(double*));
        temp.grid[jx] = (double**)malloc(gridy*sizeof(double*));
        vxc.grid[jx] = (double**)malloc(gridy*sizeof(double*));
        if (mapcore==1) {
            xnewup[jx] = (double**)malloc(gridy*sizeof(double*));
            ynewup[jx] = (double**)malloc(gridy*sizeof(double*));
            znewup[jx] = (double**)malloc(gridy*sizeof(double*));
            xnewdn[jx] = (double**)malloc(gridy*sizeof(double*));
            ynewdn[jx] = (double**)malloc(gridy*sizeof(double*));
            znewdn[jx] = (double**)malloc(gridy*sizeof(double*));
        }
    }
}

```

```

if (mapkin==2) {
    kdenhi.grid[jx] = (double**)malloc(gridy*sizeof(double*));
    kdeneq.grid[jx] = (double**)malloc(gridy*sizeof(double*));
    kdenlo.grid[jx] = (double**)malloc(gridy*sizeof(double*));
}
if (nspin==2) {
    core2.grid[jx] = (double**)malloc(gridy*sizeof(double*));
    temp2.grid[jx] = (double**)malloc(gridy*sizeof(double*));
    vxc2.grid[jx] = (double**)malloc(gridy*sizeof(double*));
}
for(jy=0; jy<gridy; jy++) {
    core.grid[jx][jy] = (double*)malloc(gridz*sizeof(double));
    cp.grid[jx][jy] = (double*)malloc(gridz*sizeof(double));
    cp_Y.grid[jx][jy] = (double*)malloc(gridz*sizeof(double));
    etothi.grid[jx][jy] = (double*)malloc(gridz*sizeof(double));
    etoteq.grid[jx][jy] = (double*)malloc(gridz*sizeof(double));
    etotlo.grid[jx][jy] = (double*)malloc(gridz*sizeof(double));
    temp.grid[jx][jy] = (double*)malloc(gridz*sizeof(double));
    vxc.grid[jx][jy] = (double*)malloc(gridz*sizeof(double));
    if (mapcore==1) {
        xnewup[jx][jy] = (double*)malloc(gridz*sizeof(double));
        ynewup[jx][jy] = (double*)malloc(gridz*sizeof(double));
        znewup[jx][jy] = (double*)malloc(gridz*sizeof(double));
        xnewdn[jx][jy] = (double*)malloc(gridz*sizeof(double));
        ynewdn[jx][jy] = (double*)malloc(gridz*sizeof(double));
        znewdn[jx][jy] = (double*)malloc(gridz*sizeof(double));
    }
    if (mapkin==2) {
        kdenhi.grid[jx][jy] = (double*)malloc(gridz*sizeof(double));
        kdeneq.grid[jx][jy] = (double*)malloc(gridz*sizeof(double));
        kdenlo.grid[jx][jy] = (double*)malloc(gridz*sizeof(double));
    }
    if (nspin==2) {
        core2.grid[jx][jy] = (double*)malloc(gridz*sizeof(double));
        temp2.grid[jx][jy] = (double*)malloc(gridz*sizeof(double));
        vxc2.grid[jx][jy] = (double*)malloc(gridz*sizeof(double));
    }
}
}
etothi.volvox = vol1;
etoteq.volvox = vol2;
etotlo.volvox = vol3;
fprintf(cplog, "Allocated memory for calculated data grids\n\n");
return 0;
}

int AllocInt(struct ContactVol * map) {
    /* called by: main */
    /* calls: none */
    int gridx=ngx+1, gridy=ngy+1, gridz=ngz+1, i=0, jx=0, jy=0;
    map->neighcount = (int***)malloc(gridx*sizeof(int**));
    map->neighcount2 = (int***)malloc(gridx*sizeof(int**));
    map->swj = (double***)malloc(gridx*sizeof(double**));
}

```

```

map->swjk = (double***)malloc(gridx*sizeof(double**));
for (jx=0; jx<gridx; jx++) {
    map->neighcount[jx] = (int**)malloc(gridy*sizeof(int*));
    map->neighcount2[jx] = (int**)malloc(gridy*sizeof(int*));
    map->swj[jx] = (double**)malloc(gridy*sizeof(double*));
    map->swjk[jx] = (double**)malloc(gridy*sizeof(double*));
    for (jy=0; jy<gridy; jy++) {
        map->neighcount[jx][jy] = (int*)malloc(gridz*sizeof(int));
        map->neighcount2[jx][jy] = (int*)malloc(gridz*sizeof(int));
        map->swj[jx][jy] = (double*)malloc(gridz*sizeof(double));
        map->swjk[jx][jy] = (double*)malloc(gridz*sizeof(double));
    }
}
for(i=0; i<NEQVOX; i++) {
    map->neighkey[i] = (int***)malloc(gridx*sizeof(int**));
    map->ionmap[i] = (int***)malloc(gridx*sizeof(int**));
    map->wj[i] = (double***)malloc(gridx*sizeof(double**));
    for(jx=0; jx<gridx; jx++) {
        map->neighkey[i][jx] = (int**)malloc(gridy*sizeof(int*));
        map->ionmap[i][jx] = (int**)malloc(gridy*sizeof(int*));
        map->wj[i][jx] = (double**)malloc(gridy*sizeof(double*));
        for(jy=0; jy<gridy; jy++) {
            map->neighkey[i][jx][jy] = (int*)malloc(gridz*sizeof(int));
            map->ionmap[i][jx][jy] = (int*)malloc(gridz*sizeof(int));
            map->wj[i][jx][jy] = (double*)malloc(gridz*sizeof(double));
        }
    }
}
fprintf(cplog, "Allocated memory for integration maps\n");
return 0;
}

int PrintResults(struct CrystData * gridin, struct CrystData * gridout) {
    /* called by: main */
    /* calls: ElementName, OutputWeight, PrintCoeff */
    char element[10], filename[STRMAX];
    int i=0;
    FILE * fptr;
    strncpy(filename, cpoutname, STRMAX);
    strcat(filename, "-averaged.xsf", STRMAX);
    fptr = fopen(filename, "w");
    OutputXSF(fptr, gridin, gridout);
    fclose(fptr);
    PrintCoeff(gridin, gridout);
    if (printvmap==1) OutputWeight(gridin, &vmap, gridout);
    strncpy(filename, cpoutname, STRMAX);
    strcat(filename, "-geo", STRMAX);
    fptr = fopen(filename, "w");
    for (i=0; i<gridin->nion; i++) {
        ElementName(gridin->zatomic[i], element);
        fprintf(fptr, "%s %20.14f %20.14f %20.14f\n", element,
            gridin->xcart[i]*R_BOHR, gridin->ycart[i]*R_BOHR, gridin->zcart[i]*R_BOHR);
    }
}

```

```

fclose(fptr);
strncpy(filename, cpoutname, STRMAX);
strncat(filename, "-cell", STRMAX);
fptr = fopen(filename, "w");
fprintf(fptr, "%20.14f %20.14f %20.14f\n", gridin->cella_x*R_BOHR, gridin->cella_y*R_BOHR,
gridin->cella_z*R_BOHR);
fprintf(fptr, "%20.14f %20.14f %20.14f\n", gridin->cellb_x*R_BOHR, gridin->cellb_y*R_BOHR,
gridin->cellb_z*R_BOHR);
fprintf(fptr, "%20.14f %20.14f %20.14f\n", gridin->cellc_x*R_BOHR, gridin->cellc_y*R_BOHR,
gridin->cellc_z*R_BOHR);
fclose(fptr);
printf(" Projections finished\n");
return 0;
}

/* MAIN FUNCTION */

int main(int argc, char * argv[]) {
/* calls: AllocAll, AssignContact, AverageContact, CalcCP, CoordSearch, CoreUnwarp, ErrorCheck,
GridStats, IdentifyXC, MapEntot, OutputXSF, PrintAverage, PrintResults, ReadAll, SetOptions
*/
char logname[STRMAX], option[STRMAX];
int errchk=0;

printf("\n FREDRICKSON GROUP DFT-CHEMICAL PRESSURE ANALYSIS\n");
printf(" What is the prefix of your Abinit _o_ files? ");
scanf("%s", abinitname);
printf(" What is the name of your Abinit outfile?      ");
scanf("%s", abinitout);
printf(" Choose a name for your CP output files:      ");
scanf("%s", cpoutname);
snprintf(logname, STRMAX, "%s-cplog", cpoutname);
cplog = fopen(logname, "w");
fprintf(cplog, "FREDRICKSON GROUP DFT-CHEMICAL PRESSURE ANALYSIS\n");
fprintf(cplog, "Last modified: 8 March 2016\n");

retry_default:
printf(" Would you like to use the defaults? [yes/no] ");
scanf("%s", &option);
if (option[0]=='N' || option[0]=='n') standard = 0;
else if (option[0]=='Y' || option[0]=='y') standard = 1;
else {
printf(" Invalid input. Please try again\n");
goto retry_default;
}
printf("\n");
fprintf(cplog, "Echo of input: %s %s %s %s\n", abinitout, abinitname, cpoutname, option);
fprintf(cplog, "All values are in a.u. unless otherwise noted\n\n");
if (standard==1) {
fprintf(cplog, "Selected default options:\n");
fprintf(cplog, "Map kinetic, local, hartree, and exchange-correlation energy terms\n");
fprintf(cplog, "With hirshfeld-inspired core unwarping and symmetry restoration\n");
fprintf(cplog, "And hirshfeld-inspired integration: l_max=%d and tolerance=%.2f%%\n\n", lmax,
tolerance*100);
}
}

```

```

} else {
    errchk = SetOptions(); /* user input of custom settings */
    if (errchk!=0) goto end;
}

if (mapcore==1 || scheme==1) printf(" Reading files. Please wait a moment to enter profile
names...\n");
else printf(" Reading files\n");
errchk = ReadAll(); /* assigns volhi, voleq, vollo */
if (errchk!=0) goto end;
if (mapcore==1 || scheme==1 || isradii==1) SymAtoms(&deneq, &smap);
if (mapcore==1 || scheme==1) {
    errchk = ReadProfile(&deneq); /* radial electron density profiles */
    if (errchk!=0) goto end;
}
if (isradii==1) SetBubbles(&deneq); /* bubble radii for distance-based contact volumes */
if (mapxc==1) {
    errchk = IdentifyXC(ixc); /* determine which XC functional was used in Abinit */
    if (errchk!=0) goto end;
}
errchk = ErrorCheck(volhi, voleq, vollo); /* check that volumes and ions make sense */
if (errchk!=0) goto end;

printf("\n Creating energy density maps\n");
errchk = AllocAll(volhi, voleq, vollo); /* allocate memory dynamically for voxel grids */
errchk = MapEntot(&denhi, &denhi2, &kdenhi, &kdenhi2, &pothi, &pothi2,
    &vhxchi, &vhxchi2, &vhahi, &vhahi2, dshi, volhi, &etothi);
if (errchk!=0) goto end;
errchk = MapEntot(&deneq, &deneq2, &kdeneq, &kdeneq2, &poteq, &poteq2,
    &vhxceq, &vhxceq2, &vhaeq, &vhaeq2, dseq, voleq, &etoteq);
if (errchk!=0) goto end;
errchk = MapEntot(&denlo, &denlo2, &kdenlo, &kdenlo2, &potlo, &potlo2,
    &vhxclo, &vhxclo2, &vhalo, &vhalo2, dslo, vollo, &etotlo);
if (errchk!=0) goto end;

errchk = Getkm(&deneq); /* determines appropriate supercell */
if (errchk!=0) goto end;
if (mapcore==1) {
    printf(" Performing core unwarping\n");
    errchk = CoreUnwarp(&denhi, &deneq, &denlo, &etothi, &etotlo);
    if (errchk!=0) goto end;
}

printf("\n Creating chemical pressure map\n");
errchk = CalcCP(&denhi, &deneq, &denlo, &etothi, &etotlo, &cp);
if (errchk!=0) goto end;
GridStats(&cp, "CP XSFile stats"); /* calculates statistical values of the voxel grid */
fclose(cplog); /* close to ensure writing of CPmap log */
cplog = fopen(logname, "a"); /* reopen for CPintegrate */

errchk = AllocInt(&vmap); /* allocate memory dynamically for integration grids */
printf(" Creating list of coordination\n");
errchk = CoordSearch(&cp, &vmap);
if (errchk!=0) goto end;

```

```

printf(" Assigning %d x %d x %d = %d voxels to contact volumes\n", ngx, ngy, ngz,
ngx*ngy*ngz);
AssignContact(&vmap, &cp);

printf(" Averaging within voxels\n");
AverageContact(&vmap, &cp, &cp_Y);
PrintAverage(&cp, &cp_Y); /* prints integrated CP to the screen and log file */
PrintResults(&cp, &cp_Y); /* makes all necessary files for Figuretool */
GridStats(&cp_Y, "Averaged CP XSFile stats");

end:
if (errcount==0) {
printf(" Logfile %s is ready to view. Goodbye!\n\n", logname);
fprintf(cplog, "Normal exit without incident\n");
} else {
printf(" Logfile %s is ready to view\n", logname);
if (errcount==1) printf(" There is %d warning\n\n", errcount);
else printf(" There are %d warnings\n\n", errcount);
fprintf(cplog, "\n*****\n");
fprintf(cplog, "Random errors can occur when nproc is not a factor of nkpt\n");
fprintf(cplog, "As a last resort re-run Abinit with 1 processor\n");
fprintf(cplog, "*****\n");
fprintf(cplog, "Last errchk value was %d\n", errchk);
if (errcount==1) fprintf(cplog, "Exited with %d warning\n", errcount);
else fprintf(cplog, "Exited with %d warnings\n", errcount);
}
fclose(cplog);
return 0; /* memory deallocation is handled automatically by the OS */
}

```